

# Superconducting hybrid devices in proximitized InAs two-dimensional electron gases

**Inauguraldissertation**

zur  
Erlangung der Würde eines Doktors der Philosophie  
vorgelegt der  
Philosophisch-Naturwissenschaftlichen Fakultät  
der Universität Basel

von

**Carlo Ciaccia**

Basel, 2024

Genehmigt von der Philosophisch-Naturwissenschaftlichen Fakultät  
auf Antrag von  
Erstbetreuer: Prof. Dr. Christian Schönenberger  
Zweitbetreuer: Prof. Dr. Dominik Zumbühl  
Externer Experte: Prof. Dr. Pasquale Scarlino

Basel, 27.02.2024

Prof. Dr. Marcel Mayor  
Dekan

# Contents

<b>1. Introduction</b>	<b>1</b>
<b>2. Theoretical Concepts</b>	<b>5</b>
2.1. 2DEG	5
2.1.1. Spin Orbit Interaction	8
2.2. Superconductivity	9
2.2.1. Effect of Finite Temperature	10
2.2.2. Effect of Finite Magnetic Field	12
2.3. Josephson Junctions	13
2.3.1. Semiconducting Weak Links	15
2.3.2. Probing the Josephson Effect	20
2.4. The Transmon Qubit	31
2.4.1. An Artificial Two-level System	32
2.4.2. Readout and Control	35
2.4.3. Flux and Gate Tunable Transmon	37
2.5. Josephson Parametric Amplifiers	41
<b>3. Materials</b>	<b>43</b>
3.1. Proximitized 2DEGs	43
3.2. InAs 2DEG on InP Substrate	45
3.2.1. Wafer Characterization	46
3.3. InAs 2DEG on GaAs Substrate	52
3.3.1. Wafer Characterization	53
3.4. Granular Aluminium	54
<b>4. Fabrication Procedures</b>	<b>57</b>
4.1. Epi-Al/InAs Devices	57
4.2. High Kinetic Inductance Resonators	60
4.2.1. NbTiN Sputtering	61
4.2.2. Granular Aluminium Evaporation	63
<b>5. Granular Aluminium Resonators on InP</b>	<b>69</b>
5.1. grAl at KIT	69
5.1.1. $Q_i$ Power Dependence	73
5.2. grAl at Uni Basel	75
5.2.1. Power Dependence	77
5.2.2. Temperature Dependence	78

5.2.3. Excess Quasiparticles Dynamics . . . . .	81
5.3. Conclusion . . . . .	83
<b>6. Gate-tunable Josephson Diode in Proximitized InAs Supercurrent Interferometers</b>	<b>85</b>
6.1. Introduction . . . . .	86
6.2. Device and Basic Properties . . . . .	88
6.3. Josephson Diode Effect . . . . .	91
6.4. Gate Tunable Diode Efficiency . . . . .	94
6.5. Conclusion . . . . .	97
<b>7. Charge-4e supercurrent in a two-dimensional InAs-Al superconductor-semiconductor heterostructure</b>	<b>99</b>
7.1. Introduction . . . . .	100
7.2. Results and Discussion . . . . .	102
7.2.1. Device and procedures . . . . .	102
7.2.2. Ac and dc Josephson effect from single junction . . . . .	104
7.2.3. Ac and dc Josephson effect from a SQUID . . . . .	107
7.2.4. Shapiro steps . . . . .	111
7.3. Conclusion . . . . .	112
<b>8. Hybrid SQUIDs for CQED</b>	<b>115</b>
8.1. Gate Tunable Transmon . . . . .	115
8.2. Flux and Gate Tunable Transmon . . . . .	119
8.2.1. Gate Response of Individual Junctions . . . . .	120
8.2.2. Flux Response . . . . .	123
8.3. Flux and Gate Tunable Josephson Parametric Amplifier . . . . .	125
8.3.1. Gate and Flux Response . . . . .	127
8.3.2. Gain . . . . .	128
8.4. Conclusions . . . . .	130
<b>9. Summary and Outlook</b>	<b>133</b>
<b>Bibliography</b>	<b>135</b>
<b>A. Extended Setup - grAl on InP</b>	<b>153</b>
<b>B. Gate Tunable JD - Supplementary</b>	<b>155</b>
B.1. Fabrication & Measurement Set-up . . . . .	155
B.2. Estimation of Loop Inductances . . . . .	156
B.3. Retrapping versus Switching Current . . . . .	157
B.4. SQUID Oscillations at Different Gate Voltages . . . . .	159
B.5. Model Including Loop Inductances . . . . .	160
B.6. Comparison to Diode Effect due to Loop Inductances . . . . .	161

---

B.7. Conditions for a Diode Effect in a SQUID Device . . . . .	162
<b>C. Charge-4e Supercurrent - Supplementary</b>	<b>165</b>
C.1. Methods . . . . .	165
C.2. Extended Setup Description . . . . .	165
C.3. Peaks amplitude dependence on External Flux . . . . .	167
C.4. Evolution of the 4e Peak amplitude with Gate voltages Configuration . . . . .	171
<b>D. Hybrid SQUIDs for CQED - Supplementary</b>	<b>175</b>
D.1. Extended Setup - Gate and Flux Tunable Transmon . . . . .	175
D.2. Two-tone Maps Individual Junctions . . . . .	177
D.3. Additional Two-tone Maps as a Function of Flux . . . . .	177
D.4. Extended Setup - Josephson Parametric Amplifier . . . . .	178
<b>E. Fabrication Recipes</b>	<b>181</b>
E.1. Epi-Al/InAs Devices . . . . .	181
E.2. NbTiN resonators . . . . .	185
E.3. GrAl resonators . . . . .	187
<b>Curriculum Vitae</b>	<b>189</b>
<b>Publications</b>	<b>191</b>
<b>Acknowledgements</b>	<b>193</b>



# 1 Introduction

---

The pursuit of understanding and harnessing quantum phenomena is a cornerstone of scientific exploration which has contributed to many technological advances, including quantum computation. The promises that quantum algorithms can be performed exponentially faster than their classical counterparts, has led scientists and engineers to build a new type of information processors based on so called quantum bits or qubits, basic computational units which store information in a superposition of quantum states [1, 2]. However, many challenges and open questions remain on the way to build a large scale functional quantum processor, such as improving the ability to write, control and readout the qubit state while at the same time decoupling it from external noise sources. To tackle these issues, numerous platforms have emerged including neutral atoms [3], trapped ions [4], semiconducting quantum dots [5] and superconducting circuits [6]. Within the field of solid state physics the leading platform is currently the one based on superconducting qubits. These qubits are constructed from collective electromagnetic modes of macroscopic electrical circuit elements and offer the attractive feature of having an energy spectrum which can be designed by the choice of circuit parameters. In addition to the qubit itself, a superconducting quantum processor also requires a set of low-dissipative components in order to control and readout the qubit, such as quantum-noise-limited parametric amplifiers.

To individually address qubit states in a superconducting circuit, a non linear element is required. The most common building block of superconducting quantum devices is the Josephson tunnel junction [7], a non-linear inductor that is made of two superconducting electrodes (S) separated by an insulating (I) tunnel barrier. For a sufficiently thin tunnel barrier, a supercurrent can flow between the electrodes, characterized by the so called current-phase relation (CPR). The CPR dictates the supercurrent flow depending on the phase drop of the superconducting order parameter across the electrodes. Therefore, the shape of the CPR also determines the Hamiltonian of the circuit and its use as a qubit [8], parametric amplifier [9, 10] or other devices, such as superconducting diodes [11]. By connecting two or more junctions in a loop, forming what is know as a superconducting quantum interference device (SQUID), it becomes possible to engineer an effective Josephson element with an arbitrary CPR, and consequently a system with an arbitrary Hamiltonian. The partic-

ular use of the device will depend not only on the CPR of the junction but as well on the circuit architecture designed around it. One limitation of using SIS junctions is that the shape of the CPR can hardly be modified after fabrication because it is fixed by the physical dimensions of the barrier.

A promising alternative is based on Josephson junctions made of a semiconducting weak link, for example a nanowire, a van der Waals material or a two-dimensional electron gas (2DEG). The gate tunability of the semiconductor allows tuning the CPR of the junction and loosens the constraints on the fabrication of hybrid semiconducting-superconducting devices. Furthermore, the CPR of hybrid junctions is not simply sinusoidal, as for SIS junctions, but contains higher order harmonics, and interference effects between these non-sinusoidal components at finite magnetic flux contributes additional flexibility to the device design [12–14]. With a semiconducting weak link and a non-sinusoidal CPR, it becomes possible to adjust the Hamiltonian of the system continuously and over a wide range with a loop consisting of only two junctions. Several circuit elements, including superconducting diodes [15, 16], qubits [17, 18] and parametric amplifiers [19] have already been realized using a single hybrid Josephson junction with a 2DEG as weak link. Here, the advantages of using a 2DEG are its wide gate tunability and top-down fabrication techniques, which are difficult to realize with nanowires and van der Waals materials. There are, however, some issues that affect 2DEGs, such as microwave losses and decoherence sources originating from the substrate which the material is grown upon and from the heterostructure itself.

In continuation of the results obtained with a single junction, in this thesis we report the realization of hybrid superconducting quantum devices using SQUIDs consisting of two planar Josephson junctions formed in an InAs 2DEG proximitized by an epitaxial aluminium layer [20, 21]. For the first time, we harness interference effects between the non-sinusoidal components of the CPR of these hybrid junctions to realize a gate and flux tunable superconducting diode. Using the same technique, we also investigate the performance of a qubit and a parametric amplifier based on hybrid SQUIDs. In addition, we probe the response of high impedance superconducting resonators on InP substrates, on top of which InAs 2DEGs are most commonly grown. We show that, at least for these type of resonators, the substrate is not a limiting factor. Our results pave the way for the realization of superconducting devices which can be operated in different regimes and tuned continuously from one regime to the other while maintaining a simple and minimalistic design.

The thesis is organized as follows. In Chapter 2 we present the underlying theoretical framework of 2DEGs and Josephson junctions. We discuss advantages and disadvantages of the two methods used later on in the thesis to probe



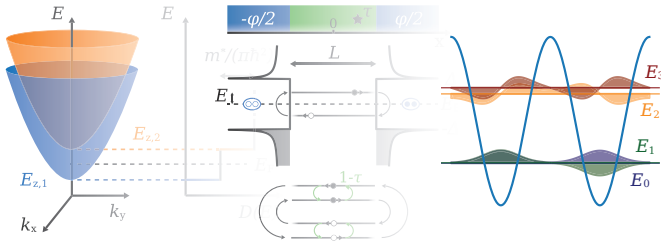
---

the Josephson effect, namely switching current experiments and Josephson radiation measurements. We also present the equations governing the Hamiltonian of one of the most popular superconducting qubit, the transmon, and give a brief introduction to parametric amplification. Chapter 3 describes the preliminary characterization procedures of the proximitized InAs 2DEGs used in this thesis and introduces granular aluminium, a high kinetic inductance superconductor with promising applications for high impedance superconducting circuits. Chapter 4 contains a detailed description of the fabrication procedures of both hybrid devices and evaporated/sputtered superconducting resonators. Next, we move to discuss specific experimental results. Chapter 5 investigates the microwave compatibility of granular aluminium resonators on InP substrates, outlining the limiting factors for the resonators quality factor. Chapter 6 investigates a gate-tunable Josephson diode in a two-dimensional hybrid SQUID. We discuss its properties and the maximum diode efficiency achieved. In Chapter 7, using the same device, we focus on the emergence of charge-4e supercurrent and introduce a novel method to deduce the harmonic content of highly transmissive Josephson junctions by performing Josephson radiation experiments. Chapter 8 explores the use of hybrid SQUIDs for circuit quantum electrodynamics. We show our results on a gate and flux tunable transmon as well as some preliminary results on a hybrid Josephson parametric amplifier. Finally, Chapter 9 concludes the thesis by summarizing key findings, discussing their implications, and outlining potential future directions.



## 2 Theoretical Concepts

---



In this chapter we discuss the key theoretical concepts required to understand the phenomena investigated in the thesis. Namely, we will outline the basic properties of a semiconducting two-dimensional electron gas (2DEG), we will cover superconductivity and the Josephson effect, and finally we will conclude with an overview on superconducting quantum circuits, such as the transmon qubit and the Josephson parametric amplifier.

### 2.1. 2DEG

The advent of 2DEGs has been the key to enable numerous milestone experiments within condensed matter physics, starting from the ones that investigate integer [22] and fractional quantum Hall effect [23], moving to ballistic transport studies such as conductance quantization [24], Aharonov-Bohm interference [25] and many more. Two-dimensional electron gasses are also the building block of High Electron Mobility Transistors (HEMTs), a crucial component for signal amplification in high-frequency electronics.

The motion of electrons in a 2DEG is confined in a two-dimensional plane by means of potential wells, or quantum wells (QW), obtained by engineering the band alignment of semiconducting heterostructures. These structures consist of several material layers grown via molecular beam epitaxy (MBE) under ultra-high-vacuum conditions, ensuring high compositional purity in each layer, defect-free interfaces and atomically precise layer thickness. The resulting minimal lattice disorder, and the confined electronic motion are the reasons for the high electron mobility observed in these systems. The mean free path

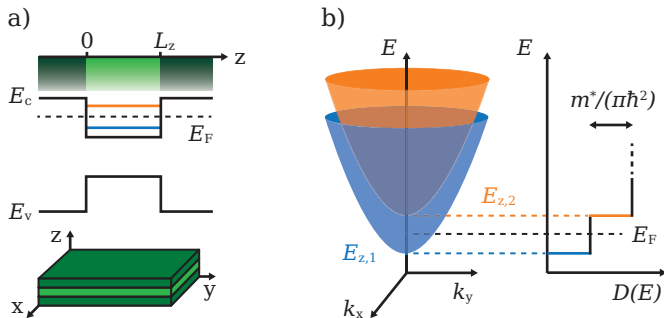


**Figure 2.1.** a) The two-dimensional electron gas (2DEG) is formed in a low band gap material (light green) of thickness  $L_z$ , sandwiched between two large band gap materials (dark green).  $E_c$   $E_v$  represent the conduction and valence band edge respectively. In this case, the Fermi energy  $E_F$  lies within the conducting band of the low gap material. Confinement in the  $z$ -direction leads to quantized energy levels (blue and orange) in the potential well formed by the band gap misalignment. b) Energy dispersion  $E$  as a function of the wave vectors  $k_x$  and  $k_y$ .  $E_{z,1}$  and  $E_{z,2}$  are the energies of the first two quantized states in the potential well. Step-like density of states  $D(E)$  corresponding to this type of energy dispersion.

$l_e$  measured in 2DEGs can be on the order of a few microns [26], making them an exceptional platform for exploring and studying quantum effects. Furthermore, MBE-grown heterostructures offer the possibility to precisely tune the elemental composition of each layer, allowing to realize potential wells tailored to the specific application.

Confining an electronic system involves imposing boundary conditions on the electron wavefunctions. As a consequence, both the wave vector  $k$  and the energy levels of the electrons will be quantized into discrete values. Let us consider the case of a small band gap material sandwiched between two large band gap materials. In Fig.2.1a) we plot the evolution of the bottom of the conduction band and the top of the valence band as determined by the materials crystal structure along the growth- $(z)$ -direction. We consider the case when the chemical potential at zero temperature, also called Fermi energy  $E_F$ , is located in the conduction band. The position of  $E_F$  depends on the materials forming the stack, and can be further adjusted by adding dopant layers during the heterostructure growth. In this case, electrons in the conduction band of the central semiconductor are trapped along  $z$  by potential barriers originating from discontinuities in the energy gap, whereas they are free to

move in the  $xy$ -plane. The width of the well is given by  $L_z$ , and the dimensions of the sample in the  $x$  and  $y$  direction are  $L_x$  and  $L_y$  respectively. The wavefunction and energies of the quantised states can be calculated by solving the Schrödinger equation within the effective mass approximation, which treats charge carries moving in the periodic potential of the lattice as if they were free particles with an effective mass  $m^*$  [27].

We divide the problem in two parts: the free motion in the  $xy$ -plane, and the confined motion along the  $z$ -axis. The total wavefunction can be written as:

$$\Psi(x, y, z) = \phi(x, y)\psi(z). \quad (2.1)$$

Since in the  $xy$ -plane the motion is free, electron wavefuntions are described by plane waves of the form:

$$\phi(x, y) = \frac{1}{L_x L_y} e^{i(k_x x + k_y y)}, \quad (2.2)$$

where  $k_x$  and  $k_y$  are the electron wave vectors in the  $x$  and  $y$  direction. The energy corresponding to this motion is the kinetic energy of a free electron with effective mass  $m^*$  which is given by  $E_{xy}(k_x, k_y) = \hbar^2(k_x^2 + k_y^2)/(2m^*)$ .

To find the expression of  $\psi(z)$  instead, it is necessary to know the expression of the confining potential  $V(z)$  and solve the Schrödinger equation:

$$-\frac{\hbar^2}{2m^*} \frac{\partial^2 \psi(z)}{\partial z^2} + V(z)\psi(z) = E_z \psi(z). \quad (2.3)$$

Here we consider the simplest case of infinitely high confining barriers. The general solution of  $\psi(z)$  inside the well can be written as a combination of forward and backward propagating plane waves:

$$\psi(z) = A e^{i(k_z z)} + B e^{-i(k_z z)}, \quad (2.4)$$

where  $k_z$  is the electron wave vector in the  $z$  direction. Since the barrier are infinitely high, we impose  $\psi(0) = \psi(L_z) = 0$ . As a consequence, only quantized values of  $k_z$  are permitted within the well, specifically in units of  $k_{z,n} = \frac{\pi n}{L_z}$  with  $n$  being an integer. The allowed energy levels in the well will also be quantized  $E_{z,n} = \hbar^2 k_{z,n}^2 / (2m^*)$  with energy spacing between two consecutive levels proportional to  $\frac{1}{L_z^2}$ . In practical cases, without infinite barriers, the exact values of  $E_{z,n}$  and their separation will depend on the shape of the confining potential. In Fig. 2.1b) we plot the total energy dispersion relation  $E = E_{z,n} + E_{xy}(k_x, k_y)$ , consisting of  $n$  parabolic sub-bands vertically shifted by  $E_{z,n}$ .

Assuming spin degenerate energy levels, the density of states per sub-band in a two-dimensional system is a constant value given by  $D(E) = m^*/(\pi\hbar^2)$  [27, 28]. Knowing the expression of  $D(E)$  allows us to compute the density of electrons  $n_e$  in a 2DEG. When a single sub-band is occupied,  $n_e$  is given by:

$$n_e = \int_{E_{z,1}}^{E_F} D(E)dE = \frac{m^*}{\pi\hbar^2}(E_F - E_{z,1}) = \frac{k_F^2}{2\pi}, \quad (2.5)$$

where we have written  $(E_F - E_{z,1}) = \frac{\hbar^2 k_F^2}{2m^*}$  in terms of the Fermi wave vector  $k_F$ . The Fermi velocity and Fermi wavelength are instead defined as  $v_F = \hbar k_F/m^*$  and  $\lambda_F = 2\pi/k_F$  respectively.

Another important parameter of a 2DEG is the electron mobility  $\mu$ , defined as the change in the electrons drift velocity  $v_d$  with respect to the applied electric field [27, 28]. Both  $\mu$  and  $n_e$  can be determined from Hall bar measurement as described in Section 3.2. From such measurements, the electron mean free path can be calculated as [28]:

$$l_e = v_d\tau_e \approx v_F\tau_e = \frac{\hbar\mu\sqrt{2\pi n_e}}{e}, \quad (2.6)$$

where we have approximated the drift velocity with the Fermi velocity, and have written the average scattering time of electrons as  $\tau_e = m^*\mu/e$ . The electron mean free path is one of the reference length scales which determine the transport regime of our devices.

The 2DEGs investigated in this thesis are formed in a 7 nm-thick InAs layer sandwiched between two  $\text{In}_{1-x}\text{Ga}_x\text{As}$  barrier. A detailed description of the heterostructure together with a discussion of the 2DEG transport properties are presented in Chapter 3.

### 2.1.1. Spin Orbit Interaction

In the previous section we have neglected the effect of the electron spin and derived a doubly degenerate energy dispersion  $E_\uparrow(\vec{k}) = E_\downarrow(\vec{k})$  for spin  $\uparrow$  and spin  $\downarrow$  electrons, characterized by  $\vec{k} = (k_x, k_y)$ . Introducing an external magnetic field  $\vec{B}$  allows us to differentiate the spin-degenerate sub-bands, which get split by the Zeeman energy  $E_Z = E_\uparrow - E_\downarrow = g\mu_B B$  [28], where  $g$  is the Lande g-factor and  $\mu_B$  is the Bohr's magneton.

In addition, when electrons traverse the crystal with momentum vector  $\vec{k}$ , they encounter an effective magnetic field caused by their interaction with the

electric field of the lattice, denoted as  $\vec{\mathcal{E}}$ . This effect, known as the spin-orbit interaction (SOI), gives rise to [28]:

$$\vec{B}_{\text{SO}} = -\frac{1}{2} \frac{\hbar}{c^2 m_e} \vec{k} \times \vec{\mathcal{E}}, \quad (2.7)$$

where  $m_e$  is the electron mass and  $c$  is the speed of light in vacuum.

As a consequence, analogously to the effect of an external magnetic field, SOI can lift the degeneracy of the electron energy dispersion. In general, this effect is stronger in crystals composed of elements with large nuclear charge (consequently large  $\vec{\mathcal{E}}$ ) and with broken spatial inversion symmetry. In two-dimensional systems, we can identify two influences related to SOI which affect the dispersion within a specific energy band. On one hand, crystal lattice asymmetries are responsible for the Dresselhaus contribution, and on the other hand, structure inversion asymmetries, produced by the confinement potential of the heterostructure are responsible for the Rashba contribution. The Hamiltonian for a 2DEG in a zincblende crystal in the presence of SOI can be approximated by [28]:

$$H_{\text{SO}} = H_0 + \alpha_{\text{R}}(\sigma_x k_y - \sigma_y k_x) + \beta_{\text{D}}(\sigma_x k_x - \sigma_y k_y), \quad (2.8)$$

where  $\sigma_x$  and  $\sigma_y$  are the components of the Pauli spin vector in the  $x$ - and  $y$ -direction.  $H_0$  is the electrons Hamiltonian in the absence of SOI, while the coefficients  $\alpha_{\text{R}}$  and  $\beta_{\text{D}}$  describe the Rashba and Dresselhaus contribution to SOI respectively.

The dominant SOI contribution in InAs 2DEGs is the Rashba term [28, 29]. This can be electrically tuned via a top gate voltage producing additional electric field in the growth direction [30–32]. While in this thesis we will not make direct use of the spin dependent energy dispersion in the 2DEG, we wanted to point it out here because of its promising applications in spin qubits [33–37].

## 2.2. Superconductivity

Superconductivity stands as one of the most intriguing phenomena in physics, featuring materials that below a certain critical temperature  $T_c$  conduct electricity without any resistance and expel magnetic fields. This section aims to investigate the fundamental aspects behind this intriguing behaviour, exploring the quantum mechanics and macroscopic phenomena that define the unique properties of superconductors.

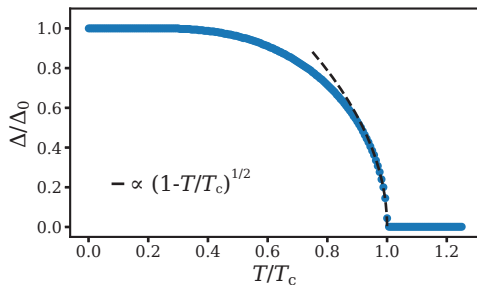


**Figure 2.2.** a) Temperature dependence of the superconducting gap  $\Delta$  numerically evaluated from BCS theory [41] The black dashed line shows the approximate analytical dependence for  $T \sim T_c$ .

At a microscopic scale, the behaviour of a superconductor reflects the dynamics of its charge carriers, and in particular the properties of their collective motion. According to the Bardeen-Cooper-Schrieffer (BCS) theory of conventional superconductors, electrons with opposite spin and momentum in these materials form Cooper pairs and condense into a common ground state [38]. The superconducting condensate is characterized by a complex order parameter or energy gap with magnitude  $\Delta$  corresponding to the strength of the pairing interaction, and with a phase factor  $e^{i\varphi}$  which represents the macroscopic coherence of the system. The attractive interaction that causes electrons at the Fermi energy to form Cooper pairs creates a gap in the single-particle density of states where scattering would normally occur. The BCS theory predicts the following expression for the density of states of quasiparticle excitations out of the superconducting ground state [39]:

$$D_s(E) = D(E_F) \frac{|E|}{\sqrt{E^2 - \Delta^2}} \theta(|E| - \Delta), \quad (2.9)$$

where  $D(E_F)$  is the density of states at the Fermi energy in the normal state, and  $\theta$  is the Heaviside function. The absence of available states within the gap leads to the phenomenon of zero-resistance current flow. The expulsion of magnetic field from the bulk of superconductor, the so called Meissner effect [40], is instead caused by a dissipationless screening current flowing in a narrow region below the surface.

### 2.2.1. Effect of Finite Temperature

At zero temperature and magnetic field the superconducting energy gap can be expressed within the BCS theory as

$$\Delta_0 = 1.76 k_B T_c. \quad (2.10)$$



As the temperature of the system is increased, thermal energy disrupts the pairing and forms normal-conducting excitations, also called quasiparticles, out of the superconducting ground state. Eventually, above  $T_c$ , the material reverts to its normal, non-superconducting state.

The temperature dependence of the gap can be computed numerically using BCS theory [41]. This is shown in Fig. 2.2:  $\Delta$  remains nearly constant up to  $\sim 0.4T_c$  and drops to zero near  $T_c$ . The gap dependence for  $T \approx T_c$  can be approximated as [41]:

$$\frac{\Delta(T)}{\Delta_0} \approx 1.74 \left(1 - \frac{T}{T_c}\right)^{1/2}, \quad (2.11)$$

depicted by the black dashed line.

The density of thermal quasiparticles  $n_{\text{QP}}$  at temperature  $T$  is given by [42, 43]:

$$n_{\text{QP}} = D(E_F) \sqrt{2\pi\Delta k_B T} e^{-\frac{\Delta}{k_B T}}, \quad (2.12)$$

where  $D(E_F)$  is the density of states at the Fermi energy in the normal state.

It is important to notice that although superconductors conduct dc current without any resistance, at finite frequencies the excitation of quasiparticles adds dissipation to the circuit. This can be understood by modelling the ac response of the superconductor with a two-fluid model, which considers the total response as the sum of the contribution from  $n_s$  superconducting electrons and  $n_n$  normal electrons. Within this model, the complex conductivity of a superconducting wire is written as [41]:

$$\sigma(\omega) = \sum_{j=n,s} [\sigma_{1j}(\omega) - i\sigma_{2j}(\omega)], \quad \text{with} \quad (2.13)$$

$$\sigma_{1j} = \frac{n_j e^2 \tau_j}{m_e} \frac{1}{1 + \omega^2 \tau_j^2}, \quad (2.14)$$

$$\sigma_{2j} = \frac{n_j e^2 \tau_j}{m_e} \frac{\omega \tau_j}{1 + \omega^2 \tau_j^2}, \quad (2.15)$$

where  $\tau_n$  and  $\tau_s$  are the average scattering times of the two fluids,  $m_e$  is the electron mass, and  $\omega$  is the frequency of the applied ac field. For  $\tau_s \rightarrow \infty$  the real part of the conductivity  $\sigma_{1s}$  becomes proportional to a Dirac delta function  $\delta(\omega)$ . This reflects the fact that for a dc field, the superconductor response is dissipationless. However, at all non zero frequencies the normal fluid contribution will cause finite dissipation. Even at temperatures well below  $T_c$ , non-thermal quasiparticles produced, for example, by electromagnetic

noise or by the impact of high energy particles on the substrate, will limit the ac response of the superconductor [44–46].

The imaginary part of the conductivity  $\sigma_{2s}$  for  $\tau_s \rightarrow \infty$  instead is a measure of the inertia of superconducting charge carriers. Being the scattering time divergent, the ac field will have to overcome a finite inertia of the charge carriers in order to drive the superconducting fluid. This is commonly referred to as the kinetic inductance  $L_{\text{kin}}$  of the superconductor. For  $\omega \rightarrow 0$  its value is obtained by setting:

$$\frac{1}{Z} = -\frac{i}{\omega L_{\text{kin}}} = \frac{tW}{l} \sigma_{2s} \rightarrow L_{\text{kin}} = \frac{l}{tW} \frac{m_e}{n_s e^2}. \quad (2.16)$$

Here  $Z$  represents the wire impedance,  $t$  is the film thickness, and  $W$  and  $l$  stand for the wire width and length respectively. In the design of superconducting circuits, the kinetic inductance becomes an important parameter in case of thin films of disordered superconductors.

The kinetic inductance of the condensate in the low frequency limit ( $0 \ll \hbar\omega \ll 2\Delta_0$ ) can be related to the normal state resistance of the wire  $R_n$  by [41, 47, 48]:

$$L_{\text{kin}/\square} = \frac{\hbar R_n}{\pi \Delta_0} \frac{W}{l} \tanh^{-1} \left( \frac{\Delta_0}{2k_B T} \right), \quad (2.17)$$

Based on this simple relation, given the superconducting gap or the critical temperature, it is possible to estimate the kinetic inductance in the superconducting state by measuring the normal-state resistance.

### 2.2.2. Effect of Finite Magnetic Field

Applying an external magnetic field breaks the degeneracy of electrons with opposite spin and momentum involved in the formation of Cooper pairs, and eventually destroys the superconducting state. Two important length scales have to be defined when describing response of a superconductor to a magnetic field: the coherence length  $\xi$  and the penetration depth  $\lambda_p$ .

The coherence length is the distance over which electrons participating in the pairing will propagate during the interaction time  $\hbar/\Delta$  and it is typically associated to the size of the Cooper pairs. For crystalline superconductors it is given by  $\xi_0 = \hbar v_F/\Delta$ , while for disordered superconductors in the diffusive regime  $l_e < \xi_0$  it reduces to [39]:

$$\xi = \sqrt{\frac{\hbar D}{2\Delta}}, \quad (2.18)$$

where  $D = v_F l_e / 2$  is the electrons diffusion coefficient in 2D.

As previously mentioned, superconductors tend to expel external magnetic fields by reactive screening currents flowing in a region close to the surface. The thickness of this region, across which the magnetic field decays exponentially, is the superconductor penetration depth  $\lambda_p$ . In case of magnetic fields homogeneous over the superconductor coherence length,  $\lambda_p$  can be approximated with the value found by the London theory [49]:

$$\lambda_L = \left( \frac{m_e}{\mu_0 n_s e^2} \right)^{1/2}. \quad (2.19)$$

However, in the presence of disorder, the mean free path is reduced and the ability of the condensate to screen external magnetic fields is weakened. This is approximated by an effective increased penetration depth [41]:

$$\lambda_{p,\text{eff}} = \lambda_L \left( 1 + \frac{\xi_0}{l_e} \right)^{1/2}. \quad (2.20)$$

The behaviour of superconductors in a magnetic field depends on the relative values of the penetration depth and the coherence length. In so called type-I superconductors, where  $\lambda_p < \xi$ , the magnetic field is expelled from the bulk up to a critical magnetic field  $B_c$  after which superconductivity is destroyed at once. In contrast, if  $\lambda_p > \xi$ , above a first critical field value  $B_{c1}$ , it becomes thermodynamically favoured for the magnetic field to penetrate the superconductors in units of flux quantum  $\Phi_0 = h/(2e)$ . The magnetic field penetrates in the form of so called Abrikosov vortices, which are normal regions separated from the superconducting regions by circulating screening currents. The density of vortices increases with magnetic field until a second critical value  $B_{c2}$ , above which superconductivity is fully destroyed. Although magnetic vortices create areas with decreased superconducting gap, serving as quasiparticles traps [50, 51], uncontrolled vortex motion within a quantum circuit acts as a noise source [52].

For conventional bulk superconductors,  $\lambda_p \sim 50$  nm and  $\xi \sim 1.6$   $\mu\text{m}$  [53, 54], so that they show type-I behaviour. However, in thin films, the mean free path decreases due to scattering at the film boundaries, leading to a larger  $\lambda_p$  and a smaller  $\xi$ . As a consequence, superconductors that are of type-I in bulk can become type-II in thin films.

## 2.3. Josephson Junctions

The Josephson effect describes the dissipationless current flow between two superconducting electrodes separated by a weak link. The effect is named after

B. D. Josephson who theoretically predicted the effect for two superconductors separated by a thin insulating barrier in 1962 [55]. Afterwards, supercurrent flow was observed with any kind of material or constriction that would locally weaken the superconducting condensate.

In this type of junctions, commonly referred to as Josephson junctions (JJs), the dissipationless current of Cooper pairs is induced by a difference in the macroscopic phases between the superconducting electrodes  $\varphi = \varphi_1 - \varphi_2$ , and it is sustained up to a critical current value  $I_c$ . The relation between the current  $I$  flowing through the JJ and  $\varphi$  is called current-phase relation (CPR), and its analytical expression depends on the type of weak link. For a superconductor-insulator-superconductor (SIS) junction, the CPR takes the form of the first Josephson equation:

$$I = I_c \sin(\varphi). \quad (2.21)$$

Passing a constant dc current  $I$  through a JJ will result in a constant phase difference  $\varphi = \arcsin(I/I_c)$  (modulo  $2\pi$ ). At  $I = I_c$ , the phase is equal to its critical value  $\varphi_c$  corresponding to the maximum of the CPR. For a sinusoidal JJ  $\varphi_c = \pi/2$ . We notice that the other solution for the phase at constant bias current  $\varphi = \pi - \arcsin(I/I_c)$  (modulo  $2\pi$ ) is a local maxima in the potential energy  $E_{\text{pot}}$  of the junction [56], and therefore is unstable.

When  $I$  exceeds  $I_c$ , the junction switches to the normal state and develops a finite voltage drop. According to the second Josephson equation, this voltage drop is determined by the time evolution of the phase difference across the electrodes as [41]:

$$V = \frac{\hbar}{2e} \frac{\partial \varphi}{\partial t} = \frac{2\pi}{\Phi_0} \frac{\partial \varphi}{\partial t}. \quad (2.22)$$

Taking the time derivative of the CPR and making use of the second Josephson relation in Eq (2.22), we obtain:

$$\frac{\partial I}{\partial t} = \frac{\partial I}{\partial \varphi} \frac{\partial \varphi}{\partial t} = \frac{2e}{\hbar} \frac{\partial I}{\partial \varphi} V. \quad (2.23)$$

From the above equation we see that JJs effectively behave as non linear inductors. The inductance of the Josephson junction, an essential component of many quantum circuits, can be written as:

$$L_J(\varphi) = \left( \frac{2\pi}{\Phi_0} \frac{\partial I(\varphi)}{\partial \varphi} \right)^{-1}. \quad (2.24)$$

At zero phase in a SIS junction,  $L_J$  becomes  $\frac{2\pi}{\Phi_0 I_c}$ .

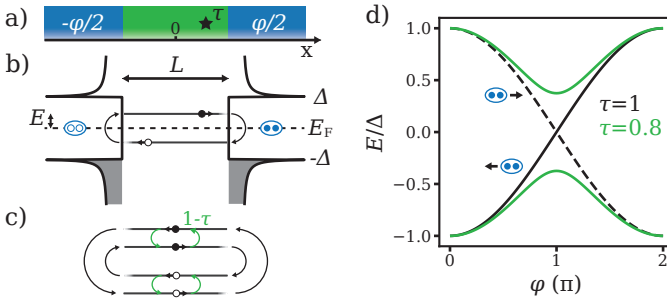


**Figure 2.3.** a) A hybrid Josephson junction formed by a semiconducting weak link (green) of length  $L$  sandwiched between two superconducting electrodes (blue). A phase difference of  $\varphi$  is applied between the electrodes. The transmission probability across the weak link is limited to  $\tau \in [0, 1]$  by local impurities which are depicted as a star. b) An electron with excitation energy  $E$  is Andreev reflected into a hole which then undergoes the same process at the opposite interface. If the phase acquired in a round trip is a multiple of  $2\pi$ , Andreev bound state (ABS) will form. c) Local impurities couple electrons at the same excitation energy moving left and right. d) Energy dispersion of ABS at  $\tau = 1$  and  $\tau = 1$  for a short junction  $L \ll \xi$ . When  $\tau = 1$ , the energy dispersion for right moving (solid line), and left moving (dashed line) electrons is degenerate at  $\varphi = \pi$ . This degeneracy is lifted for  $\tau \neq 1$ .

In the following we will discuss the expression for the CPR of a Josephson junction where the insulating barrier is replaced with a semiconducting weak link (e.g. a two-dimensional electron gas).

### 2.3.1. Semiconducting Weak Links

The process governing the supercurrent flow in superconductor-semiconductor-superconductor (hybrid) Josephson junctions are coherent Andreev reflections at the interfaces between the semiconductor and the superconductor. Similar to Fabry-Pérot resonances in an optical cavity, resonant electronic modes can form in the semiconducting weak link at specific energies, which transfer Cooper pairs from one side of the junction to the other. In the following, we will start by considering a single conduction channel in the zero temperature limit, and afterwards, we will extend the discussion to finite temperatures and multichannel junctions.

## Single Channel

When an electron within the semiconductor reaches one of the interfaces with the superconductor, because of the absence of accessible single-particle states within the gap, it must be reflected. If it is normal-reflected as an electron, there is no charge transfer, and therefore no net-current across the interface. However, a spin  $\uparrow$  electron reaching the interface can also pair with a spin  $\downarrow$  electron with opposite momentum and enter the superconductor as a Cooper pair. The missing spin  $\downarrow$  electron can equivalently be seen as a spin  $\uparrow$  hole having the same energy of the incoming electron and approximately the same momentum, which is retro-reflected towards the other interface [57–59]. During this process, referred to as Andreev reflection, a charge of  $2e$  is transferred to one superconducting electrodes. The retro-reflected hole can undergo the same process at the opposite interface and be Andreev-reflected again as an electron. Andreev reflection is a phase coherent process, and if the total phase acquired over a round trip is a multiple of  $2\pi$  stationary modes known as Andreev bound states (ABSs) will form. Figure 2.3 illustrates the process for a semiconducting weak link of length  $L$  sandwiched between two electrodes made of the same superconductor. Over a round trip of two consecutive Andreev reflection, a Cooper pair is transferred from one electrode to the other.

The probability of Andreev reflection is weakened by the presence of a potential barrier at the interface between the semiconductor and the superconductor as discussed in the Blonder, Tinkham and Klapwijk theory [60]. In the following, we consider the case of Andreev reflection probability equal to one, and hence of a perfect interface.

To calculate the energies of the ABSs we have to find an expression for the total phase acquired during a round trip. We assume a one dimensional wire, and that the left and right electrodes have a superconducting phase equal to  $-\varphi/2$  and  $\varphi/2$  respectively, so that the phase difference between the electrodes is  $\varphi$ . The total phase acquired in a round trip consists of the phase picked up after the reflection at each of the two interfaces and the phase accumulated while traversing the semiconducting region. When the coherence length of the superconductor  $\xi$  is much larger than  $L$ , we can neglect the contribution coming from the time spent in weak link and write the total phase as [59]:

$$\varphi_{\text{tot}} = -2 \arccos \left( \frac{E}{\Delta} \right) \pm \varphi \quad (2.25)$$

where the  $\pm$  sign stand for a left and right moving electron respectively, and  $E$  is the excitation energy of the electron, which we take to be  $|E| < \Delta$ .

In the most general case, we have to take into account the finite length of the weak link. Additionally, we must factor in the transmission probability  $\tau$  which

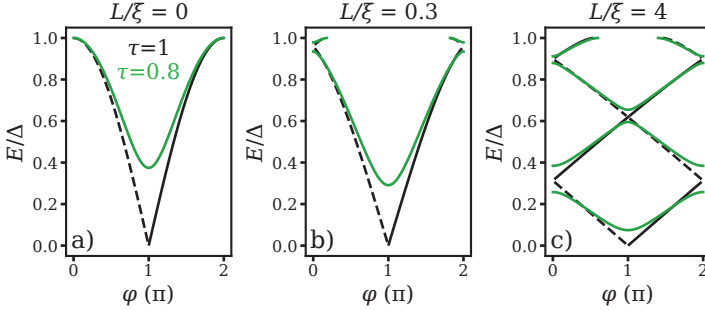


**Figure 2.4.** Numerical solution of the ABS energies for different ratios between the junction length  $L$  and the coherence length  $\xi$  of the superconductor in the electrodes. From a) to c), as we increase  $L$ , more states become available in the gap and get pushed to lower energies. The green and the black lines indicate the energy dispersion for  $\tau = 0.8$  and  $\tau = 1$ . Solid and dashed lines help to distinguish between the energy dispersion of left and right moving electrons in the case of  $\tau = 1$ .

might differ from unity due, for example, to impurities in the semiconductor. In this case,  $\varphi_{\text{tot}}$  takes the form [59, 61]:

$$\varphi_{\text{tot}} = -2 \arccos\left(\frac{E}{\Delta}\right) + 2 \frac{L}{\xi} \frac{E}{\Delta} \pm \arccos\left(\tau \cos(\varphi) + (1 - \tau) \cos\left(\frac{Lx_r}{\xi} \frac{E}{\Delta}\right)\right), \quad (2.26)$$

which is derived including the presence of a point impurity at position  $x_0 \in [-L/2, L/2]$  and where  $x_r = 2x_0/L$ . For  $\tau = 1$  and  $L \ll \xi$  we recover Eq.(2.25). Andreev bound states will form at energies  $E$  that satisfy  $\varphi_{\text{tot}} = 0$  (modulo  $2\pi$ ). An analytical expression for the stationary solutions of Eq.2.26 does not exist. In Fig. 2.4 we plot numerical solutions for  $E/\Delta > 0$  at different ratios  $L/\xi$  for  $\tau = 1$  and  $\tau = 0.8$ . When increasing the junction length, more states enter the gap, some of which with relatively low energies. These low energy states can absorb photons and act as source of dissipation in microwave circuits [62–64]. Therefore, short junctions, with  $L \ll \xi$ , are typically preferred in many applications. However, the minimum junction length achievable is often limited by the fabrication procedure. In the present work (see Chapter 4), we were able to fabricate junctions  $\sim 150$  nm long. Given the typical coherence length in Al thin films  $\xi \sim 500$  nm [41], this results in a ratio  $L/\xi \sim 0.3$ . In addition, in a two-dimensional system, when the width of the junction is much larger than the Fermi wavelength of electrons in the weak link, there can be conductive channels with a transversal component of momentum. The effective length of these channels can be much longer than the physical length

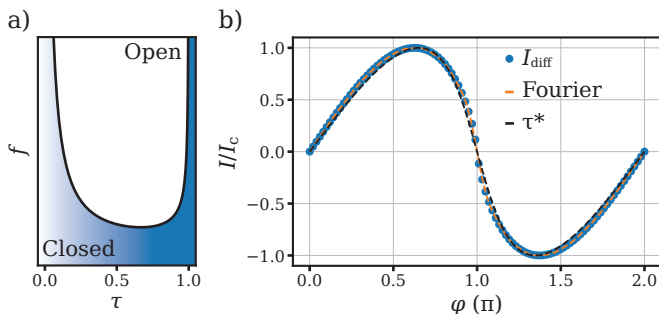


**Figure 2.5.** a) Bimodal distribution of transmission probabilities. The distribution peaks for channels having low transmission probability (closed), giving little contribution to the supercurrent, and for channels with high transmission probability (open), which carry most of the supercurrent. b) The blue curve shows the current-phase relation of a short diffusive Josephson junction. The orange dashed curve is a fit to the blue curve with a sine Fourier series from which we extract  $|c_2/c_1| \sim 0.2$ . The black dashed curve is a fit to Eq (2.34) from which we extract an effective transmission probability  $\tau^* \sim 0.86$ .

of the junction, and they can therefore induce more states in the gap.

In the limit  $L \ll \xi$ , it is possible to derive an analytical expression for the ABS energies taking into account the junction transparency [63, 65, 66]:

$$E_A^\pm = \pm \Delta \sqrt{1 - \tau \sin^2(\varphi/2)}. \quad (2.27)$$

At zero temperature, only the lowest energy ABS is occupied, and the corresponding supercurrent is given by:

$$I(\varphi) = \frac{2e}{\hbar} \frac{\partial E_A^-}{\partial \varphi} = \frac{e\Delta}{2\hbar} \frac{\tau \sin(\varphi)}{\sqrt{1 - \tau \sin^2(\varphi/2)}}. \quad (2.28)$$

At finite temperature instead, the ABSs population is given by the Fermi distribution, and the CPR takes the form [67]:

$$I(\varphi) = \frac{e\Delta}{2\hbar} \frac{\tau \sin(\varphi)}{\sqrt{1 - \tau \sin^2(\varphi/2)}} \tanh \left( \frac{\Delta \sqrt{1 - \tau \sin^2(\varphi/2)}}{2k_B T} \right). \quad (2.29)$$

### Many Channels

Typically, hybrid Josephson junctions contain several conduction channels each characterized by a different transmission probability  $\tau_n$  contributing  $I_n$



to the total supercurrent. The number  $N$  of conduction channels can be estimated from the ratio between the width of the junction  $W$  and the Fermi wavelength  $\lambda_F$  of electrons using  $N \approx 2W/\lambda_F$  [28]. The InAs two-dimensional electron gases used in this thesis, typically have  $\lambda_F$  of approximately  $\sim 10$  nm (see Chapter 3 and Ref. [68, 69]). Since we fabricate junctions which are at least  $1 \mu\text{m}$  wide, this results in approximately 100 conduction channels. Given this dense spectrum of ABSs, the total current for short junctions  $L \ll \xi$  and at zero temperature can be written in integral form as the sum over all transmission probability values:

$$I(\varphi) = \frac{e\Delta}{2\hbar} \sin(\varphi) \int_0^1 f(\tau) \frac{\tau}{\sqrt{1 - \tau \sin^2\left(\frac{\varphi}{2}\right)}} d\tau \quad (2.30)$$

where  $f(\tau)$  is the distribution function of the transmission probabilities. In the diffusive limit, the  $f(\tau)$  can be calculated with random matrix theory and has been found to be [70–72]:

$$f(\tau) = \frac{\pi\hbar G_N}{2e^2} \frac{1}{\tau\sqrt{1-\tau}}, \quad (2.31)$$

where  $G_N$  is the junction normal state conductance.

By inserting the expression of  $f$  in the diffusive limit into Eq. (2.30), the total CPR becomes [73]:

$$I_{\text{diff.}}(\varphi) = \frac{\pi G_N \Delta}{e} \cos\left(\frac{\varphi}{2}\right) \operatorname{arctanh}\left[\sin\left(\frac{\varphi}{2}\right)\right]. \quad (2.32)$$

In Fig. 2.5a) we plot the bimodal distribution of transmission probabilities given by Eq. (2.31) together with the corresponding CPR given by  $I_{\text{diff.}}(\varphi)$ . The Josephson junctions in this study are about  $150$  nm long, the mean free path of the InAs 2DEG is approximately  $l_e \sim 200$  nm and they typically have multiple conduction channels. As a consequence, Eq. (2.32) can well describe their CPR.

In general, any CPR can be expressed in a Fourier series as:

$$I(\varphi) = \sum_{m=1}^{\infty} c_m \sin(m\varphi), \quad (2.33)$$

where the  $\sin(m\varphi)$  terms correspond to processes involving the simultaneous, coherent transport of  $m$  Cooper-pairs [74, 75] carrying a charge  $m \times 2e$ . When the CPR can be parametrized by the junction transparency  $\tau$ , then the more

transparent a junction is, the higher the ratio between the amplitude of successive harmonics  $|c_{m+1}(\tau)/c_m(\tau)|$ .

Another commonly used way of describing the junction CPR is to assume that transport is determined by  $N$  channels all with an effective transmission probability  $\tau^*$  [76]:

$$I(\varphi) = N \frac{e\Delta}{2\hbar} \frac{\tau^* \sin(\varphi)}{\sqrt{1 - \tau^* \sin^2(\varphi/2)}}. \quad (2.34)$$

We fit the CPR given by Eq. (2.32) with a Fourier series, and with Eq (2.34). We extract a  $|c_2/c_1|$  ratio of  $\sim 0.2$  and an effective transmission probability of  $\sim 0.86$ . Knowing the harmonic content of the CPR of a Josephson junction is a fundamental aspect in the design of any quantum circuit. As shown in Fig. 2.5b) the Fourier fit follows the CPR at all values of  $\varphi$ . The fit with Eq (2.34) instead, deviated from the CPR around  $\varphi = \pi$ . This highlights the limitations of Eq (2.34) in capturing the behaviour of an arbitrary CPR. However,  $\tau^*$  can still be used to describe the behaviour of a junction with a few highly transmissive channels [76].

### Spin Orbit Interaction

So far, as we will do for the rest of this work, we have assumed that spin  $\uparrow$  and spin  $\downarrow$  electrons are degenerate and that each Andreev bound state is doubly occupied. However, SOI in the weak link can add an additional flavour to the picture. The presence of SOI can split the ABSs and produce spin-selective transitions which can be accessed by microwave photons. Here, we will not discuss these additional effects, and direct the interested reader to Ref. [59, 77–79].

### 2.3.2. Probing the Josephson Effect

In this section we discuss the techniques used in this thesis to characterize the Josephson effect. First, we investigate the interference pattern in the critical current of a junction as a function of a magnetic field applied perpendicular to the junction area - the Fraunhofer pattern. Afterwards, we present the dc and the ac methods to access the harmonic content of the current-phase relation of the junction.

#### Fraunhofer Pattern

The Josephson effect commonly manifest itself as interference patterns arising as the phase difference between the electrodes  $\varphi$  is changed - i.e. by an external

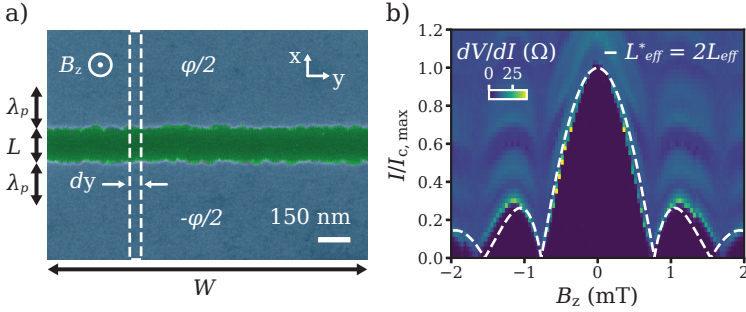


**Figure 2.6.** a) False-colour SEM image of a Josephson junction made of an InAs two-dimensional electron gas weak link sandwiched between two Al electrodes (see Chapter 3 for details). The length  $L$  and the width  $W$  of the junction are indicated by the arrows as well as the superconductor penetration depth  $\lambda_p$ . The white dashed line indicates the contour used to calculate changes in the phase difference between the electrodes  $\varphi$  as a function of the applied magnetic field  $B_z$ . b) Measured Fraunhofer pattern for a junction with  $W \sim 2.5 \mu\text{m}$  and  $L \sim 150 \text{ nm}$ . The map of differential resistance  $dV/dI$  as a function of current bias  $I$  and  $B_z$  is overlaid with the theoretical curve obtained from Eq. (2.36). To match the theory to the experiment we set  $L_{\text{eff}}^* = 2L_{\text{eff}}$ , with  $L_{\text{eff}} = L + 2\lambda_p$ .

magnetic field. Let us consider a Josephson junction as in Fig. 2.6, having length  $L$  and width  $W$ . We want to understand how  $\varphi$  evolves as a function of a magnetic field applied perpendicularly to the junction area  $B_z$ . Because of the continuity of the superconducting order parameter, when integrating the changes in its phase along a close path, the integral must be an integer multiple of  $2\pi$ . Applying this condition to the path indicated with the white dashed line in Fig. 2.6a), extending over a distance  $dy$ , we obtain [56]:

$$\frac{\partial\varphi}{\partial y} = \frac{2\pi}{\Phi_0} B_z L_{\text{eff}} \rightarrow \varphi(y) = \frac{2\pi}{\Phi_0} B_z y L_{\text{eff}} = \frac{2\pi\Phi_{\text{ext}}}{\Phi_0}, \quad (2.35)$$

where  $\Phi_{\text{ext}}$  is the magnetic field flux through the junction, and  $L_{\text{eff}} = L + 2\lambda_p$  takes into account the fact that the magnetic field will penetrate over a distance given by the superconducting penetration depth in both electrodes. Also, we have dropped the integration constant since the initial value of  $\varphi$  will be irrelevant in the following discussion.

Integrating the CPR of the junction expressed in Fourier series over the junction width we obtain the dependence of the supercurrent on the applied

magnetic field:

$$I(B_z, \varphi) = \int_{-W/2}^{W/2} \frac{I(B_z, \varphi, y)}{W} dy = \frac{1}{W} \int_{-W/2}^{W/2} \sum_{m=0}^{\infty} c_m(y) \cdot \sin(mky) dy, \quad (2.36)$$

where  $k = \frac{2\pi}{\Phi_0} B_z L_{\text{eff}}$ . The evolution of the critical current  $I_c$  as a function of magnetic field, commonly referred to as Fraunhofer pattern, is obtained by taking the absolute value of Eq. (2.36),  $I_c(B_z) = |I(B_z, \varphi)|$ . In general, the Fourier coefficients  $c_m$  depend on  $y$ , and the Fraunhofer pattern embeds this dependence. However, while it is straightforward to generate  $I_c(B_z)$  knowing  $c_m(y)$ , extracting the critical current distribution along  $y$  from a measurement of the Fraunhofer pattern is not easy, as many equivalent solutions exist.

In Fig.2.6b), we overlay the Fraunhofer pattern obtained from measurements with the calculated  $I_c(B_z)$ . The junction has an InAs two-dimensional electron gas as a weak link and a 10 nm-thick aluminium film as superconducting electrodes. The width and length of the junction are  $W \sim 2.5\mu\text{m}$  and  $L \sim 150$  nm respectively. The theoretical curve is derived from Fourier coefficients obtained by fitting Eq. (2.32). We assume homogeneity along the  $y$  direction, meaning  $c_m(y) \sim c_m$  for all  $m$ , and use  $\lambda_p = 200$  nm as previously reported [54] for thin Al films. In the differential resistance map as a function of current bias  $I$  and  $B_z$ , we identify the critical current  $I_c$  as the boundary between the superconducting regime (dark blue) and the ohmic regime (turquoise). Both curves are normalized with respect to the maximum critical current value. In order to match the theoretical curve to the experimental one, we have to use an effective length two times larger than the expected one  $L_{\text{eff}}^* = 2L_{\text{eff}}$ . In this way, the first minima align with the numerically calculated values. The periodicity of the oscillations however, is different for the two curves. This discrepancy is typically attributed to flux focusing effect from the superconducting banks [69]. Due to the Meissner effect, field lines will be expelled from the superconductor and lead to a larger effective field in the junction.

## Superconducting Quantum Interference Devices

Superconducting quantum interference devices (SQUIDs) are the building blocks of numerous quantum technologies, with applications in sensing [80], qubits[81, 82] and amplifiers[83, 84].

SQUIDs are typically realized in two ways, either with a single Josephson junction or with two Josephson junctions embedded in a superconducting loop. These two realization are historically named based on their readout methods. Loops with a single JJ are known as radio frequency (rf) SQUIDs, and the junction is typically probed by coupling the loop to a resonant tank circuit. On

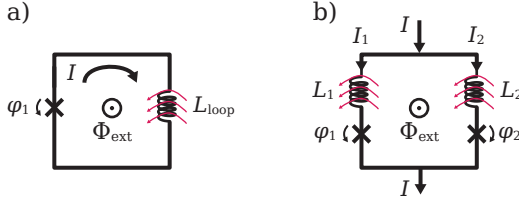


**Figure 2.7.** a) Schematic of a) rf SQUID and a b) dc SQUID. The magnetic field flux through the loop is indicated with  $\Phi_{\text{ext}}$ . The phase drop over the junctions are given by  $\varphi_i$  with  $i = 1, 2$ . The current  $I$  flowing through the SQUID causes an additional magnetic field flux (purple lines) due to the loop inductances  $L_{\text{loop}}$  and  $L_1, L_2$ .

the other hand, loops with two JJs are known as direct current (dc) SQUIDS, and are typically studied by measuring their switching current. Examples of a dc and a rf SQUID are shown in Fig. 2.7. Loop inductances  $L_{\text{loop}}$ , given by the sum of the geometrical inductance  $L_{\text{geo}}$  and the kinetic inductance  $L_{\text{kin}}$ , also need to be taken into account in the device description when they become comparable to the Josephson inductances.

In both implementations the phase difference across the JJ (or the JJs) in the SQUID is related to externally applied field by the so called fluxoid relation [56, 85]:

$$\varphi_{\text{tot}} = \varphi - \frac{2\pi\Phi_{\text{ext}}}{\Phi_0} + \frac{2\pi}{\Phi_0} L_{\text{loop}} I(\varphi) \stackrel{!}{=} 2n\pi, \quad (2.37)$$

$$\varphi_{\text{tot}} = \varphi_1 - \varphi_2 - \frac{2\pi\Phi_{\text{ext}}}{\Phi_0} + \frac{2\pi}{\Phi_0} [L_2 I_2(\varphi_2) - L_1 I_1(\varphi_1)] \stackrel{!}{=} 2n\pi, \quad (2.38)$$

where  $\varphi_1$  and  $\varphi_2$  are the internal phases of JJ<sub>1</sub> and JJ<sub>2</sub> in the dc SQUID. In this second case, we have separated the contribution of the loop inductance over the two arms of the SQUID, indicated with  $L_1$  and  $L_2$ . The flux of the external magnetic field  $B_{\text{ext}}$  through the SQUID is given by  $\Phi_{\text{ext}} = B_{\text{ext}}A$ , where  $A$  is the area of the loop.

Let us consider Eq. (2.37) for a rf SQUID, with  $n = 0$  and for a SIS junction with current phase relation  $I(\varphi) = I_c \sin(\varphi)$ . In the absence of loop inductances the relation between the internal phase  $\varphi$  and the external phase  $\varphi_{\text{ext}} = \frac{2\pi\Phi_{\text{ext}}}{\Phi_0}$  is approximately linear, and by applying a given magnetic field, one can phase bias the junction to any value  $\varphi \in [0, 2\pi]$ . However, when increasing either  $L_{\text{loop}}$  or  $I_c$ , the function  $\varphi_{\text{ext}}(\varphi)$  develops regions with negative derivative. This leads to hysteresis in  $\varphi(\varphi_{\text{ext}})$  as illustrated in Fig.2.8 for a

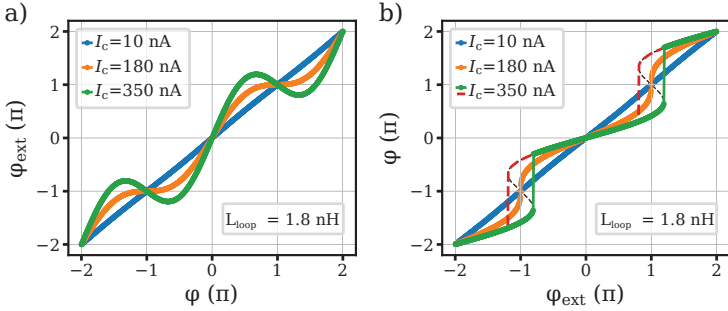


**Figure 2.8.** a) The external phase  $\varphi_{\text{ext}}$  as a function of internal phase  $\varphi$  for an rf SQUID with loop inductance  $L_{\text{loop}} = 1.8$  nH and sinusoidal current-phase relation. For low critical current  $I_c$  the relation is nearly linear, but becomes nonlinear as  $I_c$  is increased. For the chosen loop inductance, the crossover to the hysteretic regime appears for  $I_c \sim 180$  nA (green curve). (b) The internal phase as function of external phase. The relation is found by inverting the curve shown in a). In the hysteretic regime, the phase bias values  $\varphi = (2n + 1)\pi$  are not accessible and the value of the phase can take on two values depending on the sweep direction: when sweeping  $\varphi_{\text{ext}}$  from left to right the phase stays on the green branch while it follows the red dashed branch upon reversing flux bias direction.

fixed value of  $L_{\text{loop}} = 1.8$  nH. In the hysteretic regime, the phase biasing at  $\varphi = (2n + 1)\pi$ , with  $n$  an integer, become inaccessible. For a SIS junction the condition for the onset of hysteresis in  $\varphi(\varphi_{\text{ext}})$  is given by [86]:

$$L_{\text{loop}} I_c > \frac{\Phi_0}{2\pi}. \quad (2.39)$$

In case of a non-sinusoidal CPR as in Eq. 2.32, at a given value of loop inductance, the hysteretic regime is entered already at lower critical current values. We solve numerically  $\varphi(\varphi_{\text{ext}})$  for  $L_{\text{loop}} = 1.8$  nH, and find the onset of hysteresis at  $I_{c,\text{sin}} \sim 180$  nA and  $I_{c,\text{diff}} \sim 90$  nA for a sinusoidal and a many channel diffusive CPR respectively. These are important design considerations when characterizing the CPR of a Josephson junction with an rf SQUID.

Coupling the SQUID to a tank resonant circuit can provide several information about the junction under study, including the harmonic content of the CPR, and the microwave response of the junction [86]. A more compact way of characterizing a JJ, which does not require an additional microwave circuit, is to embed it in a dc SQUID. This is a particularly interesting device since it allows to combine the CPR of two or more JJ in an effective Josephson

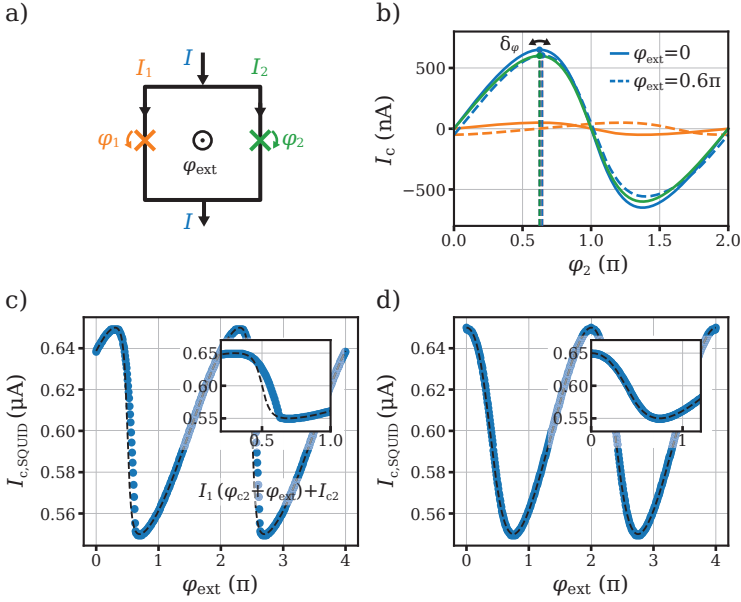


**Figure 2.9.** a) Schematic of a dc SQUID without loop inductances. The colour code matches the one for the curves in b): orange and green indicate the current flowing through the left  $JJ_1$  and right  $JJ_2$  Josephson junction respectively; in blue we indicate the total current in the SQUID, sum of  $I_1$  and  $I_2$ . b) Individual current-phase relation (CPR) of the two junctions in orange and green as a function of the phase drop  $\varphi_2$ . The expression of the CPR is given by Eq. (2.28) with  $\tau_1 = \tau_2 = 0.8$ . The critical current ratio is  $I_{c2}/I_{c1} = 12$ . In blue, the total CPR of the SQUID. When the externally applied phase  $\varphi_{\text{ext}}$  is zero, the critical phase value of the SQUID  $\varphi_{c,\text{SQUID}}$  matches the critical phase value of the large junction  $\varphi_{c,\text{SQUID}}$ , as indicated by the vertical dashed lines. At finite magnetic field  $\varphi_{c,\text{SQUID}}$  is shifted compared to  $\varphi_{c2}$  by  $\delta_\varphi$ . c) We compare the critical current of the SQUID as a function of magnetic field as obtained from  $\max_{\varphi_2} [I_1(\varphi_2 + \varphi_{\text{ext}}) + I_2(\varphi_2)]$  (blue) and from Eq. (2.40). We set  $\tau_2 = 0.001$  and  $\tau_1 = 0.99$ . d) Same as in c) for  $\tau_1 = \tau_2 = 0.8$ .

element with an arbitrary harmonic content.

A dc SQUID is measured by passing a dc current  $I$  through the loop and recording the switching to the normal state. The total current flowing through

the device is the sum of the current in each junction  $I = I_1(\varphi_1) + I_2(\varphi_2)$ . From Eq.(2.37) for  $n = 0$  and neglecting the role of loop inductances, we see that the phase drops over the junctions are related by  $\varphi_1 = \varphi_2 + \varphi_{\text{ext}}$ . If we consider an asymmetric SQUID, where the critical current of one junction is much larger than the other  $I_{c2} \gg I_{c1}$ , the switching dynamics of the device from the superconducting to the normal state will give us access to the CPR of the small JJ. This is illustrated in Fig. 2.9b): increasing the current bias  $I$  of the SQUID, close to the critical current of JJ<sub>2</sub>, the phase  $\varphi_2$  will be fixed around its critical value  $\varphi_2 = \varphi_{c2} + \delta_\varphi$ . The total CPR can be then expressed as:

$$I(\varphi_{\text{ext}}) \approx I_1(\varphi_{c2} + \varphi_{\text{ext}}) + I_2(\varphi_{c2}). \quad (2.40)$$

Therefore, measuring the critical current of the SQUID allows to directly visualize  $I_1(\varphi_{\text{ext}})$  provided that  $\varphi_2$  does not deviate significantly from  $\varphi_{c2}$  [76, 87].

Recently, the authors in Ref. [88] highlighted that this methods can give misleading results depending on the CPR of JJ<sub>2</sub> (also called reference junction) and JJ<sub>1</sub> (also called junction under study). They have summarised their findings with the following condition, which is necessary to access the real CPR of the studied junction:

$$\begin{cases} \max \partial_{\varphi_2} I_2 > -\max \partial_{\varphi_1} I_1 \\ \min \partial_{\varphi_2} I_2 > -\min \partial_{\varphi_1} I_1. \end{cases} \quad (2.41)$$

The equation above states that the oscillations in the derivative of the studied CPR should fall inside the oscillations in the derivative of the reference CPR.

In Fig. 2.9c) and d) we compare the value of critical current as it would appear from current bias measurement from an asymmetric SQUID, with the CPR of the junction under study. The first curve (scatter plot with blue markers) is obtained by extracting the maximum of  $I(\varphi_2, \varphi_{\text{ext}}) = I_1(\varphi_2 + \varphi_{\text{ext}}) + I_2(\varphi_2)$  at different values of  $\varphi_{\text{ext}}$ . The second curve (black dashed line) is plotted using Eq. (2.40). We use for CPRs the expression for a single channel short diffusive junction as given in Eq. (2.28) with transmission probabilities  $\tau_1$  and  $\tau_2$ . We normalize the CPR so that we can fix  $I_{c2}/I_{c1} = 12$ . In Fig. 2.9c) we compare the two curves for  $\tau_1 = 0.99$  and  $\tau_2 = 0.001$ . This configuration, where a low transmission probability SIS reference junction is used to extract the CPR of high transmission probability junctions, was actually the one used in the paper where this method was first developed [87]. The SQUID oscillations in this case fail to reproduce the CPR of the studied junction for external phase values such that  $\varphi_{\text{ext}} + \varphi_{c2} \approx \pi$ . This is a result of the fact that  $\partial_{\varphi_1} I_1$  does not fall inside  $\partial_{\varphi_2} I_2$  in such phase bias range. The two curves overlap better when the junctions have the same transmission probabilities



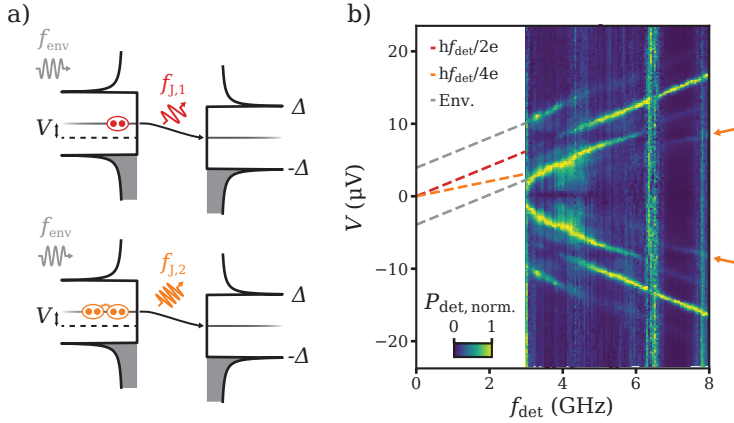


**Figure 2.10.** a) Schematic of Cooper pair transport in a Josephson junction with voltage bias  $V$ . Transfer of one (red) and two (orange) Cooper pairs (with charge  $2e$  and  $4e$ ) results in photon emission at frequency  $f_{J,1}$  and  $f_{J,2}$  respectively. A photon emitted from Cooper pairs transport can either take or give part of its energy to an environmental photon at frequency  $f_{env}$ . b) Normalized power  $P_{det, norm.}$  as a function of  $V$  and detection frequency  $f_{det}$ . Emission lines corresponding to transport of one and two Cooper pair are indicated by the red and orange dashed lines. Single Cooper pair emission processes assisted by environmental photons are shown with dashed grey lines. The relative intensity of the emission peaks depends on  $f_{det}$ . Around  $f_{det} \sim 7$  GHz, it is possible to distinguish the  $4e$  emission process from the others, and indicated by the orange lines.

$\tau_1 = \tau_2 = 0.8$ , as shown in Fig. 2.9d).

As mentioned before, in addition to being a great characterization tool, SQUIDs can be used to engineer an effective Josephson junction with an almost arbitrary CPR. By properly designing the loop inductances, the critical currents and transmission probabilities of the junctions (gate tunable in the case of semiconducting weak link), it becomes possible, at finite magnetic flux, to obtain a CPR with the desired harmonic content. This finds applications in superconducting electronics [12, 89] superconducting qubits [13, 90, 91] as well as quantum limited parametric amplifiers [83, 84].

## Josephson Radiation

Another characterization method, which in principle removes the need of embedding the junction in a loop to access the harmonic content of its CPR, is the measurement of Josephson radiation. In the normal state, the voltage drop over the junction is governed by the second Josephson equation given by Eq. (2.22). Applying a constant voltage bias  $V$  over the junction, the phase will linearly evolve in time according to:

$$\varphi = \frac{2e}{\hbar} Vt. \quad (2.42)$$

Substituting this equation into the expansion in Fourier series of the CPR of a JJ we get:

$$I(t) = \sum_{m=1}^{\infty} c_m \sin(m \frac{2e}{\hbar} Vt). \quad (2.43)$$

As a consequence, an applied dc voltage causes an ac supercurrent oscillating at the Josephson frequency  $f_J = 2eV/h$ . This transforms into the emission of microwave photons at  $f_J$ . In the presence of higher harmonics, photon emission at higher frequencies  $f_{J,m} = m \times 2eV/h$  also occurs [74, 75]. The amplitude of the Fourier coefficients  $c_m$  in Eq. (2.43) reflects the probability of photon emission due to coherent transfer of single ( $m = 1$ ) or multiple ( $m > 1$ ) Cooper pairs, as illustrated in Fig. 2.10a).

Josephson radiation can be measured by connecting one electrode of the junction to a power spectrum analyser (detector), as detailed in Chapter 7 and Appendix C. The probability of photon emission due to Cooper pair transport depends on the impedance of the environment surrounding the Josephson junction [92], which in turns has a complex behaviour as a function of frequency. The frequency dependence of the environmental impedance can be engineered, but it is also influenced by standing wave patterns in the measurement rf lines due to spurious impedance mismatch conditions. In Fig. 2.10b) we show a typical radiation spectrum obtained by measuring the emission power as function of detection frequency  $f_{\text{det}}$  and voltage drop  $V$  for a junction similar to the one in Fig. 2.6. A peak in the measured power occurs when the Josephson radiation frequency matches  $f_{\text{det}}$ .

In addition to the peak corresponding to the fundamental Josephson emission at  $f_{J,1}$ , there are replicas of it appearing at a constant frequency offset on the right and on the left of the predicted peak position. These extra processes can be understood as a photon from a spurious environmental mode which is upconverted to a detector photon by taking up the energy  $2eV$  provided by the inelastic transfer of a Cooper-pair (right shift in frequency). The energy

balance in this case reads  $hf_{\text{det}} = hf_{\text{env}} + 2eV$ , where  $f_{\text{env}}$  corresponds to the resonant frequency of an environmental cavity. Such resonance can be caused for example by a standing wave pattern along the microwave lines. The complementary process is also possible, meaning that a photon coming from a Cooper-pair transfer can be downconverted to a detector photon by giving up the energy  $hf_{\text{env}}$  to the environment (left shift in frequency). The energy balance in this case reads  $hf_{\text{det}} = 2eV - hf_{\text{env}}$ . At  $f_{\text{det}} > 6$  GHz, their contribution diminishes, while the peak corresponding to the transfer of two Cooper pairs at  $f_{J,2}$  becomes visible.

Measuring Josephson radiation requires engineering the switching behaviour to ensure a (approximately) constant voltage drop over the junction in the frequency range we have access to. For a typical measurement bandwidth from 3 GHz to 8 GHz, this means trying to stabilize the voltage in a range within  $\sim \pm 15$   $\mu\text{V}$  (see Fig. 2.10b).

The switching dynamics of a JJ are well captured by the resistively and capacitively shunted junction (RCSJ) model. Within the RCSJ model, the junction is described as a parallel circuit consisting of an ideal JJ with current phase relation  $I(\varphi)$ , shunted with a capacitor  $C$  and a resistor  $R$ . The equivalent circuit diagram is shown in Fig. 2.11a). The capacitor accounts for the geometrical capacitance between the electrodes, while the resistor describes dissipation in the system. In general,  $R$  depends on the current bias  $I$ , but for simplicity we will assume it to be constant and equal to the normal state resistance of the junction. Applying Kirchhoff's laws and using the second Josephson equation we obtain the following differential equation for the time evolution of the phase across the junction [56]:

$$I = \frac{\hbar^2}{2eC} \frac{d^2\varphi}{dt^2} + \frac{\hbar}{2eR} \frac{d\varphi}{dt} + I_c g(\varphi) + I_N, \quad (2.44)$$

where  $g(\varphi)$  is the dimensionless shape of the CPR and  $I_N$  is a noise term that we assume to be thermal noise at a temperature  $T$ . We solve the equation numerically for different values of  $I$  following the code presented in the supplementary of Ref. [93]. Knowing  $\varphi(t)$ , the dc voltage is calculated as  $V = \frac{\hbar}{2e} \left\langle \frac{d\varphi(t)}{dt} \right\rangle$ . The switching behaviour of a junction is often categorized by the Stewart-McCumber parameter, defined as:

$$\beta_C = \frac{2e}{\hbar} I_c R^2 C. \quad (2.45)$$

The  $IV$  curve in different limit scenarios are plotted in Fig. 2.11b) for a sinusoidal CPR with  $g = \sin(\varphi)$ . In the simulation, we fix  $T = 0.10$  K for the electronic temperature of realistic experimental scenarios. In so called underdamped junction, characterized by  $\beta_C \gg 1$ , increasing the bias current from

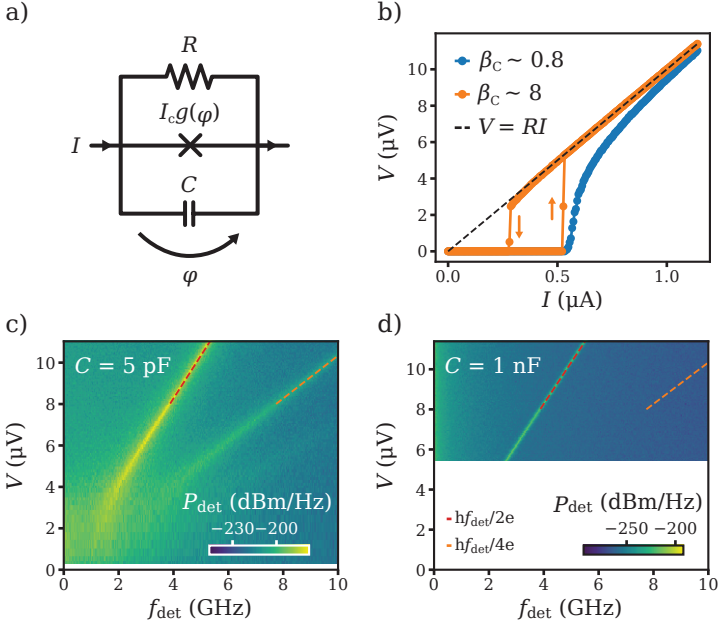


**Figure 2.11.** a) Circuit diagram of the resistively ( $R$ ) and capacitively ( $C$ ) shunted junction (RCSJ) model for a Josephson junction with current-phase relation  $I_c g(\varphi)$ . b) Voltage  $V$  as a function of current  $I$  as obtained from solutions of Eq. (2.44) using the code presented in Ref. [93]. Both the blue and the orange curve are obtained for  $R = 10 \Omega$ ,  $I_c = 500 \text{ nA}$ ,  $g(\varphi) = \sin(\varphi)$  and  $T = 0.1 \text{ K}$ , but they differ for the value of  $C$ . For the blue curve we set to  $C = 1 \text{ pF}$ , corresponding to a Stewart-McCumber parameter  $\beta_C \sim 0.8$  (overdamped regime). For the orange curve we set to  $C = 50 \text{ pF}$ , corresponding to a Stewart-McCumber parameter  $\beta_C \sim 8$  (underdamped regime). Reversing the current bias direction (orange arrows), the underdamped curve shows hysteresis. The black dashed line follows  $V = RI$ . c) Power spectral density of  $V(t)$  calculated as in Ref. [93] for  $R = 10 \Omega$ ,  $I_c = 500 \text{ nA}$  and  $C = 1 \text{ pF}$ . The red and orange dashed lines represent the expected peak position of the  $2e$  and  $4e$  emission processes respectively. d) Same as in c) but for  $C = 1 \text{ nF}$ .

zero, the resistance jumps to its normal state value right after reaching the critical current. When reversing the current direction, the junction stays in normal state even for  $I < I_c$ , because it takes time to dampen the phase oscillations. When  $\beta_C \ll 1$  instead, the junction is in the so called overdamped regime, the switching is more gradual and does not show hysteresis. In the overdamped

regime, since there is no sudden jump in the  $IV$  curve, more voltage bias values are accessible, which would benefit radiation measurements. However, in this case the voltage drop close to the switching is not stable because part of the current will flow as Josephson and displacement current, which are not constant in time. Voltage fluctuations will appear in the emission spectrum as higher order peaks even in the case of  $g = \sin(\varphi)$ , hindering to observe the real harmonic content of the CPR [93]. To reduce this effect, it is necessary to increase  $C$  to reach the linear regime where  $V = RI$  faster. This is illustrated in Fig. 2.11(c) and d) where we plot the power spectral density of  $V(t)$  as calculated from Eq. (2.44) for  $C = 1$  pF and  $C = 1$  nF. For the case of  $C = 1$  pF, the accessible voltage bias range increases, but spurious peaks appear in the power spectrum. Instead, in the case of  $C = 1$  nF, spurious peaks disappear, but the accessible voltage bias range decreases. Another option to alleviate the effect of non constant voltage drop in overdamped junctions, is to decrease  $I_c$  so that the voltage bias values where radiation occurs are further away from the switching.

Despite of the many caveats, measurements of Josephson radiation are a powerful tool to characterize the harmonic content of a CPR. We will use this tool in Chapter 7 to investigate the effective CPR of a dc SQUID formed by two hybrid junctions as a function of flux.

In the next section, we move on to introduce the applications of Josephson junctions and SQUIDs for superconducting qubits.

## 2.4. The Transmon Qubit

The basic building block of a quantum computer is a quantum bit (qubit), a quantum two level system, that stores information in the superposition of two quantum states [1]. One prevalent approach to build a quantum processor involves superconducting qubits. These qubits store information within the quantum properties of nanofabricated, anharmonic oscillators made from superconducting circuit components. Unlike various other platforms—like electron spins in silicon, quantum dots or trapped ions whose energy states relies on natural microscopic quantum systems, the energy-level characteristics of superconducting qubits can be tailored by adjusting circuit element parameters.

In this section, we introduces the widely used transmon qubit, an essential component in contemporary superconducting qubits. We discuss the equations governing its energy spectrum as an artificial two-level system, and its coupling to an external resonator.

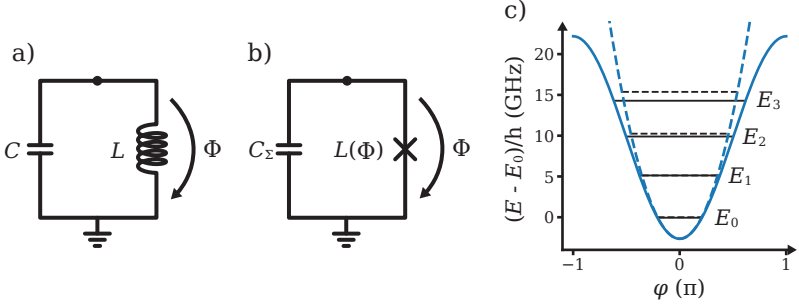


**Figure 2.12.** a) Schematic of a LC circuit with a linear inductor  $L$ . The magnetic flux through the inductor is indicated by  $\Phi$ . b) Schematic of a LC circuit with a non-linear inductor realized with a Josephson junction. The total capacitance of the circuit  $C_\Sigma$  is the sum of the shunt capacitance  $C$  as before, and of the junction capacitance  $C_J$ . c) Potential energy as a function of phase  $\varphi = 2\pi\Phi/\Phi_0$  (in blue) and eigenenergies  $E_i$  (in black) for a harmonic oscillator as in a) (dashed curves) and a anharmonic oscillator as in b) (solid curve). The eigenenergies for the anharmonic oscillator are calculated in the transmon limit with  $E_J/E_C \sim 50$ , where  $E_J = \frac{2\pi\Phi I_c}{\Phi_0}$  and  $E_C = e^2/(2C_\Sigma)$ .

### 2.4.1. An Artificial Two-level System

In order to derive the energy spectrum of a transmon qubit, we have to diagonalize its Hamiltonian, and for this we need a quantum description of the corresponding electrical circuit. Let us start by considering a simple circuit as shown in Fig. 2.12a), consisting of an inductance  $L$  and a capacitance  $C$  connected in parallel. The classical Hamiltonian  $H$  of this circuit is the sum of the charging energy  $\frac{Q^2}{2C}$  on the capacitor and the inductive energy  $\frac{\Phi^2}{2L}$  on the inductor:

$$H = \frac{Q^2}{2C} + \frac{\Phi^2}{2L}, \quad (2.46)$$

where  $\Phi$  is the magnetic flux through the inductor and  $Q$  represent the charge on the capacitor.

In analogy to a mechanical harmonic oscillator made of a mass attached to a spring, we can interpret the above expression as the sum of a kinetic energy term and a potential energy term, and identify  $\Phi$  and  $Q$  as canonical variables satisfying Poisson brackets. Anticipating the use of a non-linear inductor (the Josephson junction), a convenient choice is to treat  $\Phi$  as generalized position coordinate, and  $Q$  as generalized momentum. In this way, we can determine with  $\Phi$  both the voltage drop over the inductor  $V = \dot{\Phi}$  and the current pass-

ing through it  $I = g(\Phi)$ , where  $g(\Phi)$  represents the inductor constitutive law. Through canonical quantization we can then introduce the quantum mechanical operators  $\hat{\Phi}$  and  $\hat{Q}$  satisfying the commutation relation  $[\hat{\Phi}, \hat{Q}] = i\hbar$ .

Similar to a mechanical quantum harmonic oscillator,  $\hat{\Phi}$  and  $\hat{Q}$  can be expressed in terms of the raising and lowering operators  $\hat{a}^\dagger$ ,  $\hat{a}$ :

$$\hat{a} = \frac{1}{2} \left( \frac{\hat{\Phi}}{\Phi_{\text{ZPF}}} + i \frac{\hat{Q}}{Q_{\text{ZPF}}} \right), \quad (2.47)$$

$$\hat{a}^\dagger = \frac{1}{2} \left( \frac{\hat{\Phi}}{\Phi_{\text{ZPF}}} - i \frac{\hat{Q}}{Q_{\text{ZPF}}} \right), \quad (2.48)$$

$$\hat{\Phi} = \Phi_{\text{ZPF}}(\hat{a} + \hat{a}^\dagger), \quad (2.49)$$

$$\hat{Q} = -iQ_{\text{ZPF}}(\hat{a} - \hat{a}^\dagger), \quad (2.50)$$

where,  $\Phi_{\text{ZPF}} = \sqrt{\frac{\hbar Z_0}{2}}$  and  $Q_{\text{ZPF}} = \sqrt{\frac{\hbar}{2Z_0}}$  represent the zero-point fluctuations of flux and charge respectively, and  $Z_0 = \sqrt{L/C}$  is the circuit characteristic impedance.

The Hamiltonian of the system becomes [8]:

$$\hat{H} = \hbar\omega_0 \left( \hat{a}^\dagger \hat{a} + \frac{1}{2} \right) = \hat{H} = \hbar\omega_0 \left( \hat{n} + \frac{1}{2} \right), \quad (2.51)$$

where  $\hat{n}$  is the photon number operator and  $\omega_0 = 1/\sqrt{LC}$  is the circuit resonance frequency. In the basis of the eigenvectors of  $\hat{n}$ , denoted as  $|n\rangle$ , the eigenenergies of the circuit are:

$$E_n = \hbar\omega_0 \left( n + \frac{1}{2} \right). \quad (2.52)$$

The quantum harmonic oscillator is an important building block of circuit quantum electrodynamics, since every linear system can be decomposed into a set of independent harmonic modes. In particular, the Hamiltonian of a transmission line resonator can be written as [8]:

$$\hat{H} = \sum_{m=0}^{\infty} \left( \hbar\omega_m \hat{a}_m^\dagger \hat{a}_m + \frac{1}{2} \right), \quad (2.53)$$

where  $\hat{a}_m^\dagger$  and  $\hat{a}_m$  are the field operators of mode  $m$  and  $\omega_m$  is the resonance frequency of the mode. The expression for  $\omega_m$  depends on the geometry of the resonator and on the boundary conditions as detailed in Ref. [94]. Typically, our focus lies in understanding a circuit behaviour within a specific frequency

range. In these scenarios, isolating a single mode becomes practical, allowing us to disregard the dynamics associated with other modes.

However, the parabolic potential given by  $\frac{\Phi^2}{2L}$  produces eigenenergies which are equally spaced by  $\hbar\omega_0$ , as depicted in Fig. 2.12c). This makes it impossible to isolate two energy levels with distinct energy spacing that we would like to use as a computational space. To do that, we have to replace  $L$  with a non linear inductor - i.e. a Josephson junction (see Fig. 2.12b)). Let us consider a SIS junction with current-phase relation given by  $I(\Phi) = I_c \sin(2\pi\Phi/\Phi_0)$ , where we have used  $\varphi = 2\pi\Phi/\Phi_0$ . The inductive energy associated with this element is

$$E_L(\Phi) = \int I(\Phi)d\Phi = -E_J \cos\left(\frac{2\pi\Phi}{\Phi_0}\right), \quad (2.54)$$

where  $E_J = \frac{2\pi\Phi I_c}{\Phi_0}$  is the so called Josephson energy.

The Hamiltonian of this new circuit is given by:

$$\hat{H}_T = \frac{\hat{Q}^2}{2C_\Sigma} + E_L(\Phi) = \frac{\hat{Q}^2}{2C_\Sigma} - E_J \cos\left(\frac{2\pi\hat{\Phi}}{\Phi_0}\right) = 4E_C \hat{N}^2 - E_J \cos(\hat{\varphi}), \quad (2.55)$$

where we have introduced the charge number operator  $\hat{N} = \hat{Q}/(2e)$  and the phase operator  $\hat{\varphi} = (2\pi/\Phi_0)\hat{\Phi}$ , and we have defined the charging energy  $E_C = e^2/(2C_\Sigma)$ . Notice that in this case the total capacitance  $C_\Sigma$  is the sum of the shunt capacitance  $C$  and the junction capacitance  $C_J$ . This Hamiltonian can be diagonalized numerically if written in the eigenbasis of  $\hat{N}$ , when it takes the form [95]:

$$\hat{H}_T = 4E_C \sum_{N=-\infty}^{\infty} (N - N_g)^2 |N\rangle\langle N| - \frac{E_J}{2} \sum_{N=-\infty}^{\infty} (|N\rangle\langle N+1| + |N+1\rangle\langle N|). \quad (2.56)$$

The energy spectrum of  $\hat{H}_T$  is governed by the ratio  $E_J/E_C$ . The eigenenergies for  $E_J/E_C \sim 50$ , where the transmon is commonly designed, are shown in Fig. 2.12c) superimposed with the cosine potential provided by the Josephson junction. In this case, the transition energy  $E_{01}$  between the ground and the first excited state differs from the transition energy  $E_{12}$  between the first and the second excited state.

In the so called transmon limit, where  $E_J/E_C \gg 1$ , the eigenfunctions are delocalized in the charge space and localized in the phase space. As a consequence, the system is insensitive to charge fluctuations. On the other hand, phase fluctuations can be assumed to be small  $\delta\varphi \ll 1$ . This large  $E_J/E_C$  ratio, obtained by shunting the Josephson junction with a large capacitance,



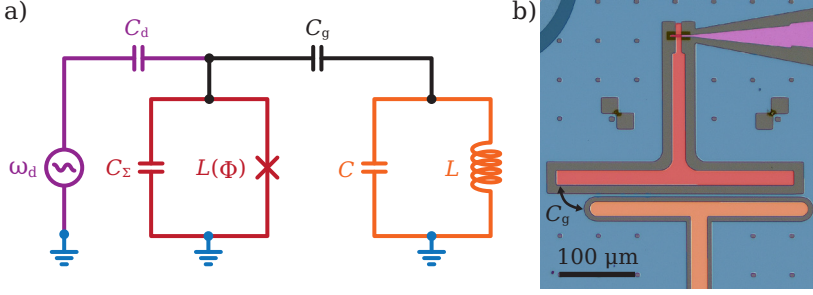


**Figure 2.13.** a) Schematic of a transmon qubit (red) coupled to one mode of a transmission line resonator (orange) and to an additional drive port (purple). The transmon has a total capacitance  $C_\Sigma$  and a non linear inductance given by  $L(\Phi)$ , with  $\Phi$  being the magnetic field flux through the inductor. The resonator mode is modelled via an harmonic oscillator with capacitance  $C$  and inductance  $L$ . The drive port is connected to an ac voltage source at frequency  $\omega_d$ . Coupling to the resonator and the drive port is controlled via the capacitances  $C_g$  and  $C_d$  respectively. b) False colour optical image of a transmon qubit. The colour code corresponds to the schematic in a). The transmon capacitance is formed by the T-shaped metalling island and ground (in blue). The Josephson junction shorts the island to ground.  $C_g$  is given by the spacial overlap between the island the the end of the resonator central conductor.  $C_d$  is formed by the overlap of the island with the drive line, which are electrically isolated with a dielectric layer.

is the reason for the longer coherence time in the transmon qubit compared to previous implementations [96]. In this limit, the frequency of the first energy transition  $f_{01}$  and the anharmonicity  $\alpha$  of the energy spectrum, can be approximated by:

$$\omega_{01} = \frac{E_{01}}{\hbar} \approx \frac{\sqrt{8E_J E_C} - E_C}{\hbar}, \quad (2.57)$$

$$\alpha = \frac{E_{12} - E_{01}}{\hbar} \approx \frac{E_C}{\hbar}. \quad (2.58)$$

Typical transmon qubits have a critical current of  $I_c \sim 25$  nA and a total parallel capacitance  $C_\Sigma \sim 65$  fF, resulting in  $f_{01} \sim 5$  GHz and  $\alpha \sim -350$  MHz.

### 2.4.2. Readout and Control

Now that we have introduced the quantum harmonic oscillator (a superconducting resonator) and the transmon artificial atom, we can discuss their interaction. Because of their large size, coming from the need of a large shunt

capacitance, it is natural to couple transmon qubits and microwave resonators capacitively via a spatial overlap.

A schematic of a resonator coupled through a gate capacitance  $C_g$  to a transmon qubit is shown in Fig. 2.13. If we consider only one mode in the resonator, with resonance frequency  $\omega_r$ , and only the first two levels  $E_0$  ( $|g\rangle$ ) and  $E_1$  ( $|e\rangle$ ) in the transmon energy spectrum, the Hamiltonian of the coupled system can be described by the well known Jaynes-Cummings (JC) Hamiltonian [95, 97]:

$$H_{JC} = \hbar\omega_r \hat{a}^\dagger \hat{a} + \frac{\hbar\omega_{01}}{2} \hat{\sigma}_z + \hbar g (\hat{a}^\dagger \hat{\sigma}^- + \hat{a} \hat{\sigma}^+), \quad (2.59)$$

where  $\hat{\sigma}_z = |e\rangle\langle e| - |g\rangle\langle g|$  is the Pauli  $z$ -matrix,  $\hat{\sigma}^- = |g\rangle\langle e|$  and  $\hat{\sigma}^+ = |e\rangle\langle g|$  are the components of the Pauli  $x$ -matrix, and  $\hat{a}$ ,  $\hat{a}^\dagger$  are the field operators for the resonator. The coupling constant  $g$  is given by [8]:

$$g = \omega_r \frac{C_g}{C_\Sigma} \left( \frac{E_J}{2E_C} \right)^{\frac{1}{4}} \sqrt{\frac{\pi Z_r}{R_Q}} \quad (2.60)$$

where  $Z_r = \sqrt{L/C}$  is the resonator impedance and  $R_Q = h/e^2$  is the resistance quantum. It should be noted that the Hamiltonian in Eq. (2.59) holds for weak coupling, meaning  $g \ll \omega_r, \omega_{01}$ .

For solutions of Eq. (2.59), we refer to Ref. [8]. Here, we want to discuss a particular case when the detuning  $\Delta_{qr} = \omega_{01} - \omega_r$  between frequency of the qubit and the resonance frequency of the resonator is sufficiently large, so that  $g/\Delta_{qr} \ll 1$ . In this case, the JC Hamiltonian can be approximately diagonalized as [98]:

$$H_{JC} \approx \frac{\hbar}{2} (\omega_{01} + \chi_{qr}) \hat{\sigma}_z + \frac{\hbar}{2} (\omega_r + \chi_{qr} \hat{\sigma}_z) \hat{a}^\dagger \hat{a}, \quad (2.61)$$

whose solutions are the pairs of atom-field states  $|g, n\rangle$  with the transmon in the ground state and  $n$  photons in the cavity, and  $|e, n-1\rangle$  with the transmon in the excited state and  $n-1$  photons in the cavity. The qubit state information is encoded in the frequency shift of the readout resonator, given by  $\chi_{qr} = \frac{g^2}{\Delta_{qr}}$ . This technique employed for measuring the qubit state is termed quantum non-demolition, since it preserves the qubit's state after the readout. In addition, by rearranging the terms in Eq. (2.61) it becomes visible that the number of photons inside the resonator is reflected by the qubit frequency, which is shifted by  $2\chi_{qr}n$  [98]. This effect is commonly referred to as a Stark shift.

To drive transitions between the ground and the excited state, an additional term has to be added to the system Hamiltonian. This is typically achieved

by providing an additional port capacitively coupled to the qubit, as shown in Fig. 2.13a). The drive term can be taken of the form  $\Omega \hat{\sigma}_x \cos(\omega_d t)$ , where  $\hat{\sigma}_x$  is Pauli x-matrix,  $\Omega$  is the drive amplitude and  $\omega_d$  the drive frequency. Because of the finite overlap in charge space,  $|g\rangle$  and  $|e\rangle$  possess a finite electric dipole moment the drive couples to in order to drive transitions between them. The transition rate is determined by the generalized Rabi frequency  $\Omega_R = \sqrt{\Omega^2 + \Delta_{\text{qd}}^2}$ , where  $\Delta_{\text{qd}} = \omega_{01} - \omega_d$ .

In Eq. (2.59) we have neglected the effect of photon losses and decoherence, for which we refer to Ref. [6]. In practice it is possible to drive the qubit and read its state via the dispersive shift on the readout resonator, provided that the loss and decoherence rates are slower than the drive and readout processes.

### 2.4.3. Flux and Gate Tunable Transmon

Let us now consider the case of a transmon qubit where the Josephson junction is made of a semiconducting weak link. The critical current of this type of junction is typically tunable via a gate voltage  $V_G$  and the corresponding qubit is commonly referred to as gate tunable transmon (gatemon). As we have seen in Section 2.3.1, the CPR of such junctions is often non-sinusoidal and can be parametrized by the transmission probability  $\tau$  through the weak link. Here for simplicity we consider single channel Josephson junctions with aluminium leads (with a superconducting gap of  $\Delta \sim 200 \mu\text{eV}$ ). The Josephson potential can be expanded in cosine Fourier series as [99]:

$$E_L(\varphi, \tau) = - \sum_{m=0}^{\infty} c_m(\tau) \cos(m\varphi), \quad (2.62)$$

which in the charge number basis becomes:

$$E_L = - \sum_{m=0}^{\infty} c_m(\tau) \sum_{N=-\infty}^{\infty} |N\rangle \langle N+m| + |N+m\rangle \langle N|. \quad (2.63)$$

The  $m^{\text{th}}$  harmonic term corresponds to the transfer of  $m$  Cooper pairs across the junction. In matrix form, the corresponding Fourier coefficient  $c_m(\tau)$  will occupy the  $m^{\text{th}}$  off-diagonal positions below and above the diagonal of the Hamiltonian. The eigenstates and eigenenergies of the system can be then obtained as in the transmon case.

The ability to adjust the critical current of the junction, thereby tuning the qubit frequency using a gate, has gathered significant interest in these devices [17, 100, 101]. Moreover, introducing flux tunability by incorporating an extra non-sinusoidal junction in parallel (see Fig. 2.14) offers the potential

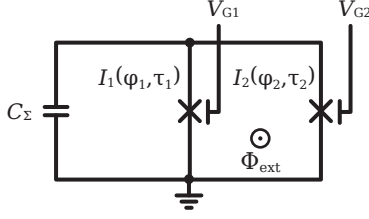


**Figure 2.14.** a) Schematic of a gate and flux tunable transmon with a total capacitance  $C_\Sigma$  and an effective Josephson junction formed by the parallel of two Josephson junctions threaded by a magnetic field flux  $\Phi_{\text{ext}}$ . Each junction is characterized by a current-phase relation  $I_i(\varphi_i, \tau_i)$  with  $\varphi_i$  being the phase drop over the junction and  $\tau_i$  the transmission probability. The critical current can be further tuned by a set of local electrostatic gates  $V_{G1}$  and  $V_{G2}$ .

to create an effective Josephson junction with a customizable CPR. This enables the realization of a qubit with a versatile energy spectrum. Compared to equivalent implementations of flux tunable qubits with SIS junctions, using semiconducting weak links allows to reduce the number of junctions needed for a particular design thanks to interference effects between the higher order harmonics of the CPRs.

Neglecting loop inductances, the expression of the Josephson potential for two junctions with a non-sinusoidal CPR in parallel reads:

$$E_L(\varphi_2, \varphi_{\text{ext}}, \tau_1, \tau_2) = - \sum_{m=1}^{\infty} c_{1,m}(\tau_1) \cos[m(\varphi_2 + \varphi_{\text{ext}})] - \sum_{m=1}^{\infty} c_{2,m}(\tau_2) \cos(m\varphi_2), \quad (2.64)$$

where  $\tau_1$  and  $\tau_2$  are the transmission probabilities of  $\text{JJ}_1$  and  $\text{JJ}_2$  respectively, and we have used  $\varphi_{\text{ext}} = 2\pi\Phi_{\text{ext}}/\Phi_0 = \varphi_1 - \varphi_2$ . In the charge number basis, the first term in Eq. (2.64) is given by:

$$E_{L,1} = - \sum_{m=0}^{\infty} c_m(\tau_1) \sum_{N=-\infty}^{\infty} |N\rangle \langle N+m| e^{im\varphi_{\text{ext}}} + |N+m\rangle \langle N| e^{-im\varphi_{\text{ext}}}. \quad (2.65)$$

Depending on the flux position and the value of the transmission probabilities, the SQUID behaves as an effective Josephson element with Josephson potential  $E_L(\varphi_2, \varphi_{\text{ext}}, \tau_1, \tau_2)$ .

In Fig. 2.15 we plot the transition energy  $E_{01}$  between the two lowest states and the anharmonicity  $\alpha$  of the system as a function of  $\varphi_{\text{ext}}$  for different transmission probabilities. We fix  $\tau_2 = 0.6$  and  $E_C = 250$  MHz, and increase  $\tau_1$

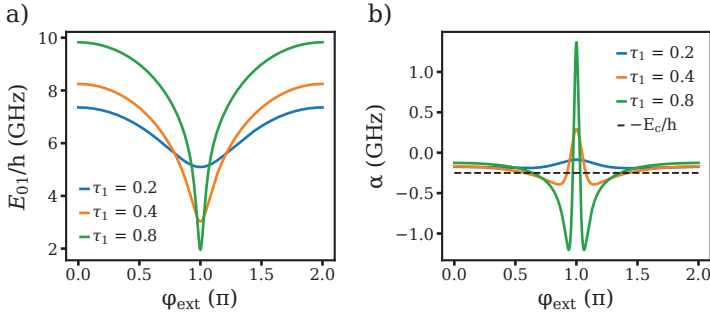


**Figure 2.15.** a) Transition energy  $E_{01}$  from the ground to the first excited state as a function of external phase  $\varphi_{\text{ext}}$  for a flux tunable gatemon. The transmission probability of one junction has been fixed to  $\tau_2 = 0.6$ , and we plot  $E_{01}$  for different values of  $\tau_1$ .  $E_C$  is  $-250$  MHz for all curves. b) Anharmonicity  $\alpha$  as a function of  $\varphi_{\text{ext}}$  for different values of  $\tau_1$  as in a) The black dashed line shows the value of  $\alpha$  as calculated in the transmon limit for a sinusoidal current-phase relation.

from 0.2 to 0.4 and 0.8. For all curves, at  $\varphi_{\text{ext}} = \pi$  the qubit frequency reaches its minimum as the inductive energy also reaches its lowest value. However, the shape of the oscillations depends on the asymmetry between the transmission probabilities of the junctions. The behaviour of the transition energy as a function of  $\varphi_{\text{ext}}$  hinders changes in the Josephson potential for the three cases. Instead, this becomes visible in the dependence of  $\alpha$  on  $\varphi_{\text{ext}}$  for the three cases. Changes in the Josephson potential change the relative spacing between energy levels. Compared to the case of sinusoidal junctions, here the interference between higher harmonics can produce large changes (in the order of GHz) in the anharmonicity of the spectrum, similar to what happens in so called fluxonium qubit [82, 102].

A particularly interesting energy spectrum is obtained for  $\tau_1 = \tau_2$  and  $\varphi_{\text{ext}} = \pi$ . In this configuration, the first and all the odd harmonics in the two JJs interfere destructively. The result is a  $\pi$ -periodic Josephson potential coming from the sum of the second (and all the even) harmonics in the CPR of the junctions. The supercurrent in this configuration is being carried by pairs of Cooper pairs with charge  $4e$ , and the two lowest eigenstates of the system correspond to an odd or even number of Cooper pairs on the island.

In Fig. 2.16a) we plot the eigenstates of the system superimposed with the Josephson potential. The two lowest and almost degenerate eigenstates  $E_0$

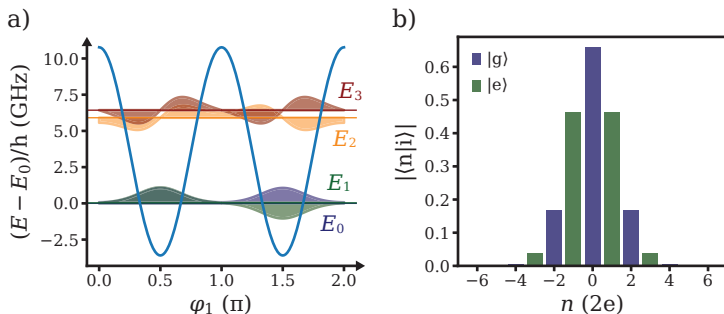


**Figure 2.16.** a) Josephson potential (blue curve) with eigenenergies and wavefunctions for the first four eigenstates of parity protected qubit as a function of phase  $\varphi_2$ . The energy spectrum is obtained for an external phase  $\varphi_{\text{ext}} = \pi$  and for a transmission probability  $\tau = \tau_1 = \tau_2 = 0.8$ .  $E_C$  has been fixed to  $-250$  MHz. b) Occupation probability of the ground  $|g\rangle$  and excited  $|e\rangle$  state of the parity protected qubit in the charge basis.  $|g\rangle$  and  $|e\rangle$  correspond respectively to a superposition of an even and an odd number of Cooper pairs on the island.

and  $E_1$  correspond to a symmetric and antisymmetric superposition of the phase particle being trapped in the potential minima at 0 and  $\pi$ . In charge space these two levels encode a different Cooper pair parity, and they do not overlap. As a consequence, the electric dipole moment associated with transitions from  $E_0$  to  $E_1$  is zero. In the absence of coupling between  $E_0$  to  $E_1$  this kind of qubit has a large relaxation time, but at the same time it cannot be directly driven through a capacitively coupled port. Additionally, the qubit is severely limited by magnetic fluctuations, which tilt the Josephson potential and couple the two parity states [13, 91].

This so called parity protected qubit was originally proposed and realized with SIS junctions arranged in a rhombus geometry to produce the  $\pi$ -periodic Josephson potential [103]. Few years later, the implementation with only two gate tunable nanowire based junctions followed [90]. Even if effort has been put in recent years to reduce the effect of magnetic noise in this kind of device [13, 104], mostly by concatenating several SQUIDS in parallel or in series, the realization of a parity protected qubit with coherence time comparable to single junction transmon is still missing. A promising alternative is to use a two-dimensional semiconducting platform to combine both gate tunability and scalability.

## 2.5. Josephson Parametric Amplifiers

This section is a consequence of a personal interest in one of the most important device in any cryogenic setups operating with superconducting qubits: the Josephson parametric amplifier (JPA). There are numerous comprehensive articles and reviews in literature to which we refer the reader for a detailed explanation of the operational principles and applications of this device [9, 10, 105]. Here we give a brief overview of the main concepts, and discuss how a JPA, normally realized with SIS Josephson junctions, can benefit from using a gate tunable weak link. While several implementations of a JPA with hybrid junctions have already been shown [19, 106, 107], in the following we are going to focus once again on how to harness the interference effects between non-sinusoidal CPRs of two junctions in a SQUID.

To effectively measure the state of a qubit, amplification of extremely small signals is crucial. This often requires employing multiple amplifiers in a series while minimizing the additional noise introduced. The noise figure, or equivalently the effective noise temperature, of an amplifier chain is determined by the first amplifier in the chain. Hence, it is important to start the amplification process as close as possible to the qubit, with a device operating at the same temperature. In contrast to standard HEMT amplifiers, which dissipate too much power, superconducting parametric amplifiers can be located on the mixing chamber plate at 20 mK together with the qubit(s).

The key ingredients of a parametric amplifier are a resonant structure - i.e. a LC oscillator -, and a parameter, entering the expression for the resonance frequency, which can be modulated by an external input. The typical analogy used to understand parametric amplifiers is to field of quantum optics. There, a medium with a non-linear relative dielectric constant  $\epsilon_{\text{eff}}$ , which depends on the applied electric field  $\mathcal{E}$ , causes frequency mixing between photons propagating through it [108]. Depending on the properties of the medium, two main processes are possible. When the dielectric constant is proportional to the amplitude of the electric field, a three-wave mixing process takes place, where a photon from a pump field is converted to a signal and a idler photons with frequencies following the relation  $\omega_P = \omega_S + \omega_I$ . Instead, when the dielectric constant is proportional to the intensity of the electric field  $\mathcal{E}^2$ , a four-wave mixing process takes place, where two pump photons are converted into a signal and a idler photon satisfying  $\omega_P + \omega_P = \omega_S + \omega_I$ . In both cases, one converts energy from the pump to the signal and idler modes and produce gain.

The relative dielectric constant of a medium determines the speed at which electromagnetic waves propagate through it  $v_{\text{ph}} = c/\sqrt{\epsilon_{\text{eff}}}$  where  $c$  is the speed of light in vacuum. In superconducting circuits, the phase velocity in a LC

circuit is given by  $v_{\text{ph}} \propto 1/\sqrt{LC}$ , from which  $\epsilon_{\text{eff}} \propto LC$ . As we have seen in the previous chapters, a parameter which can be easily modulated in LC circuits realized with Josephson junctions, is the Josephson inductance. Which amplification process is allowed depends then on the topology of the circuit or equivalently from its Hamiltonian.

Let us consider an LC circuit and let us replace the inductance with a generic Josephson element with potential energy  $U(\varphi)$ , where  $\varphi$  is the phase drop over the element. The Hamiltonian of the circuit is given by  $\hat{H} = 4E_C \hat{N}^2 - U(\hat{\varphi})$ . By Taylor expanding the potential close to its global minimum and by expressing the charge number and the phase operator in terms of the bosonic raising and lowering operators we obtain [14, 109]:

$$\hat{H} = \hbar\omega_r \hat{a}^\dagger \hat{a} + \sum_{m \geq 3} \hbar g_m (\hat{a} + \hat{a}^\dagger)^m, \quad (3)$$

where  $\omega_r = \sqrt{\frac{8E_C a_2}{\hbar^2}}$  is the circuit resonance frequency,  $a_2$  is the second-order Taylor coefficient and  $g_m$  denotes the  $m^{\text{th}}$ -order non-linearity of the Hamiltonian.

The third-order non-linearity  $g_3$ , governs three-wave mixing processes, while the fourth-order non-linearity  $g_4$  is responsible for four-wave mixing processes. For applications, three-wave mixing amplification is typically preferred since it is more energy efficient (one pump photon is converted to one signal photon) and because it is easier to filter the pump tone out from the measurement (typically  $\omega_P \approx 2\omega_S$ ).

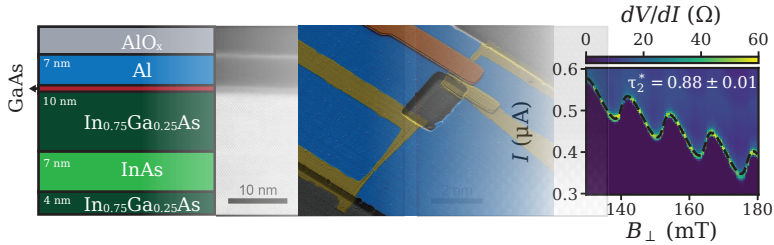
However, amplifiers based on three-wave mixing need more design efforts. In particular, to avoid limiting the maximum input signal power causing the gain to drop, it is necessary to design a circuit with large  $g_3$  but small  $g_4$  [84, 110, 111]. In Ref. [84] the authors address the problem with superconducting non-linear asymmetric inductive elements (SNAILS) based on SIS junctions. In Ref. [14] instead the authors propose to use a SQUID based on single channel hybrid junctions. Both works are based on SQUID devices, but while Ref. [84] focuses on engineering the asymmetry between the SQUID arms, Ref. [14] proposes a way to exploit the interference between higher order harmonics of the junction CPRs. In Section 8.3 we show preliminary results on a JPA realized using a SQUID made of multichannel hybrid junctions which is in principle able to combine the benefits of both approaches.

And that's it, with these concepts and premises at hand, we are ready to go.



# 3 Materials

---



In this chapter we discuss the materials of choice in this thesis. First, we describe the proximitized InAs two-dimensional electron gas (2DEG) provided by the groups of Michael Manfra and Giorgio Biasiol. Then, in Section 3.4, we introduce granular aluminium, a high kinetic inductance superconductor that we use to test the microwave compatibility of high-impedance resonators on an InP substrate.

## 3.1. Proximitized 2DEGs

While superconductors offer intriguing properties on their own, their interaction with semiconductors introduces a new dimension to the research landscape. A proximitized semiconductor, meaning a semiconductor that inherits superconducting properties due to the close proximity to a superconductor, is a combined system where the unique attributes of both material systems come to play. The semiconductor retains its electrically tunable properties, while the superconductor carries dissipationless current.

In the quest for achieving the best proximitized two-dimensional electron gas (2DEG), several research groups have proposed different recipes and combinations of materials. The initial effort to realize hybrid two-dimensional devices involved attempting to contact surface inversion or sub-surface 2DEGs with superconductors evaporated *ex situ*, primarily using materials such as aluminium (Al) or niobium (Nb) [68, 69, 112–119]. Historically, surface inversion 2DEGs were predominantly used because of the larger and easily accessible

contact area. However, being at the surface, the mobility of electrons is limited by interface scattering and strongly depends on the details of the fabrication process. On the other hand, sub-surface 2DEGs can have higher mobilities, but obtaining transparent and homogeneous superconducting contact in a reproducible way is more challenging. In both cases, the *ex situ* evaporation of the superconductor created poor interface quality, which reduced the superconducting proximity effect.

A fundamental breakthrough on the path toward superconducting - semiconducting hybrids was the first successful realization of an epitaxial interface between InAs nanowires and Al. This achievement was made possible by depositing the superconductor *in situ*, within the same Molecular Beam Epitaxy (MBE) chamber in which the wires were grown, all while maintaining a vacuum environment [120, 121]. Tunnel spectroscopy measurements revealed a hard superconducting gap, in contrast to experiments where the superconductor was evaporated *ex situ*, leading to inevitable interface impurities that softened the gap. Briefly after the success with nanowires, in Ref. [20] the authors managed to epitaxially grow Al on a InAs 2DEG. In this case, the InAs quantum well was grown in close proximity to the surface, but was protected by a barrier of  $\text{In}_{0.81}\text{Ga}_{0.19}\text{As}$  with a thickness of approximately  $d \sim 10$  nm. This arrangement allows the 2DEG to inherit the properties of the superconductor while retaining the large effective g-factor of the semiconductor  $g^* \sim -15$  [29] and a significantly high mobility  $\mu \sim 10\,000 \text{ cm}^2 \text{ V}^{-1} \text{ s}^{-1}$ .

The choice of both InAs and Al comes as a compromise between material properties and ease of fabrication. Among the most commonly used III-V materials, InAs occupies an intermediate position between GaAs and InSb in terms of spin-orbit coupling, electron mobility, and the development of fabrication processes. A unique characteristic of InAs, within the III-V group, is that the energy bands bend down at the surface, effectively pinning the Fermi level in the conduction band. This feature allows the fabrication of Ohmic contacts and improves the proximity effect. As a superconductor, Al possesses several advantageous properties. It is chemically stable, forming a self-limiting oxide layer that preserves the quality of the epitaxial interface. It has a critical temperature of approximately  $T_{c,\text{Al}} \sim 1.2$  K [122], which is lower than other commonly used superconductors such as Niobium for which  $T_{c,\text{Nb}} \sim 9$  K [123]. However,  $T_{c,\text{Al}}$  is still high enough to be suitable to use in dilution cryostats with a base temperature of 20 mK. Additionally, it has a relatively small lattice mismatch with several common semiconductors.

This material system has been grown in different versions [21, 124–126] and is used by several research groups for applications in superconducting electronics and spintronics [15, 89, 127], superconducting qubits [17], parametric

amplifiers [19], and to investigate topological phase transitions [128–130].

More recently, high mobility ( $\mu \sim 500\,000\text{ cm}^2\text{ V}^{-1}\text{ s}^{-1}$ ) shallow two - dimensional hole gases (2DHG) in germanium [131] have attracted an increased interest as a promising alternative to III-V materials. Germanium has a large and gate tunable effective g-factor, can be isotopically purified reducing the detrimental effect of nuclear spins on the coherence of different types of qubits [132], and can be integrated on silicon wafers. Ballistic supercurrent have been observed over a  $1\text{ }\mu\text{m}$  long Josephson junction made of *ex situ* evaporated Al [133, 134], but the realization of an epitaxial interface to the superconductor is still missing.

In this thesis, we investigate proximitized InAs 2DEGs provided by the groups of Michael Manfra at Purdue University and of Giorgio Biasiol at the Istituto Officina dei Materiali (IOM) in Trieste. These two materials are similar to each other, with the difference that the wafer stacks provided by the group in Purdue start from an InP substrate, while those provided by IOM start from a GaAs substrate. As a consequence, the composition of the buffer layers used to match the lattice constants of InP and GaAs to that of InAs is different, but the active region stays the same. The choice of InP originally came from moderate compatibility with superconducting microwave resonators [17]. However, since both wafer stacks are piezoelectric, realizing resonators with high quality factor is a challenging task.

### 3.2. InAs 2DEG on InP Substrate

The two-dimensional electron gases provided by the group of Michael Manfra are grown by molecular beam epitaxy (MBE) on semi-insulating Fe-doped InP (001) substrates. A graded buffer layer, with a thickness of  $\sim 1\text{ }\mu\text{m}$  consisting of different compositions of  $\text{In}_{1-x}\text{Al}_x\text{As}$  ( $x$  varying from 0.52 to 0.84), is used to match the lattice constant of InP ( $\sim 5.87\text{ }\text{\AA}$ ) to the one of InAs ( $\sim 6.06\text{ }\text{\AA}$ ). The 2DEG is formed within an InAs layer with a thickness of  $7\text{ nm}$ , which is sandwiched between two  $\text{In}_{0.75}\text{Ga}_{0.25}\text{As}$  barriers. Because the bandgap of InAs is smaller than that of  $\text{In}_{0.75}\text{Ga}_{0.25}\text{As}$ , this material stack forms a quantum well potential for the electrons within the InAs layer. The bottom barrier has a thickness of  $4\text{ nm}$ , while the top barrier is  $10\text{ nm}$ , to achieve good isolation from the surface, and good coupling to the superconductor. An additional barrier consisting of 2 monolayers of GaAs is added at the end of the semi-conducting stack to protect the 2DEG during etching. Finally,  $10\text{ nm}$  of Al are grown *in situ* without breaking vacuum in the MBE chamber, ensuring a transparent interface between the semiconductor and the superconductor. Figure 3.1 shows a transmission electron microscope image of the wafer stack and

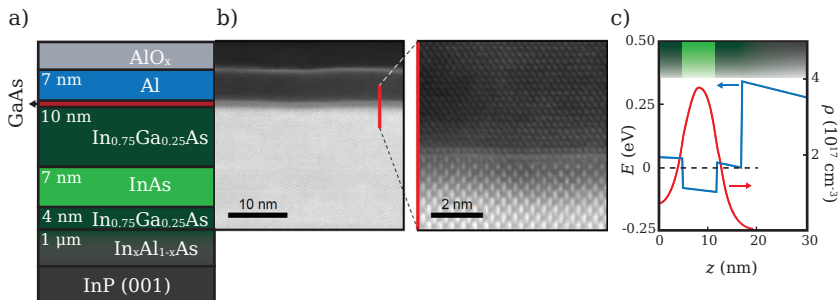


**Figure 3.1.** a),b) Illustration and transmission electron image of the top layers of the wafer stack. The substrate is  $\sim 500 \mu\text{m}$  thick. Figure adapted from [135]. c) Conduction band energies and electrons wavefunction probability density  $\rho$  along the growth direction  $z$ . Figure adapted from [20].

the electrons wavefunction probability density  $\rho$  in the quantum well as obtained from a Schrödinger-Poisson solver. A finite probability at the interface with the superconductor and an epitaxial interface result in a robust proximity effect.

### 3.2.1. Wafer Characterization

This section is primarily concerned with three key characteristics of the wafer: the mobility of the 2DEG, the superconducting properties of the Al film, and the supercurrent properties of hybrid Josephson junctions realized with the proximitized 2DEG.

#### Hallbar - Electron Density and Mobility

Standard Hall bar measurements are used to extract the peak mobility as a function of the electron density  $n$  of the 2DEG. The device is shown in Fig. 3.2a). We achieve galvanic isolation of the Hall bar from the rest of the chip by removing the aluminium layer, the 2DEG, and approximately 300 nm of the buffer layer. Subsequently, we selectively remove the aluminium from a stripe that is  $W = 20 \mu\text{m}$  wide and  $L = 150 \mu\text{m}$  long to expose the 2DEG. An oxide layer, 15 nm thick, separates the 2DEG from a Ti/Au electrostatic gate  $V_{\text{TG}}$  that is evaporated on top in order to tune the electron density. An AC current bias of  $I = 5 \text{ nA}$  is passed through the device as we measure the longitudinal  $V_{\text{xx}}$  and transverse  $V_{\text{xy}}$  voltage drop over the Hall bar as a function of perpendicular magnetic field  $B_{\perp}$  and  $V_{\text{TG}}$ .

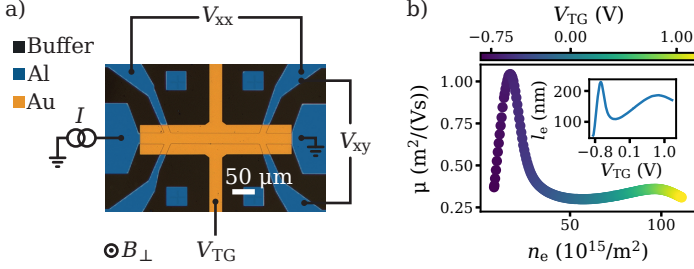


**Figure 3.2.** a) False colour optical image of a typical Hall bar device for mobility measurement. It shows the aluminium (Al) leads (blue) used for wire bonding, and the gold (Au) topgate electrode  $V_{TG}$  (yellow) used to tune the electron density in the InAs. Below the gate, the Al has been removed and the exposed InAs is isolated from the Au electrode with an Hafnium oxide layer (not visible). We source a dc current  $I$  superimposed with a small ac component, and we measure the longitudinal  $V_{xx}$  and transversal  $V_{xy}$  voltage drop over the device. We also apply a perpendicular magnetic field  $B_{\perp}$ . b) Mobility  $\mu$  as a function of carrier density  $n_e$  at different gate voltage as extracted from Hall bar measurement  $T \sim 250\text{mK}$ . The inset shown the electron mean free path  $l_e$  as a function of  $V_{TG}$ .

The electron density  $n$  and mobility  $\mu$  can be calculated as [28]:

$$n_e = \frac{1}{e\partial\rho_{xy}/\partial B_{\perp}}, \quad (3.1)$$

$$\mu = \frac{1}{en_e\rho_{xx}}, \quad (3.2)$$

where  $\rho_{xx} = \frac{V_{xx}}{I} \frac{W}{L}$  and  $\rho_{xy} = \frac{V_{xy}}{I}$ . Figure 3.2b) shows the evolution of  $n_e$  and  $\mu$  as a function of  $V_{TG}$ . As the electron density increases from negative to positive gate voltages, the mobility peaks at around  $\mu_{\max} \sim 10\,400\text{ cm}^2\text{ V}^{-1}\text{ s}^{-1}$  and then saturates to  $\sim 3\,000\text{ cm}^2\text{ V}^{-1}\text{ s}^{-1}$ . This behavior reflects that at low electron density, the mobility of the 2DEG is limited by scattering off background impurities, whereas at positive gate voltages, as electrons approach the surface, the mobility is constrained by surface defects. The mean free path  $l_e$  is calculated as [28]:

$$l_e = \frac{\hbar\mu}{e} \sqrt{2\pi n_e}. \quad (3.3)$$

This device yielded a maximum mean free path of approximately  $l_{e,\max} \sim 200\text{ nm}$ . However, because of inhomogeneities during the growth in regions close to the edges, the mean free path can vary depending on the position

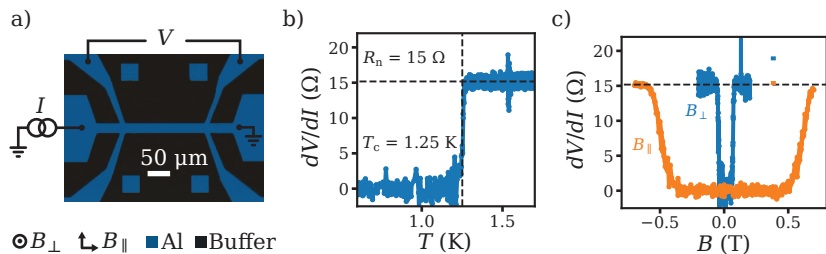


**Figure 3.3.** a) False colour optical image of an aluminium (Al) bar device used to extract the critical temperature  $T_c$  and the normal state resistance  $R_n$  of the superconducting film. We source a dc current  $I$  superimposed with a small ac component, and we measure the voltage drop  $V$  over the device. We can apply a magnetic field perpendicular  $B_\perp$  and parallel  $B_\parallel$  to the film plane. b) Differential resistance  $dV/dI$  as a function of temperature  $T$ . The vertical and horizontal dashed lines indicate the value of  $T_c$  and  $R_n$ . c) Differential resistance as a function of perpendicular and (nominally) parallel magnetic field.

on the wafer where the chip is cleaved from. Additionally,  $l_e$  depends on the specific fabrication round, as the 2DEG is sensible to surface treatments.

### Al Film - $L_{\text{kin}}$

The epitaxial aluminium films evaporated on this wafer stack are 10 nm in order to sustain high in-plane magnetic field. As such, they have a considerable fraction on kinetic inductance  $L_{\text{kin}}$  that one has to take into account for device fabrication. To estimate its value, we measure the critical temperature  $T_c$  and the normal state resistance  $R_n$  of an aluminium bar as shown in Fig. 3.3. We extract a  $R_n$  of approximately  $15 \Omega$  and a  $T_c$  of approximately  $1.25 \text{ K}$ . Using Eq. 2.17 at  $T = 20 \text{ mK}$ , with  $\Delta_0 = 1.76 k_B T_c$ , we extract a kinetic inductance per square  $L_{\text{kin}/\square} \sim 4.85 \text{ pH}$ .

The critical magnetic field of aluminium films increases with decreasing thickness, and the in-plane critical field  $B_{\parallel,c}$  of 10 nm of Al is expected in the range from 1 T to 2 T [122, 135]. In Fig. 3.3c) we plot the differential resistance  $dV/dI$  of the Al bar as a function of perpendicular  $B_\perp$  and parallel  $B_\parallel$  magnetic field. In order to measure the highest value of  $B_{\parallel,c}$  it is important to correct for any misalignment of the applied magnetic field. Without the aid of a 3-axis vector to correct for small misalignments, here we could obtain an increase of the critical field from  $B_{\perp,c} \sim 50 \text{ mT}$  (out of sample plane) to  $B_{\parallel,c} \sim 0.5 \text{ T}$  (in-plane).

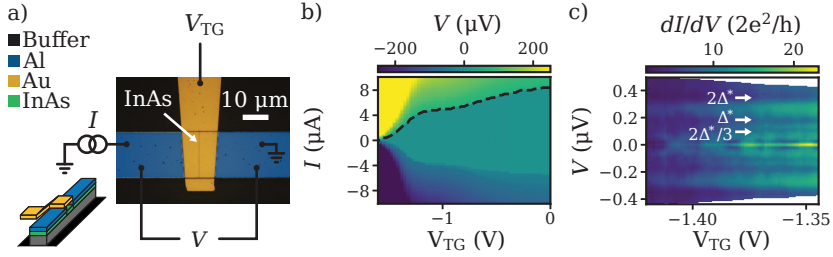


**Figure 3.4.** a) False colour electron image of a hybrid Josephson junction. The inset shows a 3D representation of the structure. The aluminium (Al) leads (blue) are used for wire bonding, and the gold (Au) topgate electrode  $V_{TG}$  (yellow) changes the electron density in the weak link. Below the gate, the Al has been removed and the exposed InAs is isolated from the Au electrode with an Hafnium oxide layer (not visible). We source a dc current  $I$  superimposed with a small ac component, and we measure the voltage drop  $V$  over the device. b) Voltage drop as a function of  $I$  and  $V_{TG}$ . The black dashed line shows the junction critical current. c) Differential conductance  $dI/dV$  as a function of  $V$  and  $V_{TG}$ . Multiple Andreev reflection processes are visible as dips in  $dI/dV$  at positions  $V = 2\Delta^*/n$ , where  $\Delta^*$  is the superconducting gap induced in the InAs below the leads, and  $n$  is an integer.

### Hybrid Josephson Junction - $\Delta^*$ and $\tau^*$

In this section, we characterize transport in hybrid Josephson junctions realized in the proximitized 2DEG. The key features of these hybrid junctions are the wide gate tunability of their critical current, and the high harmonic content of their current-phase relation (CPR), which here we parametrize with an effective transmission probability  $\tau^*$ .

In Fig. 3.4a) we show an example of a Josephson junction obtained by selectively removing a  $L = 200$  nm long stripe from a  $W = 20 \mu\text{m}$  wide Al bar. Considering as coherence length of the electrodes the one of Al thin films,  $\xi \sim 500$  nm [41], with  $l_e \approx L < \xi$ , this junction is in the short diffusive regime. A global topgate  $V_{TG}$ , isolated from the junction by 15 nm of  $\text{HfO}_2$ , is used to tune the carrier density of the InAs weak link and therefore the critical current of the junction. Figure 3.4b) shows the voltage drop over the junction  $V$  measured as a function of current bias  $I$  and  $V_{TG}$ . The critical current  $I_c$ , indicated by the black dashed line, can be tuned from approximately  $8 \mu\text{A}$  down to zero.

In Fig. 3.4c) we plot the differential conductance  $dI/dV$  of the junction

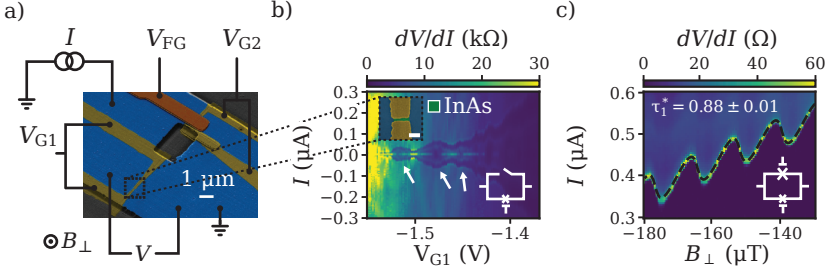


**Figure 3.5.** a) False colour electron image of a superconducting quantum interference device (SQUID) with aluminium (Al) leads (blue). Each Josephson junction is equipped with a set of local electrostatic gates (in orange and yellow):  $V_{G1}$  controls the critical current of the first junction  $JJ_1$ , while  $V_{G2}$  and  $V_{FG}$  control the second junction  $JJ_2$ . We source a dc current  $I$  superimposed with a small ac component, and we measure the voltage drop  $V$  across the device. The perpendicular magnetic field is indicated as  $B_{\perp}$ . The arms of  $V_{G1}$  are separated by 40 nm, and form a narrow constriction in the InAs (green) as shown by the inset in b), corresponding to the region inside the black dashed line in a) The scale bar is the inset is 200 nm. b) Differential resistance  $dV/dI$  of  $JJ_1$  as a function of  $I$  and  $V_{G1}$ , while  $JJ_2$  is pinched off. At sufficiently negative gate voltage values the narrow constriction acts as a superconducting quantum point contact. We observe critical current revivals as indicated by the white arrows. c)  $dV/dI$  as a function of  $I$  and  $B_{\perp}$  in an asymmetric SQUID configuration where  $I_{c,2} \approx 10 I_{c,1}$  at  $V_{G1} = -1.475$  V and  $V_{G2} = 0$  V. The current-phase relation of  $JJ_1$  is fitted with Eq. (3.6) to extract an effective transmission probability  $\tau^* \sim 0.88$ .

as a function of  $V$  and  $V_{TG}$ . In high transmission probability junctions, one expects dips in differential conductance at positions  $V = 2\Delta^*/n$  [136]. We observe dips in the  $dI/dV$  curves at positions corresponding to  $n = 1, 2$  and 3 multiple Andreev reflections (MAR), and we extract a value of the induced gap of  $\Delta^* \sim 180 \mu\text{eV}$ . Using the carrier density  $n_e(V_{TG} = 0 \text{ V}) \sim 112 \times 10^{15} \text{ m}^{-2}$  as extracted from Hall bar measurements on the same wafer, we calculate a Fermi wavelength  $\lambda_F = \sqrt{2\pi/n_e} \sim 8 \text{ nm}$ , that corresponds to approximately  $N = 2W/\lambda_F \sim 5000$  conduction channels in the junction [28]. Instead, the number of channels obtained by considering a short ballistic junction ( $\tau^* = 1$ ) with critical current  $I_c = 8 \mu\text{A}$ , is an order of magnitude lower  $N = 2\hbar I_c/e\Delta \sim 400$  (see Section 2.3.1). This indicates that transport across the junction is determined by many channels with a wide distribution of transmission probabilities.



To directly visualize the CPR of the junction, we move to a dc SQUID geometry. A typical device is shown in Fig. 3.5a). The carrier density in each junction can be locally tuned with a set of independent topgates  $V_{G1}$  and  $V_{G2}$  for JJ<sub>1</sub> and JJ<sub>2</sub> respectively. To address the few channels regime, we realize a SQPC with a split gate having  $\sim 40$  nm separation between the arms. One of the junctions is equipped with an additional finger gate  $V_{FG}$  to fine tune the carrier density in the remaining conducting channels. With standard lockin techniques we measure the differential resistance  $dV/dI$  of the SQUID as a function of gate voltages and perpendicular magnetic field  $B_{\perp}$ .

In Fig. 3.5b) we plot  $dV/dI$  of JJ<sub>1</sub> close to pinch off as a function of  $I$  and  $V_{G1}$  when JJ<sub>2</sub> is depleted (represented with an open circuit). We do not observe critical current plateaus as expected in ballistic SQPC [134, 137], but we measure resonances in  $I_c$  (white arrows) that can be attributed to opening and closing of highly transmissive channels [138–140].

To estimate the transmission probability of the junction we gate tune the SQUID in an asymmetric configuration where the critical current  $I_{c,2}$  of JJ<sub>2</sub> is much larger than the critical current  $I_{c,1}$  of JJ<sub>1</sub> ( $I_{c,2} \approx 10 I_{c,1}$ ). In this configuration, the phase drop  $\varphi_2$  over JJ<sub>2</sub> will remain approximately constant around  $\varphi_{c,2}$ , and the oscillation of the critical current as a function of perpendicular magnetic field will reproduce the CPR of JJ<sub>1</sub>. This can be understood by inserting the fluxoid relation  $\varphi_1 - \varphi_2 = 2\pi\Phi_{\text{ext}}/\Phi_0$  into the expression of the total current flowing through the SQUID:

$$I = I_1(\varphi_1) + I_2(\varphi_2) \approx I_1(2\pi\Phi_{\text{ext}}/\Phi_0 + \varphi_2) + I_2(\varphi_2), \quad (3.4)$$

where  $\Phi_{\text{ext}} = B_{\perp}A$  and  $A$  is the area enclosed by the superconducting loop.

Increasing the current bias, the SQUID will switch to the normal state at a current value  $I_c \approx I_1(2\pi\Phi_{\text{ext}}/\Phi_0 + \varphi_{c,2}) + I_2(\varphi_{c,2})$ . Figure 3.5c) shows the measurement result for a device similar to the one in Fig. 3.5a). We plot  $dV/dI$  of the SQUID as a function of  $I$  and  $B_{\perp}$ . At each magnetic field value, the critical current, indicated by the black dashed line, is extracted from the maximum in differential resistance. The CPR of a short diffusive junction in the zero temperature limits reads[141]:

$$I(\varphi) = \sum_j \left( \frac{\tau_j e \Delta}{\hbar} \right) \frac{\sin(\varphi)}{\sqrt{1 - \tau_j \sin^2(\varphi/2)}}, \quad (3.5)$$

where  $\tau_j$  is the transmission probability per mode. In multichannel devices with disorder, the distribution of transmission eigenvalues is given by Eq. 2.32. We approximate this complex CPR with a single-channel CPR with an effective

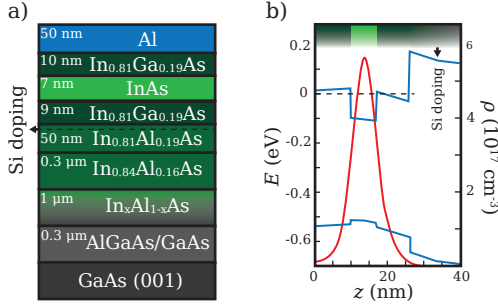


**Figure 3.6.** a) Illustration of the top layers of the wafer stack. The substrate is  $\sim 500 \mu\text{m}$  thick. b) Conduction band energies and electrons wavefunction probability density  $\rho$  along the growth direction  $z$ . Figure adapted from [124].

transmission probability  $\tau^*$  written as:

$$I(\varphi) = N \frac{e\Delta}{2\hbar} \frac{\tau^* \sin(\varphi)}{\sqrt{1 - \tau^* \sin^2(\varphi/2)}}. \quad (3.6)$$

We subtract the linear background coming from the Fraunhofer pattern of the reference junction, and we fit the oscillations in  $I_c$  with Eq. (3.6) using  $N \frac{e\Delta}{2\hbar}$  as a single fit parameter. We extract an effective transmission probability  $\tau_1^* \sim 0.88$ . As discussed in Section 2.3.2, this method of investigating the junction harmonic content has several limitations [88]. However, it gives a good estimate assuming that both junctions have similar  $\tau^*$ .

### 3.3. InAs 2DEG on GaAs Substrate

The two-dimensional electron gases provided by the group of Giorgio Biasiol are grown by MBE on semi-insulating GaAs (001) substrates. Also in this case, a 1 μm thick graded buffer of In<sub>1-x</sub>Al<sub>x</sub>As ( $x$  varying from 0.15 to 0.81) is used to release the strain coming from the lattice mismatch between GaAs ( $\sim 5.65 \text{ \AA}$ ) and InAs ( $\sim 6.06 \text{ \AA}$ ). A superlattice layer of AlGaAs/GaAs is inserted between the GaAs and the graded buffer layer to block impurities from the substrate and flatten the surface. An additional 300 nm thick In<sub>0.84</sub>Al<sub>0.16</sub>As layer is grown on top of the buffer layer to further reduce strain. The 2DEG is formed in a 7 nm thick InAs layer sandwiched between 10 nm of In<sub>0.81</sub>Ga<sub>0.19</sub>As on top and at the surface and 9 nm of In<sub>0.81</sub>Ga<sub>0.19</sub>As together with 50 nm of In<sub>0.81</sub>Al<sub>0.19</sub>As at the bottom. The In<sub>0.81</sub>Al<sub>0.19</sub>As barrier also contains a silicon doping layer used to provide carriers to the 2DEG. Finally, without breaking the MBE vacuum, 50 nm of Al are evaporated on top. Figure 3.6 shows a

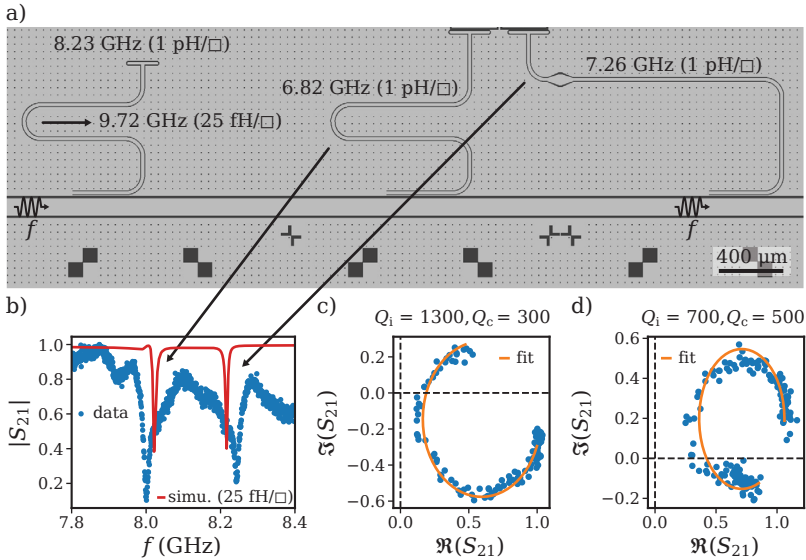


**Figure 3.7.** a) Design of a chip consisting of three superconducting coplanar transmission line resonators inductively coupled to a common feedline. The chip has been fabricated using as a superconductor the epitaxial aluminium film of the wafers in Fig. 3.6. The expected resonance frequencies for a kinetic inductance per square of  $L_{\text{kin}}/\square = 1 \text{ pH}$  are indicated on top of the corresponding resonator. The expected resonance frequencies for a negligibly small kinetic inductance ( $L_{\text{kin}}/\square = 25 \text{ fH}$ ) are pointed at with black arrows. b) Magnitude of the reflection coefficient  $|S_{21}|$  as a function of frequency  $f$  measured using a vector network analyser. The red solid line shows the result of a Sonnet simulation with  $L_{\text{kin}}/\square = 25 \text{ fH}$ . c) and d) Circular fit on the resonance at  $\sim 8 \text{ GHz}$  and  $\sim 8.25 \text{ GHz}$  respectively. The internal quality factor  $Q_i$  and the coupling quality factor  $Q_c$  for each resonance are given on top each fit.

schematic of the full wafer stack and the electron wavefunction probability density  $\rho$  in the 2DEG obtained from a Schrödinger-Poisson solver. As for the previous structure,  $\rho$  is not zero at the interface with the superconductor.

### 3.3.1. Wafer Characterization

Details about the growth and the characterization of this second type of wafer can be found in Ref. [124, 142–144]. Since we only received the first sample from this wafer during the final stage of the thesis, we did not perform any

dc characterization, but instead we directly proceeded to device design based on the information we found in literature and those provided to us by our collaborators in Trieste and Budapest.

### Al Film - $L_{\text{kin}}$

One important parameter that was missing, in particular for the design of resonators made of the epitaxial Al film, was the kinetic inductance of this new film. Based on the value of kinetic inductance per square that we extracted for the 10 nm Al film, from Eq. 2.17 we were expecting  $L_{\text{kin}/\square}$  to be around 1 pH/ $\square$ . To verify this, we fabricated three  $\lambda/4$  hangers transmission line resonators inductively coupled to a common feedline. The design is shown in Fig. 3.7: one resonator is far away from the others, while the other two are coupled at the voltage antinode. Their resonance frequencies, estimated using a finite-element simulation software (Sonnet) with  $L_{\text{kin}/\square} = 1$  pH, were expected at 6.82 GHz, 7.26 GHz, 8.23 GHz. For the simulation, we have used  $\epsilon_{\text{GaAs}} = 12.35$  [145] as the dielectric constant of the GaAs substrate.

To define the central conductor we etch away the Al, together with the 2DEG and  $\sim 400$  nm of buffer layer. The etching techniques are detailed in Chapter 4. The measurement (see Fig. 3.7) shows two resonances around 8 GHz and 8.25 GHz. In contrast with our expectations, we have to set in the simulation a negligibly small kinetic inductance ( $L_{\text{kin}/\square} = 25$  fH) to match the data (red solid line in Fig. 3.7b)). Using  $L_{\text{kin}/\square} = 25$  fH, the resonance that we expected at 8.23 GHz gets instead pushed up to 9.7 GHz falling outside of the measurement bandwidth. We use a circular fitting procedure [146] to extract the coupling and the internal quality factors of the two resonators. The simulated coupling quality factors  $Q_{c,\text{simu.}} \sim 1400$  for the resonance at 8 GHz and  $Q_{c,\text{simu.}} \sim 1800$  for the resonance at 8.25 GHz, differs by more than a factor of three compared to the measured one:  $Q_c \sim 300$  for the resonance at 8 GHz and  $Q_c \sim 500$  respectively. This discrepancy is most probably caused by an overetching of the ground plane stripe separating the resonators from the feedline. We extract  $Q_i \approx 1300$  for the resonance at 8 GHz and  $Q_i \approx 700$  for the resonance at 8.25 GHz. The relatively low internal quality factor of the resonators might be caused by a combination of dielectric losses in the substrate and in the buffer layer.

## 3.4. Granular Aluminium

In this section, we summarize the key properties of a high kinetic inductance material called granular aluminium, explaining the reasons why it is attracting increasing interest in the superconducting circuit community and why we in

particular wanted to use it.

The experiment we intended to perform was motivated by recent developments in coupling a superconducting resonator to the spin of a trapped quasiparticle in a hybrid Josephson Junction. In Ref. [78], the authors inductively couple a resonator to the an InAs nanowire junction and show a dispersive shift dependent on the spin orientation of the occupied Andreev bound state (ABS). While this technique enables the authors to read out the quasiparticle spin, they cannot directly drive the spin in their setup.

In our case, we wanted to exploit the fact that spin orbit interactions in a InAs 2DEG give rise to an effective electric dipole moment of the quasiparticle spin transition [37], which can couple to the electric field fluctuations at the voltage antinode of a resonator. As the electric field fluctuations are proportional to the square root of the resonator impedance, what we needed was a high kinetic inductance superconductor compatible with our fabrication process.

Superconductivity in so called granular aluminium (grAl) films, which in general denotes disordered Al films, was first discovered exactly 70 years ago by W. Buckel and R. Hilsch in Göttingen [147]. In this original publication the authors evaporated Al on a quartz substrate at 4 K, and they measured a critical temperature  $T_c \sim 2.59$  K for a 20 nm thick film, well above the literature value of 1.2 K [122]. Interestingly, when they cycled the chip to room temperature and cooled it down again, the  $T_c$  enhancement vanished. They attributed the rise in  $T_c$  to the emergence of crystallographic defects in the film induced by the low deposition temperature, and the disappearance of this effect during the second cooldown to the film's recrystallization at room temperature.

After more than 10 years from that discovery, Abeles and Cohen [148, 149] stabilized the enhancement of  $T_c$  by evaporating Al at room temperature in a partial oxygen pressure  $p_{O_2}$ . Presumably, due the precipitation of oxygen in the form of Al oxide at the boundaries between Al grains, these granular films did not recrystallize after thermal cycling. In 1973, G. Deuthscher [150], used electron diffraction to investigate the crystallinity of the Al grains, and measured the normal state film resistivity  $\rho_n$  and  $T_c$  as a function of grain size. He observed an increase  $\rho$  as a function of oxygen pressure and a dome shape behaviour of  $T_c(\rho_n)$ . The grain size on the other hand, decreased with increasing  $p_{O_2}$  eventually saturating at around 3 nm.

More recently, after  $\sim 40$  years since the last publication, grAl has gained renewed interest thanks to the work in the groups of the same G. Deuthscher

at Tel-Aviv University and of I. Pop at the Karlsruhe Institute of Technology (KIT). The group in Israel has been focused on understanding the superconducting properties of grAl [151–154], whereas the group in KIT has used this material system for kinetic inductance detectors [155, 156], to investigate the effect of quasiparticles on superconducting resonators [157–159], for superconducting qubits [102, 160, 161] and more.

Granular aluminium offers several advantages compared to other platforms such as Josephson junctions arrays or other disordered superconductors (mostly nitrides), commonly used to realize high impedance resonators. The fabrication of Josephson junction arrays relies on the inductance of hundreds of junctions patterned in a compact geometry to reduce stray capacitance [82, 162, 163]. In this platform, it is difficult to achieve at the same time a high impedance, while minimizing the addition of unwanted non-linearities to the quantum circuit [162, 164]. Disordered superconductors such as NbTi, TiN, or NiTiN thin films, allow to reduce the effects of these non-linearities [165]. However, the maximum achievable kinetic inductance is limited in the range of a few hundreds  $\text{pH}/\square$  when the film is thinner than 10 nm [166–169]. Granular aluminium films instead, have a normal state resistivity which can be varied, depending on the partial oxygen pressure during evaporation, from  $\rho_n = 1 \mu\Omega \text{cm}$  to  $1 \times 10^4 \mu\Omega \text{cm}$ . The ratio between the zero temperature superconducting gap  $\Delta_0$  and the critical temperature of the film increases up to  $\Delta_0/k_b T_c \sim 2.2$  [150, 155] compared to the BCS value of 1.76. By inserting these values in Eq. 2.17, assuming a film thickness of  $t = 20 \text{ nm}$ , one finds that it is possible to obtain a kinetic inductance per square up to  $L_{\text{kin}}/\square \sim 2.5 \text{ nH}$ .

In previous projects within the group, NbTiN films were sputtered over the entire chip, and the patterning achieved through inductive coupled plasma (ICP) etching. In our case, the detrimental effects of highly energetic ions on the substrate posed a significant concern due to the presence of the near-surface 2DEG. The large kinetic inductance of grAl, and its compatibility with standard lift-off processes, made it our material of choice. We present the fabrication process in Section 4.2.2, and discuss the quality of grAl resonators on a InP substrate in Ch. 5.

# 4 Fabrication Procedures

---



This chapter contains an overview of the fabrication processes we have used to realize hybrid epitaxial Al/InAs devices on both InP and GaAs substrates, as well as high kinetic inductance resonators on InP substrates. We show the fabrication of devices made entirely from the epi-Al/InAs system. In this case, all components, including the microwave circuit and the junction are already electrically connected. This removes the need for additional and often critical contacting steps. However, the kinetic inductance of the epitaxial aluminium film is sometimes not enough for specific applications which require high impedance resonators. Here we show the fabrication of high kinetic inductance superconducting resonators made of NbTiN and granular aluminium thin films on InP substrates. The aim is to extract an upper bound to the quality factor achievable with high impedance resonators on II-V materials.

## 4.1. Epi-Al/InAs Devices

This section outlines the fabrication process of both dc and rf devices entirely (except for the electrostatic gates) realized using the epitaxial aluminium. A more detailed description is given in the Appendix E.1 and fantastically explained in Ref. [170]. These kind of structures are particularly flexible since they mostly rely on top-down fabrication steps. However, the overall quality of the final device can be constrained by several factors. Resonators may experience limitations due to losses stemming from the substrate and dielectric materials in the buffer layer, as well as inductive losses within the thin epitaxial aluminium layer. Additionally, the performance of the junction can be adversely affected by quasiparticle poisoning in the absence of effective quasi-

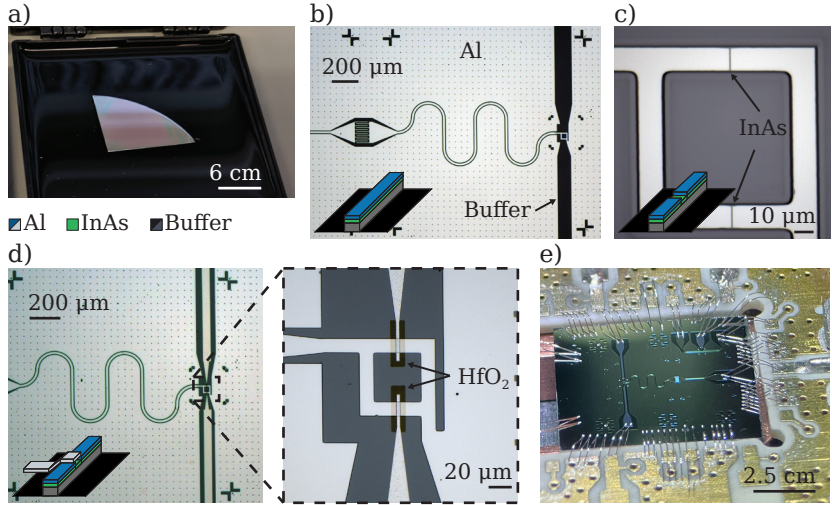


**Figure 4.1.** a) Starting point of device fabrication: a quarter of 2-inch wafer. In the next panels, the aluminium (Al) is gray in the optical images while it is shown in gray or in blue in the schematics depending on whether it represents an electrostatic gate or epitaxial film. The buffer layer will be in different shades of dark grey or in black in both the images and the schematics. The InAs is shown in green in the schematics and pointed at with arrows when visible in the optical images. b) In the first step, we define the leads or the central conductor for the case of a transmission line resonator as shown in the optical image. We etch away the Al, the InAs and part of the buffer to define the shape of the electrical circuit. The inset schematically shows the result of this first step. c) We define the Josephson junction by selectively removing the Al from narrow stripes along the leads. d) Afterwards, we selectively grow an hafnium oxide ( $\text{HfO}_2$ ) layer at the position indicated by the arrows to galvanically isolate the electrostatic gates which are evaporated on top. e) Finally, we directly bond on the epitaxial Al.

particle abatement mechanisms.

We typically start from a quarter of a 2-inch wafer as shown in Fig. 4.1a). To cleave the wafer into chips of the desired dimensions, typically  $10 \times 5$  cm, we spin coat a protective layer of  $\sim 200$  nm of PMMA 950K (AR-P 672.045). Every time before spinning a resist to be used as a mask, we clean the chip with 5 min dip in 1-3 Dioxolane followed by a 30 s rinse in acetone and IPA.



The mask for etching the mesa and to define the device template consists of two layers of PMMA 950 with a total thickness of  $\sim 400$  nm. Two layers are used instead of just one in order to have a more stable mask during the wet etch. Windows in the mask are patterned using standard e-beam lithography (EBL) followed by a development in a 1:3 mixture of methylisobutylketone (MIBK) and IPA for 1 min. We remove PMMA residues with 1 min in a low power (30 W) oxygen plasma and post-bake the resist at  $120^\circ\text{C}$  for 2 min to improve its adhesion to the substrate and remove the undercut (the post-bake step is repeated after every wet etch). First, we use a Transene D-type solution at a temperature of  $50^\circ\text{C}$  to etch away the epitaxial aluminium, with the etching time determined by the thickness of the film. We always check the outcome of this step with an optical microscope, since if the etching is not complete, Al residues will act as a disordered mask for the mesa etch solution, practically wasting the chip. The mesa etch solution consists of a mixture 220:55:3:3 of  $\text{H}_2\text{O}:\text{C}_6\text{H}_8\text{O}_7:\text{H}_3\text{PO}_4:\text{H}_2\text{O}_2$  mixed in this order, and works equally well for both the wafer stacks used in this thesis. We wait 5 min after having added  $\text{H}_2\text{O}_2$  and before dipping the chip to have a stable etching rate of  $\sim 30$  nm/min of the buffer on the InP substrates and of  $\sim 50$  nm/min of the buffer on GaAs substrates. In order to remove partially conductive layers in the buffer, we etch deep trenches of minimum 300 nm and 450 nm respectively. The result of this step is shown in Fig. 4.1b).

Afterwards, the Josephson junctions are defined following the same e-beam procedure, and the Al film is selectively removed using Transene D. The minimum junction length we have managed to achieve with a uniform etch profile along the junction was around 150 nm for a width of  $3\ \mu\text{m}$  (see Fig. 4.1c)).

Around 25 nm to 35 nm of Hafnium oxide ( $\text{HfO}_2$ ) are grown via atomic layer deposition (ALD), either across the entire wafer or in localized regions to isolate the subsequent electrostatic gate layer. To mitigate any etch marks that may arise during the liftoff of the ALD-grown dielectric, we use a three-layers PMMA stack and an acceleration voltage of 10 kV, which increases the undercut of the exposed profile. An important parameter is the growth temperature. Figure 4.2 shows a comparison between the mobilities as a function of carriers density of two Hall bars where the oxide was grown at  $200^\circ\text{C}$  and  $90^\circ\text{C}$ . The mobility decreases by a factor of 2 when the oxide is grown at high temperature. We speculate that this is due to inter-diffusion of atoms between the layers in the buffer, that changes the strain profile and therefore the 2DEG mobility. We grow the oxide at  $90^\circ\text{C}$ , and wait 3 min per precursor pulse for the reaction to be complete, with a recipe we have learned from Asbjørn C. C. Drachmann from the Niels Bohr Institute in Copenhagen.

Finally, we use an e-beam evaporator to deposit the electrostatic gates (see

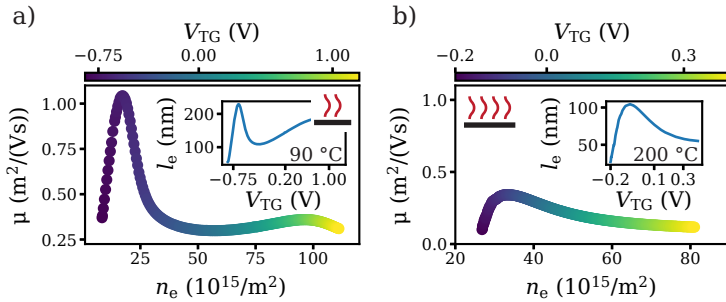


**Figure 4.2.** a) Mobility  $\mu$  as a function of carrier density  $n_e$  at different gate voltage as extracted from Hall bar measurement at  $T = 250\text{mK}$ . The inset shows the electron mean free path  $l_e$  as a function of  $V_{\text{TG}}$ . The hafnium oxide layer in this case was grown at  $90^\circ\text{C}$ . b) Same as in a) for a chip from the same wafer, where the hafnium oxide was grown at  $200^\circ\text{C}$ .

Fig. 4.1d)). This is done in either one or two steps depending on the gate geometry. When the design includes split gates or fine structures, we first pattern those using a thin resist stack and a low e-beam aperture, and then we pattern the bonding pads, with a thicker resist and evaporating a lot of metal at different tilt angles to be sure to climb the mesa walls. Typically we evaporate Ti/Au (5/20 nm) for the fine structures and Ti/Au or Ti/Al (10/300 nm) for the pads.

We bond the final device with a semi-automatic bonder from Bondtec<sup>®</sup> equipped with a 5630i bonding head and a  $30\mu\text{m}$  thick Al wire. This specific head is particularly well-suited for bonding on very brittle III-V substrates. It employs a double-sided clamp to hold the wire in place, and the wire is cut after the second bond with a rapid movement of the clamp itself. In contrast to deep-access bonding heads or similar equipment, where the wire is cut by moving the stage, this method enables a faster, more precise and more reliable bonding process. The result is shown in Fig. 4.1e).

## 4.2. High Kinetic Inductance Resonators

In this section, we outline the fabrication of NbTiN and granular aluminium thin films on double polished InP (001) substrates as a first step to couple high impedance superconducting resonators to proximitized InAs Josephson junctions. While the fabrication of NbTiN resonators had already been well established within our group at the beginning of this work (as detailed in

Ref. [86]), the procedure for granular aluminium was learned from the group of Ioan Pop at the Karlsruhe Institute of Technology and subsequently brought in-house.

#### 4.2.1. NbTiN Sputtering

For our purposes, designing and characterizing NbTiN resonators served as a reproducibility test before transitioning to the more challenging fabrication of grAl-based resonators. In previous projects within the group, NbTiN films were deposited onto relatively large 4-inch wafers, and the patterning achieved through inductive coupled plasma (ICP) etching. In our case, the detrimental effects of highly energetic ions on the substrate posed a significant concern due to the presence of the near-surface 2DEG. As a consequence, we chose to lift-off the sputtered films, and limit the formation of metallic residues on the mask edges by employing a multilayer resist stack and a minimalistic design.

To pattern the resonators we have used both e-beam and optical lithography. The main disadvantage of optical lithography is that most resist developers contain a percentage of tetramethylammonium hydroxide (TMAH) that etches Al. As a consequence, patterning hybrid devices that contain Al films carries significant risks, as any inaccuracies in the writing or development process can lead to the loss of an entire chip. Nevertheless, optical exposure is much faster and allows fast characterization of different designs (when the exposure works).

The InP substrate is cleaned with 5 min sonication in 1-3 Dioxolane followed by an acetone and IPA rinse, and blow dry. To increase the undercut of the e-beam exposure, we spin coat a more sensitive bottom layer resist consisting of 2 layers of EL6 (MMA(8.5)MAA from MicroResist) and one layer of less sensitive PMMA 950K. We then pattern the design using 30 kV of acceleration voltage, and develop the resist for 60 s in MIBK:IPA (1:3). For optical lithography, we spin coat LOR3A as a bottom layer, and S1805 as top layer. and expose the design using a laser writer with 6 mW of power. We develop the resist for 50 s in MF319 followed by a 60 s rinse in DI water.

Sputtering of NbTiN is obtained in a AJA<sup>®</sup> ATC Orion 8 sputtering machine from a NbTi target in a N<sub>2</sub> atmosphere. We deposit 20 nm at a rate of approximately 0.2 nm s<sup>-1</sup>, corresponding to a sheet kinetic inductance of  $\sim 10$  pH. We strip the resist with 30 min in Dioxolane at room temperature followed by 30 min in acetone at 50 °C and a 30 s rinse in IPA before blow dry. At the end, the ground plane is defined by a 150 nm thick gold layer sputtered on the backside of the chip, while we protect the frontside with a layer of PMMA.

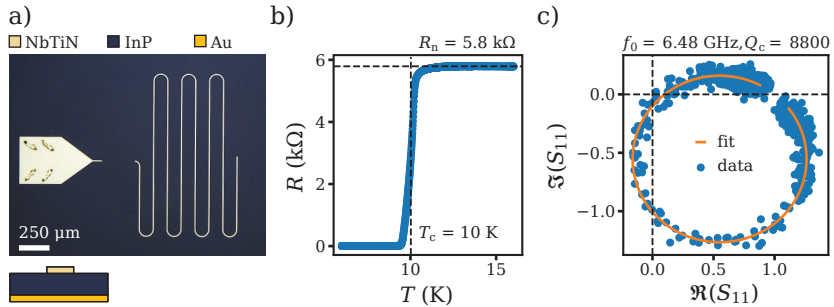


**Figure 4.3.** a) False colour optical image of a NbTiN resonator (light yellow) on a InP substrate (dark blue). The ground plane is defined by a gold (Au) layer (yellow) evaporated on the back of the chip. b) Resistance  $R$  as a function of temperature  $T$  of a NbTiN bar used to extract the critical temperature  $T_c$  and the normal state resistance  $R_n$  of the superconducting film. c) Circular fit on the resonance at  $f_0 \sim 6.48$  GHz. We extract a coupling quality factor  $Q_c \sim 8800$ .

A typical device is shown in Fig. 4.3a). It consists of a  $\lambda/2$  stripline resonator capacitively coupled to a launching pad. The resonator is measured at  $T \approx 1.6$  K using a variable temperature insert (see Appendix SETUP for details). Figure. 4.3c) shows the complex reflection coefficient  $S_{11}$  and the result of a circle fit used to extract the resonance frequency  $f_0 \sim 6.485$  GHz and the coupling quality factor  $Q_c \sim 8800$ . The internal quality factor  $Q_i$  was in this case  $\sim 7200$ .

We estimate the resonance frequency and the coupling strength with Sonnet simulations, using  $\epsilon_{\text{InAs}} = 12.55$  as relative dielectric constant of the InP substrate [171]. To extract the kinetic inductance per square of 20 nm of NbTiN we measure the resistance of a film as a function of temperature. This is shown in Fig. 4.3b). Using Eq. 2.17, together with the expression for the zero temperature NbTiN superconducting gap  $\Delta_0 = 1.86k_B T_c$  [172], we extract a kinetic inductance per square  $L_{\text{kin}}/\square \sim 7.55$  pH. From the simulations, setting this value of  $L_{\text{kin}}/\square$  we obtain a resonance frequency  $f_{0,\text{simu.}} \sim 6.768$  GHz, in good agreement with the measured one. On the other hand, the simulated coupling quality factor  $Q_{c,\text{simu.}} \sim 4500$  differs by a factor of 2 compared to the measured one. This discrepancy can be caused by standing waves patterns in the rf lines due to spurious impedance mismatches.

The impedance and the resonance frequency of the resonator can also be estimated by calculating the geometrical inductance  $L_{\text{geo}}$  and the capacitance

$C$  of a straight microstrip with length  $l$ , having a width  $w$ , and separated by a distance  $h$ , given by the thickness of the substrate, from the ground plane. The expression for  $L_{\text{geo}}$  and  $C$  in case of a straight microstrip are given by [173]:

$$L_{\text{geo}} = \frac{60l}{\nu_0} \log \left( \frac{8h}{w} + \frac{w}{4h} \right) \quad (4.1)$$

$$C = \frac{\epsilon_{\text{eff}} l}{60\nu_0 \log \left( \frac{8h}{w} + \frac{w}{4h} \right)} \quad (4.2)$$

$$\epsilon_{\text{eff}} = \frac{\epsilon_r + 1}{2} + \frac{\epsilon_r - 1}{2} \left[ \left( 1 + \frac{12h}{w} \right)^{-\frac{1}{2}} + 0.04 \left( 1 - \frac{w}{h} \right)^2 \right] \quad (4.3)$$

where  $\nu_0$  is the speed of light in vacuum,  $\epsilon_r$  is the relative dielectric constant of the substrate, and  $\epsilon_{\text{eff}}$  is the effective permittivity of the microstrip. The impedance and the resonance frequency of a  $\lambda/2$  microstrip are given by:

$$f_0 = \frac{v_{\text{ph}}}{2l} = \frac{1}{2l\sqrt{L_l C_l}} \quad (4.4)$$

$$Z_r = \sqrt{\frac{L_l}{C_l}} \quad (4.5)$$

where  $L_l = L_{\text{geo},l} + L_{\text{kin},l}$  and  $C_l$  are the total inductance and capacitance per unit length of the line. Inserting our design parameters in the above equation, we obtain  $f_0 \sim 5.839$  GHz and  $Z_r \sim 180 \Omega$ . The lower value of resonance frequency obtained from this calculation compared to the measured or simulated one can be explained by the fact that bending the microstrip (as in Fig. 4.3a)) effectively reduces its electrical length [173] and thus increases its resonance frequency.

Being overall satisfied with the compact design and with the agreement to the simulations, and we moved to the fabrication of granular aluminium.

#### 4.2.2. Granular Aluminium Evaporation

I acquired knowledge about the fabrication procedure of grAl from the group of Ioan M. Pop at the Karlsruhe Institute of Technology (KIT), and in particular from Mahya Khorramshani, to whom I express sincere gratitude for her patience and availability. Throughout this period, we successfully fabricated and measured grAl resonators on InP substrates using the KIT facilities. Patterning is done entirely using a reverse optical lithography routine, and grAl is evaporated using a Plassys MEB 550S<sup>®</sup> e-beam evaporator. Details about the fabrication can be found elsewhere [51, 98]. The measurements we have performed at KIT on these resonators are outlined in Chapter 5. In the following, we outline the implementation and testing processes for evaporation

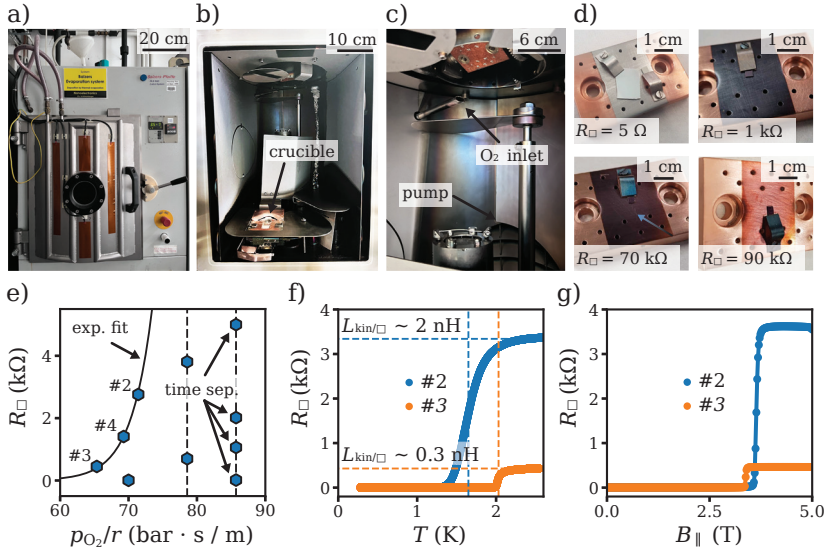


**Figure 4.4.** a) Balzers-Pfeiffer<sup>®</sup> PLS 500 Labor-System e-beam evaporator used for the evaporation of granular aluminium (grAl). b) Inside of the chamber and c) zoom-in on the oxygen  $\text{O}_2$  inlet. The positions of the copper boat for the aluminium (Al) crucible and of the pump are indicated by the arrows. d) Colors of the evaporated film for different oxygen partial pressure  $p_{\text{O}_2}$  and consequently different room temperature sheet resistance  $R_{\square}$ . All film have the same nominal thickness of  $\sim 20\text{nm}$ . In the bottom left panel we observe a clear gradient in film colour, indicate by the arrow, which corresponds to the direction along which  $\text{O}_2$  reaches the sample. e)  $R_{\square}$  as a function of the ratio between  $p_{\text{O}_2}$  and the Al evaporation rate  $r$  for different films. The dependence of  $R_{\square}$  on  $p_{\text{O}_2}/r$  can be fitted with an exponential in case of evaporation rounds close to each other in time, but is random for evaporation separated by a long time distance. In this last case, the same  $p_{\text{O}_2}/r$  ratio results in different values of  $R_{\square}$  as indicated by the vertical dashed lines. f)  $R_{\square}$  as a function of temperature  $T$  and parallel magnetic field  $B_{\parallel}$  for film #2 and #3. From Eq. 2.17 we extract a sheet kinetic inductance of  $L_{\text{kin},\square} \sim 2 \text{ nH}$  (film #2) and  $L_{\text{kin},\square} \sim 0.3 \text{ nH}$  (film #3). g)  $R_{\square}$  as a function of parallel magnetic field  $B_{\parallel}$  for film #2 and #3. Both films shows an in plane critical field  $B_{\parallel,c} > 2.5 \text{ T}$ .

of grAl in Basel, established together with Alessia Pally.

## Fabrication in Basel

The spin coating, exposure and lift off procedures are the same as outlined in Section 4.2.1. The evaporation step instead deserves some more attention. Pictures of the machine we have used for grAl evaporation in Basel from the outside and the inside of the chamber are shown in Fig. 4.4a)-c). The system is a Balzers-Pfeiffer<sup>®</sup> PLS 500 Labor-System e-beam evaporation machine, with a crucible to host the evaporated metal positioned around 60 cm below the substrate holder. The Al target sits in a reinfiltrated graphite crucible which is inserted into a water cooled copper holder. We equipped the system with an additional copper rod close to the sample that we use to inject oxygen into the chamber. The base pressure before starting the evaporation is around  $2 \times 10^{-7}$  mbar. We evaporate 25 nm of titanium with the substrate shutter closed to condition the chamber and improve the pressure. Next, we heat up the Al target until we reach a rate of  $1.4 \text{ \AA s}^{-1}$ . We introduce oxygen into the chamber using a voltage controlled valve that allows to tune the oxygen partial pressure by  $\pm 0.1 \times 10^{-6}$  mbar. When the desired parameter set is reached, we evaporate 20 nm of grAl.

Figure 4.4 shows the results of four different evaporations obtained by slightly varying the partial oxygen pressure  $p_{\text{O}_2}$  and the evaporation rate  $r$ . The colour of the film changes from silvery to dark blue to almost transparent as the film sheet resistance  $R_{\square}$  increases. We measure  $R_{\square}$  on test stripes  $10 \mu\text{m}$  wide and 1 mm long patterned with e-beam lithography. We were able to tune  $R_{\square}$  over a wide range, but unfortunately we did not always have consistent results. Table 4.1 summarizes the film  $R_{\square}$  obtained with varying parameters in different moments in time. Some entries are also plotted in Fig. 4.4e) as a function of the ratio  $p_{\text{O}_2}/r$ . The evolution of  $R_{\square}$  with  $p_{\text{O}_2}/r$  can be fitted with an exponential when points correspond to subsequent evaporations. However, we notice that the same combination of parameters repeated after some time results in a wide variation of film resistance. The behaviour can be attributed to several factors, including:

1. Drift in pressure sensor readings over time.
2. Contamination from the crucible: the elevated temperatures reached by the crucible during evaporation can lead to contamination of the target material. The interaction between the material and the crucible can cause impurities to transfer, affecting the purity of the deposited film.
3. Breaking of crucible: the beam current has to be increased slowly to prevent thermal shock to the crucible. However, despite this precaution, the crucible still breaks sometimes. In such cases, it is necessary to replace the broken crucible with a new one and fill it with fresh ma-

**Table 4.1.** Example Table

#	Date	$p_{\text{O}_2}$ (mbar)	$r$ ( $\text{\AA s}^{-1}$ )	$R_{\square}$ ( $\Omega$ )	Comments
1	08.12.21	1.20e-5	1.2	90.1e3	
2	15.12.21	1.00e-5	1.4	2.76e3	
3	16.12.21	0.92e-5	1.4	450	
4	18.12.21	0.97e-5	1.4	1.41e3	
5	11.02.22	0.98e-5	1.4	5	New pressure sensor
6	12.02.22	1.20e-5	1.4	1.06e3	
7	23.02.22	1.20e-5	1.4	5.01e3	
8	05.04.22	1.20e-5	1.4	14	
9	06.04.22	1.40e-5	1.4	29.2e3	
10	06.04.22	1.30e-5	1.4	15.3e3	Crucible breaks
11	07.04.22	1.20e-5	1.4	61.3e3	
12	12.04.22	1.20e-5	1.4	1.99e3	
13	13.04.22	1.10e-5	1.4	3.80e3	
14	14.04.22	1.10e-5	1.4	701	

terial. Unfortunately, this replacement causes a reset of the deposition parameters.

4. Oxidation of the target: when the target material interacts with atmospheric oxygen, it forms oxide layers that alter its properties and affect subsequent depositions.

To compensate for the effect of these variations, several evaporations are necessary to calibrate the set of parameters needed to achieve a given sheet kinetic inductance. To have more control on this type of evaporation we plan to replace the voltage regulated valve with an oxygen flow controller, to evaporate Al without crucible, and install an in-situ resistance measurement device.

In Fig.4.4f) and Fig.4.4g) we show the dependence of  $R_{\square}$  as a function of temperature  $T$  and parallel magnetic field for film #2 and #3. In this range of resistivity, the ratio  $\Delta_0/k_{\text{B}}T_{\text{c}}$  for grAl varies in between 2 and 2.2 [150, 155]. From Eq. 2.17, assuming  $\Delta_0/k_{\text{B}}T_{\text{c}} = 2.2$ , we extract a kinetic inductance per square  $L_{\text{kin}/\square}$  of  $\sim 2$  nH and  $\sim 0.3$  nH respectively. This is more than 2 orders of magnitude larger than what obtained with 20 nm of NbTiN. Both films had an in-plane critical magnetic field larger than 2.5 T. The value of critical field that we obtain is smaller than previously reported values [174], probably due to an imperfect alignment.

The design of the grAl-based resonator we have fabricated in Basel is similar

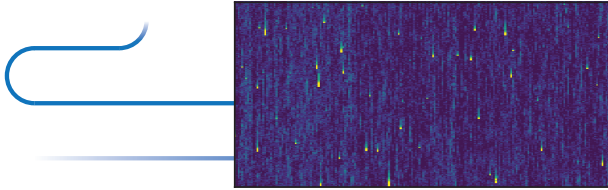


to the one we have used for NbTiN resonators. The measurements results can be found in Chapter 5.



# 5 Granular Aluminium Resonators on InP

---



In this chapter, we investigate the limiting factors of the internal quality factor  $Q_i$  of high-impedance resonators on a piezoelectric substrate, i.e. InP (001). Reference [175] addresses the same problem for low-impedance aluminium resonators fabricated on a GaAs (001) substrate. The study highlights that energy losses arising from the conversion of the electric field in the resonators into bulk and surface acoustic waves, effectively limit the  $Q_i$  of these resonators to  $\sim 10^4$ . Our goal is to investigate whether the large electric field fluctuations in high-impedance resonators pose an additional limitation on their  $Q_i$  when employed on such substrates.

In the following, we discuss measurements of granular aluminium (grAl) resonators evaporated on Fe-doped InP (001) substrates. To gain insights on the factors limiting their  $Q_i$  we analyse the power and temperature dependence of two distinct batches of resonators fabricated at KIT and at Uni Basel.

## 5.1. grAl at KIT

The design of grAl resonators fabricated and measured at KIT, is the same as in Ref. [157]. We show the measurements of two InP chips each hosting a set of three 20 nm thick resonators with lateral dimensions  $A = (420 \times 5) \mu\text{m}^2$ ,  $B = (1000 \times 40) \mu\text{m}^2$  and  $C = (600 \times 10) \mu\text{m}^2$ , as shown in Fig. 5.1a). We measure the normal state sheet resistance  $R_{\square}$  of the films using test pads evaporated simultaneously with the resonators: the rightmost chip has  $R_{\square} = 0.9 \text{ k}\Omega$  and the leftmost chip has  $R_{\square} = 2.8 \text{ k}\Omega$ . Both chips sit at one end of a copper waveguide used to provide a low loss microwave environment [176, 177]. The coupling to each resonator is determined by the transversal electric

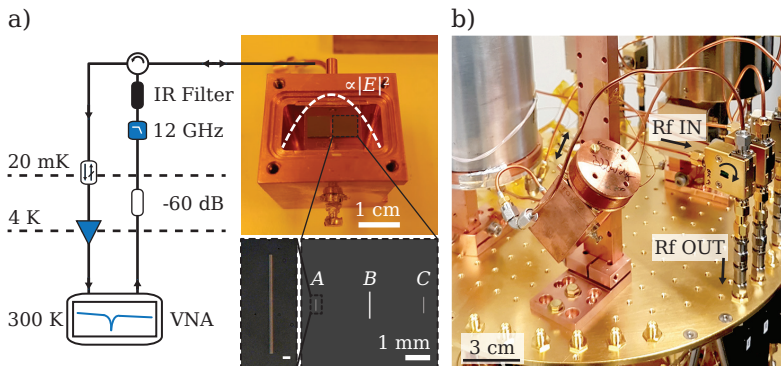


**Figure 5.1.** a) Simplified measurement schematic: the input signal is provided by a vector network analyser (VNA), and reaches a circulator after 60 dB of nominal attenuation distributed along the line, a bandpass filter at 12 GHz and an infrared filter (IR). The signal is subsequently directed into a copper waveguide, whose endpoint houses two InP chips. Each chip contains three resonators of varying dimensions labelled A, B, and C. The transverse electric field profile is represented by the white dashed line. The reflected signal is then directed to the amplification line. It passes through an isolator before being amplified by a combination of a HEMT and a room temperature amplifier. b) Setup at the mixing chamber. The waveguide has no permalloy or superconducting shielding.

field profile inside the waveguide. We perform standard microwave reflection measurements in a Qinu dilution cryostat with a base temperature of 20 mK. Figure 5.1b) shows the setup at the mixing chamber plate consisting of the waveguide, the wiring, and a circulator used to redirect incoming and outgoing signals. The waveguide is thermally anchored to a copper holder attached to the mixing chamber. It is equipped with a magnetic coil, although this will not be used in the following, and it has not no permalloy or superconducting shielding against stray magnetic fields.

From a circular fit of the complex reflection coefficient  $S_{11}$ , we extract the resonance frequency  $f_0$ , the coupling quality factor  $Q_c$  and  $Q_i$  of all resonances at an average circulating photon number  $\bar{n} \sim 1 - 10$ . The value of  $\bar{n}$  is calculated near the resonance frequency as [178]:

$$\bar{n} = 4P_{\text{in}} \frac{Q_i^2}{hf_0^2 Q_c}, \quad (5.1)$$

where  $P_{\text{in}}$  is the power reaching the device, accounting for  $\sim -60$  dB of nomi-

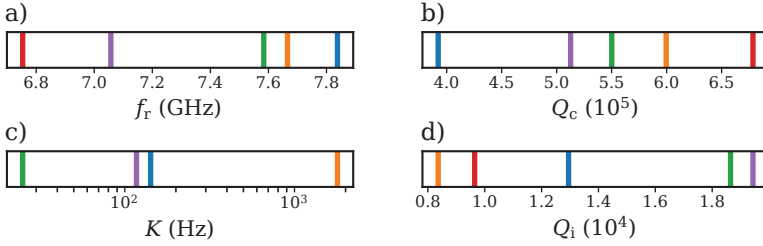


**Figure 5.2.** Overview of fit parameters for the five resonances detected, each associated with a specific colour. a) resonance frequency  $f_0$ , b) coupling quality factor  $Q_c$ , c) Kerr coefficient  $K$  and d) internal quality factor  $Q_i$ .  $f_0$ ,  $Q_c$  and  $Q_i$  are extracted from a circle fit with  $\bar{n} \sim 1 - 10$  average circulating photons in the resonators.  $K$  is extracted for 4 resonance from a fit to the power dependence of their resonance frequencies (see text).

nal attenuation and  $\sim -13$  dB of cables losses, and  $Q_1 = (1/Q_i + 1/Q_c)^{-1}$  is the loaded or total quality factor. To characterize the resonators non-linearities, we extract the self-Kerr coefficient  $K$ , defined as the resonance frequency shift per photon, from a linear fit to  $f_0 = -K\bar{n}$ . We measure a total of 5 resonances out of 6. The results are summarized in Fig. 5.2, where the resonances have been assigned different colours. In the following, we try to attribute each resonance to a resonator, or at least to one of the two InP chips.

Figure 5.3 shows the power dependence of the resonances around 7.666 GHz (orange) and 6.754 GHz (red). In both cases the dip in  $|S_{11}|$  corresponding to the resonance frequency, shifts on a faster timescale compared to the measurement time (0.5 s/trace). Interestingly, the resonance at 6.754 GHz appears to fluctuate between four discreet values. The parameters plotted in Fig. 5.2 associated to the red resonance are extracted from a fit of the uppermost dip at  $P = -43$  dBm. We attribute this instability to non-equilibrium quasiparticles, likely generated by external radiation, stray electromagnetic fields, or environmental noise. The impact of quasiparticles on high-kinetic inductance resonators has been extensively investigated in prior studies [43, 156, 157, 163, 179]. Our device lacks adequate protection against these effects. It does not have a permalloy or a superconducting shield, and it is placed close to both a magnetic coil with unfiltered dc lines and to a circulator, which also contains magnetic elements. When a source of quasiparticles reaches the resonator it breaks Cooper pairs and causes a change in its kinetic inductance, consequently shifting its resonance frequency. The effect and the dynamics of quasiparticles on grAl resonators evaporated on InP will be further discussed in Section 5.2.3.

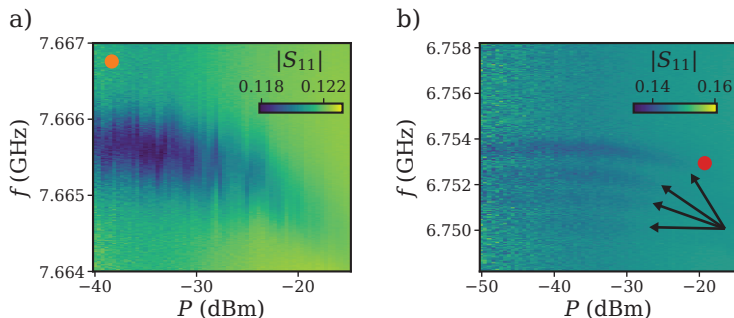


**Figure 5.3.** Magnitude of the reflection coefficient  $|S_{11}|$  as a function of VNA output power  $P$  for a) the orange resonator at around  $f_0 \sim 7.666$  GHz and for b) the red resonator at around  $f_0 \sim 6.754$  GHz. Each trace in a) takes 50 ms and each trace in b) takes 100 ms. Both resonances shift in time, but interestingly, the one in b) seems to oscillates between four discreet values.

From these considerations, we tend to attribute the red and orange resonances to two resonators on the chip with the larger kinetic inductance, and therefore larger fluctuations in resonance frequency. The missing resonance could be assigned to the smallest resonator on this chip, which is either too weakly coupled to the input port or too susceptible to quasiparticle fluctuations.

On the other hand, we attribute the green, purple and blue resonances to the resonators on the right chip with the lower kinetic inductance. These resonances have a self-Kerr of approximately 25 Hz, 120 Hz and 140 Hz respectively. Being  $K$  inversely proportional resonator volume [180], we tend to attribute these resonances to resonator B, C, and A. The relatively low value of  $K$  is a key property of grAl compared to other systems used to realize superinductors such as Josephson junction arrays ( $K \sim \text{MHz}$  [162, 164]) or other disordered superconductors ( $K \sim \text{kHz}$  [165]). That is because to effectively function as an inductor in a quantum circuit, it is desirable to minimize the introduction of unwanted non-linearities.

The  $Q_i$  of all resonances (extracted at low photon number) is in the range of  $10^4$ , comparable to what has been measured in low impedance resonators on GaAs substrates [175]. This suggests that the high impedance of these resonators is not a limiting factor for their use in superconducting circuits on InP.

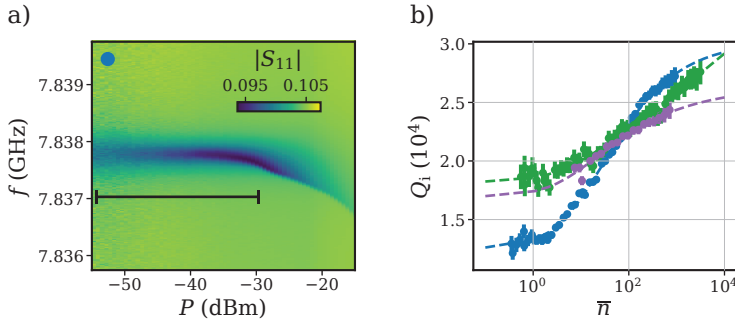


**Figure 5.4.** a) Magnitude of the reflection coefficient  $|S_{11}|$  as a function of VNA output power  $P$  for the blue resonator at around  $f_0 \sim 7.838$  GHz. b) Internal quality factor  $Q_i$  as a function of average circulating photon number  $\bar{n}$  in the blue resonator, and in the green and purple resonators, with resonance frequencies around 7.584 GHz and 7.057 GHz respectively. The maximum power at which we perform the fit is determined by the bifurcation of the resonance. The power range we use to extract  $Q_i(\bar{n})$  for the blue resonator is indicated by the black line in a). The dashed lines are fits to Eq. (5.2).

### 5.1.1. $Q_i$ Power Dependence

To gain more insights about the origin of losses in these resonators, we investigate the power dependence of the  $Q_i$  of the green, the purple, and the blue resonances at around 7.584 GHz, 7.057 GHz and 7.838 GHz respectively.

Figure 5.4a) shows an example of the power dependence of the blue resonance. The time per trace was in this case 0.25 s, and the resonance position appears stable compared to the red and orange resonances. The black solid line highlights the power range we use to extract  $Q_i$  as a function of the average number of circulating photons in the resonator  $\bar{n}$ .

The dependence of  $Q_i$  on  $\bar{n}$  can be caused either by saturation of two-level-systems (TLSs) in the substrate [181, 182], or by the activation of quasiparticles (QP) trapped in subgap states [183, 184]. In the following, we will discuss these processes in more detail.

Changes in both  $f_0$  and  $Q_i$  due to the presence of an ensemble of TLSs are governed by variations in the real part and imaginary part respectively of the effective dielectric function  $\epsilon_{\text{eff}}(f)$ . These variations are driven by the response of the ensemble within the microwave field of the resonator [182].

**Table 5.1.** Table summarizing the results of the fit to Eq. (5.2) of the power dependence of the resonators internal quality factor  $Q_i$  on the average number of circulating photons  $\bar{n}$ .

$f_0$ (GHz)	$Q_{0,\text{TLS}} (10^4)$	$\beta$	$n_c$	$Q_A (10^4)$
7.584 (green)	$2.5 \pm 1.0$	$0.09 \pm 0.05$	$2.9 \pm 1.7$	$6.6 \pm 6.8$
7.057 (purple)	$4.7 \pm 2.9$	$0.35 \pm 0.29$	$4.3 \pm 1.1$	$2.6 \pm 0.3$
7.838 (blue)	$2.14 \pm 0.06$	$0.49 \pm 0.04$	$4.6 \pm 0.8$	$3.02 \pm 0.08$

Resonant TLSs behaves like absorbers at the resonance frequency effectively subtracting photons from the resonator. At sufficiently high  $\bar{n}$  (larger than a critical photon number  $n_c$ ) and temperature ( $k_b T \gg hf_0$ ), TLSs become saturated and are unable to absorb additional photons. The resonator  $Q_i$  depends on  $\bar{n}$  and  $T$  according to [181, 182]:

$$\frac{1}{Q_{i,\text{TLS}}} = \frac{1}{Q_{0,\text{TLS}}} \frac{\tanh\left(\frac{\hbar f_0}{k_b T}\right)}{(1 + \bar{n}/n_c)^\beta} + \frac{1}{Q_A}, \quad (5.2)$$

where  $Q_{0,\text{TLS}}$  is the quality factor due to the TLS at low temperature and low photon number, and  $Q_A$  represents the quality factor due to all losses other than TLSs.

In Fig 5.4b) we plot the extracted  $Q_i$  as a function of  $\bar{n}$  for all three resonances. For the purple resonance, we were not able to measure the saturation of  $Q_i$  at low  $\bar{n}$  without adding further attenuation on the input line. To each curve we superimpose a fit to Eq. (5.2) using  $f_0$  and  $T = 20$  mK as fixed parameters. The results are summarized in Table 5.1. The contribution of TLSs to losses depends on the participation ratio of the electric field contained in the resonator and the one in the substrate. We measure less than a factor of 2 difference between the single photon  $Q_i$  of resonators that differ 7 to 20 times in volume. We also observe only a moderate increase, again of less than a factor of two, between the  $Q_i$  at  $\bar{n} = 1$  and  $\bar{n} = 10^3$ . These results points in the direction that other loss mechanisms contribute to the observed power dependence and to limit  $Q_i$ .

Another possible source for the power dependence of  $Q_i$  is QP activation. While thermal QP are practically zero at temperatures  $< 40$  mK, it has been shown [185–187] that non-thermal QP can persist even at very low temperature and provide additional losses to the system. In fact, in all disordered superconductors, spatial variations of the order parameter produce a subgap tail in the quasiparticle density of state where QP can be trapped for a long



**Table 5.2.** Table summarizing the results of the fit to Eq. (5.3) of the power dependence of the resonators internal quality factor  $Q_i$  on the average number of circulating photons  $\bar{n}$ .

$f_0$ (GHz)	$Q_B$ ( $10^4$ )	$b$ ( $10^{-5}$ )	$\gamma$
7.584 (green)	$1.86 \pm 0.01$	$1.85 \pm 0.04$	$0.02 \pm 0.004$
7.057 (purple)	$1.70 \pm 0.09$	$1.9 \pm 0.3$	$0.08 \pm 0.05$
7.838 (blue)	$1.23 \pm 0.01$	$4.91 \pm 0.07$	$0.15 \pm 0.01$

time before recombining [188]. In Ref. [157], the authors derive a phenomenological model to account for photon assisted quasiparticles (QP) excitation and recombination. The change in  $Q_i$  as a function of  $\bar{n}$  due resistive losses introduced by quasiparticles can be written as:

$$\frac{1}{Q_{i,\text{QP}}} = b \left( \frac{1}{1 + \frac{\gamma \bar{n}}{1 + \frac{1}{2}(\sqrt{1+4\gamma\bar{n}}-1)}} - 1 \right) + \frac{1}{Q_B}, \quad (5.3)$$

where  $\gamma$  and  $b$  are constants that account for quasiparticle-photon coupling, quasiparticle generation and quasiparticle recombination rates. The results of the fit of Eq. (5.3) to the data in Fig. 5.4b) are summarized in Table 5.2. For all resonances we extract values of  $\gamma$  lower than what has been reported in Ref. [157]. Being  $\gamma$  proportional to QP-photon coupling, this suggests a reduced QP-photon coupling in our system.

Further studies are needed to elucidate the origin of the power dependence and of the limit on  $Q_i$ . One has to compare measurements of resonators made of different materials and with a different participation ratios. Here, the observed power dependence could be due to both TLS and QP.

## 5.2. grAl at Uni Basel

In this section, we discuss the measurements on resonators fabricated during evaporation #14 in Table 4.1. The normal state sheet resistance of this film is  $R_{\square} = 0.7$  k $\Omega$ . The device, fabricated with standard e-beam lithography as described in Section 4.2.1, is shown in Fig. 5.5a). The bonding pad is connected to a standard reflectometry setup and measurements are performed in a dilution cryostat with a base temperature of 50 mK equipped with a 3-axis vector magnet (see Appendix. A for details). The magnitude of the reflection coefficient  $|S_{11}|$  as a function of the VNA frequency is shown in Fig. 5.5b). We measure resonances corresponding to the fundamental mode, and to the 2<sup>nd</sup>, 3<sup>rd</sup> and 4<sup>th</sup> harmonic modes of the resonator at 3.5509 GHz, 5.1825 GHz,

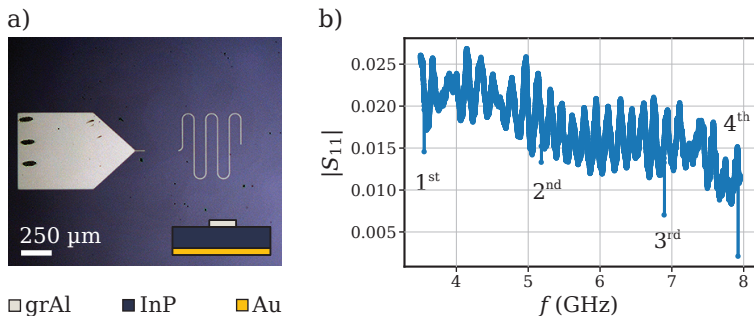


**Figure 5.5.** a) False colour optical image of a granular aluminium resonator (light yellow) on a InP substrate (dark blue). The ground plane is defined by a gold (Au) layer (yellow) evaporated on the back of the chip. b) Magnitude of the reflection coefficient  $|S_{11}|$  as a function of VNA frequency  $f$ . We measure resonances corresponding to the fundamental mode and up to the fourth harmonic mode.

6.8945 GHz and 7.9219 GHz respectively. From Sonnet simulations, by matching the simulated resonance frequency of fundamental mode to the measured one, we extract a kinetic inductance per square  $L_{\text{kin}/\square} \sim 285$  pH. However, the frequencies of the higher harmonic modes extracted from the simulation with this value of kinetic inductance do not match the measured ones. We attribute the mismatch to inhomogeneities in the resonator, caused, for example, by a gradient in the film resistivity along the resonator length. From a circle fit to the fundamental resonator mode, we extract a coupling factor  $Q_c \sim 10^5$  an order of magnitude larger than the one obtained from simulations  $Q_{c,\text{simu}} \sim 10^4$ . We are not sure what this discrepancy can be attributed to. One contributing factor could be the formation of standing waves along the reflectometry setup, and along the launching pad itself.

Using the equations for the capacitance and inductance of a straight microstrip as presented in Section 4.2.1, we estimate a resonator impedance of  $Z_r \sim 750 \Omega$ . Compared to the NbTiN resonator in Section 4.2.1, this resonator is more compact and it has  $\sim 5$  times higher impedance for the same film thickness  $t = 20$  nm. This means that grAl allows to fabricate high impedance resonators which occupy little space on the chip, using simple lift off procedures and with less constraints on the film thickness.

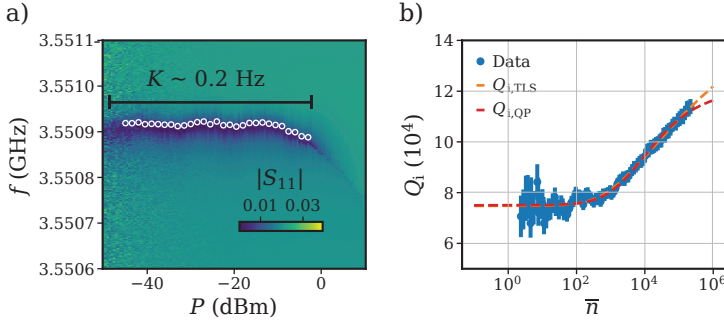


**Figure 5.6.** a) Magnitude of the reflection coefficient  $|S_{11}|$  as a function of VNA output power  $P$  for the resonator fundamental mode. From the shift in resonance frequency (white circles) with power we extract a Kerr coefficient  $K \sim 0.2$  Hz. b) Internal quality factor  $Q_i$  as a function of average circulating photon number  $\bar{n}$ . The power range we use to extract  $Q_i(\bar{n})$  is indicated by the black line in a). The orange and the red dashed lines are fit to Eq. (5.2) and Eq. (5.3) respectively.

### 5.2.1. Power Dependence

Similarly to the discussion on the grAl resonators fabricated at KIT, in this section we discuss the dependence of  $f_0$  and  $Q_i$  on the input power.

Figure 5.6a) shows the power dependence of the resonance frequency of the fundamental mode. The black solid line indicates the power range before bifurcation where we fit the resonance to extract  $f_0$ ,  $(\bar{n})$  and  $Q_i$ . From a linear fit to  $f_0(\bar{n})$  we extract a self-kerr  $K \sim 0.2$  Hz. The dependence of  $Q_i$  on  $(\bar{n})$  is plotted in Fig. 5.6b). We fit this data to Eq.(5.2) and extract  $Q_{0,\text{TLS}} = (14 \pm 3) \times 10^4$ ,  $Q_A = (16 \pm 3) \times 10^4$ ,  $n_c = 730 \pm 200$  and  $\beta = 0.19 \pm 0.07$ . Since the curve does not reach saturation at high photon numbers, there is a relatively large uncertainty in the fit parameters. The single photon  $Q_i$  is approximately  $8 \times 10^4$ , and increases less than a factor of 2 with input power up to  $\sim 12 \times 10^4$

In Fig. 5.6b) we also plot the fit of the data to Eq. (5.3). At large input power the fit deviates from the data because we go outside the range of validity of the model Eq. (5.3) is based on. From the fit, we extract values of  $Q_B = (7.50 \pm 0.03) \times 10^4$  and  $b = (5.0 \pm 0.1) \times 10^{-6}$ , which are comparable to what has been observed for grAl resonators on sapphire substrates [157]. The value of  $\gamma$  we extract, of  $(2.7 \pm 0.3) \times 10^{-4}$ , is instead three orders of magnitude lower than what has been reported in Ref. [157], supporting the hypothesis of

a reduced QP-photon coupling in our system.

Since we lack the comparison with data from resonators with different participation ratio, it is difficult to pinpoint the main origin of the  $Q_i$  power dependence. If our device was limited by excess quasiparticles in the substrate,  $Q_B$  would correspond to a fractional quasiparticles density of [51, 157, 174]:

$$x_{\text{QP}} = \frac{N_{\text{QP}}}{N_{\text{CP}} + N_{\text{QP}}} \approx \frac{1}{Q_B} \approx 10 \times 10^{-6} \quad (5.4)$$

comparable to previously reported values [157, 185, 187]. Here,  $N_{\text{CP}}$  and  $N_{\text{QP}}$  are the total number of Cooper pairs and quasiparticles respectively. We will further discuss the effect of excess QP and their dynamics in Section 5.2.3.

## 5.2.2. Temperature Dependence

In this section we complement the previous discussion with the analysis of the temperature dependence of  $f_0$  and  $Q_i$ .

The resonance frequency depends on the temperature  $T$  of the substrate because of two main contributions: a reduction in the density of Cooper pairs, resulting in changes to the kinetic inductance of the film as temperature increases, and changes in the  $\epsilon_{\text{eff}}(f)$  due to off-resonance TLSs [182]. In the following, we analyse these processes in more detail.

The shift in resonance frequency due to changes in kinetic inductance can be written as [157, 189, 190]:

$$\delta f_{0,\text{CP}}(T) = f_0(T) - f_0 = f_0 \frac{\alpha}{2} \sqrt{\frac{\pi k T_c}{T}} \exp\left(\frac{-k T_c}{T}\right) \quad (5.5)$$

where  $\alpha$  is the kinetic inductance fraction  $L_{\text{kin}}/(L_{\text{kin}} + L_{\text{geo}})$  and  $T_c$  is the film critical temperature. We include possible variations of the ratio  $k = \Delta_0/(k_B T_c)$ , where  $\Delta_0$  is the zero temperature superconducting gap, from the standard BCS value of 1.76.

Figure 5.7a) shows a fit of  $\delta f_0(T)$  for the fundamental mode to Eq. (5.5) using  $k T_c$  as a single fit parameter. We extract  $\alpha \sim 0.83 \pm 0.3$  and  $k T_c \sim 3.6 \pm 0.1$ . We compare the value of  $\alpha$  extracted from the fit to the value obtained by calculating  $L_{\text{geo}}$  from Eq. (4.1). We use  $L_{\text{kin}/\square} = 285$  pH as obtained by matching the measured resonance to the simulated one. Inserting the design parameters we extract  $\alpha \sim 0.96$ . This suggests that the geometrical inductance is in practice higher than what has been calculated from Eq. (4.1), probably because of

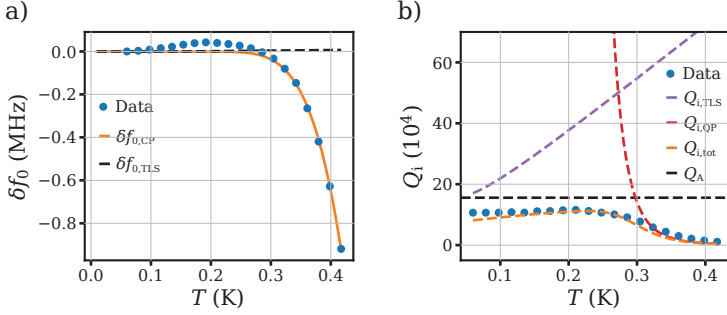


**Figure 5.7.** a) Shift in resonance frequency  $\delta f_0$  as a function of temperature  $T$ . the orange line is a fit to Eq. (5.5). The black dashed line is the expected  $\delta f_0$  due to an increase in temperature according to Eq. (5.6) using  $Q_{0, \text{TLS}}$  as extracted from the fit in Fig. 5.6. b) Temperature dependence of the resonator internal quality factor  $Q_i$  overlapped with the contributions from two levels systems  $Q_{i, \text{TLS}}(T)$  (purple), quasiparticles  $Q_{i, \text{QP}}(T)$  (red), and residual loss mechanisms  $Q_A$  (black). The sum of all different contributions  $Q_{i, \text{tot}}(T)^{-1} = 1/Q_{i, \text{TLS}}(T) + 1/Q_{i, \text{QP}}(T) + 1/Q_A$  is plotted in orange.

the meandered structure of the resonator.

By measuring  $|S_{11}|$  as a function of temperature away from the resonance frequency, we estimate the  $T_c \sim 1.9$  K for this film. This corresponds to  $k \sim 1.9$ , using the product  $kT_c$  obtained from the fit, in line with the experimental value for grAl [102, 150].

The second contribution to  $\delta f_0(T)$  comes from off-resonant TLSs, and can be written as [182]:

$$\delta f_{0, \text{TLS}}(T) = \frac{f_0}{\pi Q_{0, \text{TLS}}} \left[ \Re \left\{ \Psi \left( \frac{1}{2} + \frac{hf_0}{2\pi i k_B T} \right) \right\} - \log \left( \frac{hf_0}{2\pi k_B T} \right) \right], \quad (5.6)$$

where  $\Psi$  is the complex digamma function. According to the equation above, off-resonance TLSs cause a initial negative shift of the resonance frequency as function of temperature, followed by a positive shift. In the data in Fig 5.7a) we indeed observe an initial increase in  $f_0$  before of the effects of the increasing kinetic inductance. We then calculate  $\delta f_{0, \text{TLS}}(T)$  using  $Q_{0, \text{TLS}}$  as extracted from the fit of Eq. 5.2 to the data in Fig. 5.6b). This is shown by the black dashed line in Fig 5.7a). The effect of off-resonance TLSs is negligible, and does not explain the initial increase in  $f_0$  we see in the data. Instead, we tend to attribute this behaviour due to residual vortices being trapped within the

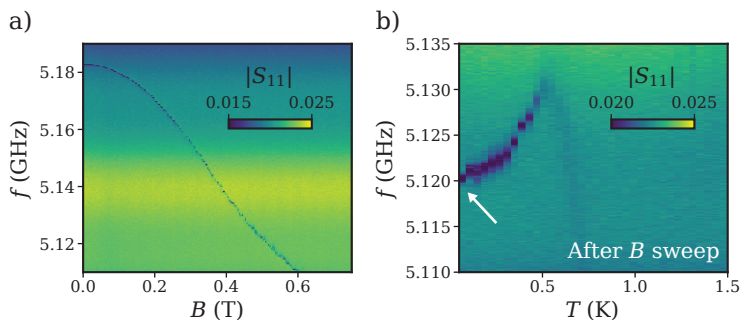


**Figure 5.8.** a) Magnitude of the reflection coefficient  $|S_{11}|$  as a function of VNA frequency  $f$  and parallel magnetic field  $B$ . b)  $|S_{11}|$  as a function of  $f$  and temperature  $T$ , measured after a), and after  $B$  has been swept back to zero. The resonance frequency at base temperature is lower compared to its value before the field sweep as indicated by the white arrow. The upward shift in resonance frequency as the temperature is increased is attributed to the removal of vortices from the film.

resonators. These vortices are removed as the temperature increases, prior to the effects due to a decrease in the Cooper pair density.

This explanation is supported by the behaviour observed in a measurement of the resonance frequency of the second harmonic mode  $f_0^{2\text{nd}}$  as a function of temperature, performed after a magnetic field sweep. In Fig. 5.8 we plot the dependence of  $f_0^{2\text{nd}}$  as a function of magnetic field  $B$ . The field is applied using only the  $z$ -axis of a 3-axis vector magnet, which is roughly parallel to the sample plane. However, we do not compensate for the sample tilt, and as a consequence, the applied field also has a perpendicular component. Similarly to temperature, also a magnetic field can break Cooper pairs thus causing a decrease in the resonance frequency. In addition, the finite out-of-plane component causes vortices to be trapped in the film. As a consequence, when the field is swept back to zero, we measure a dip in  $S_{11}$  at a lower frequency,  $\sim 5.12$  GHz, compared to the value before the magnetic sweep, at  $\sim 5.1825$  GHz. Next, in Fig. 5.8b), we plot the temperature dependence of the same resonance, measured right after the magnetic field sweep. Here,  $f_0^{2\text{nd}}$  increases by more than  $\sim 10$  MHz before decreasing due to kinetic inductance effects. This supports the hypothesis of trapped vortices as the reason for the observed initial increase in  $f_0$  observe in Fig 5.7a).

To conclude, in Fig.5.7b) we plot the  $Q_i$  of the fundamental resonator mode

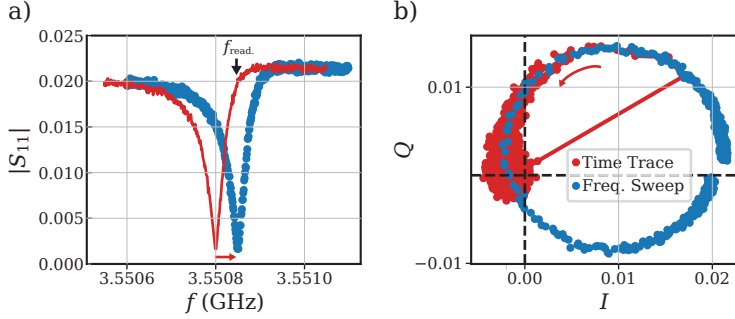


**Figure 5.9.** a) In blue, magnitude of the reflection coefficient  $|S_{11}|$  as a function of VNA frequency  $f$  of the fundamental resonator mode. A quasiparticle burst event causes a shift (that here we assume to be rigid) of the resonator response to lower frequencies (red curve). Monitoring the  $S_{11}$  at fixed frequency  $f_{\text{read}}$ , we can resolve the shift in time. b)  $S_{11} = I + iQ$  in the  $IQ$  plane. A frequency sweep (blue) is overlapped with a time trace (red) measured at  $f_{\text{read}}$ . A quasiparticle burst is identified by a sudden jump in the resonator response followed by a decay back to the equilibrium value (red arrow).

as a function of temperature, superimposed with the contributions coming from TLSs ( $Q_{i,\text{TLS}}$ ), quasiparticles ( $Q_{i,\text{QP}}$ ), and residual loss channels ( $Q_A$ ). We extract  $Q_{i,\text{TLS}}(T)$  and  $Q_A$  using the parameters obtained from the fit of Eq. (5.2) to the data in Fig. 5.6b). As temperature increases,  $Q_i$  decreases due to the larger resistive loss coming from the increase in the equilibrium quasiparticles density  $n_{\text{QP}}$ . We model the dependence of  $Q_i$  on  $n_{\text{QP}}$  as [43, 175]:

$$\frac{1}{Q_{i,\text{QP}}} = \frac{\alpha}{\pi} \sqrt{\frac{2\Delta_0}{hf_0}} \frac{\sqrt{2\pi k_B T \Delta_0} \exp\left(-\frac{\Delta_0}{k_B T}\right)}{\Delta_0} \quad (5.7)$$

We plot  $Q_{i,\text{QP}}(T)$  using the parameters extracted from the fit of Eq. (5.8) to the data in Fig. 5.7a), with  $\Delta_0 = kT_c k_B$ . The orange dashed line shows the total  $Q_{i,\text{tot}}(T)^{-1} = 1/Q_{i,\text{TLS}}(T) + 1/Q_{i,\text{QP}}(T) + 1/Q_A$ , which well reproduces the data.

### 5.2.3. Excess Quasiparticles Dynamics

As mentioned in Section 5.1.1 and Section 5.2.1, a potential limitation to the  $Q_i$  of these resonators might stem from non-equilibrium excess quasiparticles

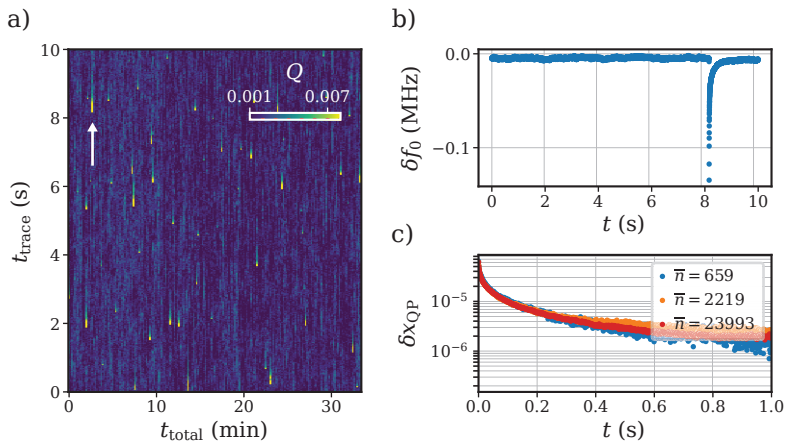


**Figure 5.10.** a) Continuous monitoring of the  $Q$  component of the resonator response at fixed frequency. We record multiple traces, covering a total time of about 35 min. Approximately every 40 s, sudden jumps of the resonator response are observed, followed by a slow relaxation over  $\sim 1$  s. b) Plot of the time trace indicated by the arrow in a), where changes in  $I$  and  $Q$  have been converted to resonance frequency shift  $\delta f_0$ . c) Multiple events are averaged (see Ref. [157]) and further converted to fluctuations in the fractional quasiparticle density  $\delta x_{\text{QP}}$ . We do not observe a dependence of the relaxation time on the average number of circulating photons  $\bar{n}$ .

within the substrate. As documented in prior studies [156, 191], high-energy particles, causing phonon bursts on the substrate, could potentially serve as a source for these QPs.

To explore this effect, we measure the time-dependent complex reflection coefficient  $S_{11} = I + iQ$  at a constant readout frequency  $f_{\text{read}}$ . As depicted in Fig. 5.9, the impact of a high energy particle causes a burst of QPs that leads to a red shift of the resonant curve. By monitoring  $S_{11}(t)$  at  $f_{\text{read}}$ , a QP burst event is identified by a jump in the  $IQ$  plane followed by a relaxation back to the steady state value. We focus on the fundamental mode, and we set the measurement bandwidth to 1 kHz, in order to be able to resolve the burst event in time, while still having a good signal to noise ratio. Figure 5.10a) shows a map of multiple time traces consecutively recorded over a total time of  $\sim 30$  min. Quasiparticles burst events, indicated by a peak in the imaginary part of recorded signal, occur approximately every  $\sim 40$  s.



First, we fit the resonance curve measured in the same conditions as the time trace. From this fit parameters, we can then reconstruct the time evolution of  $f_0$  from  $S_{11}(t, f_{\text{read}})$  (see Ref. [51]). A typical trace of the shift in resonance frequency as a function of time  $\delta f_0(t) = f_0(t) - f_0$  is plotted in Fig. 5.10b).

Since  $f_0$  is proportional to  $(L_{\text{kin}})^{-1/2}$  and  $L_{\text{kin}} \propto 1/n_{\text{CP}}$ , where  $n_{\text{CP}}$  is the Cooper pair density of the superconductor, one can relate the fluctuations of the resonance frequency  $\delta f_0$  to the fluctuations in the fractional quasiparticle density  $\delta x_{\text{QP}}$ :

$$\frac{\delta f_0}{f_0} = -\frac{\alpha}{2} \frac{\delta L_{\text{kin}}}{L_{\text{kin}}} = \frac{\alpha}{2} \frac{\delta N_{\text{CP}}}{N_{\text{CP}}} \approx -\frac{\alpha}{4} \frac{\delta N_{\text{QP}}}{N_{\text{CP}} + N_{\text{QP}}} = -\frac{\alpha}{4} \delta x_{\text{QP}}, \quad (5.8)$$

where  $N_{\text{CP}}$  and  $N_{\text{QP}}$  are the total number of Cooper pairs and quasiparticles respectively, and  $x_{\text{QP}} = N_{\text{QP}}/(N_{\text{CP}} + N_{\text{QP}})$  is the fractional quasiparticle density. We have used the fact that  $\delta N_{\text{QP}} = 2\delta N_{\text{CP}}$  and  $N_{\text{QP}} \ll N_{\text{CP}}$ .

In Fig. 5.10c) we plot the decay over time of  $\delta x_{\text{QP}}$  at different  $\bar{n}$ . Each curve is obtained by averaging over several QPs bursts event. We select the exponential part of the decay, chosen between 0.1 s and 0.4 s where the curve is approximately linear in logarithmic scale. From an fit to the curve in this range, we extract an average relaxation time  $\bar{\tau}$  of approximately 0.3 s. In contrast to what previously reported for grAl resonators on sapphire substrates [157], we do not observe any dependence of the QPs relaxation dynamic on  $\bar{n}$ . This could be caused by a low QP-photon coupling, as suggested by the low value of  $\gamma$  obtained in our devices. However, another reason might be the poor magnetic shielding of our setup. As previously reported [50, 187], the presence of vortices in the superconducting film due to stray magnetic field can act as QP traps and accelerate QPs relaxation. In our setup, the contribution of vortices to QPs relaxation might prevent us from discerning the effect of larger or smaller  $\bar{n}$ . Indeed, the average relaxation time we extract is a factor of 2 smaller than what reported in Ref. [157].

### 5.3. Conclusion

Granular aluminium resonators fabricated either at KIT or at Uni Basel showed the highest internal quality factor we have ever achieved on InP. We have analysed in detail their power and temperature dependence to shed light on the factors limiting their  $Q_i$ , which are attributed to the substrate and the poor magnetic shielding of the device. We record excess quasiparticles dynamics in the resonators fabricated and measured at Uni Basel, which appear to be dominated by vortices assisted relaxation and do not show dependence on the number of circulating photons. We measure values of  $Q_i$  comparable to what

has been measured on sapphire substrates ( $Q_i \sim 10^5$ ) and one order of magnitude larger than the value obtained in Ref. [175] ( $Q_i \sim 10^4$ ) for low impedance resonators on a GaAs substrate, suggesting that InP is more compatible with the fabrication of high quality superconducting microwave resonators.

These results points in favour of using grAl for hybrid quantum circuits. High impedance resonators with large vacuum electric field fluctuations could be used to enhance coupling to the spin of electrons in quantum dot [192] or to the spin of quasiparticles occupying Andreev bound states in hybrid Josephson junction [37, 79].

# 6 Gate-tunable Josephson Diode in Proximitized InAs Supercurrent Interferometers

---

## Gate-tunable Josephson diode in proximitized InAs supercurrent interferometers

Carlo Ciaccia<sup>1,\*</sup>, Roy Haller<sup>1</sup>, Asbjørn C. C. Drachmann<sup>2,3</sup>, Tyler Lindemann<sup>4,5</sup>, Michael J. Manfra<sup>4,5,6,7</sup>, Constantin Schrade<sup>2</sup> and Christian Schönenberger<sup>1,8,†</sup>

<sup>1</sup>Quantum- and Nanoelectronics Lab, Department of Physics, University of Basel, 4056 Basel, Switzerland

<sup>2</sup>Center for Quantum Devices, Niels Bohr Institute, University of Copenhagen, 2100 Copenhagen, Denmark

<sup>3</sup>NNF Quantum Computing Programme, Niels Bohr Institute, University of Copenhagen, 2100 Copenhagen, Denmark

<sup>4</sup>Department of Physics and Astronomy, Purdue University, West Lafayette, Indiana 47907, USA

<sup>5</sup>Birk Nanotechnology Center, Purdue University, West Lafayette, Indiana 47907, USA

<sup>6</sup>Elmore Family School of Electrical and Computer Engineering, Purdue University, West Lafayette, Indiana 47907, USA

<sup>7</sup>School of Materials Engineering, Purdue University, West Lafayette, Indiana 47907, USA

<sup>8</sup>Swiss Nanoscience Institute, University of Basel, 4056 Basel, Switzerland

In this chapter, published [89] in *Phys. Rev. Research* **5**, 033131 (2023) we discuss a gate and flux tunable Josephson diode, fabricated in a proximitized InAs two-dimensional electron gas.

The Josephson diode (JD) is a non-reciprocal circuit element that supports a larger critical current in one direction compared to the other. This effect has gained a growing interest because of promising applications in superconducting electronic circuits with low power consumption. Some implementations of a JD rely on breaking the inversion symmetry in the material used to realize Josephson junctions (JJs), but recent theoretical proposals have suggested that the effect can also be engineered by combining two JJs hosting highly transmitting Andreev bound states in a Superconducting Quantum Interference Device (SQUID) at a small, but finite flux bias. We have realized a SQUID with two JJs fabricated in a proximitized InAs two-dimensional electron gas (2DEG). We demonstrate gate control of the diode efficiency from zero up to around 30% at specific flux bias values which comes close to the maximum of  $\sim 40\%$  predicated in Ref. [12]. The key ingredients to the JD effect in the SQUID arrangement is the presence of highly transmitting channels in the JJs, a flux bias and an asymmetry between the two SQUID arms.

## 6.1. Introduction

A widely used device in semiconductor electronics is the  $p-n$  junction, which is a nonreciprocal element with regards to current flow, able to conduct current primarily in one direction. The presently ongoing rapid scaling of quantum computers will require low-dissipative control electronics that operate close to the quantum chip at low temperatures. These requirements have renewed the question whether there exists a superconducting equivalent of the diode, namely a device that supports a larger supercurrent in one direction than in another: the Josephson Diode (JD) [193, 194].

In a conventional Josephson Junction (JJ) [55], the current-phase relation (CPR) is sinusoidal  $I = I_c \sin(\varphi)$ , with  $I_c$  being the critical current of the junction and with the ground state corresponding to zero phase bias  $\varphi_0 = 0$ . For this conventional case, the positive critical current,  $I_c^+ = \max_{\varphi}[I(\varphi)]$  is obviously equal to the negative one  $I_c^- = |\min_{\varphi}[I(\varphi)]|$ . Since the critical supercurrent is reciprocal, there is no superconducting diode-effect (SDE).

A general CPR can have a more complex dependence on the phase [195]. But in general,  $I(\varphi)$  is a  $2\pi$ -periodic function and if either time-reversal symmetry or inversion symmetry is preserved, it is an odd function:  $I(-\varphi) = -I(\varphi)$  [193]. It can therefore be written as a Fourier series composed of  $\sin(k\varphi)$  terms where  $k$  is a positive integer and the terms for  $k > 1$  are higher harmonics. If higher harmonics are present, the CPR is called non-sinusoidal [141, 196]. Such a CPR still does not display a SDE.

A necessary but not sufficient condition for the SDE to occur is that time-reversal symmetry is broken. This can be achieved either by an external magnetic-field or by means of ferromagnetic elements built into the device. S-F-S junctions, where F (S) denotes a ferromagnet (superconductor) were proposed [197, 198], and experimentally studied in various configurations [199–201]. These junctions typically display a  $\pi$  shift in the CPR and are thus known as  $\pi$ -junctions. The energy ground state moves from  $\varphi_0 = 0$  to  $\varphi_0 = \pi$ . Despite the presence of a magnetic field and time-reversal symmetry thus being broken, these junctions do not display a SDE.

Both inversion symmetry and time-reversal symmetry are broken in so-called anomalous JJs, also known as  $\varphi_0$  junctions, where the ground state of the junction has an ‘anomalous’ shift to  $\varphi_0$  with  $0 < \varphi_0 < \pi$  [202]. This situation is achieved in multiband conductors with spin-orbit interaction [203–209]. Evidence for  $\varphi_0$  junctions has been found in experiments with nanowires with strong spin-orbit interaction [210] and in planar Josephson junction arrays [127]. An anomalous JJ is also a necessary condition, but on its own not sufficient. Indeed, a CPR of the form  $I(\varphi) = I_c \sin(\varphi - \varphi_0)$  with  $0 < \varphi_0 < \pi$  is an anomalous JJ, but still with  $I_c^+ = I_c^-$ .

The SDE has been observed in materials that display magneto-chiral anisotropy. Here, the normal-state resistivity itself depends on the sign of the current

density and the sign of the magnetic field [208, 211, 212]. While this is a small effect in normal metals, it can become large at the transition to a superconducting state [213, 214]. Recently, a large SDE was also observed in a 2D NbSe<sub>2</sub> superconductor with applied out-of-plane magnetic field [215] and even in field-free situations [193, 216, 217] including twisted graphene [218–220].

Further studies have also considered, among others, polarized supercurrents, magnetic domain walls, vortex pinning, combination of s-wave and p-wave pairing, as well as finite-momentum pairing as the origin of a SDE [221–224]. A SDE was even reported in a scanning-probe microscopy study where a single magnetic impurity was addressed on the surface of a superconductor [225].

Lastly, topological materials with helical edge states can carry supercurrents with a strong SDE [226–229]. This is evidenced in the highly asymmetric Fraunhofer pattern with the property that  $I_c(B) \neq I_c(-B)$ , where  $B$  is the magnetic field. This arises because of lack of inversion symmetry between the supercurrent flowing along the two edges of the crystal [226]. This situation is very much alike an asymmetric SQUID.

Already in the 1970s, when superconducting interference devices were studied in great detail using tunnel junctions, point contact structures and Dayem bridges, it was recognized that the critical current of a SQUID can become non-reciprocal [230–233]. The origin was understood to emerge from an asymmetry in the two SQUID arms, but the arms needed to have a non-negligible loop inductance, too. Although the CPR of each single junction was sinusoidal, the CPR became non-reciprocal for the SQUID device due to asymmetric loop inductances.

Today, tunable superconductor-semiconductor hybrid devices have become a flourishing research topic [100, 234–237]. In particular, in JJ made of semiconducting weak links, the magnitude of the supercurrent is tunable by local gate electrodes and, in some devices, the shape of the CPR can be tuned from sinusoidal to highly non-sinusoidal. Consequently, these devices provide a platform for the engineering of the SDE with unprecedented tunability. This has recently been investigated theoretically in Ref. [12, 238]. It has been shown that one can achieve a large SDE by combining two non-sinusoidal JJs in a dc-SQUID at finite flux bias even with negligible loop inductances. In this case, the non-reciprocal transport  $I_c^+ \neq I_c^-$  originates from the interference between higher-order harmonics in CPR of the JJs.

In the current work, we use gate-controlled JJs fabricated in an InAs 2DEG proximitized by an Al layer [76, 239]. These rather wide junctions contain many channels with a distribution of transmission eigenvalues. The non-sinusoidal character is due to highly transmissive channels that are present in these devices [64, 72, 240–243]. By tuning the asymmetry between the SQUID arms with the respective gate-voltages we show that we can achieve a SDE up to 30%. This comes close to the maximum theoretically predicted value [12].

In Section 6.2 we present the device geometry, the experimental set up and the basic characterization of the individual JJs. The non-reciprocal character of the dc-SQUID with JJs having a non-sinusoidal CPR is then shown in Section 6.3. We also define an analytical framework with which we are able to distinguish possible origins of the JD effect. Finally, we discuss the measured gate tunability of the diode efficiency in Section 6.4 and end with the conclusion in Section 6.5.

## 6.2. Device and Basic Properties

The circuit diagram of the device is shown in Fig. 6.1(a) and a coloured electron-microscopy picture is presented in Fig. 6.1(b). The circuit consists of a dc SQUID formed by two planar JJs realized in a shallow InAs 2DEG proximitized by Al layer. The 2DEG is obtained from a quantum well grown on an InP substrate embedded in  $\text{In}_{0.75}\text{Ga}_{0.25}\text{As}$  layers of which the top layer is 10 nm thick. The stack is terminated with an in-situ grown 10 nm thin Al layer inducing superconductivity in the 2DEG. The SQUID loop and the leads are defined by etching the Al and, additionally, 300 nm deep into the semiconductor stack. The top and bottom Josephson junctions ( $\text{JJ}_1$  and  $\text{JJ}_2$ ) in the two branches of the loop are formed by selectively removing the Al in the form of stripes with length  $L = 150$  nm and width  $W_1 = 3 \mu\text{m}$  and  $W_2 = 2.5 \mu\text{m}$ . A set of gates, G1, G2 and FG, are used to tune the critical current of the junctions by applying appropriate gate voltages  $V_{G1}$ ,  $V_{G2}$  and  $V_{FG}$ . They are made of two Ti/Au layers, isolated from the Al and from each other by hafnium dioxide ( $\text{HfO}_2$ ) layers.  $V_{G1}$  extends over the whole width of  $\text{JJ}_1$ , while  $V_{G2}$  is shaped to gradually deplete  $\text{JJ}_2$  laterally, creating a Superconducting Quantum Point Contact (SQPC). An additional gate,  $V_{FG}$ , can be used to fine tune the charge carrier density in the SQPC. However, throughout the experiment the QPC functionality is not used and  $V_{FG}$  is kept at 0 V.

Our setup sources a current using a  $1 \text{ M}\Omega$  resistor in series to a dc voltage superposed by a small ac component with frequency  $f = 17.7$  Hz, supplied by a lock-in amplifier. The ac component has an amplitude of 5 nA. The SQUID is additionally shunted at the source to ground with a resistor  $R_S = 10 \Omega$  directly placed on the sample holder. This shunt resistor has two purposes: a) it limits the maximum voltage that appears over the junction in the normal state, and thus, the heating; and (b) it adds damping to the device avoiding hysteretic switching when assessing the critical current in experiments. We measure the differential resistance of the shunted device using a voltage amplifier and lock-in techniques. In all plots where a measured differential resistance  $dV/dI$  is shown the shunt resistor was not subtracted. The measurements presented in the following were obtained with the SQUID device operating in a dilution

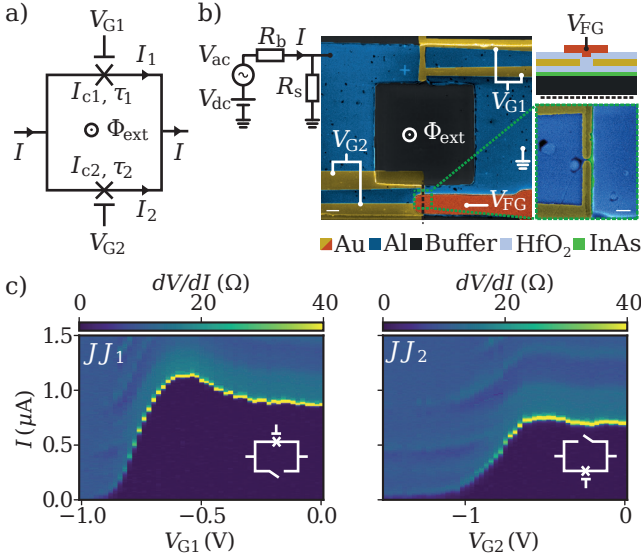


**Figure 6.1.** (a) Circuit schematic of a dc SQUID threaded by the external flux  $\Phi_{\text{ext}}$ , formed by two gate tunable JJs with non-sinusoidal CPRs with critical currents  $I_{c1}$ ,  $I_{c2}$ , and transparencies  $\tau_1$ ,  $\tau_2$ . (b) False-color electron micrograph of the device. The loop consists of a 10 nm Al film (blue) grown on top of an InAs 2DEG (green). The JJs are defined by selectively removing the Al over 150 nm long stripes on each branch of the loop. Electrostatic gates (yellow and orange) tune the charge carrier density in the junction. We use 15 nm of  $\text{HfO}_2$  (light blue) as a gate dielectric. On the right, a zoom-in of  $JJ_2$  is shown before adding the FG. On top, we show a cross-sectional schematic of the gate configuration of  $JJ_2$  along the dashed black line. The scale bar in the main figure is 1  $\mu\text{m}$  and in the zoom-in it is 300 nm. Dc and ac current bias are defined through the voltage drop over a large series resistor with value  $R_b = 1 \text{ M}\Omega$ . The SQUID is shunted to ground with a parallel resistor of value  $R_s = 10 \Omega$ . (c) Differential resistance of  $JJ_1$  (left) and  $JJ_2$  (right) as a function of gate voltage and current bias. While one junction is being measured, the other is pinched-off. The top junction has a slightly higher critical current due to the different channel widths of  $W_1 = 3 \mu\text{m}$  and  $W_2 = 2.5 \mu\text{m}$ .

refrigerator with a base temperature of  $\sim 50 \text{ mK}$ .

In Fig. 6.1(c) we show the measured differential resistance of  $JJ_1$  (left) and

$JJ_2$  (right) as a function of gate voltage and bias current. In the following, we approximate the critical current  $I_{ci}$  of the  $i$ th-junction,  $i = \{1, 2\}$ , by the current bias value at which the maximum value in differential resistance is measured. Here, the bias current is swept from zero to  $1.5 \mu\text{A}$ , looking at transitions from the superconducting to the normal state. From the measurements we extract  $I_{ci}(V_{Gi})$ . The critical current of both junctions can be tuned from a few nA close to pinch-off at negative gate-voltages  $V_{G(1,2)} \lesssim -1 \text{ V}$  to approximately  $1 \mu\text{A}$ . The key features of these hybrid semiconducting-superconducting JJs are the gate tunable critical current and the non-sinusoidal CPR.

In the short-junction limit, i.e. for junctions with a length  $L$  shorter than the superconducting coherence length  $\xi$  in the normal metal, the zero temperature limit of the supercurrent  $I(\varphi)$  is given by [141]:

$$I(\varphi) = \sum_j \left( \frac{\tau_j e \Delta}{\hbar} \right) \frac{\sin(\varphi)}{\sqrt{1 - \tau_j \sin^2(\varphi/2)}}. \quad (6.1)$$

Here,  $\tau_j$  is the transmission probability per channel  $j$ . In multichannel devices with disorder, a universal distribution function of transmission eigenvalues was obtained [70? –72]. The distribution is bimodal with many low transmissive channels that contribute little to the current, but also with some channels having a transmission probability close to 1. These high-transmissive channels lead to the overall non-sinusoidal character. This is approximated with an effective (but constant) transmission probability  $\tau^*$  per channel and written as a single channel non-sinusoidal CPR given by:

$$I(\varphi) = \frac{I_c}{A_N} \frac{\sin(\varphi)}{\sqrt{1 - \tau^* \sin^2(\varphi/2)}}. \quad (6.2)$$

For the later discussion of the measurements the critical current  $I_c$  of the junction and a unit-less normalization parameter  $A_N$  are introduced. The ratio  $I_c/A_N$  is given by  $N\tau^*e\Delta/\hbar$  with  $N$  the number of channels. Note, for the single junction we have  $I(-\varphi) = -I(\varphi)$  and thus  $I_c^+ = I_c^- = I_c$ . It is also seen that for small values of  $\tau^*$  the CPR approaches a sinusoidal dependence. From experimental  $I(\varphi)$  curves, we deduce the critical current  $I_c$  of each junction,  $\tau^*$  and  $A_N$ . Note, that only two parameters are independent.

As shown in Fig. 6.1(a) the total supercurrent  $I$  across the SQUID is the sum of the currents flowing in both branches  $I_1$  and  $I_2$  through the two JJs:

$$I(\varphi_1, \varphi_2) = I_1(\varphi_1) + I_2(\varphi_2). \quad (6.3)$$

The two junctions are described by  $I_{c1}, I_{c2}$  and  $\tau_1^*, \tau_2^*$ . The uniqueness of phase around the loop leads to the so-called fluxoid relation (modulo  $2\pi$ )

$$\varphi_1 - \varphi_2 = 2\pi\Phi_{\text{ext}}/\Phi_0 = \varphi_{\text{ext}}, \quad (6.4)$$



where  $\Phi_{\text{ext}}$  denotes the externally induced flux,  $\Phi_0 = h/2e$  the superconducting flux quantum and  $\varphi_{\text{ext}}$  the respective phase. In this form of the fluxoid relation the loop inductance has been neglected. For a finite loop inductance there is an additional flux contribution which depends on the currents  $I_1$  and  $I_2$  flowing in each arm. It has been shown that asymmetric loop inductances can also induce a superconducting SDE [85, 233, 244]. To estimate the role of loop inductances in our experiment we perform a full analysis with equations given in the appendix, specifically in Appendix B.5. Taking Eq. 6.3 and Eq. 6.4 together yields an effective superconducting junction with a CPR

$$I(\varphi) = I_1(\varphi) + I_2(\varphi - \varphi_{\text{ext}}). \quad (6.5)$$

For a simple sinusoidal CPR, the addition of the two terms yields a  $\varphi_0$ -junction without a SDE, even when the two JJ have different critical currents. In contrast, in the presence of higher order harmonics, which appear for a non-sinusoidal CPR, constructive and destructive interference effects, acting opposite for the two current bias directions, give rise to unequal critical currents  $I_c^+ \neq I_c^-$ , and thus to a SDE [12, 238].

### 6.3. Josephson Diode Effect

Figure 6.2(a) shows the differential resistance of the SQUID as a function of current bias and perpendicular magnetic field  $B_{\perp}$ , the latter providing the flux  $\Phi_{\text{ext}}$  through the SQUID loop. We have chosen a gate configuration with  $V_{G1} = V_{G2} = 0$  V for which the two critical currents are similar:  $I_{c1} = 0.87 \mu\text{A}$  and  $I_{c2} = 0.67 \mu\text{A}$ . A clear SDE is visible. For example, at the place of the orange arrow, we obtain  $I_c^+ = 0.64 \mu\text{A}$  and  $I_c^- = 0.4 \mu\text{A}$ .

In this experiment, the current bias is swept from negative to positive values. This means that we measure the positive switching current  $I_c^+$ , but on the negative side, we actually measure what is called the retrapping current  $I_r^-$  where the device switches from the normal to the superconducting state. Due to dissipation, the junction can overheat in the normal state giving rise to a hysteresis between the switching and retrapping currents with the retrapping current being smaller in magnitude than the switching current. This would result in an artificial SDE. To exclude this, we have measured the same plot as in Fig. 6.2(a) but sweeping now from positive to negative bias currents. The comparison shows, see Appendix B.3, that the hysteresis between retrapping and switching currents is small and can be neglected. Physically, this is the case thanks to the low shunt resistant of  $R_s = 10 \Omega$  which limits the voltage over the junction to  $< 25 \mu\text{V}$ , and thus, limits the heating.

Another strong argument against an artificial effect is seen in Fig. 6.2(a) when one looks at the switching values at the place of the red arrow, where

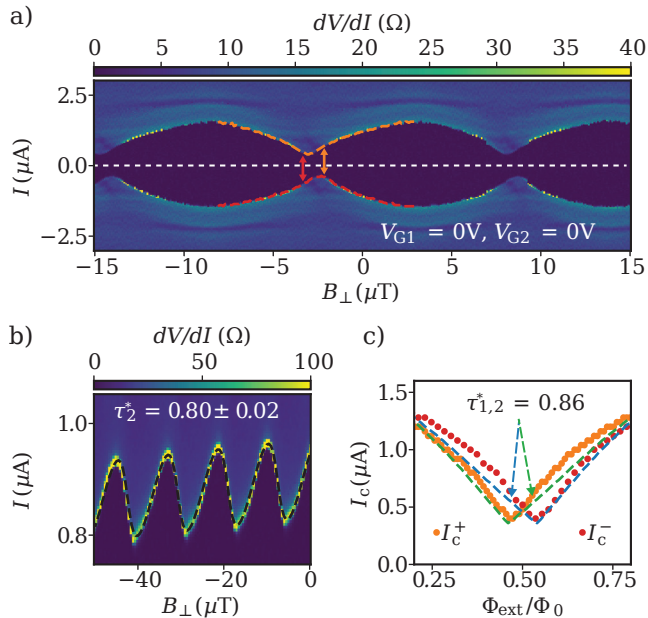


**Figure 6.2.** (a) SQUID oscillations with  $V_{G1} = V_{G2} = 0$ . The critical current  $I_c^+$  and the retrapping current  $I_r^-$  over one flux period are highlighted in orange and red respectively. At fixed magnetic field, the absolute value of the critical current in the two sweep directions is not the same. This is best seen in the region  $-5 < B_\perp < 0 \mu\text{T}$  with a visible example taken at the red and orange arrows, where the SDE has a magnitude of  $\sim 23\%$ . (b) Measurement for a strongly asymmetric SQUID setting with  $V_{G1} = 0 \text{ V}$  and  $V_{G2} = -1.1 \text{ V}$ . Here, the junction with the large critical current  $JJ_1$  serves as the reference junction. As a consequence, the critical current as a function of flux now reflects the CPR of the weaker junction  $JJ_2$ . The CPR is strongly non-sinusoidal and a fit (black dashed line) yields  $\tau_2^* = 0.8$ . (c) Plot of the extracted  $I_c^+$  (orange) and  $I_c^-$  (red) taken from the measurement in (a) and from a measurement where we sweep the current bias from positive to negative values (see Appendix B.3). The dashed two curves (green and blue) show simplified model fits with  $\tau_{1,2}^* = 0.86$  and the critical currents of the junctions taken from Fig. 6.1(c)

$I_c^+ = 0.44 \mu\text{A}$  and  $I_r^- = 0.6 \mu\text{A}$ . Here, the sign of the SDE is reversed,  $I_c^+ < I_r^-$ . This cannot be explained by a hysteresis between the switching and retrapping currents, since the retrapping current should always be smaller than

the switching current.

As introduced before, a contribution from loop inductances may generate the SDE, too, if the loop inductances in the two arms are different. Applying finite element simulations, Appendix B.2, we obtain  $L_1 \approx 39$  pH and  $L_2 \approx 44$  pH. The relative phase shift between the two SQUID arms due to the loop inductances at a bias current  $I = 1 \mu\text{A}$  is only  $\frac{2\pi}{\Phi_0}(L_2 - L_1)I \sim 0.03$  rad, and gives a small contribution to the SDE. We properly simulate the effect of the loop inductances on the critical current of the SQUID in Appendix B.6 and find that the loop inductances alone cannot explain the observed SDE in our experiment.

We also note that the measured CPR of the SQUID in Fig. 6.2(a) is periodic with a periodicity of  $11.6 \mu\text{T}$ . Since this should correspond to an added flux quantum  $\Phi_0$  in the area  $A_h$  of the inner SQUID hole, we obtain for  $A_h = 175 \mu\text{m}^2$ . This is approximately a factor of 2.3 bigger than the geometrical area defined by the etched square-shaped hole of size  $75 \mu\text{m}^2$ . This discrepancy can be attributed to the flux-focussing effect [245]. The magnetic field above the superconductor is screened by the Meissner effect leading to an enhanced magnetic field within the inner hole. The enhancement factor can be estimated by the ratio of the outer superconducting loop area of  $\approx 150 \mu\text{m}^2$  relative to  $A_h$ , which yields a factor of 2 in good agreement with the experiment.

In a sufficiently asymmetric SQUID configuration one can measure the CPR of the weak junction alone [196]. Figure 6.2(b) shows a measurement of the CPR of a single junction, obtained during the same cool-down. Here,  $V_{G1} = 0$  V and  $V_{G2} = -1.1$  V so that the current in  $\text{JJ}_1$  is large  $\sim 0.9 \mu\text{A}$  and in  $\text{JJ}_2$  it is small  $\sim 0.1 \mu\text{A}$ . In such a situation  $\text{JJ}_1$  acts as reference junction and the critical current of the weak junction  $\text{JJ}_2$  can be obtained from Eq. 6.5 as

$$I_c^+ = \max_{\varphi} (I_1(\varphi) + I_2(\varphi - \varphi_{\text{ext}})) \quad (6.6)$$

$$I_c^+(\varphi_{\text{ext}}) \simeq I_{c1} + I_2(\tilde{\varphi}_1 - \varphi_{\text{ext}}), \quad (6.7)$$

where  $\tilde{\varphi}_1$  is the phase value for which  $\text{JJ}_1$  has its maximal value  $I_{c1}$ . Hence, we see that under the condition that the reference junction dominates, we obtain the phase dependence of the critical current of the weak junction from the flux dependence of the critical current of the SQUID. Applying Eq. 6.2 to fit the measured data yields for the effective transmission probability  $\tau^* = 0.8 \pm 0.02$ . This is a large value, showing that the CPR is strongly non-sinusoidal, something that is visibly seen in the graph of Fig. 6.2(b). If one makes use of the universal bimodal distribution function of transmission eigenvalues to determine  $\tau^*$  [70? -72], one obtains  $\tau^* = 0.866$ . Including different devices nominally fabricated the same way, we always find a large effective transmission value of order  $\sim 0.8$  in agreement with theoretical expectations for a multichannel disordered junction in the short junction limit.

In Fig. 6.2(c) we compare the oscillations of  $I_c^+$  and  $I_c^-$  as a function  $\Phi_{\text{ext}}$  with the simplified model of Eq. 6.5. We take the measured critical currents of the two junctions as input parameters, i.e.  $I_{c1} = 0.87 \mu\text{A}$  and  $I_{c2} = 0.67 \mu\text{A}$ , and assume  $\tau_1^* = \tau_2^* = \tau^*$  as a single fitting parameter. The best agreement is obtained for  $\tau^* = 0.86$ . We note, that a similar model calculation based only on loop inductances barely matches the measurement. It is shown as a comparison in Appendix B.6.

The fits for  $I_c^+$  (green) and  $I_c^-$  (blue) reproduce the relative shift along the flux axis very well. The shape of the curves is, however, not reproduced so well. In the region  $\Phi_{\text{ext}}/\Phi_0 \in [0.25, 0.5]$  and  $\Phi_{\text{ext}}/\Phi_0 \in [0.5, 0.75]$  respectively, the measured  $I_c^+$  and  $I_c^-$  curves are higher than what is obtained with the model. Deviations between the experimental and the modelled curves could be attributed to the choice of CPR used in the model. First, we considered an average transparency instead of a distribution of transparencies. Second, the expression of the current carried by the Andreev bound states could be different from Eq. 6.2, since our junctions could be in a regime intermediate to the short and long junction limit. And, in the third place, spin-orbit effects may affect the CPR, too. For junctions of similar length in the same material system, it has been shown that spin-orbit interaction splits the ABS into spinful states with different dispersion relations [?]. Noticeably, the experiment indicates that these deviations result in an increase of the SDE compared to what is predicted by the simple model.

Having established that a SDE appears in a SQUID with junctions having a non-sinusoidal CPR with asymmetry, we summarize in Table 6.1 the necessary conditions for the SDE (DE). To describe the asymmetry we introduce two asymmetry parameters  $\alpha$  and  $\beta$  for the critical currents and the effective transmission probabilities, respectively:

$$\alpha = \frac{I_{c1} - I_{c2}}{I_{c1} + I_{c2}} \quad \text{and} \quad \beta = \frac{\tau_1^* - \tau_2^*}{\tau_1^* + \tau_2^*} \quad (6.8)$$

An extended table, which also considers the effect of loop inductances, is presented in Appendix B.7. It shows that the diode effect appears when the SQUID arms are asymmetric. The only exception is for sinusoidal JJs, where an asymmetry in the critical currents is not enough to produce a diode effect.

## 6.4. Gate Tunable Diode Efficiency

The SDE can be quantified via the diode efficiency, defined as

$$\eta = \frac{I_c^+ - I_c^-}{I_c^+ + I_c^-}. \quad (6.9)$$

**Table 6.1.** Conditions for obtaining a SDE (DE). An extended table that includes the loop inductances can be found in Appendix B.7. The first column is used to distinguish the classical sinusoidal CPR ( $\tau^* = 0$ ) from a strongly skewed CPR described by a highly transmissive ballistic JJ with an effective transmission probability  $\tau^* > 0$ .  $\alpha$  ( $\beta$ ) denotes the asymmetry in critical currents (transmission probabilities) of the two junctions.

$\tau^*$	$\alpha$	$\beta$	SDE
0	0	n.a.	no
0	$\neq 0$	n.a.	no
$\neq 0$	0	0	no
$\neq 0$	0	$\neq 0$	yes
$\neq 0$	$\neq 0$	0	yes
$\neq 0$	$\neq 0$	$\neq 0$	yes

In Fig. 6.3, we show the magnitude of the diode efficiency  $|\eta|$  as a function of external flux  $\Phi_{\text{ext}}/\Phi_0$  for different gate configurations as obtained from the experiment (left) and as calculated from the model (right). In the model, we make use of the relation between critical current and gate voltage of the individual junctions  $I_{\text{ci}}(V_{\text{Gi}})$  and use these values as input parameters in the first approximation. We also use the simulated loop inductance values from which we obtain the phase response due to screening  $\varphi_L = 4\pi\bar{I}_c\bar{L}/\Phi_0$ , the loop inductance asymmetry  $\gamma = (L_1 - L_2)/(L_1 + L_2)$  with  $L_1$ ,  $L_2$ , and  $\bar{I}_c$  and  $\bar{\tau}^*$  the respective mean values. We assume that the effect of the gate voltage is mainly to change the critical current value  $I_{\text{ci}}$  through the number of channels  $N$ , while  $\tau_1^*$  roughly stays constant. We fix  $\tau_1^* = \tau_2^* = 0.86$ , but we note that the calculated  $\eta$  plot is insensitive if one varies  $\tau_2^*$  between 0.8 and 0.9.

In Fig. 6.3(a), we plot  $|\eta|$  for different values of  $V_{\text{G2}}$  at fixed  $V_{\text{G1}}$ . Both in the experiment and in the model,  $|\eta|$  drops for  $-0.7 < V_{\text{G2}} < -0.5$  V. As seen in Fig. 6.1(c), this corresponds to a gate configuration with  $I_{\text{c1}} \approx I_{\text{c2}}$ , so that  $\alpha \approx 0$ . As expected, the absence of critical current asymmetry decreases the diode efficiency. To obtain in the model the same diode efficiencies  $\eta$  as measured, we had to increase the critical current of JJ<sub>1</sub>. In the experiment, we had  $V_{\text{G1}}$  fixed at  $-0.79$  V, which would correspond to  $I_{\text{c1}} = 470$  nA. However, in order to match the model with the data, we had to use 710 nA, corresponding to  $V_{\text{G1}} = -0.74$  V, as indicated in the top left corner of the figure. Without this correction, the measured  $|\eta|$  values would have been larger than what the model predicts. We attribute this difference in gate voltage to gate-jumps that occur from time-to-time. We note, that there are days between the measure-

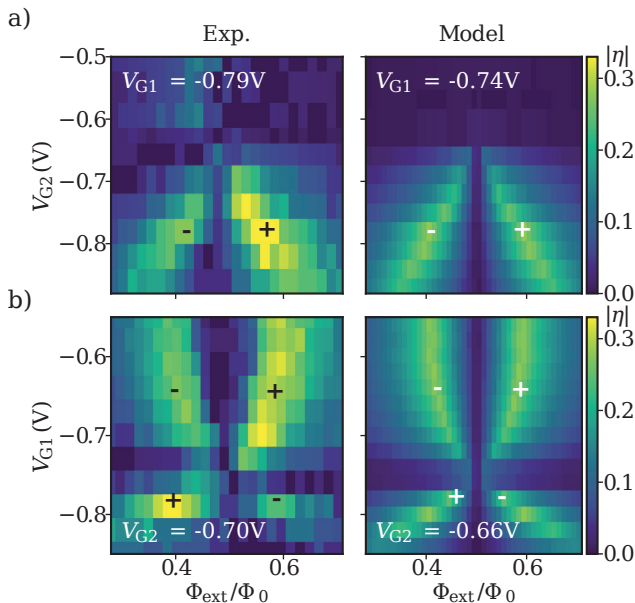


**Figure 6.3.** Magnitude of the diode efficiency  $|\eta|$  as a function of external flux  $\Phi_{\text{ext}}$  for different gate configurations as obtained from the measurements (left) and as calculated from the model (right). The sign of  $\eta$  is indicated on the visible lobes with + and -. The model takes into account the numerically simulated loop inductances, their asymmetry, and the values  $I_{c(1,2)}$  of the two junctions obtained from the measurements in Fig. 6.1(c). The JJ transparencies were fixed to  $\tau_1^* = \tau_2^* = 0.86$ . (a)  $|\eta|$  as a function of  $V_{G2}$  at fixed  $V_{G1}$ , and (b)  $|\eta|$  as a function of  $V_{G1}$  at fixed  $V_{G2}$ . Note, that for  $\Phi_{\text{ext}}/\Phi_0 = 0.5$ , which equals  $\varphi_{\text{ext}} = \pi$ ,  $\eta = 0$  independent on any other parameters.

ments in Fig. 6.1(c) and in Fig. 6.2(a).

In Fig. 6.3(b) we show the dependence of  $|\eta|$  as a function of  $V_{G1}$  at fixed  $V_{G2} = -0.7$  V. As before, to match the model to the experiment, we had to increase  $I_{c2}$  from the initially measured value of 590 nA at  $V_{G2}$  to 650 nA, which correspond to  $I_{c2}$  measured at  $V_{G2} = -0.66$  V.

Both in the experiment and in the model one can observe the typical butterfly pattern of  $\eta$  as predicted in Ref. [12]. The two arms of maximum  $|\eta|$  meet at the point of minimum asymmetry at  $\Phi_{\text{ext}}/\Phi_0 = 0.5$  for  $V_{G2} \approx -0.65$  V and

$V_{G1} \approx -0.75$  V for (a) and (b) respectively, where  $\eta$  drops to 0.

The model qualitatively reproduce the gate dependence of the diode efficiency very well. We obtain a maximum  $|\eta|$  of  $\simeq 0.3$  from the experiment. This 30% efficiency is much larger than what has previously been obtained in a SQUID with asymmetric loop inductance [246]. Taking a SQUID model with a single channel JJ junction, we numerically find for the maximum efficiency  $\eta = 0.37$ . This is obtained for  $\tau_1 = 1$  and  $\tau_2 = 0.75$  or the reversed. This could be achieved by combining a single channel ballistic  $\tau = 1$  Josephson junction realized in atomic contacts [196] with a semiconductor-superconductor hybrid device as we have discussed here.

## 6.5. Conclusion

In conclusion, we have investigated the origin of the Superconducting Diode Effect (SDE) in a supercurrent interferometer realized in a proximitized InAs quantum well stack. We show that in such a system the SDE can originate from the non-sinusoidal character of the JJs, and hence, reflecting a subtle interference between higher-order harmonics of the CPRs of the individual JJs. In addition to higher harmonics, an asymmetry either in the composition of the Fourier components in the CPR or in the critical current of the two JJ, and a finite flux bias  $\varphi_{\text{ext}} \neq \{0, \pi\}$  is required to obtain a SDE. These later conditions ensure that time-reversal symmetry and inversion symmetry are both broken. A similar conclusion was drawn by a recent experimental study in three terminal devices, where a SDE was realized [247]. Further, during the reviewing process we got aware of a similar study in a dc SQUID realized in a Ge quantum well structure [248]. Future directions include the possibility to concatenate more SQUIDs in parallel in order to further increase the diode efficiency as was proposed in Ref. [12].





# 7 Charge-4e supercurrent in a two-dimensional InAs-Al superconductor-semiconductor heterostructure

---

## Charge-4e supercurrent in a two-dimensional InAs-Al superconductor-semiconductor heterostructure

Carlo Ciaccia,<sup>1,\*</sup> Roy Haller,<sup>1</sup> Asbjørn C. C. Drachmann,<sup>2,3</sup> Tyler Lindemann,<sup>4,5</sup>  
Michael J. Manfra,<sup>4,5,6,7</sup> Constantin Schrade,<sup>2</sup> and Christian Schönberger<sup>1,8</sup>

<sup>1</sup>Quantum- and Nanoelectronics Lab, University of Basel, CH-4056 Basel, Switzerland

<sup>2</sup>Center for Quantum Devices, Niels Bohr Institute,  
University of Copenhagen, 2100 Copenhagen, Denmark

<sup>3</sup>NNF Quantum Computing Programme, Niels Bohr Institute, University of Copenhagen, Denmark

<sup>4</sup>Department of Physics and Astronomy, Purdue University, West Lafayette, Indiana 47907, USA

<sup>5</sup>Birk Nanotechnology Center, Purdue University, West Lafayette, Indiana 47907, USA

<sup>6</sup>School of Electrical and Computer Engineering,  
Purdue University, West Lafayette, Indiana 47907, USA

<sup>7</sup>School of Materials Engineering, Purdue University, West Lafayette, Indiana 47907, USA

<sup>8</sup>Swiss Nanoscience Institute, University of Basel, Klingelbergstrasse 82, Basel, Switzerland

In this chapter, published [249] in *arXiv* 2306.05467 (2023) we introduce a novel method to deduce the harmonic content of highly transmissive Josephson junctions by performing emission spectroscopy experiments. With this experiment we can convincingly demonstrate the cancellation of the fundamental harmonic for a symmetric SQUID configuration at half the flux quantum, and we can do this quantitatively.

Superconducting qubits with intrinsic noise protection offer a promising approach to improve the coherence of quantum information. Crucial to such protected qubits is the encoding of the logical quantum states into wavefunctions with disjoint support. Such encoding can be achieved by a Josephson element with an unusual charge-4e supercurrent emerging from the coherent transfer of pairs of Cooper-pairs. In this work, we demonstrate the controlled conversion of a conventional charge-2e dominated to a charge-4e dominated supercurrent in a superconducting quantum interference device (SQUID) consisting of gate-tunable planar Josephson junctions (JJs). We investigate the ac Josephson effect of the SQUID and measure a dominant photon emission at twice the fundamental Josephson frequency together with a doubling of the number of Shapiro steps, both consistent with the appearance of charge-4e

supercurrent. Our results present a step towards novel protected superconducting qubits based on superconductor-semiconductor hybrid materials.

## 7.1. Introduction

The Josephson effect describes the dissipationless current flow between two weakly coupled superconductors. Today, numerous technologies are based on this fundamental quantum phenomenon, ranging from superconducting qubit devices [250–254] to parametric amplifiers [111, 255, 256].

Regardless of whether the weak link consists of an insulator or a normal conducting material, the supercurrent is a periodic function of the phase difference  $\varphi$  between the superconductors [195]. In a Josephson tunnel junction, the supercurrent arises from the coherent tunnelling of individual Cooper-pairs through the insulating barrier, each carrying a charge  $2e$  [7]. The current-phase relation (CPR) in this case is given by  $I(\varphi) = I_c \sin(\varphi)$ , with  $I_c$  being the critical current. However, when the superconductors are separated by a conducting weak link, such as a semiconductor or a metal, coherent transport of multiple Cooper-pairs can also occur, resulting in a non-sinusoidal CPR [76, 87, 257–259]. In general, the CPR of the junction can be expanded in a Fourier series as:

$$I(\varphi) = \sum_{m=1}^{\infty} c_m \sin(m\varphi). \quad (7.1)$$

The  $\sin(m\varphi)$  terms correspond to processes involving the simultaneous, coherent transport of  $m$  Cooper-pairs [74, 75] carrying a charge  $m \times 2e$ . The amplitude of the higher harmonic terms  $c_m$ ,  $m > 1$ , reflects the probability of multi-Cooper-pair transport and decreases with higher harmonics, indicating that transport across the junction arises mainly from individual Cooper-pairs. Often, the CPR can be described by the junction transparency  $\tau$ , defined as the transmission probability of electron in the weak link. The more transparent a junction is, the higher the ratio between successive Fourier coefficients  $|c_{m+1}(\tau)/c_m(\tau)|$ .

Several theoretical proposals [13, 91, 260–266] have investigated possible advantages of using a so-called  $\sin(2\varphi)$  Josephson junction for the realization of a parity protected superconducting qubit. In this case, the parity of the Cooper pairs is protected by using a Josephson element with a dominant second harmonic term  $c_2$  in Eq.(7.1), corresponding to the supercurrent being carried by pairs of Cooper pairs with charge  $4e$ . The qubit states can be therefore encoded into the even and odd parity of the number of Cooper-pairs on a superconducting island.

Important steps towards realizing a parity protected qubit have been taken with SQUIDS made of tunnel junctions arranged in a rhombus geometry [103, 104]. By designing the loop inductances and the junctions position, it possible to engineer a CPR with a large second harmonic component  $|c_2/c_1| \sim 0.5$  [267], corresponding to an effecting transparency  $\tau^* \sim 1$  [74]. When the magnetic flux through the SQUID is tuned to half a flux quantum  $\Phi_0/2$ , the first harmonic is suppressed due to destructive interference, leaving a dominant second harmonic term. This method relies on the fabrication of identical junctions, and departures from symmetry spoils parity protection.

A promising alternative approach is based on gate tunable hybrid superconducting - semiconducting materials with high transparency channels. In Ref. [90] the authors realize a  $\sin(2\varphi)$  element with a SQUID made of proximitized InAs nanowires, where local gate control of each junction allows precise balancing of the first harmonics. They show that the qubit relaxation time increases by an order of magnitude when the qubit is tuned close to the protected regime. However, for practical use of the parity protected qubit, the Josephson energy of the second harmonics in the balanced configuration must be at the same time much larger than the residual Josephson energy coming from the first harmonics (for a long relaxation time) and much larger than the island charging energy (for small dephasing rate). The few conduction channels in the nanowires limit the maximum obtainable critical current and make the last requirement difficult to satisfy.

Hybrid two-dimensional materials have seen in recent years a great improvement in growth techniques that allow up-scaling and offer the advantage of wide gate tunability and top-down fabrication [133, 268]. In this work, we report the observation of a  $4e$  supercurrent in a SQUID consisting of two planar Josephson junctions formed in an InAs two-dimensional electron gas (2DEG) proximitized by an epitaxial Al layer [20, 21]. Even if the operation of superconducting qubits has already been shown in this material platform [17], the realization of high quality resonators on III-V substrates remains a challenging task. Therefore, here we investigate the contribution of the  $4e$  supercurrent by measuring the evolution in frequency of the ac Josephson radiation emitted by the SQUID as a function of a dc bias voltage. The high transparency of these JJs [76] allows us to engineer an effective CPR in which the first harmonic is suppressed due to destructive interference, leaving a dominant second harmonic term. To achieve this, we balance the critical current of the junctions with local gate voltages and tune the magnetic flux through the SQUID loop to half a flux quantum  $\Phi_0/2$ . In the balanced configuration, radiation measurements reveal a pronounced suppression of emission at the fundamental Josephson frequency in favour of a strong ac signal at twice this frequency. We corroborate this finding by additionally detecting fractional half Shapiro

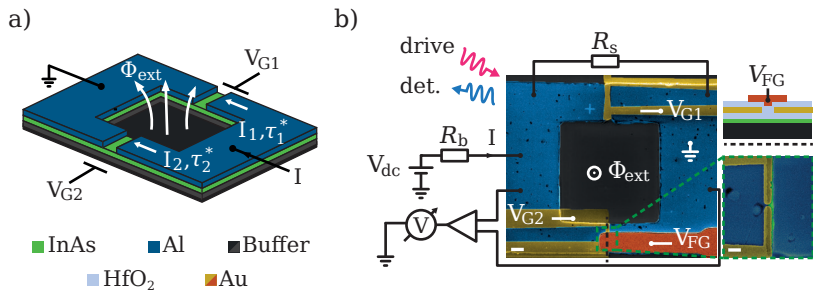


**Figure 7.1.** a) Circuit schematic of a dc SQUID formed by two gate tunable JJs with effective transmission probabilities  $\tau_1^*$ ,  $\tau_2^*$ , threaded by the external flux  $\Phi_{\text{ext}}$ . b) False color electron micrograph of the device and experimental setup. Each junction is fabricated by selectively removing the epi-Al layer (blue) over 150 nm long stripes. The charge carrier density in the exposed InAs 2DEG (green) is tuned by a set of electrostatic gates (yellow and orange) galvanically isolated from the loop by 15 nm of  $\text{HfO}_2$  (light blue). Dc and ac current bias are defined through the voltage drop over a bias resistor  $R_b = 1 \text{ M}\Omega$ . The SQUID is shunted to ground with  $R_s = 10 \Omega$ . We send a microwave tone to the device, and also detect photon emission. The scale bar in the main figure is  $1 \mu\text{m}$ , and the scale bar in the zoom-in is  $300 \text{ nm}$ .

steps, characteristic of a  $\sin(2\varphi)$  junction.

## 7.2. Results and Discussion

### 7.2.1. Device and procedures

A simplified schematic of the device is shown in Fig. 7.1a). A superconducting loop, threaded by an external magnetic flux  $\Phi_{\text{ext}}$ , is interrupted on each arm by a section where the superconductor has been selectively removed. The Josephson junctions are formed in an InAs 2DEG (green) which is proximitized by the close vicinity to an epitaxial Al layer (blue) grown on top. By locally removing the Al top layer with etching techniques that are detailed in Section C.1, we form InAs weak links. Local gate electrodes,  $V_{G1}$  and  $V_{G2}$ , allow us to tune the electron density in the weak links and, consequently, adjust the critical currents of the JJs. The hereby formed Josephson junctions are symmetric by design, but the wet etching step produced two different widths:  $\sim 3 \mu\text{m}$  for  $\text{JJ}_1$  and  $\sim 2.5 \mu\text{m}$  for  $\text{JJ}_2$ . Despite of fabrication-related asymmetries, we were still able to tune the SQUID into a symmetric configuration by leveraging the gate tunability of the semiconducting weak link. Junctions

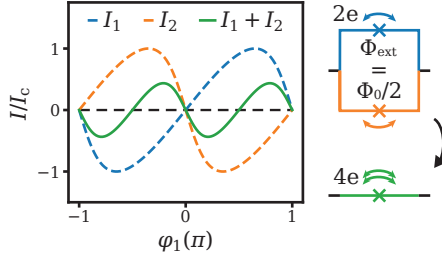


**Figure 7.2.** Individual components  $I_1$  (blue) and  $I_2$  (orange) and total current (green) flowing through a symmetric SQUID as a function of the phase drop  $\varphi_1$  at  $\Phi_{\text{ext}} = \Phi_0/2$ . The CPR of both junctions is plotted using a single channel short diffusive model with an effective transparency  $\tau^* = 0.86$ . The current is normalized to units of the critical current  $I_c$ . The schematic on the right helps visualizing the requirements for a  $\sin(2\varphi)$  junction: a dominant  $4e$  supercurrent is obtained with a symmetric SQUID biased at  $\Phi_0/2$ .

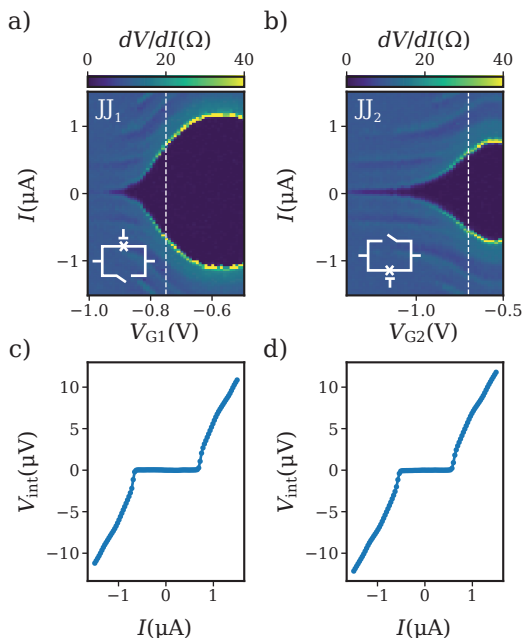
this wide typically contain many conduction channels with a bimodal distribution of transparency values distributed between zero and one [70? –72]. Earlier experiments on the same material platform have shown that the CPR in these junctions can be described by a single channel short diffusive junction model [76, 89] with an effective transparency  $\tau^* \sim 0.86$ .

Fig. 7.1b) depicts a false-color electron micrograph of the device and the experimental setup. We apply a dc-current via the voltage drop over a bias resistor  $R_b = 1 \text{ M}\Omega$ . We damp the SQUID with a shunt resistor  $R_s = 10 \text{ }\Omega$  to enable a continuous transition from the superconducting to the normal conducting state. The  $10 \text{ }\Omega$ -shunt increases the region of stable voltage drop across the junction, and at the same time it reduces both heating and hysteretic behaviours. The differential resistance is measured using standard lockin techniques. Furthermore, the microwave-setup allows probing the ac Josephson effect in two ways. On one hand, the Josephson radiation emitted from the SQUID under finite dc bias can be detected with a spectrum analyser. Second, the reverse experiment can be performed, namely, irradiating the device with a microwave tone and measuring its dc response.

Fig. 7.2 shows the interference between the supercurrent  $I_1$  flowing in  $\text{JJ}_1$  (blue dashed curve) and the supercurrent  $I_2$  in  $\text{JJ}_2$  (orange dashed curve) at  $\Phi_{\text{ext}} = \Phi_0/2$ . The total supercurrent flowing through the SQUID (green solid curve) is:

$$I = I_1(\varphi_1, \tau_1^*) + I_2(\varphi_2, \tau_2^*). \quad (7.2)$$

The phase drops over the two JJs are related by the fluxoid relation  $\varphi_1 - \varphi_2 =$



**Figure 7.3.** a) and b). Differential resistance  $dV/dI$  of  $JJ_1$  and  $JJ_2$  as a function of gate voltage  $V_{G1}, V_{G2}$  and current bias  $I$ . c) and d).  $IV_{\text{int}}$ -curves at  $V_{G1} = -0.75$  V and  $V_{G2} = -0.7$  V obtained by integrating the corresponding  $dV/dI$  along the white dashed lines shown in a) and b).

$2\pi\Phi_{\text{ext}}/\Phi_0$ . Here, we have assumed that the phase difference between the two JJs is solely given by the externally applied flux, neglecting loop and mutual inductances, which is justified in our device [89]. When the loop is flux biased at  $\Phi_{\text{ext}} = \Phi_0/2$  and the JJs are the same ( $\tau_1^* = \tau_2^*$ ), Cooper-pairs are transferred with the same amplitude but opposite phase through the SQUID arms, resulting in a destructive interference of the  $2e$  contribution with periodicity  $2\pi$  and in a constructive interference of the  $4e$  supercurrent with periodicity  $\pi$ . In this way, it is possible to engineer an effective  $\sin(2\varphi)$  junction.

### 7.2.2. Ac and dc Josephson effect from single junction

In the following, we characterize the dc and ac Josephson effect of the individual JJs. To this end, we measure the gate dependence of the critical current

and the radiation spectrum of each junction, while the neighbouring one is fully depleted.

Figure 7.3a) and Fig. 7.3b) show the differential resistance of  $JJ_1$  and  $JJ_2$  as a function of current bias  $I$  for different gate-voltages. We identify the critical current  $I_c$  as the boundary between the superconducting regime (dark blue) and the ohmic regime (turquoise). At negative gate voltages ( $V_{G1} \leq -0.9$  V and  $V_{G2} \leq -1.5$  V)  $I_c$  is negligibly small, but it can be gradually increased with increasing  $V_{Gi}$ .  $I_{c,\max}$  saturates to  $I_{c1,\max} = 1.1$   $\mu$ A for  $JJ_1$  and  $I_{c2,\max} = 0.8$   $\mu$ A for  $JJ_2$  at around  $V_{Gi} = 0.5$  V. The slight differences in the gate dependence of the two junctions is attributed to a different junction width and gate geometry. To estimate the  $I_c R_n$  product of the junctions, we measure the resistance at voltage bias larger than twice the superconducting gap of the leads as obtained from multiple Andreev reflection measurements conducted on a different chip of the same wafer. Subtracting the shunt resistor, we obtain a normal state resistance of the junction  $R_n \sim 90$   $\Omega$ , corresponding to a  $I_c R_n \sim 90$   $\mu$ V. We also note that potential errors in estimating  $R_n$  might have led to an underestimation of the  $I_c R_n$  product. Nonetheless, the significantly large  $I_c R_n$  product indicates a high-quality Josephson junction with a uniform current distribution.

In Fig. 7.3c) and Fig. 7.3d), the  $IV$ -curves at  $V_{G1} = -0.75$  V and  $V_{G2} = -0.7$  V, respectively are obtained by integrating the measured  $dV/dI$  curves along the white dashed lines in Fig. 7.3a) and Fig. 7.3b). Both junctions show an ohmic behaviour down to 2  $\mu$ V, which allows stable voltage biasing in the microwave regime of the Josephson emission.

According to the ac Josephson effect, the phase difference of a voltage biased Josephson junction will evolve linearly in time following

$$\varphi(t) = \frac{2\pi}{\Phi_0} Vt, \quad (7.3)$$

with  $V$  being the voltage drop across the junction. Consequently, an applied dc voltage causes a oscillating supercurrent at the Josephson frequency  $f_J = 2eV/h$ . This transforms into the emission of microwave photons at  $f_J$ . If higher harmonics are present, photon emission at higher frequencies  $f_{J,m} = m \times 2eV/h$  also occurs [93, 269]. In Fig. 7.4a) we show the expected peak evolution in the emission spectrum of voltage biased JJ as a function of detection frequency  $f_{\text{det}}$  and  $V$ . For every voltage bias position, peaks emerge in the emission spectrum, if the detection frequency matches an integer multiple of the Josephson frequency  $f_{\text{det}} = f_{J,m}$ . These peaks induce a fan-like pattern, capturing the linear relation between voltage and the emission frequency with slope  $h/(m2e)$ . Emission lines evolving as  $hf_{\text{det}}/(m2e)$  correspond to the coherent transport of  $m$  Cooper-pairs across the junction

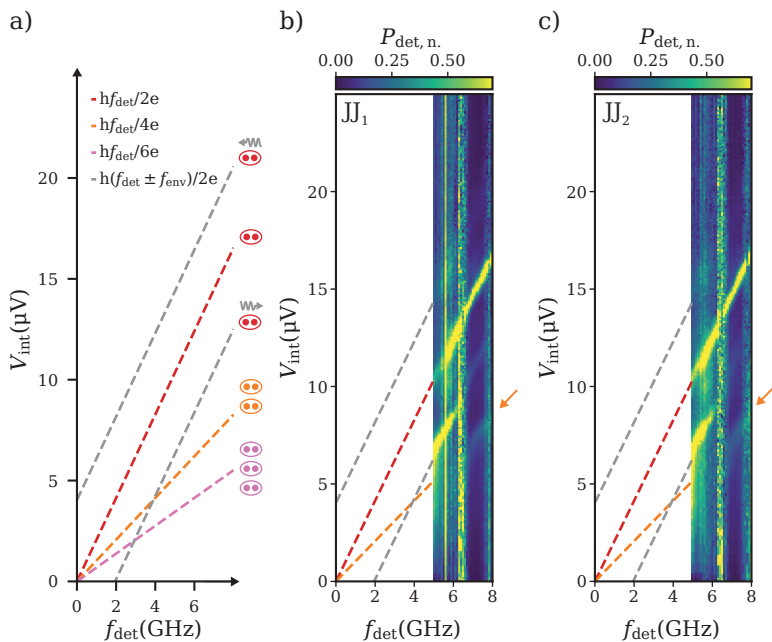


**Figure 7.4.** a) Illustration of the expected peak evolution in the emission spectrum of voltage biased JJ as a function of detection frequency  $f_{\text{det}}$ . A junction with finite transparency emits photons at the fundamental Josephson frequency (red dashed line) and integer multiples of it (orange and pink dashed lines), here corresponding to the coherent transport of pairs of Cooper-pairs. The dashed grey lines indicate processes associated to the up- and down-conversion of environmental photons. b) and c) Normalized radiation power  $P_{\text{det,norm.}}$  as a function of  $f_{\text{det}}$  and  $V_{\text{int}}$  for the same configuration of c) and d) in Fig. 7.3. The orange arrow points to the  $4e$  emission peak.

(red, orange, and pink dashed lines for  $m = 1, 2,$  and  $3$ ). In addition to the fan-like pattern, replicas of the Josephson emission lines can appear at a constant frequency offset on the right and on the left of the predicted peak position due to photon-assisted emission through environmental modes [270]. A photon from a spurious environmental mode can be upconverted to a detector photon by taking up the energy  $2eV$  provided by the inelastic tunnelling of a Cooper-pair (right shift in frequency). The energy balance in this case reads  $hf_{\text{det}} = hf_{\text{env}} + 2eV$ , where  $f_{\text{env}}$  corresponds to the resonant frequency of an environmental cavity. Such resonance can be caused for example by a standing



wave pattern along the microwave lines. The complementary process is also possible, meaning that a photon coming from a Cooper-pair tunnelling can be downconverted to a detector photon by giving up the energy  $hf_{\text{env}}$  to the environment (left shift in frequency). The energy balance in this case reads  $hf_{\text{det}} = 2eV - hf_{\text{env}}$ .

In Fig. 7.4b) and Fig. 7.4c) we plot the normalized radiation power  $P_{\text{det, norm}}$  as a function of  $f_{\text{det}}$  and  $V_{\text{int}}$  for JJ<sub>1</sub> and JJ<sub>2</sub> respectively. The power is normalized at each detection frequency to compensate for the frequency-dependent background. A pronounced emission peak at frequency  $f_{J,1}$  (red dashed line) corresponding to the 2e single Cooper-pair transport is measured over the entire frequency range from 5 GHz to 8 GHz. The signal due to the 4e double Cooper-pair transport at frequency  $f_{J,2}$  (orange dashed line) is weaker but becomes clearly visible in the emission spectrum around 7 GHz (orange arrow). Emission peaks at frequencies corresponding to higher harmonics,  $m > 2$ , are below our detection limit. In addition to the fan-like pattern, there is a strong replica of the fundamental Josephson emission appearing at a constant frequency offset ( $f_{\text{env}} \sim 1.95$  GHz) on the right of the predicted peak position. Its contribution diminishes for  $f_{\text{det}} > 6$  GHz. Changes in power spectrum as a function of detection frequency arise from a frequency-dependent probability of photon emission due to inelastic Cooper pair tunnelling. The emission probability depends on the impedance of the environment surrounding the Josephson junction [? ], which in turns has a complex behaviour as a function of frequency caused, for example, by standing wave patterns in the rf lines due to spurious impedance mismatch conditions. By setting  $f_{\text{det}} = 7.1$  GHz, we can disregard the contribution of this environmental mode in the following investigation.

### 7.2.3. Ac and dc Josephson effect from a SQUID

Next, we exploit the interference between the two junctions when both carry a finite supercurrent in order to realize an effective Josephson element with negligible first harmonic component. We require two conditions: (i) the flux is to be set to  $\Phi_{\text{ext}} = \Phi_0/2$ , and (ii), the JJs are gate-tuned into balance, such that  $c_{1, \text{JJ}_1} = c_{1, \text{JJ}_2}$ . The key challenge in the experiment is the balancing of the junctions. As a solution, we adopt an approach proposed in [12] that is based on the observation that  $I_c$  for the forward and reverse current-bias directions,  $I_{c,+}$  and  $I_{c,-}$ , is mismatched, unless both junctions are balanced and  $\Phi_{\text{ext}} = n\Phi_0/2$  with  $n$  being an integer. To balance the SQUID, we look at regions in gate voltage without diode effect, meaning  $I_{c,+}$  and  $I_{c,-}$  are equal (symmetric junctions).

In Fig. 7.5 we measure the SQUID in three different configurations. Firstly,

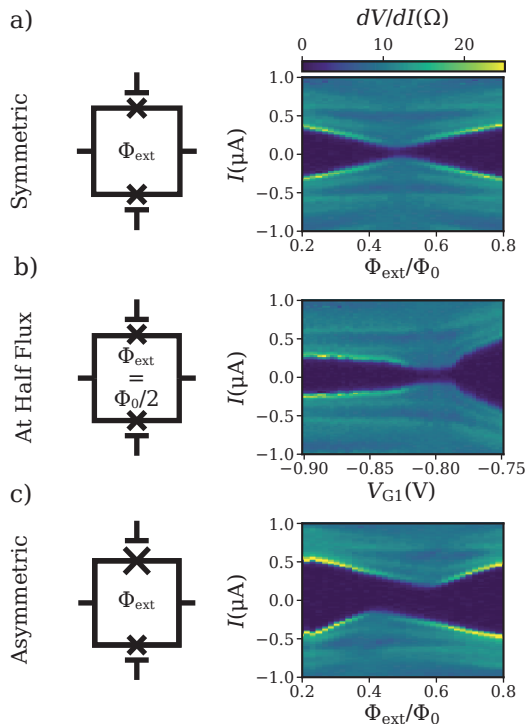


**Figure 7.5.** a) Differential resistance  $dV/dI$  of the SQUID as a function of external flux  $\Phi_{\text{ext}}$  and current bias  $I$  for symmetric junctions. Here,  $V_{G1} = -0.865$  V and  $V_{G2} = -0.9$  V. In this balanced configuration, there is no diode effect. In b), we bias the SQUID at  $\Phi_{\text{ext}} = \Phi_0/2$ , and fix  $V_{G2} = -0.875$  V. We measure the SQUID differential resistance as a function of current bias and  $V_{G1}$ . Moving from left to right, we go from  $I_{c2} > I_{c1}$  to  $I_{c1} > I_{c2}$ , crossing a balanced configuration. c) Same as in a), but for  $V_{G1} = -0.9$  V and  $V_{G2} = -1$  V. In this unbalanced configuration, there is diode effect.

we fix the gate voltages such that the junctions are symmetric and sweep  $\Phi_{\text{ext}}$ . Secondly, we fix  $V_{G2}$  and sweep  $V_{G1}$  at  $\Phi_{\text{ext}} = \Phi_0/2$ . Finally, we fix the gate voltages and sweep  $\Phi_{\text{ext}}$  in the case of asymmetric junctions.

In Fig. 7.5a) we plot the SQUID differential resistance  $dV/dI$  as a function of current bias  $I$  and  $\Phi_{\text{ext}}$  in a gate configuration where  $I_{c1} \approx I_{c2}$ . No diode effect is observed over the entire flux bias range. Differences between the

gate values at which symmetry is achieved and those expected from Fig. 7.3a) and Fig. 7.3b) are caused by the fact that the critical current of each junction depends on whether the junction is measured individually or embedded in SQUID [271]. Simultaneously, we measure the SQUID ac emission at fixed detection frequency  $f_{\text{det}} = 7.1$  GHz. Figure 7.6a) shows the normalized radiation power  $P_{\text{det,norm.}}$  as a function of  $\Phi_{\text{ext}}$  and integrated voltage drop over the SQUID  $V_{\text{int}}$ . Because the signal peaks at  $V_m = hf_{\text{det}}/(m2e)$ , we scale the voltage axis by  $hf_{\text{det}}/2e$ . The emission pattern changes in a striking manner around  $\Phi_{\text{ext}} = \Phi_0/2$ . The fundamental Josephson signal at a scaled  $V_{\text{int}} = 1$ , corresponding to the  $2e$  supercurrent, vanishes almost completely, while a sharp bright peak at a scaled  $V_{\text{int}} = 1/2$  appears, that corresponds to the radiation signal coming from the simultaneous inelastic transport of pairs of Cooper-pairs. An additional horizontal line is visible in the map due to the spurious environmental mode, as addressed before. On the right panels, we plot cuts along  $V_{\text{int}}$  at  $\Phi_{\text{ext}} = 0.22 \Phi_0$  (blue) and  $\Phi_{\text{ext}} = \Phi_0/2$  (orange). The radiation power is here presented in a linear scale. At  $\Phi_{\text{ext}} = \Phi_0/2$ , the  $4e$  peak emerges as the dominant feature, yet its amplitude is approximately  $\sim 25$  times smaller compared to the amplitude of the  $2e$  peak measured at  $\Phi_{\text{ext}} = 0.22 \Phi_0$ . This is expected, since the amplitude of the power emission peak is proportional to the square of  $I_c$ , which at  $\Phi_{\text{ext}} = \Phi_0/2$  is only determined by the second harmonic of the CPR, and is  $\sim 5$  times smaller than  $I_c$  at  $\Phi_{\text{ext}} = 0.22 \Phi_0$ . A detailed analysis of the ratio between the  $4e$  and  $2e$  peaks can be found in Appendix. C.3.

We investigate the dependence of the emission spectrum as a function of  $V_{G1}$ , when the magnetic flux is set to  $\Phi_{\text{ext}} = \Phi_0/2$  and  $V_{G2} = -0.875$  V, shown in Fig. 7.5b) and Fig. 7.6b). Away from the balanced configuration, the more distinct peak in the emission spectrum is the one corresponding to the  $2e$  transport. However, once we approach the balanced situation at  $V_{G1} \sim -0.8$  V the signal at  $V_1 = hf_{\text{det}}/2e$  is suppressed, and instead, the dominant peak in the emission spectrum becomes the one at  $V_2 = hf_{\text{det}}/4e$ .

Lastly, in Fig. 7.5c) we plot the  $dV/dI$  of the SQUID as a function of  $I$  and  $\Phi_{\text{ext}}$  in a gate configuration where  $I_{c1} \neq I_{c2}$ . Apart from  $\Phi_{\text{ext}} = \Phi_0/2$ , there is a clearly visible diode effect. Figure 7.6c) shows  $P_{\text{det,norm.}}$  as a function of  $\Phi_{\text{ext}}$  in the same gate configuration. The  $2e$  emission peak remains the dominant feature throughout the whole flux bias range. Its amplitude decreases asymmetrically on the left- and right-hand side of  $\Phi_{\text{ext}} = \Phi_0/2$ , following the asymmetry of the SQUID critical current. Even though the junctions are not balanced, one can still see that the emission signal slightly increases at voltages  $V_2 = hf_{\text{det}}/4e$ , in the vicinity of  $\Phi_{\text{ext}} = \Phi_0/2$ .

These findings show that a continuous transition between a  $2e$  and a  $4e$

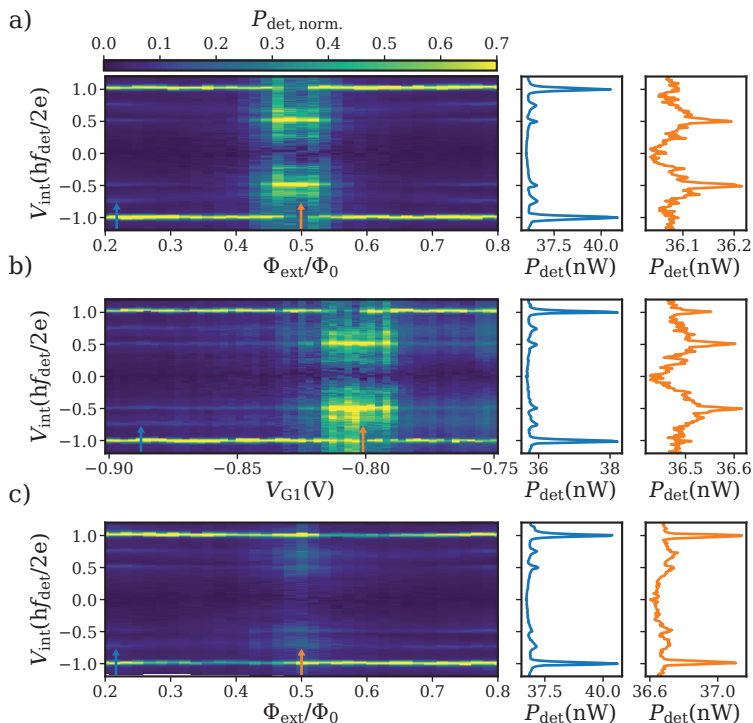


**Figure 7.6.** a) Normalized radiation power  $P_{\text{det, norm.}}$  at  $f_{\text{det}} = 7.1$  GHz plotted vs external flux  $\Phi_{\text{ext}}$  and normalized voltage drop over the SQUID  $V_{\text{int}}$ . The map is measured as the same time as in Fig. 7.5a). At half flux quantum, the 2e radiation signal is suppressed, and the 4e peak becomes the dominant feature. On the right, radiation power  $P_{\text{det}}$  in linear scale at  $\Phi_{\text{ext}} = 0.22 \Phi_0$  (blue) and  $\Phi_{\text{ext}} = \Phi_0/2$  (orange). b) Same as in a) but for the gate and flux configuration as in Fig. 7.5b). For specific values of  $V_{\text{G1}}$ , we see a clear increase in the visibility of the 4e peak. On the right, radiation power  $P_{\text{det}}$  in linear scale at  $V_{\text{G1}} = -0.89$  V (blue) and  $V_{\text{G1}} = -0.8$  V (orange). c) Same as in a) but for the gate configuration as in Fig. 7.5c). Here, throughout the flux bias range, the 2e peak remains the dominant feature.

supercurrent can be achieved by tuning both gate voltages and the magnetic flux. Importantly, the 4e supercurrent dominates over a finite window in parameter space and is not limited to exactly matching boundary conditions.

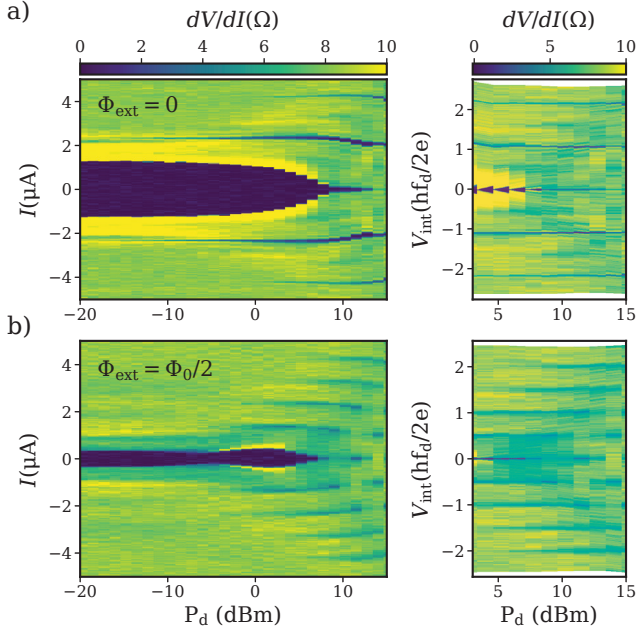


**Figure 7.7.** a) On the left, differential resistance  $dV/dI$  as a function of drive power  $P_d$  and bias current  $I$  at constant drive frequency  $f_d = 7.5$  GHz and zero external flux  $\Phi_{\text{ext}} = 0$  for  $V_{G1} = -0.73$  V and  $V_{G2} = -0.5$  V. The drops in differential resistance correspond to the emergence of Shapiro steps. On the right, differential resistance as a function of  $P_d$  plotted vs normalized voltage drop  $V_{\text{int}}$  over the SQUID. At zero flux, mostly integer Shapiro steps are visible. b) Same as in a), but at  $\Phi_{\text{ext}} = \Phi_0/2$ . The destructive interference of the first harmonics produces a CPR with double the periodicity of the individual junctions, inducing the emergence of half integer Shapiro steps.

### 7.2.4. Shapiro steps

So far, we have used the Josephson radiation measurements to identify the emergence of a  $4e$  supercurrent in the SQUID. In the last part of this work, we discuss Shapiro step measurements that complement our radiation experiment. When a microwave drive tone is sent to a JJ, distinct voltage plateaus in the  $V(I)$  characteristic appear, known as Shapiro steps [272–276]. For a conventional  $\sin(\varphi)$  junction, each plateau corresponds to a Cooper-pair absorbing  $n$  photons with frequency  $f_d$  to overcome the Shapiro step voltage  $V_n$ , and the energy relation reads  $2eV_n = nhf_d$ . The presence of higher harmonics in

the CPR of the junction changes the energy relation to  $2meV_n = nhf_d$ , corresponding to  $m$  Cooper-pairs absorbing  $n$  photons to overcome the voltage step.

We apply a microwave tone of fixed frequency  $f_d = 7.5$  GHz to the SQUID with different output power  $P_d$  values. The signal is applied to the microwave input line, connecting the device to the amplification chain through a directional coupler (see C.2). In Fig. 7.7(a), we plot the SQUID differential resistance  $dV/dI$  at  $\Phi_{\text{ext}} = 0$  as a function of current bias  $I$  and  $P_d$  in a symmetric gate configuration. In the left panel we plot  $dV/dI$  versus  $I$ , and on the right we plot the data as a function of the integrated voltage  $V_{\text{int}}$  scaled by  $hf_d/2e$ . Shapiro-steps occur at integer values of the scaled voltage as dips in differential resistance.

The data in Fig. 7.7(b) is measured for the same gate values as in Fig. 7.7(a), but at  $\Phi_{\text{ext}} = \Phi_0/2$ . In this configuration, the SQUID resembles an effective  $\sin(2\varphi)$  junction because the  $2e$  supercurrent is suppressed. The energy relation for the appearance of Shapiro steps is given in this case by  $4eV_n = nhf_d$ , resulting in a doubling of the number of observed steps. In line with the theoretical expectations [12], both integer and half-integer Shapiro steps are equally visible in the data. Differences between this measurement and Shapiro steps measurements performed on Josephson junction with a high quality factor [?] are attributed to the  $10 \Omega$ -shunt in our device.

### 7.3. Conclusion

We have demonstrated the realization of an effective  $\sin(2\varphi)$  Josephson junction using a dc SQUID consisting of two planar Josephson junctions formed in a proximitized InAs 2DEG. We probe the emergence of a dominant second harmonic in the CPR of the SQUID by measuring the ac Josephson effect as a function of gate voltages and magnetic flux. Photon emission at the fundamental Josephson frequency is suppressed when the SQUID is in a symmetric configuration and biased at half flux and instead, photons are only emitted at  $f_{J,2}$ . We provide evidence on how to continuously tune from the  $2e$  to the  $4e$  supercurrent regime by adjusting the junction gate voltages and the external magnetic flux. The results are further substantiated through complementary Shapiro step measurements in a symmetric SQUID configuration at half flux, revealing additional half-integer steps with same visibility as the integer steps.

Our results indicate, that a robust  $\sin(2\varphi)$  JJ can be engineered and could be used to realize parity-protected qubits with this material system. Such parity-protected qubit provides an alternative route to the protection of quantum information in superconducting devices and may complement alternative ap-

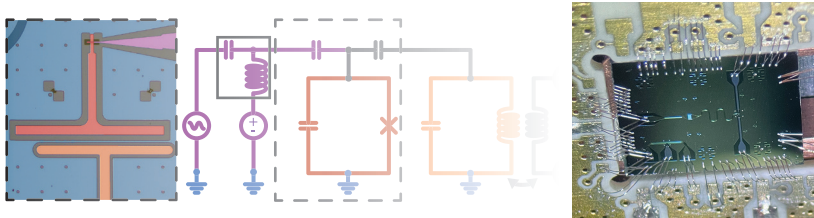
proaches based on fluxonium qubits [277–280] and qubits based on topological wavefunctions [281–287]. Looking ahead, the 2D platform would make it easier to further protect the qubit from noise and offsets by concatenating several SQUIDs in parallel [13].





## 8 Hybrid SQUIDS for CQED

---



Building upon the findings of earlier chapters, here we discuss the implementation of a gate and flux tunable transmon qubit in a proximitized two-dimensional electron gas (2DEG). We want to harness the high transmission probabilities of Josephson junctions realized in this platform and the interference effects between higher harmonics of their current-phase relation, to tune the qubit into different regime using gate and flux control. Later in this chapter, we further extend the potential uses of a proximitized two-dimensional electron gas (2DEG) to the realization of a gate and flux tunable superconducting parametric amplifier. The material of choice in the following sections is a InAs 2DEG grown by IOM in Trieste on a (001) GaAs substrate proximitized by 50 nm of epitaxial aluminium (Al).

### 8.1. Gate Tunable Transmon

We begin by examining the response of a transmon made of a single Josephson junction. Figure 8.1 shows a simplified device schematic consisting of a  $\lambda/4$  coplanar transmission line resonator inductively coupled to a feedline for readout. The resonator is also capacitively coupled to a Josephson junction (JJ) shunted to ground with a T-shaped capacitor  $C_T$ . The total parallel capacitance  $C_\Sigma$  given by the sum of  $C_T$  and the junction capacitance can be approximated by  $C_\Sigma \sim C_T$  since the contribution from the junction is negligible. The parallel of the Josephson junction and  $C_\Sigma$  defines the transmon. With Sonnet simulations, we estimate  $C_\Sigma$  to be approximately 88 fF corresponding to a charging energy  $E_C/h = e^2/C \sim 220$  MHz.

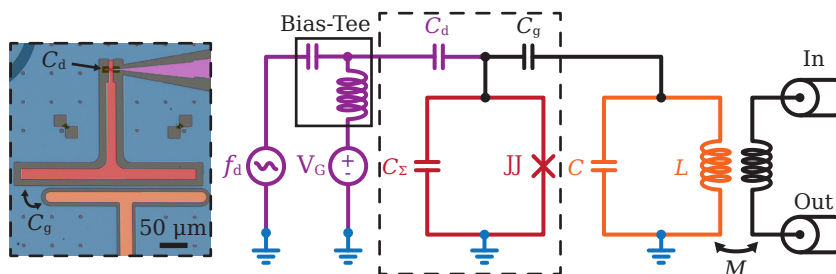


**Figure 8.1.** False colour optical micrograph of the transmon and simplified measurement setup. The readout resonator (orange) is inductively coupled to a feedline by a shared inductance  $M$ . The other end of the resonator is capacitively coupled to the transmon island by the capacitance  $C_g$ . The transmon (red) consist of a Josephson junction (JJ) shunted to ground by the capacitance  $C_\Sigma$ . An electrostatic gate  $V_G$  is used to tune the critical current of the junction. The qubit drive signal at frequency  $f_d$  is provided from the same port, capacitively coupled to the island via  $C_d$ . The dc signal and the rf drive signal are decoupled with a bias tee.

The feedline and resonator are realized within the proximitized 2DEG by selectively etching away the Al, InAs, and approximately 450 nm of the buffer layer to define the central conductor. The Josephson junction, measuring  $\sim 10 \mu\text{m}$  wide and  $\sim 300 \text{ nm}$  long, is formed by locally removing the Al. To preserve the junction from electron beam imaging procedures, the junction length is measured using a confocal optical microscope with a lateral resolution of 100 nm. Additionally, a local gate  $V_G$ , made of evaporated Al and electrically isolated from the island by 25 nm of  $\text{HfO}_2$ , enables to tune the critical current of the junction  $I_c$ . The maximum  $I_c$  is expected at positive gate voltage and the minimum  $I_c$  at negative gate voltage, when the 2DEG is depleted. Details about the fabrication procedure are given in Chapter 4. Through the same port used for the dc gate, decoupled with a bias tee, we also apply the qubit drive at frequency  $f_d$ . The coupling capacitance for the drive  $C_d$  is given by the overlap between the gate electrode and the island, determined by the width of the gate and of the junction. In this design  $C_d$  is approximately  $\sim 177 \text{ fF}$ , resulting in a strong coupling to the gate line. To reduce photon losses to this port it is crucial to reduce  $C_d$ . However, in practice, the wet etching process used to define the junction limits the minimum width achievable to  $\sim 1 \mu\text{m}$ . An alternative is to couple the drive through a dedicated port [18], and filter the gate line to reduce transmission at the qubit frequency.

The device is connected to a printed circuit board by Al wire bonds and

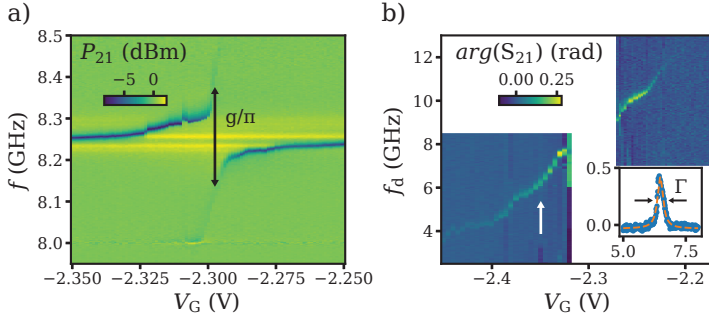


**Figure 8.2.** a) Transmitted power through the feedline  $P_{21}$  as a function of probe frequency  $f$  and gate voltage  $V_G$ . The resonator and the qubit mode vacuum Rabi split by  $\Delta f = g/\pi$  when they have the same frequency. The background has been removed by subtracting from each trace the average along the gate voltage axis. b) Continuous two-tone spectroscopy: the resonator phase response at fixed frequency  $\arg(S_{21})$  is measured as a function of drive frequency  $f_d$  and  $V_G$ . Peaks in  $\arg(S_{21})$  correspond to the qubit frequency. The background has been removed by subtracting from each trace the average along the gate voltage axis. The drive power  $P_d$  is  $-25$  dBm and a probe power  $-40$  dBm. The inset shows a vertical cut at the position indicated by the arrow. We fit  $\arg(S_{21})$  as a function of  $f_d$  with a Lorentzian to extract the qubit decay rate  $\Gamma$ .

mounted in a copper box thermally anchored to the mixing chamber of a Bluefors cryogen-free dilution refrigerator with a base temperature of  $\sim 15$  mK. The copper box is protected against stray magnetic fields with an aluminium and a permalloy shield. The dc lines are filtered at room temperature with a D-type sub connector with cut-off frequency at 640 kHz. Additional filtering is done at the 100 mK plate through QDevil RC-filters with a cut-off at 65 kHz and finally at the mixing chamber with silver epoxy filters. Incoming readout rf signals are attenuated by  $-66$  dB distributed across the cryostat plates, and then filtered with Ecosorb at the mixing chamber before reaching the transmission line. The qubit drive signal is produced by an Agilent MXG N5183B signal generator. The drive line is attenuated by  $-53$  dB and also filtered with Ecosorb. Outgoing rf signals are sent through a Silent Waves quantum-limited travelling wave parametric amplifier and further amplified by HEMT mounted on the 4 K-plate plus a room temperature amplifier. An overview of the setup is provided in Appendix D.1.

In Figure 8.2a) we plot the measured transmitted power  $P_{21}$  as a function

of probe frequency  $f$  and  $V_G$ . The measurement is performed using a Zurich Instruments SHFQA. We observe a vacuum Rabi splitting between the resonator and the qubit mode when they are brought in resonance with each other. The size of the splitting  $\Delta f_r$  when  $f_r$  is equal to the qubit frequency  $f_q$  (zero detuning), is related to the coupling  $g$  between the two modes by  $\Delta f_r = g/\pi$  [8], where  $g$  is given in  $\text{rads}^{-1}$ . From the measurement we extract  $g/(2\pi) \sim 150$  MHz. Fitting the resonator response at negative gate voltage, when the junction is pinched-off, we extract the bare resonance frequency  $f_{r,b} \sim 8.25$  GHz and the coupling quality factor  $Q_c \sim 900$ , corresponding to a coupling rate  $\kappa$  of approximately  $\sim 10$  MHz. The internal quality factor  $Q_i$  is approximately  $\sim 1300$ . Comparing the results of the fit with Sonnet simulations, we extract the kinetic inductance per square of the superconducting film  $L_{\text{kin}}/\square \sim 25$  fH. However, based on measurements of similar proximitized films (see Section 3.2.1) the design of the resonator was made assuming  $1 \text{ pH}/\square$ . As a consequence, the resonator impedance  $Z_r$  is not  $50 \Omega$ , but instead  $\sim 30 \Omega$ . With a coupling capacitance  $C_g$  of approximately  $9 \text{ fF}$ , we estimate, using Eq. (2.60), a coupling strength of  $g/(2\pi) \sim 155$  MHz in good agreement with the measured value.

We perform dispersive measurement of  $f_q$  by monitoring the resonator response at fixed frequency  $f_{\text{read}} = f_r$  as a function of a continuous drive tone applied at  $f_d$ . This is shown in Fig. 8.2b) for a drive power  $P_d$  of  $-25$  dBm and a probe power of  $-40$  dBm. At positions in gate voltage such that  $g/\Delta_{\text{qr}} = g/(f_q = f_r) \ll 1$ , when  $f_d$  matches  $f_q$ , the continuous microwave tone will incoherently drive qubit transitions and shift the resonance frequency. This will be measured as a change in the resonator response at  $f_{\text{read}}$  - e.g. as peaks in the phase response  $\text{arg}(S_{21})$ . Figure 8.2b) shows a cut in the resonator response as a function of  $f_d$  at  $V_G = -2.33$  V, corresponding to  $f_q \sim 6.5$  GHz. We fit the response with a Lorentzian to extract the qubit linewidth  $\Gamma$  and the qubit lifetime  $T = 1/\Gamma$ . At this particular frequency  $T$  is approximately  $4 \text{ ns}$ .

In Figure 8.3a) we plot  $\Gamma$  as a function of  $f_q$  as extracted from the data in Figure 8.2b). The increase in  $\Gamma$  as  $f_q$  approaches  $f_r$  (dashed line) can be explained by an increase in the Purcell decay rate as the detuning between the qubit and the resonator decreases [8]. This rate captures the fact that at low detuning, the qubit and the resonator modes hybridize, and the qubit can relax by emission of a resonator photon. In the future, to address Purcell decay to the readout resonator we can introduce a Purcell filter in between the feedline and the resonator. A Purcell filter in its simpler form consists of a low coupling quality factor resonator which allows signal readout at  $f_r$  while reducing qubit decay at  $f_q$  [6]. However, what also causes a qubit level broadening is the ac Stark shift from the resonator. The shift depends on the number of photons in the resonator and its inversely proportional to the

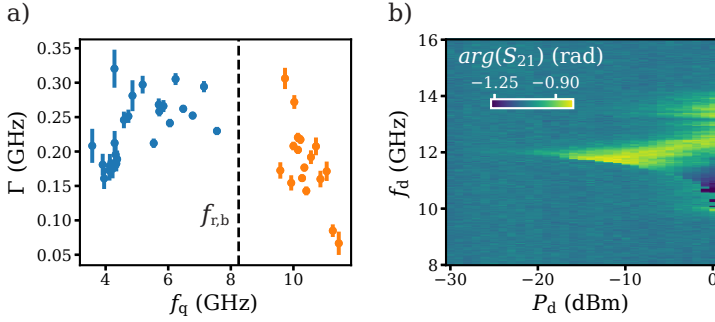


**Figure 8.3.** a) Qubit linewidth  $\Gamma$  as a function of qubit frequency  $f_q$  above (orange) and below (blue) the resonator bare resonance frequency  $f_{r,b}$  (dashed vertical line). b) Phase of the transmission coefficient  $\arg(S_{21})$  measured at fixed frequency  $f_{\text{read}} = f_r$  as a function of  $P_d$  and  $f_d$  when  $f_q \sim 12$  GHz.

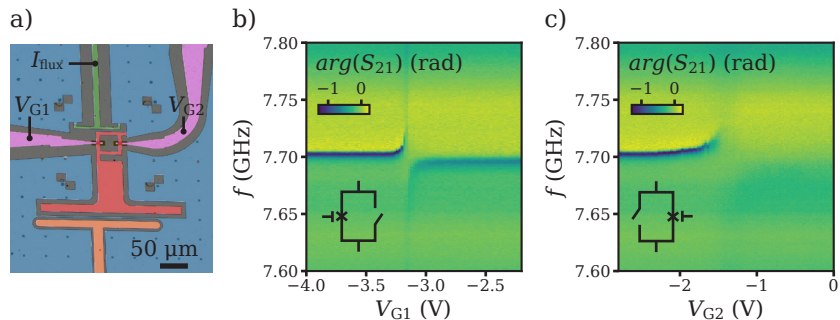
detuning [97]. As a consequence, fluctuation in the number of photons will cause a larger qubit level broadening at small detuning. The largest  $T$  we extract is approximately 10 ns, too short to perform time domain measurements.

Figure 8.3b) shows the fixed frequency phase response of the resonator as a function of  $P_d$  and  $f_d$  when the qubit frequency is approximately 12 GHz. Because of the short qubit lifetime (large  $\Gamma$ ) we do not observe multi-photon transitions with increasing drive power, and we cannot access the qubit anharmonicity.

The qubit lifetime could be limited by several factors including radiative loss through the gate, dielectric losses both in the substrate and in the  $\text{HfO}_2$  layer as well as fluctuations in the Andreev bound state (ABS) population of the junction [64], and others [18]. We will delve into the contribution of ABS in more details in the next section.

## 8.2. Flux and Gate Tunable Transmon

In this section we introduce flux tunability alongside the already gate-tunable transmon by incorporating an additional Josephson junction in parallel with the initial one forming a superconducting quantum interference device (SQUID). The design is similar to the one presented in Section 8.1. It consists of a  $\lambda/4$  coplanar transmission line resonator inductively coupled to a feedline for readout. The resonator is then capacitively coupled to a SQUID shunted ground with a T-shaped island. The total parallel capacitance  $C_\Sigma$  is approximately



**Figure 8.4.** a) False color optical image of a flux tunable transmon. A single junction is replaced with two junctions in parallel. The critical current of each junction can be tuned by a local gate  $V_{G1}$  and  $V_{G2}$ . The magnetic field flux through the loop is changed by the current  $I_{\text{flux}}$  flowing through the flux line (green). b) Phase of the transmission coefficient  $\arg(S_{21})$  as a function of probe frequency and  $V_{G1}$  when the other junction is pinched off ( $V_{G2} = -10$  V). c) Same as in b) but as a function of  $V_{G2}$  when  $V_{G1} = -10$  V.

108 fF corresponding to a charging energy  $E_C/h = e^2/C \sim 180$  MHz. The resonator geometry is the same as in Section 8.1, with an impedance of  $\sim 30 \Omega$ , but its length has been increased to bring the resonance frequency down to  $\sim 7.7$  GHz.

Figure 8.4a) shows a zoom-in on the transmon area. The capacitive island is now shorted to ground with two JJs in parallel. The critical current of each junction is tuned by a local gate  $V_{G1}$  and  $V_{G2}$ . The qubit drive port is connected to  $V_{G2}$  with a bias tee. The magnetic field flux through the loop is controlled by an on-chip flux line. Fabrication steps are the same as in Section 8.1. The junctions are  $\sim 10 \mu\text{m}$  wide and  $\sim 300$  nm long, and the loop area is  $A_{\text{loop}} \sim 40 \times 40 \mu\text{m}^2$ . The measurement setup is the same as in Section 8.1, with the only difference that the QDevil RC filters for the dc lines have now been exchanged with LC filters to limit thermal load to the cryostat when passing a current  $I_{\text{flux}}$  through the flux line.

### 8.2.1. Gate Response of Individual Junctions

For each junction, we measure the complex transmission coefficient  $S_{21}$  through the feedline as a function of probe frequency  $f$  and  $V_{Gi}$  when the other junction is pinched off. This is shown in Fig. 8.4b) and c). We observe an anticrossing

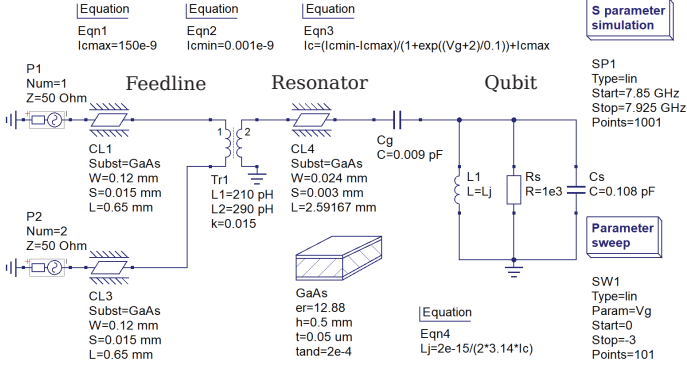


**Figure 8.5.** QUCS schematic of the device equivalent electrical circuit. The feedline and the resonator are represented as transmission lines of width  $W$ , gap  $S$  and length  $L$  on a GaAs substrate. The transmon is modelled as an RLC circuit where the inductor represents the Josephson inductance of the junction, the capacitor is given by the capacitance of the T-island, and the resistor embeds the dissipative part of the junction impedance. The values of the mutual inductance (represented by the component  $Tr1$ ), coupling capacitance  $C_g$  and island capacitance  $C_\Sigma$  are extracted from Sonnet simulations. We perform an S-parameter simulation as a function of a parameter sweep that controls the junctions critical current.

between the resonator and the qubit mode in both cases. We fit the resonator response when both junctions are depleted at sufficiently negative gate voltage to extract the bare coupling and internal quality factors,  $Q_c \sim 2700$  and  $Q_i \sim 4300$  respectively. At positive gate voltages, when the qubit frequency is above the resonator, the response is very different. When only  $JJ_1$  is conducting (at  $V_{G1} = 0$  V,  $V_{G2} = -100$  V) the quality factor of the resonance decreases to  $Q_i \sim 1200$ , while when only  $JJ_2$  is conducting (at  $V_{G2} = 0$  V,  $V_{G1} = -100$  V) the resonance becomes barely visible.

To understand this behaviour we simulate an equivalent electrical circuit where the transmon island is described within the resistively and capacitively shunted junction model (see Section 2.3.2). We use the QUCS simulation software, whose circuit schematic is shown in Fig. 8.5. The feedline and the resonator are represented as coplanar transmission lines on a GaAs substrate, and all circuit parameters are extracted from Sonnet simulations. The shunt resistance describes the dissipative component of the Josephson junction, which can be attributed to residual quasiparticles or, as investigated in Ref. [64],

to fluctuations in the ABS population. Because of the fluctuation-dissipation relation [288], changes in the occupation of ABSs due to thermal activation of microwave-induced transitions will result in a finite real part component of the junction impedance. In Ref. [64], the authors show that the value of  $R_s$  in a multichannel short-diffusive junction at the  $\pi$  point in the CPR can be as low as  $100 \Omega$ . In this device, the Josephson junctions are  $\sim 10 \mu\text{m}$  wide, therefore containing many channels with a wide distribution of transmission probabilities, and approximately  $L \sim 300 \text{ nm}$  long. This length, given the typical coherence length in Al films  $\xi \sim 500 \text{ nm}$  [41], results in a ratio  $L/\xi$  of approximately  $\sim 0.6$ . In addition, channels with a transversal component of momentum have an effective length much longer than  $L$  resulting in an even larger  $L/\xi$  ratio. As discussed in Section 2.3.1, a large value of  $L/\xi$  leads to a dense spectrum of ABS with low energies. These states exist not only near the  $\pi$  point but across the entire phase range, contributing to a low real part of the junction impedance.

We model the dependence of the critical current on the gate voltage parameter  $V_G$  with a smooth step function:

$$I_c = \frac{I_{c,\min} - I_{c,\max}}{1 + e^{\frac{V_G + 2}{0.1}}} + I_{c,\max} \quad (8.1)$$

where  $I_{c,\max}$  and  $I_{c,\min}$  are the maximum and minimum critical current of the junction. The corresponding Josephson inductance is calculated as  $L_J = \Phi/(2\pi I_c)$ . The RLC circuit modelling the transmon acts on the resonator as a frequency dependent load with resonance frequency at  $f_{\text{RLC}} = \frac{1}{2\pi\sqrt{L_J C_\Sigma}}$  and linewidth  $\Gamma_{\text{RLC}} = 1/(R_s C_\Sigma)$ . As for the quantum case, the resonator and the RLC mode will anticross when  $f_{\text{RLC}} = f_{r,\text{qucs}}$ . The absence of a quantum treatment is reflected in the absence of vacuum Rabi splitting into two resonance for a single  $V_G$  value.

From dc measurements on junctions with  $L \sim 150 \text{ nm}$  (see Chapter 6), in a  $\sim 10 \mu\text{m}$  wide junction we expect a maximum critical current of approximately  $3 \mu\text{A}$  at zero gate voltage. However, assuming  $I_{c,\max} = 3 \mu\text{A}$  in the simulation, brings  $f_{\text{RLC}}$  at  $V_G = 0$  to approximately  $50 \text{ GHz}$ , which is too high to have an influence on the resonator mode for any finite value of  $R_s$ . Therefore, in the simulation, we have to use a lower value of  $I_{c,\max}$  to observe an effect on the resonator response at  $V_G = 0$ . This is justified by the inverse dependence of the critical current of a Josephson junction on the length of the weak link [195]. We simulate the transmission coefficient  $S_{21}$  for different values of shunt resistance  $R_s$  as a function of  $f$  and  $V_G$ . In Fig. 8.6a) we plot the result of the simulation for  $R_s = 10 \text{ k}\Omega$ , and  $I_{c,\max} = 150 \text{ nA}$ , corresponding to  $f_{\text{RLC}}(V_G = 0) \sim 10 \text{ GHz}$ . On the same graph we plot  $f_{\text{RLC}}$  calculated using Eq. (8.1) to get



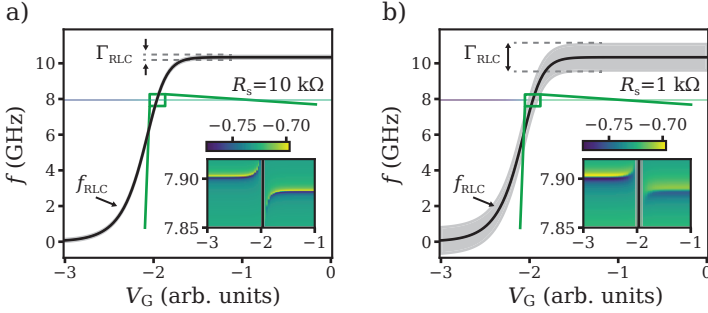


**Figure 8.6.** a) QUCS simulation of the phase of the transmission coefficient  $\arg(S_{21})$  as a function of frequency  $f$  and of the parameter  $V_G$  that controls the value of the inductance in the RLC circuit. The shunt resistor  $R_s$  is set to  $10\text{ k}\Omega$ . The frequency span on the y-axis is much larger than the simulation frequency in order to show the resonance frequency of the RLC circuit  $f_{\text{RLC}}$  (black line), and the resonance linewidth  $\Gamma_{\text{RLC}}$  (grey area). The inset shows a zoom in on the simulation results. b) Same as in a) for  $R_s = 1\text{ k}\Omega$ .

$L_J(V_G)$ . The inset shows a zoom-in on the resonator response. Here, the resonator response is approximately symmetric with respect to the point where  $f_{\text{RLC}}$  crosses  $f_{r,\text{qucs}}$ . Fig. 8.6b) shows instead the results of the simulation with  $R_s = 1\text{ k}\Omega$ . In this case, the resonator is coupled to a ten times more dissipative load. The fact that  $f_{\text{RLC}}$  is much closer to  $f_{r,\text{qucs}}$  on the right side of the crossing compared to the left side, gives rise to the asymmetry in the anticrossing as we observe in the experiment. The abrupt change in the resonance is a consequence of the fact that  $f_{\text{RLC}}$  appears as a vertical line in the voltage and frequency range we are looking at. Analogously, the disappearance of the resonance for  $\text{JJ}_2$  in Fig. 8.4c), can be attributed to a lower critical current, which would bring the qubit frequency closer to the resonator resonance frequency at zero gate voltage, or a lower value of  $R_s$  (larger dissipation).

### 8.2.2. Flux Response

We now discuss the case when both junctions carry a finite supercurrent. We perform dispersive measurements as a function of  $I_{\text{flux}}$ , which controls the magnetic field flux through the loop, and as a function of a continuous drive tone applied at  $f_d$  via the gate  $V_{G2}$ .

Two-tone spectroscopy maps at different gate voltage configurations ( $V_{G1}$ ,

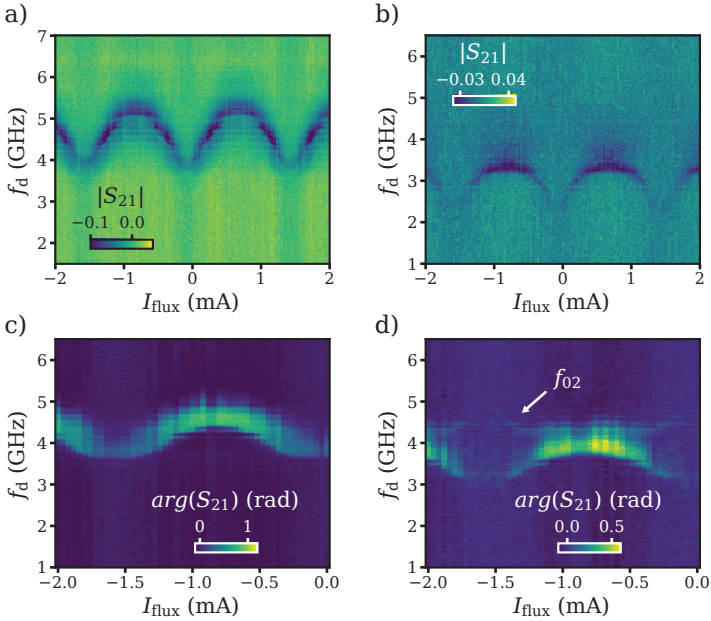


**Figure 8.7.** a) and b) Magnitude of the transmission coefficient  $|S_{21}|$  measured at fixed frequency  $f_{\text{read}} = f_r$  as a function of drive frequency  $f_d$  and flux current bias  $I_{\text{flux}}$  for  $(V_{G1} = -3.46 \text{ V}, V_{G2} = -2.42 \text{ V})$  and  $(V_{G1} = -3.49 \text{ V}, V_{G2} = -2.68 \text{ V})$  respectively. The drive power is  $-37 \text{ dBm}$  and the readout power is  $-50 \text{ dBm}$ . c) and d) Phase of the transmission coefficient  $\arg(S_{21})$  measured as in a) and b) but for  $(V_{G1} = -3.47 \text{ V}, V_{G2} = -2.51 \text{ V})$  and  $(V_{G1} = -3.47 \text{ V}, V_{G2} = -2.58 \text{ V})$  respectively. For the gate configuration in d) the two junctions have similar effective transmission probabilities. As a consequence the transition from the ground to the second excited state  $f_{02}$  becomes visible around half flux quantum  $I_{\text{flux}} \sim -1.5 \text{ mA}$ . In this case, the drive power is  $-30 \text{ dBm}$  and the readout power is  $-50 \text{ dBm}$ .

$V_{G2}$ ) are plotted in Fig. 8.7. As discussed in Section 2.4.3, we can change both the average value of  $f_q$  and its flux dependence thanks to the gate tunability and the non-sinusoidal CPR of each junction. To preserve the shape and amplitude of the oscillations of  $f_q$  with flux, and move them down in frequency, we can bring both gates to more negative voltages. This is shown in Fig. 8.7a) and b), where we plot two maps obtained for  $(V_{G1} = -3.46 \text{ V}, V_{G2} = -2.42 \text{ V})$  and  $(V_{G1} = -3.49 \text{ V}, V_{G2} = -2.68 \text{ V})$  respectively. Alternatively, we can modify the dependence of  $f_q$  on  $I_{\text{flux}}$  by changing the asymmetry in critical current

between the junctions.

In Section 2.4.3 we have discussed how the energy spectrum changes significantly as a function of flux in case of non-sinusoidal CPR with similar effective transmission probabilities. To prove this, we chose  $V_{G1}$  and  $V_{G2}$  so that the two junctions have similar Josephson energies. We chose this point as determined from two-tone spectroscopy of each junction separately (see Appendix D.2). Then, we perform two-tone spectroscopy measurements as a function of flux for different values of  $V_{G2}$ . At  $V_{G1} = -3.47$  V and  $V_{G2} = -2.58$  V the two junctions have similar Josephson energy corresponding to a qubit frequency of approximately 2 GHz. Even though in this device the broad linewidth of the qubit makes it difficult to distinguish multi-photon transitions and extract information about qubit spectrum, we are still able to resolve some features. Fig. 8.7c) and d) show two of these measurements for asymmetric and approximately symmetric junctions respectively. In case of similar effective transmission probabilities (symmetric junctions), the anharmonicity of the qubit is expected to change sign and increase in modulus when the external flux equals half flux quantum. In Fig. 8.7d) we see a second transition detaching from the main one and going up in energy at around  $I_{\text{flux}} \sim -1.5$  mA. This line can be attributed to the transition from the ground to the second excited state  $f_{02}$  involving two photons.

To better resolve the energy spectrum of the qubit and perform time domain measurements it is crucial to reduce the qubit linewidth. This can be achieved by realizing shorter and narrower junctions and by limiting photon losses through the dc control lines.

### 8.3. Flux and Gate Tunable Josephson Parametric Amplifier

In this section we present preliminary results on a Josephson parametric amplifier (JPA) realized using two gate tunable Josephson junctions arranged in a SQUID geometry. The goal is to make use of the gate tunability of hybrid junctions and the interference effects between higher order harmonics of their CPRs, to realize a JPA which can be tuned continuously from a three-wave mixing to a four-wave mixing amplification regime. A brief overview of the concepts behind parametric amplification, and references for a more in depth understanding are provided in Section 2.5.

Figure 8.8 shows the device schematic. It consists of a  $\lambda/4$  transmission line resonator capacitively coupled to a feedline and shorted to ground at the other end with a SQUID. The resonator and the feedline are realized within the same proximitized 2DEG, and with the same fabrication steps as in Sec-

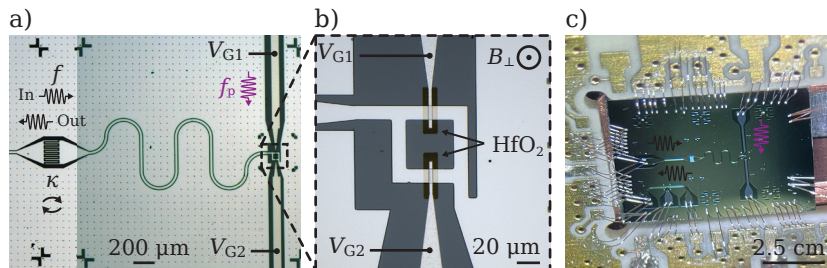


**Figure 8.8.** a) Optical image of the device. A lambda quarter transmission line resonator is capacitively coupled to an input feedline with a coupling rate  $\kappa$  and shorted to ground with a SQUID. The critical current of each junction is tuned by a local gate voltage  $V_{G1}$  and  $V_{G2}$ . We probe the resonator response at frequency  $f$ . A pump tone of frequency  $f_P$  is sent to the device via  $V_{G1}$ . The gate line and the pump line are decoupled with a bias tee. b) Zoom-in on the loop area. The magnetic field flux through the loop is controlled by the perpendicular magnetic field  $B_{\perp}$ . A locally grown  $\text{HfO}_2$  layer electrically isolate the gates from the resonator. c) Optical image of the bonded device.

tion 8.1. The junctions are  $\sim 10 \mu\text{m}$  wide and  $\sim 250 \text{ nm}$  long, and the loop area is  $A_{\text{loop}} \sim 35 \times 35 \mu\text{m}^2$ . A set of local gates  $V_{G1}$  and  $V_{G2}$  controls the charge carrier density in the weak links and tunes the corresponding critical currents.

The device is measured using a standard reflectometry setup in a Triton 200 dilution refrigerator with a base temperature of 50 mK. The input and output signal lines are connected to the device via a directional coupler positioned on the mixing chamber. The input line is attenuated by a total of  $-63 \text{ dB}$  including the  $-20 \text{ dB}$  coming from the directional coupler. The amplification chain consists of a HEMT and a room temperature amplifier. An additional line, with  $-40 \text{ dB}$  attenuation, is connected to  $V_{G1}$  and decoupled from the dc signal with a bias tee. This line is used to provide the pump tone at frequency  $f_P$ . The dc lines are filtered at room temperature with a D-type sub connector with cut-off frequency at 640 kHz and at the mixing chamber with home build silver epoxy filters. The magnetic flux through the loop is controlled with a three-axis vector magnet. As a consequence, the device has no magnetic shielding. A complete overview of the setup is shown in Appendix D.4.

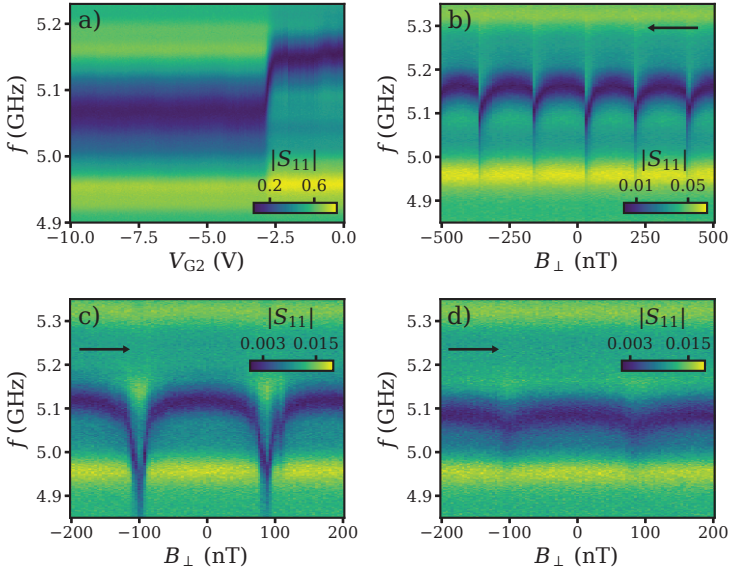


**Figure 8.9.** a) Magnitude of the reflection coefficient  $|S_{11}|$  measured as a function of probe frequency  $f$  and  $V_{G2}$ . Instead,  $V_{G1}$  does not have any effect on the resonator response. b) Magnitude of the reflection coefficient  $|S_{11}|$  measured as a function of  $f$  and perpendicular magnetic field  $B_{\perp}$  at  $V_{G2} = 0$  V. Jumps in the map correspond to jumps in the internal phase of the SQUID. c) Same as in b) but for  $V_{G2} = -2.4$  V. d) Same as in b) but for  $V_{G2} = -2.6$  V. The arrows indicate the direction of the magnetic field sweep.

### 8.3.1. Gate and Flux Response

In Fig. 8.9a), we plot the magnitude of the complex reflection coefficient  $|S_{11}|$  as a function of probe frequency  $f$  and  $V_{G2}$ . As we lower the critical current of  $JJ_2$  by applying a negative gate voltage, the resonance frequency  $f_r$  shifts down because of the larger Josephson inductance of the SQUID. For sufficiently negative values of  $V_{G2}$ ,  $JJ_2$  is fully pinched off, and the resonance frequency is only determined by the Josephson inductance of  $JJ_1$ . Unfortunately,  $f_r$  does not show any dependence on  $V_{G1}$ , indicating that the gate electrode is interrupted at some point. This can be caused either by the mesa step ( $\sim 450$  nm) or by lift-off residuals at the edge of the  $\text{HfO}_2$  layer.

Figure 8.9b) shows the dependence of  $|S_{11}|$  on the perpendicular magnetic field  $B_{\perp}$  at  $V_{G2} = 0$  V. The oscillations in the critical current of the SQUID

as a function of  $B_{\perp}$  cause oscillations of  $f_r$ . The response is hysteretic, with jumps whenever the magnetic field flux  $\Phi_{\text{ext}} = B_{\perp} A_{\text{loop}}$  is close to a multiple of half flux quantum. Similar to an rf SQUID (see Section 2.3.2), this happens whenever the inductance of the junction with the smaller critical current is not larger than the inductance of the rest of the loop [85, 289]. Decreasing the critical current in  $\text{JJ}_2$  at negative values of  $V_{G2}$ , the hysteresis is reduced and eventually removed. This is shown in Fig. 8.9c) and d). The oscillations in resonance frequency are deeper the more symmetric the junctions are, and eventually disappear when  $\text{JJ}_2$  is pinched off.

From a fit to the resonator response at  $V_{G2} = 0$  V and zero magnetic field flux we extract a coupling quality factor  $Q_c$  of approximately  $\sim 50$  corresponding to a coupling rate  $\kappa \sim 100$  MHz. The internal quality factor  $Q_i$  is also approximately 50. Most probably, the limiting factors of  $Q_i$  are once again photon losses to the gate lines and a large dissipative part of the junction impedance. From the value of  $f_r$  at  $V_{G2} = -10$  V, when  $\text{JJ}_2$  is pinched off, we can extract the Josephson inductance of  $\text{JJ}_1$ . From Sonnet simulations, by matching the simulated resonance frequency to the measured one, we obtain  $L_{J1} \sim 0.4$  nH, corresponding to a critical current  $I_{c1}$  of approximately 800 nA. This relatively low critical current, compared to what expected for short junctions of similar width, suggests a non-negligible real part of the junction impedance.

### 8.3.2. Gain

Next, we study the effect on the resonator response of a pump tone applied at a frequency  $f_P$  through  $V_{G1}$ . When the pump is connected to the gate of a hybrid JJ, a three-wave mixing amplification process is possible provided that the critical current depends linearly on the gate. In this case, the critical current, and therefore the Josephson inductance of the junction, will depend linearly on the amplitude of the pump signal, satisfying the condition for three-wave mixing [? ]. Unfortunately, in this device we cannot investigate this effect since the gate electrode to which the pump line is connected to is interrupted before reaching the junction.

In the following, keeping the external flux at zero, we monitor the resonator response as a function of the pump frequency and pump power while tuning the asymmetry between the SQUID arms using  $V_{G2}$ . In Fig. 8.10, we plot  $|S_{11}|$  as a function of  $f$  and  $f_P$  at for different values of  $V_{G2}$ . The signal power is  $P = -45$  dBm and the pump power is  $P_P = 15.5$  dBm. At  $V_{G2} = 0$  V, parametric amplification is obtained when the pump tone is positioned slightly above  $f_r$ . A single peak develops within a certain pump frequency range. As we tune  $V_{G2}$  to more negative voltages, a second region with gain appears at

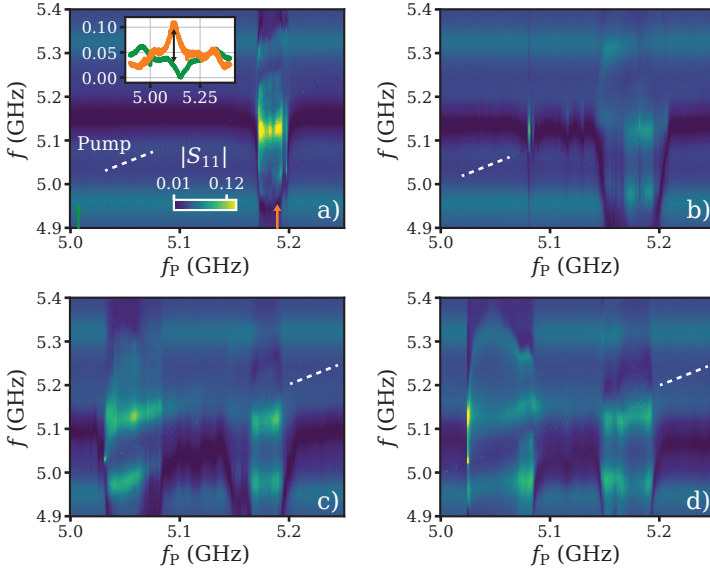


**Figure 8.10.** a) Magnitude of the reflection coefficient  $|S_{11}|$  measured as a function of probe frequency  $f$  and pump frequency  $f_P$  for a gate voltage on  $JJ_2$  of  $V_{G2} = 0$  V at  $\Phi_{\text{ext}}/\Phi_0 = 0$ . The pump tone is visible in the map as a sharp peak as indicated by the white dashed line. The inset shows vertical cuts in the map at the positions indicated by the green arrow (pump detuned from the resonance frequency) orange arrow (amplification regime) The gain is evaluated as the ratio between the orange and the green curve at the position indicated by the black arrows. b), c) and d) same as in a) but for  $V_{G2} = -2.2$  V,  $V_{G2} = -2.4$  V and  $V_{G2} = -5$  V.

lower pump frequency for  $f_P$  slightly below  $f_r$ . In this case, two peaks develop within each region. While the behaviour at  $V_{G2} = 0$  V is in agreement with a four-wave mixing process as previously reported for a parametric amplifier realized in a similar material platform [19], the reason for the double peak is still unclear. A maximum gain of 6 dB is extracted as the ratio between maximum of the trace when there is amplification and the value of  $|S_{11}|$  taken at the same frequency when the pump tone is far detuned. This is illustrated by the inset of Fig. 8.10a).

Figure 8.11a) shows the dependence of the gain profile at  $V_{G2} = 0$  V as a function of  $P_P$  with fixed pump frequency  $f_P = 5.19$  GHz. We use this

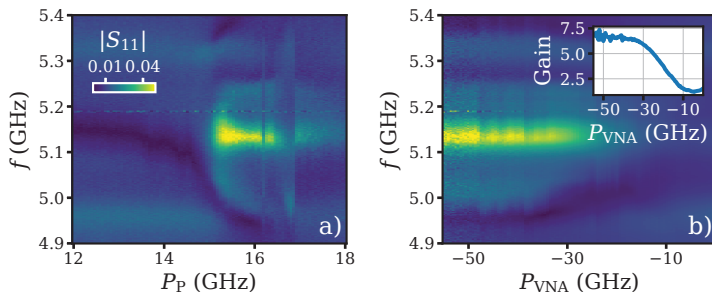


**Figure 8.11.** a) Magnitude of the reflection coefficient  $|S_{11}|$  measured as a function of probe frequency  $f$  and pump power  $P_P$  for  $V_{G2} = 0$  V at  $\Phi_{\text{ext}}/\Phi_0 = 0$ . The pump frequency is set to  $f_P = 5.19$  GHz. b)  $|S_{11}|$  as a function of signal power set on the vector network analyser  $P_{\text{VNA}}$  for  $f_P = 5.19$  GHz and  $P_P = 15.5$  dBm. The inset shows the power gain in dB calculated as the ratio between maximum of each vertical trace in the map and the value of  $|S_{11}|$  at the same frequency taken on a reference curve with the pump off.

measurement, together with the data in Fig. 8.10a) to find the optimal pump power and frequency to have maximum gain, which is obtained approximately at  $P_P = 15.5$  and  $f_P = 5.19$  GHz. In Figure 8.11b) we show the gain profile as a function of signal power for the optimal set of pump parameters. The gain stays constant for a wide range of input power.

As discussed in Ref. [84] and in Ref. [14], the third and fourth order nonlinearities in the Josephson potential of the SQUID, and the corresponding amplification processes, depend on the applied magnetic flux and on the asymmetry between the arms of the loop. However, being not satisfied with the gate response and the unstable gain profile, we did not proceed on this device to further study the gain flux dependence. Given the poor magnetic shielding, magnetic field fluctuations are expected to limit the stability of the gain profile. While this section is not conclusive, I hope it contributes as a starting point for future implementations of gate and flux tunable JPA.

## 8.4. Conclusions

Following up on our results on charge  $4e$  supercurrent in the previous chapter, we have implemented a gate and flux tunable transmon qubit. We have to improve the qubit quality factor by reducing the length of the JJs and therefore the dissipative part of the junction impedance. To address Purcell decay to the readout resonator we can introduce a Purcell filter to the design. To



reduce photon losses through the dc lines we can use a dedicated port for the drive tone and implement on chip low pass filters for the gates and the flux line. Also, we can decrease the width of the junctions to decrease the coupling capacitance to the gates.

We have also outlined some preliminary results on a JPA with a gate tunable SQUID aimed at realizing gate and flux control over the parametric amplification regime. We show gate and flux control of the resonator frequency, and a 6 dB gain at zero flux obtained with a four-wave mixing process ( $f_P \approx f_S$ ). We do not observe three-wave mixing amplification, yet. To increase the gain of the JPA, similar as in the transmon case, one needs to fabricate shorter and narrower junctions and reduce losses through the dc lines. A dedicated pump port, allowing to engineer the coupling to the pump independently on the gate capacitance would also be beneficial. To achieve three-wave mixing amplification it is necessary to gain gate control over both junctions and shield magnetic field fluctuations.



## 9 Summary and Outlook

---

The main goal of this thesis was to explore the potential use of a proximitized InAs two-dimensional electron gas (2DEG) for hybrid superconducting quantum circuits. Our approach has been to harness the inherent gate-tunability and scalability of this material platform to improve the flexibility and control of the design of superconducting circuits.

With standard characterization procedures, we have extracted the relevant material parameters such as the electron density and the mobility of the 2DEG, as well as the induced superconducting gap and the kinetic inductance of the proximitized system. In addition, we have studied both the dc and the ac Josephson effect in planar Josephson junctions (JJ) realized in this platform. A key ingredient of these devices is the non-sinusoidal character of their current-phase relation (CPR). To investigate the CPR of the JJs, we discuss advantages and disadvantages of the two characterization methods used in this thesis, namely switching current experiments in dc superconducting quantum interference devices (SQUIDs) and measurements of Josephson radiation. We estimate the effective transmission probability of these JJs using both methods.

We have detailed the fabrication process of epi-aluminium/InAs devices as well as the realization of NbTiN and granular aluminium (grAl) superconducting resonators. We have shown the fabrication of grAl resonators in Basel and the characterization of their microwave losses on InP substrates. We combine our findings with measurements of grAl resonators fabricated at KIT. Our results indicate that InP is compatible with high impedance resonators for applications in hybrid superconducting circuits. An interesting approach would be to try to control the spin of quasiparticles in Andreev bound states via the vacuum electric field fluctuations of high impedance resonators, as shown for electrons in semiconducting quantum dots [192, 290].

Making use of the interference effects of higher harmonics in the CPR of two epi-Al/InAs hybrid JJs in a SQUID, we demonstrate that we can engineer an effective Josephson element with an arbitrary CPR. This holds potential applications for several superconducting quantum devices. First, we have implemented a gate and flux tunable Josephson diode with efficiency up to  $\sim 30\%$ , close to the maximum theoretically predicted value of  $\sim 40\%$  [12]. The diode

efficiency could be further increased, up to  $\sim 80\%$  by concatenating several interferometers in parallel. Such configuration could be easily implemented within the 2DEG system.

Performing Josephson radiation experiments, we report the emergence of a charge-4e-dominated supercurrent through the SQUID corresponding to the coherent transport of pairs of Cooper pairs. This happens when the junctions are symmetric and the flux is set to half flux quantum. We demonstrate the capability to engineer a robust  $\sin(2\varphi)$  Josephson element that could be used to realize a parity protected qubit in this material system. Further investigating this effect, we have shown preliminary results on a gate and flux tunable transmon qubit. Here, a proximitized InAs 2DEG is used to realize both the JJs and the microwave circuit. This simplifies the fabrication process removing the need for typically cumbersome contacting procedures. We show that the qubit frequency can be tuned with both gate and magnetic flux. However, for practical applications, the qubit lifetime needs to be increased by improving the quality of the JJs and of the heterostructure. The optimization of the gate dielectric as well as the systematic filtering of both dc and rf control lines will also contribute to a larger qubit lifetime.

Finally, we have investigated the performances of a Josephson parametric amplifier connecting a hybrid SQUID to the current antinode of a  $\lambda/4$  transmission line resonator. We have achieved a maximum gain of 6 dB, which however, is not stable with the gate voltage. Similarly to the transmon qubit, the amplifier gain and stability would also benefit from a better quality of the junctions and from an additional filtering of the control lines. In addition, individual gate control over both junctions and magnetic shielding of the device is required to achieve a Kerr-free three-wave mixing amplification process.

This work sets the stage for future development of hybrid superconducting circuits using planar heterostructures. The fabrication procedure, the designs and the operational principles investigated in this thesis can be applied not only to InAs 2DEGs, but also to all the other emerging platforms, such as Ge/SiGe two-dimensional hole gases [132].

# Bibliography

- [1] D. P. DiVincenzo and IBM, *Fortschritte der Physik* **48**, 771 (2000).
- [2] M. A. Nielsen and I. L. Chuang, *Quantum Computation and Quantum Information: 10th Anniversary Edition* (Cambridge University Press, 2010).
- [3] K. Wintersperger, F. Dommert, T. Ehmer, A. Hoursanov, J. Klepsch, W. Maurerer, G. Reuber, T. Strohm, M. Yin, and S. Luber, *EPJ Quantum Technology* **10**, 1 (2023).
- [4] C. D. Bruzewicz, J. Chiaverini, R. McConnell, and J. M. Sage, *Applied Physics Reviews* **6**, 021314 (2019).
- [5] G. Burkard, T. D. Ladd, A. Pan, J. M. Nichol, and J. R. Petta, *Reviews of Modern Physics* **95**, 025003 (2023).
- [6] P. Krantz, M. Kjaergaard, F. Yan, T. P. Orlando, S. Gustavsson, and W. D. Oliver, *Applied Physics Reviews* **6**, 021318 (2019).
- [7] B. Josephson, *Physics Letters* **1**, 251 (1962).
- [8] A. Blais, A. L. Grimsmo, S. M. Girvin, and A. Wallraff, *Reviews of Modern Physics* **93**, 025005 (2021).
- [9] C. Eichler and A. Wallraff, *EPJ Quantum Technology* **1**, 1 (2014).
- [10] J. Aumentado, *IEEE Microwave Magazine* **21**, 45 (2020).
- [11] M. Nadeem, M. S. Fuhrer, and X. Wang, *Nature Reviews Physics* **5**, 558 (2023).
- [12] R. S. Souto, M. Leijnse, and C. Schrade, *Physical Review Letters* **129**, 267702 (2022).
- [13] C. Schrade, C. M. Marcus, and A. Gyenis, *PRX Quantum* **3**, 030303 (2022).
- [14] C. Schrade and V. Fatemi, “Dissipationless Nonlinearity in Quantum Material Josephson Diodes,” (2023), arxiv:2310.12198 [cond-mat, physics:quant-ph] .
- [15] C. Baumgartner, L. Fuchs, A. Costa, J. Picó-Cortés, S. Reinhardt, S. Gronin, G. C. Gardner, T. Lindemann, M. J. Manfra, P. E. F. Junior, D. Kochan, J. Fabian, N. Paradiso, and C. Strunk, *Journal of Physics: Condensed Matter* **34**, 154005 (2022).
- [16] N. Lotfizadeh, B. Pekerten, P. Yu, W. Strickland, A. Matos-Abiague, and J. Shabani, “Superconducting Diode Effect Sign Change in Epitaxial Al-InAs Josephson Junctions,” (2023), arxiv:2303.01902 [cond-mat] .

- [17] L. Casparis, M. R. Connolly, M. Kjaergaard, N. J. Pearson, A. Kringhøj, T. W. Larsen, F. Kuemmeth, T. Wang, C. Thomas, S. Gronin, G. C. Gardner, M. J. Manfra, C. M. Marcus, and K. D. Petersson, *Nature Nanotechnology* **13**, 915 (2018).
- [18] W. M. Strickland, J. Lee, L. Baker, K. Dindial, B. H. Elfeky, M. Hatefipour, P. Yu, I. Levy, V. E. Manucharyan, and J. Shabani, “Characterizing losses in InAs two-dimensional electron gas-based gatemon qubits,” (2023), arxiv:2309.17273 [cond-mat, physics:quant-ph] .
- [19] D. Phan, P. Falthansl-Scheinecker, U. Mishra, W. Strickland, D. Langone, J. Shabani, and A. Higginbotham, *Physical Review Applied* **19**, 064032 (2023).
- [20] J. Shabani, M. Kjaergaard, H. J. Suominen, Y. Kim, F. Nichele, K. Pakrouski, T. Stankevic, R. M. Lutchyn, P. Krogstrup, R. Feidenhans'l, S. Kraemer, C. Nayak, M. Troyer, C. M. Marcus, and C. J. Palmstrøm, *Phys. Rev. B* **93**, 155402 (2016).
- [21] J. S. Lee, B. Shojaei, M. Pendharkar, A. P. McFadden, Y. Kim, H. J. Suominen, M. Kjaergaard, F. Nichele, H. Zhang, C. M. Marcus, and C. J. Palmstrøm, *Nano Letters* **19**, 3083 (2019).
- [22] K. V. Klitzing, G. Dorda, and M. Pepper, *Physical Review Letters* **45**, 494 (1980).
- [23] D. C. Tsui, H. L. Stormer, and A. C. Gossard, *Physical Review Letters* **48**, 1559 (1982).
- [24] B. J. Van Wees, H. Van Houten, C. W. J. Beenakker, J. G. Williamson, L. P. Kouwenhoven, D. Van Der Marel, and C. T. Foxon, *Physical Review Letters* **60**, 848 (1988).
- [25] G. Timp, A. M. Chang, J. E. Cunningham, T. Y. Chang, P. Mankiewich, R. Behringer, and R. E. Howard, *Physical Review Letters* **58**, 2814 (1987).
- [26] Y. J. Chung, A. Gupta, K. W. Baldwin, K. W. West, M. Shayegan, and L. N. Pfeiffer, *Phys. Rev. B* **106**, 075134 (2022).
- [27] N. W. Ashcroft and N. D. Mermin, *Solid State Physics* (Holt, Rinehart and Winston, 1976).
- [28] T. Ihn, *Semiconductor Nanostructures: Quantum States and Electronic Transport* (OUP Oxford, 2009).
- [29] R. Winkler, *Spin—Orbit Coupling Effects in Two-Dimensional Electron and Hole Systems*, Springer Tracts in Modern Physics, Vol. 191 (Springer, Berlin, Heidelberg, 2003).
- [30] K. S. Wickramasinghe, W. Mayer, J. Yuan, T. Nguyen, L. Jiao, V. Manucharyan, and J. Shabani, *Applied Physics Letters* **113**, 262104 (2018).
- [31] E. C. T. O’Farrell, A. C. C. Drachmann, M. Hell, A. Fornieri, A. M. Whiticar, E. B. Hansen, S. Gronin, G. C. Gardner, C. Thomas, M. J. Manfra, K. Flensberg, C. M. Marcus, and F. Nichele, *Physical Review Letters* **121**, 256803 (2018).

- 
- [32] J. D. S. Witt, S. J. Pauka, G. C. Gardner, S. Gronin, T. Wang, C. Thomas, M. J. Manfra, D. J. Reilly, and M. C. Cassidy, *Applied Physics Letters* **122**, 083101 (2023).
- [33] V. N. Golovach, M. Borhani, and D. Loss, *Physical Review B* **74**, 165319 (2006).
- [34] K. D. Petersson, L. W. McFaul, M. D. Schroer, M. Jung, J. M. Taylor, A. A. Houck, and J. R. Petta, *Nature* **490**, 380 (2012).
- [35] C. Kloeffel, M. Trif, P. Stano, and D. Loss, *Physical Review B* **88**, 241405 (2013).
- [36] J. W. G. Van Den Berg, S. Nadj-Perge, V. S. Pribiag, S. R. Plissard, E. P. A. M. Bakkers, S. M. Frolov, and L. P. Kouwenhoven, *Physical Review Letters* **110**, 066806 (2013).
- [37] B. van Heck, J. I. Väyrynen, and L. I. Glazman, *Physical Review B* **96**, 075404 (2017).
- [38] J. Bardeen, L. N. Cooper, and J. R. Schrieffer, *Physical Review* **106**, 162 (1957).
- [39] T. T. Heikkilä, *The Physics of Nanoelectronics: Transport and Fluctuation Phenomena at Low Temperatures* (OUP Oxford, 2013).
- [40] W. Meissner and R. Ochsenfeld, *Naturwissenschaften* **21**, 787 (1933).
- [41] M. Tinkham, *Introduction to Superconductivity* (Courier Corporation, 2004).
- [42] J. Gao, J. Zmuidzinas, A. Vayonakis, P. Day, B. Mazin, and H. Leduc, *Journal of Low Temperature Physics* **151**, 557 (2008).
- [43] R. Barends, J. Wenner, M. Lenander, Y. Chen, R. C. Bialczak, J. Kelly, E. Lucero, P. O'Malley, M. Mariani, D. Sank, H. Wang, T. C. White, Y. Yin, J. Zhao, A. N. Cleland, J. M. Martinis, and J. J. A. Baselmans, *Applied Physics Letters* **99**, 113507 (2011).
- [44] J. Wenner, Y. Yin, E. Lucero, R. Barends, Y. Chen, B. Chiaro, J. Kelly, M. Lenander, M. Mariani, A. Megrant, C. Neill, P. J. J. O'Malley, D. Sank, A. Vainsencher, H. Wang, T. C. White, A. N. Cleland, and J. M. Martinis, *Physical Review Letters* **110**, 150502 (2013).
- [45] P. J. De Visser, D. J. Goldie, P. Diener, S. Withington, J. J. A. Baselmans, and T. M. Klapwijk, *Physical Review Letters* **112**, 047004 (2014).
- [46] X. Y. Jin, A. Kamal, A. P. Sears, T. Gudmundsen, D. Hover, J. Miloshi, R. Slattery, F. Yan, J. Yoder, T. P. Orlando, S. Gustavsson, and W. D. Oliver, *Physical Review Letters* **114**, 240501 (2015).
- [47] D. C. Mattis and J. Bardeen, *Physical Review* **111**, 412 (1958).
- [48] A. J. Annunziata, D. F. Santavicca, L. Frunzio, G. Catelani, M. J. Rooks, A. Frydman, and D. E. Prober, *Nanotechnology* **21**, 445202 (2010).

- [49] F. London, H. London, and F. A. Lindemann, *Proceedings of the Royal Society of London. Series A - Mathematical and Physical Sciences* **149**, 71 (1997).
- [50] I. Nsanzineza and B. L. T. Plourde, *Physical Review Letters* **113**, 117002 (2014).
- [51] F. Valenti, *Diagnostics and abatement of quasiparticle poisoning in superconducting quantum circuits*, Ph.D. thesis (2021).
- [52] C. Song, T. W. Heitmann, M. P. DeFeo, K. Yu, R. McDermott, M. Neeley, J. M. Martinis, and B. L. T. Plourde, *Physical Review B* **79**, 174512 (2009).
- [53] C. Kittel, *Introduction to Solid State Physics* (Wiley, 2004).
- [54] D. López-Núñez, Q. P. Montserrat, G. Rius, E. Bertoldo, A. Torras-Coloma, M. Martínez, and P. Forn-Díaz, “Magnetic penetration depth of Aluminum thin films,” (2023), arxiv:2311.14119 [cond-mat, physics:quant-ph] .
- [55] B. Josephson, *Physics Letters* **1**, 251 (1962).
- [56] R. Gross, A. Marx, and F. Deppe, *Applied Superconductivity: Josephson Effect and Superconducting Electronics*, De Gruyter Textbook (De Gruyter, 2016).
- [57] P. G. de Gennes and D. Saint-James, *Physics Letters* **4**, 151 (1963).
- [58] V. V. Shmidt and P. Müller, *The Physics of Superconductors: Introduction to Fundamentals and Applications* (Springer Science & Business Media, 1997).
- [59] C. Metzger, *Spin and Charge Effects in Andreev Bound States*, These de doctorat, université Paris-Saclay (2022).
- [60] G. E. Blonder, M. Tinkham, and T. M. Klapwijk, *Physical Review B* **25**, 4515 (1982).
- [61] P. F. Bagwell, *Physical Review B* **46**, 12573 (1992).
- [62] P. Virtanen, F. S. Bergeret, J. C. Cuevas, and T. T. Heikkilä, *Physical Review B* **83**, 144514 (2011).
- [63] L. Bretheau, Ç. Ö. Girit, M. Houzet, H. Pothier, D. Esteve, and C. Urbina, *Physical Review B* **90**, 134506 (2014).
- [64] R. Haller, G. Fülöp, D. Indolese, J. Ridderbos, R. Kraft, L. Y. Cheung, J. H. Ungerer, K. Watanabe, T. Taniguchi, D. Beckmann, R. Danneau, P. Virtanen, and C. Schönenberger, *Physical Review Research* **4**, 013198 (2022).
- [65] M. F. Goffman, R. Cron, A. Levy Yeyati, P. Joyez, M. H. Devoret, D. Esteve, and C. Urbina, *Physical Review Letters* **85**, 170 (2000).
- [66] C. Janvier, L. Tosi, L. Bretheau, Ç. Ö. Girit, M. Stern, P. Bertet, P. Joyez, D. Vion, D. Esteve, M. F. Goffman, H. Pothier, and C. Urbina, *Science* **349**, 1199 (2015).
- [67] C. W. J. Beenakker, *Physical Review Letters* **67**, 3836 (1991).



- 
- [68] H. J. Suominen, *Two-Dimensional Semiconductor-Superconductor Hybrids*, Ph.D. thesis, The Niels Bohr Institute, Faculty of Science, University of Copenhagen (2017).
- [69] M. Kjærgaard, *Proximity Induced Superconducting Properties in One and Two Dimensional Semiconductors: Towards Topological States of Matter*, Ph.D. thesis, The Niels Bohr Institute, Faculty of Science, University of Copenhagen (2015).
- [70] Y. V. Nazarov, *Physical Review Letters* **73**, 134 (1994).
- [71] C. W. J. Beenakker, *Reviews of Modern Physics* **69**, 731 (1997).
- [72] O. Dorokhov, *Solid State Communications* **51**, 381 (1984).
- [73] I. O. Kulik and A. N. Omel'yanchuk, *JETP Letters* **21**, 96 (1975).
- [74] T. T. Heikkilä, J. Särkkä, and F. K. Wilhelm, *Physical Review B* **66**, 184513 (2002).
- [75] M. Chauvin, P. vom Stein, H. Pothier, P. Joyez, M. E. Huber, D. Esteve, and C. Urbina, *Physical Review Letters* **97**, 067006 (2006).
- [76] F. Nichele, E. Portolés, A. Fornieri, A. M. Whiticar, A. C. C. Drachmann, S. Gronin, T. Wang, G. C. Gardner, C. Thomas, A. T. Hatke, M. J. Manfra, and C. M. Marcus, *Physical Review Letters* **124**, 226801 (2020).
- [77] L. Tosi, C. Metzger, M. F. Goffman, C. Urbina, H. Pothier, S. Park, A. L. Yeyati, J. Nygård, and P. Krogstrup, *Physical Review X* **9**, 011010 (2019).
- [78] M. Hays, V. Fatemi, K. Serniak, D. Bouman, S. Diamond, G. de Lange, P. Krogstrup, J. Nygård, A. Geresdi, and M. H. Devoret, *Nature Physics* **16**, 1103 (2020).
- [79] M. Hays, V. Fatemi, D. Bouman, J. Cerrillo, S. Diamond, K. Serniak, T. Connolly, P. Krogstrup, J. Nygård, A. Levy Yeyati, A. Geresdi, and M. H. Devoret, *Science* **373**, 430 (2021).
- [80] M. Wyss, K. Bagani, D. Jetter, E. Marchiori, A. Vovelaki, B. Gross, J. Riederbos, S. Gliga, C. Schönenberger, and M. Poggio, *Physical Review Applied* **17**, 034002 (2022).
- [81] M. D. Hutchings, J. B. Hertzberg, Y. Liu, N. T. Bronn, G. A. Keefe, M. Brink, J. M. Chow, and B. L. T. Plourde, *Physical Review Applied* **8**, 044003 (2017).
- [82] V. E. Manucharyan, J. Koch, L. I. Glazman, and M. H. Devoret, *Science* **326**, 113 (2009).
- [83] P. Winkel, I. Takmakov, D. Rieger, L. Planat, W. Hasch-Guichard, L. Grünhaupt, N. Maleeva, F. Foroughi, F. Henriques, K. Borisov, J. Ferrero, A. V. Ustinov, W. Wernsdorfer, N. Roch, and I. M. Pop, *Physical Review Applied* **13**, 024015 (2020).

- [84] N. E. Frattini, V. V. Sivak, A. Lingenfelter, S. Shankar, and M. H. Devoret, *Physical Review Applied* **10**, 054020 (2018).
- [85] J. Clarke and A. I. Braginski, eds., *The SQUID Handbook, Fundamentals and Technology of SQUIDs and SQUID Systems, Vol. I* (WILEY-VCH Verlag GmbH, Weinheim, Germany, 2004).
- [86] R. Haller, *Probing the Microwave Response of Novel Josephson Elements*, Thesis, University of Basel (2021).
- [87] M. L. Della Rocca, M. Chauvin, B. Huard, H. Pothier, D. Esteve, and C. Urbina, *Physical Review Letters* **99**, 127005 (2007).
- [88] I. Babich, A. Kudriashov, D. Baranov, and V. S. Stolyarov, *Nano Letters* **23**, 6713 (2023).
- [89] C. Ciaccia, R. Haller, A. C. C. Drachmann, T. Lindemann, M. J. Manfra, C. Schrade, and C. Schönenberger, *Physical Review Research* **5**, 033131 (2023).
- [90] T. W. Larsen, M. E. Gershenson, L. Casparis, A. Kringhøj, N. J. Pearson, R. P. G. McNeil, F. Kueemeth, P. Krogstrup, K. D. Petersson, and C. M. Marcus, *Physical Review Letters* **125**, 056801 (2020).
- [91] W. C. Smith, A. Kou, X. Xiao, U. Vool, and M. H. Devoret, *npj Quantum Information* **6**, 8 (2020).
- [92] S. Jebari, F. Blanchet, A. Grimm, D. Hazra, R. Albert, P. Joyez, D. Vion, D. Estève, F. Portier, and M. Hofheinz, *Nature Electronics* **1**, 223 (2018).
- [93] R. Haller, M. Osterwalder, G. Fülöp, J. Ridderbos, M. Jung, and C. Schönenberger, *Physical Review B* **108**, 094514 (2023).
- [94] M. Göppl, A. Fragner, M. Baur, R. Bianchetti, S. Filipp, J. M. Fink, P. J. Leek, G. Puebla, L. Steffen, and A. Wallraff, *Journal of Applied Physics* **104**, 113904 (2008).
- [95] U. Vool and M. Devoret, *International Journal of Circuit Theory and Applications* **45**, 897 (2017).
- [96] J. Koch, T. M. Yu, J. Gambetta, A. A. Houck, D. I. Schuster, J. Majer, A. Blais, M. H. Devoret, S. M. Girvin, and R. J. Schoelkopf, *Physical Review A* **76**, 042319 (2007).
- [97] A. Blais, R.-S. Huang, A. Wallraff, S. M. Girvin, and R. J. Schoelkopf, *Physical Review A* **69**, 062320 (2004).
- [98] P. Winkel, *Superconducting quantum circuits for hybrid architectures*, Ph.D. thesis (2020).
- [99] D. Willsch, D. Rieger, P. Winkel, M. Willsch, C. Dickel, J. Krause, Y. Ando, R. Lescanne, Z. Leghtas, N. T. Bronn, P. Deb, O. Lanes, Z. K. Mineev, B. Dening, S. Geisert, S. Günzler, S. Ihssen, P. Paluch, T. Reisinger, R. Hanna, J. H. Bae, P. Schüffegen, D. Grützmacher, L. Buimaga-Iarinca, C. Morari, W. Wernsdorfer, D. P. DiVincenzo, K. Michielsen, G. Catelani, and I. M. Pop, “Observation of Josephson Harmonics in Tunnel Junctions,” (2023), [arxiv:2302.09192](https://arxiv.org/abs/2302.09192) [cond-mat, physics:quant-ph] .

- 
- [100] T. W. Larsen, K. D. Petersson, F. Kuemmeth, T. S. Jespersen, P. Krogstrup, J. Nygård, and C. M. Marcus, *Physical Review Letters* **115**, 127001 (2015).
- [101] H. Zheng, L. Y. Cheung, N. Sangwan, A. Kononov, R. Haller, J. Ridderbos, C. Ciaccia, J. H. Ungerer, A. Li, E. P. A. M. Bakkers, A. Baumgartner, and C. Schönberger, “Coherent control of a few-channel hole type gatemon qubit,” (2023), [arxiv:2312.06411](https://arxiv.org/abs/2312.06411) [cond-mat, physics:quant-ph] .
- [102] L. Grünhaupt, M. Spiecker, D. Gusenkova, N. Maleeva, S. T. Skacel, I. Takmakov, F. Valenti, P. Winkel, H. Rotzinger, W. Wernsdorfer, A. V. Ustinov, and I. M. Pop, *Nature Materials* **18**, 816 (2019).
- [103] M. T. Bell, J. Paramanandam, L. B. Ioffe, and M. E. Gershenson, *Physical Review Letters* **112**, 167001 (2014).
- [104] S. Gladchenko, D. Olaya, E. Dupont-Ferrier, B. Douçot, L. B. Ioffe, and M. E. Gershenson, *Nature Physics* **5**, 48 (2009).
- [105] V. E. Manucharyan, E. Boaknin, M. Metcalfe, R. Vijay, I. Siddiqi, and M. Devoret, *Physical Review B* **76**, 014524 (2007).
- [106] G. Butseraen, A. Ranadive, N. Aparicio, K. Rafsanjani Amin, A. Juyal, M. Esposito, K. Watanabe, T. Taniguchi, N. Roch, F. Lefloch, and J. Renard, *Nature Nanotechnology* **17**, 1153 (2022).
- [107] J. Sarkar, K. V. Salunkhe, S. Mandal, S. Ghatak, A. H. Marchawala, I. Das, K. Watanabe, T. Taniguchi, R. Vijay, and M. M. Deshmukh, *Nature Nanotechnology* **17**, 1147 (2022).
- [108] G. Grynberg, A. Aspect, and C. Fabre, *Introduction to Quantum Optics: From the Semi-classical Approach to Quantized Light* (Cambridge University Press, Cambridge, 2010).
- [109] A. Miano, V. Joshi, G. Liu, W. Dai, P. Parakh, L. Frunzio, and M. Devoret, *PRX Quantum* **4**, 030324 (2023).
- [110] V. Sivak, N. Frattini, V. Joshi, A. Lingenfelter, S. Shankar, and M. Devoret, *Physical Review Applied* **11**, 054060 (2019).
- [111] A. Miano, G. Liu, V. V. Sivak, N. E. Frattini, V. R. Joshi, W. Dai, L. Frunzio, and M. H. Devoret, *Applied Physics Letters* **120** (2022).
- [112] S. G. Lachenmann, A. Förster, I. Friedrich, D. Uhlisch, T. Schäpers, A. Kastalsky, and A. A. Golubov, *Applied Superconductivity* **6**, 681 (1999).
- [113] M. Amado, A. Fornieri, F. Carillo, G. Biasiol, L. Sorba, V. Pellegrini, and F. Giazotto, *Physical Review B* **87**, 134506 (2013).
- [114] Z. Wan, A. Kazakov, M. J. Manfra, L. N. Pfeiffer, K. W. West, and L. P. Rokhinson, *Nature Communications* **6**, 7426 (2015).
- [115] F. Giazotto, K. Grove-Rasmussen, R. Fazio, F. Beltram, E. H. Linfield, and D. A. Ritchie, *Journal of Superconductivity* **17**, 317 (2004).

- [116] H. Takayanagi and T. Kawakami, *Phys. Rev. Lett.* **54**, 2449 (1985).
- [117] A. Richter, M. Koch, T. Matsuyama, and U. Merkt, *Superconductor Science and Technology* **12**, 874 (1999).
- [118] J. Nitta, T. Akazaki, H. Takayanagi, and K. Arai, *Phys. Rev. B* **46**, 14286 (1992).
- [119] H. Kroemer, C. Nguyen, and E. L. Hu, *Solid-State Electronics* **37**, 1021 (1994).
- [120] P. Krogstrup, N. L. B. Ziino, W. Chang, S. M. Albrecht, M. H. Madsen, E. Johnson, J. Nygård, C. M. Marcus, and T. S. Jespersen, *Nature Materials* **14**, 400 (2015).
- [121] W. Chang, S. M. Albrecht, T. S. Jespersen, F. Kuemmeth, P. Krogstrup, J. Nygård, and C. M. Marcus, *Nature Nanotechnology* **10**, 232 (2015).
- [122] R. Meservey and P. M. Tedrow, *Journal of Applied Physics* **42**, 51 (2003).
- [123] S. Kittiwatanakul, N. Anuniwat, N. Dao, S. A. Wolf, and J. Lu, *Journal of Vacuum Science & Technology A* **36**, 031507 (2018).
- [124] M. Sütő, T. Prok, P. Makk, M. Kirti, G. Biasiol, S. Csonka, and E. Tóvári, *Physical Review B* **106**, 235404 (2022).
- [125] E. Cheah, D. Z. Haxell, R. Schott, P. Zeng, E. Paysen, S. C. Ten Kate, M. Coraiola, M. Landstetter, A. B. Zadeh, A. Trampert, M. Sousa, H. Riel, F. Nichele, W. Wegscheider, and F. Krizek, *Physical Review Materials* **7**, 073403 (2023).
- [126] T. Zhang, T. Lindemann, G. C. Gardner, S. Gronin, T. Wu, and M. J. Manfra, *Physical Review Materials* **7**, 056201 (2023).
- [127] C. Baumgartner, L. Fuchs, A. Costa, S. Reinhardt, S. Gronin, G. C. Gardner, T. Lindemann, M. J. Manfra, P. E. Faria Junior, D. Kochan, J. Fabian, N. Paradiso, and C. Strunk, *Nature Nanotechnology* **17**, 39 (2022).
- [128] A. M. Whiticar, A. Fornieri, E. C. T. O'Farrell, A. C. C. Drachmann, T. Wang, C. Thomas, S. Gronin, R. Kallaher, G. C. Gardner, M. J. Manfra, C. M. Marcus, and F. Nichele, *Nature Communications* **11**, 3212 (2020).
- [129] M. C. Dartiailh, W. Mayer, J. Yuan, K. S. Wickramasinghe, A. Matos-Abiague, I. Žutić, and J. Shabani, *Physical Review Letters* **126**, 036802 (2021).
- [130] A. Banerjee, O. Lesser, M. A. Rahman, H.-R. Wang, M.-R. Li, A. Kringhøj, A. M. Whiticar, A. C. C. Drachmann, C. Thomas, T. Wang, M. J. Manfra, E. Berg, Y. Oreg, A. Stern, and C. M. Marcus, *Physical Review B* **107**, 245304 (2023).
- [131] A. Sammak, D. Sabbagh, N. W. Hendrickx, M. Lodari, B. Paquelet Wuetz, A. Tosato, L. Yeoh, M. Bollani, M. Virgilio, M. A. Schubert, P. Zaumseil, G. Capellini, M. Veldhorst, and G. Scappucci, *Advanced Functional Materials* **29**, 1807613 (2019).

- 
- [132] G. Scappucci, C. Kloeffel, F. A. Zwanenburg, D. Loss, M. Myronov, J.-J. Zhang, S. De Franceschi, G. Katsaros, and M. Veldhorst, *Nature Reviews Materials* **6**, 926 (2021).
- [133] N. W. Hendrickx, D. P. Franke, A. Sammak, M. Kouwenhoven, D. Sabbagh, L. Yeoh, R. Li, M. L. V. Tagliaferri, M. Virgilio, G. Capellini, G. Scappucci, and M. Veldhorst, *Nature Communications* **9**, 2835 (2018).
- [134] N. W. Hendrickx, M. L. V. Tagliaferri, M. Kouwenhoven, R. Li, D. P. Franke, A. Sammak, A. Brinkman, G. Scappucci, and M. Veldhorst, *Physical Review B* **99**, 075435 (2019).
- [135] A. M. Whiticar, *Flux Dependence of Topological Superconductivity in Two-Dimensional Heterostructures*, Ph.D. thesis, The Niels Bohr Institute, Faculty of Science, University of Copenhagen (2020).
- [136] M. Kjaergaard, H. J. Suominen, M. P. Nowak, A. R. Akhmerov, J. Shabani, C. J. Palmström, F. Nichele, and C. M. Marcus, *Physical Review Applied* **7**, 034029 (2017).
- [137] H. van Houten and C. W. J. Beenakker, *Physica B: Condensed Matter Analogies in Optics and Micro-Electronics*, **175**, 187 (1991).
- [138] S. Hart, Z. Cui, G. Ménard, M. Deng, A. E. Antipov, R. M. Lutchyn, P. Krogstrup, C. M. Marcus, and K. A. Moler, *Physical Review B* **100**, 064523 (2019).
- [139] A. Kringhøj, B. Van Heck, T. W. Larsen, O. Erlandsson, D. Sabonis, P. Krogstrup, L. Casparis, K. D. Petersson, and C. M. Marcus, *Physical Review Letters* **124**, 246803 (2020).
- [140] V. Chidambaram, A. Kringhøj, L. Casparis, F. Kuemmeth, T. Wang, C. Thomas, S. Gronin, G. C. Gardner, Z. Cui, C. Liu, K. Moors, M. J. Manfra, K. D. Petersson, and M. R. Connolly, *Physical Review Research* **4**, 023170 (2022).
- [141] M. C. Koops, G. V. van Duyneveldt, and R. de Bruyn Ouboter, *Physical Review Letters* **77**, 2542 (1996).
- [142] F. Capotondi, G. Biasiol, I. Vobornik, L. Sorba, F. Giazotto, A. Cavallini, and B. Fraboni, *Journal of Vacuum Science & Technology B: Microelectronics and Nanometer Structures Processing, Measurement, and Phenomena* **22**, 702 (2004).
- [143] D. Ercolani, G. Biasiol, E. Cancellieri, M. Rosini, C. Jacoboni, F. Carillo, S. Heun, L. Sorba, and F. Nolting, *Physical Review B* **77**, 235307 (2008).
- [144] A. Benali, P. Rajak, R. Ciancio, J. R. Plaisier, S. Heun, and G. Biasiol, *Journal of Crystal Growth* **593**, 126768 (2022).
- [145] C. B. Rogers, G. H. B. Thompson, and G. R. Antell, *Applied Physics Letters* **11**, 353 (1967).

- [146] S. Probst, F. B. Song, P. A. Bushev, A. V. Ustinov, and M. Weides, *Review of Scientific Instruments* **86**, 024706 (2015).
- [147] W. Buckel and R. Hilsch, *Zeitschrift für Physik* **138**, 109 (1954).
- [148] B. Abeles, R. W. Cohen, and G. W. Cullen, *Physical Review Letters* **17**, 632 (1966).
- [149] R. W. Cohen and B. Abeles, *Physical Review* **168**, 444 (1968).
- [150] G. Deutscher, H. Fenichel, M. Gershenson, E. Grünbaum, and Z. Ovadyahu, *Journal of Low Temperature Physics* **10**, 231 (1973).
- [151] N. Bachar, *Spin-Flip Scattering in Superconducting Granular Aluminum Films*, Ph.D. thesis (2014).
- [152] N. Bachar, S. Lerer, A. Levy, S. Hacoheh-Gourgy, B. Almog, H. Saadaoui, Z. Salman, E. Morenzoni, and G. Deutscher, *Physical Review B* **91**, 041123 (2015).
- [153] U. S. Pracht, T. Cea, N. Bachar, G. Deutscher, E. Farber, M. Dressel, M. Scheffler, C. Castellani, A. M. García-García, and L. Benfatto, *Physical Review B* **96**, 094514 (2017).
- [154] S. Avraham, S. Bachar, A. Glezer Moshe, E. Farber, and G. Deutscher, *Applied Physics Letters* **123**, 172601 (2023).
- [155] F. Levy-Bertrand, T. Klein, T. Grenet, O. Dupré, A. Benoît, A. Bideaud, O. Bourrion, M. Calvo, A. Catalano, A. Gomez, J. Goupy, L. Grünhaupt, U. V. Luepke, N. Maleeva, F. Valenti, I. M. Pop, and A. Monfardini, *Physical Review B* **99**, 094506 (2019).
- [156] F. Valenti, F. Henriques, G. Catelani, N. Maleeva, L. Grünhaupt, U. Von Lüpke, S. T. Skacel, P. Winkel, A. Bilmes, A. V. Ustinov, J. Goupy, M. Calvo, A. Benoît, F. Levy-Bertrand, A. Monfardini, and I. M. Pop, *Physical Review Applied* **11**, 054087 (2019).
- [157] L. Grünhaupt, N. Maleeva, S. T. Skacel, M. Calvo, F. Levy-Bertrand, A. V. Ustinov, H. Rotzinger, A. Monfardini, G. Catelani, and I. M. Pop, *Physical Review Letters* **121**, 117001 (2018).
- [158] D. Gusenkova, F. Valenti, M. Spiecker, S. Günzler, P. Paluch, D. Rieger, L.-M. Pioraş-Ţimbolmaş, L. P. Zârbo, N. Casali, I. Colantoni, A. Cruciani, S. Pirro, L. Cardani, A. Petrescu, W. Wernsdorfer, P. Winkel, and I. M. Pop, *Applied Physics Letters* **120**, 054001 (2022).
- [159] K. Borisov, D. Rieger, P. Winkel, F. Henriques, F. Valenti, A. Ionita, M. Wessbecher, M. Spiecker, D. Gusenkova, I. M. Pop, and W. Wernsdorfer, *Applied Physics Letters* **117**, 120502 (2020).
- [160] P. Winkel, K. Borisov, L. Grünhaupt, D. Rieger, M. Spiecker, F. Valenti, A. V. Ustinov, W. Wernsdorfer, and I. M. Pop, *Physical Review X* **10**, 031032 (2020).

- [161] D. Rieger, S. Günzler, M. Spiecker, P. Paluch, P. Winkel, L. Hahn, J. K. Hohmann, A. Bacher, W. Wernsdorfer, and I. M. Pop, *Nature Materials* **22**, 194 (2023).
- [162] N. A. Masluk, I. M. Pop, A. Kamal, Z. K. Mineev, and M. H. Devoret, *Physical Review Letters* **109**, 137002 (2012).
- [163] U. Vool, I. M. Pop, K. Sliwa, B. Abdo, C. Wang, T. Brecht, Y. Y. Gao, S. Shankar, M. Hatridge, G. Catelani, M. Mirrahimi, L. Frunzio, R. J. Schoelkopf, L. I. Glazman, and M. H. Devoret, *Physical Review Letters* **113**, 247001 (2014).
- [164] T. Weißl, B. Küng, E. Dumur, A. K. Feofanov, I. Matei, C. Naud, O. Buisson, F. W. J. Hekking, and W. Guichard, *Physical Review B* **92**, 104508 (2015).
- [165] C. Joshi, W. Chen, H. G. LeDuc, P. K. Day, and M. Mirhosseini, *Physical Review Applied* **18**, 064088 (2022).
- [166] P. C. J. J. Coumou, M. R. Zuiddam, E. F. C. Driessen, P. J. de Visser, J. J. A. Baselmans, and T. M. Klapwijk, *IEEE Transactions on Applied Superconductivity* **23**, 7500404 (2013).
- [167] C. X. Yu, S. Zihlmann, G. Troncoso Fernández-Bada, J.-L. Thomassin, F. Gustavo, É. Dumur, and R. Maurand, *Applied Physics Letters* **118**, 054001 (2021).
- [168] R. Gao, H.-S. Ku, H. Deng, W. Yu, T. Xia, F. Wu, Z. Song, M. Wang, X. Miao, C. Zhang, Y. Lin, Y. Shi, H.-H. Zhao, and C. Deng, *Advanced Materials* **34**, 2201268 (2022).
- [169] J. H. Ungerer, D. Sarmah, A. Kononov, J. Ridderbos, R. Haller, L. Y. Cheung, and C. Schönenberger, *EPJ Quantum Technology* **10**, 1 (2023).
- [170] M. Kjaergaard and C. University, *Proximity Induced Superconducting Properties in One and Two Dimensional Semiconductors*, Ph.D. thesis.
- [171] R. E. Neidert, S. C. Binari, and T. Weng, *Electronics Letters* **18**, 987 (1982).
- [172] T. Hong, K. Choi, K. Ik Sim, T. Ha, B. Cheol Park, H. Yamamori, and J. Hoon Kim, *Journal of Applied Physics* **114**, 243905 (2013).
- [173] T. C. Edwards, *Foundations for Microstrip Circuit Design* (Wiley, 1981).
- [174] L. Grünhaupt, “Granular aluminium superinductors,” <https://publikationen.bibliothek.kit.edu/1000097320> (2019).
- [175] M. Scigliuzzo, L. E. Bruhat, A. Bengtsson, J. J. Burnett, A. F. Roudsari, and P. Delsing, *New Journal of Physics* **22**, 053027 (2020).
- [176] A. Kou, W. C. Smith, U. Vool, I. M. Pop, K. M. Sliwa, M. Hatridge, L. Frunzio, and M. H. Devoret, *Physical Review Applied* **9**, 064022 (2018).
- [177] D. Zoepfl, P. R. Muppalla, C. M. F. Schneider, S. Kasemann, S. Partel, and G. Kirchmair, *AIP Advances* **7**, 085118 (2017).

- [178] S. J. Weber, K. W. Murch, D. H. Slichter, R. Vijay, and I. Siddiqi, *Applied Physics Letters* **98**, 172510 (2011).
- [179] S. E. de Graaf, L. Faoro, L. B. Ioffe, S. Mahashabde, J. J. Burnett, T. Lindström, S. E. Kubatkin, A. V. Danilov, and A. Ya. Tzalenchuk, *Science Advances* **6**, eabc5055 (2020).
- [180] N. Maleeva, L. Grünhaupt, T. Klein, F. Levy-Bertrand, O. Dupre, M. Calvo, F. Valenti, P. Winkel, F. Friedrich, W. Wernsdorfer, A. V. Ustinov, H. Rotzinger, A. Monfardini, M. V. Fistul, and I. M. Pop, *Nature Communications* **9**, 3889 (2018).
- [181] J. Burnett, L. Faoro, and T. Lindström, *Superconductor Science and Technology* **29**, 044008 (2016).
- [182] D. P. Pappas, M. R. Vissers, D. S. Wisbey, J. S. Kline, and J. Gao, *IEEE Transactions on Applied Superconductivity* **21**, 871 (2011).
- [183] E. M. Levenson-Falk, F. Kos, R. Vijay, L. Glazman, and I. Siddiqi, *Physical Review Letters* **112**, 047002 (2014).
- [184] A. Rothwarf and B. N. Taylor, *Physical Review Letters* **19**, 27 (1967).
- [185] I. M. Pop, K. Geerlings, G. Catelani, R. J. Schoelkopf, L. I. Glazman, and M. H. Devoret, *Nature* **508**, 369 (2014).
- [186] J. Aumentado, M. W. Keller, J. M. Martinis, and M. H. Devoret, *Physical Review Letters* **92**, 066802 (2004).
- [187] C. Wang, Y. Y. Gao, I. M. Pop, U. Vool, C. Axline, T. Brecht, R. W. Heeres, L. Frunzio, M. H. Devoret, G. Catelani, L. I. Glazman, and R. J. Schoelkopf, *Nature Communications* **5**, 5836 (2014).
- [188] A. Bespalov, M. Houzet, J. S. Meyer, and Y. V. Nazarov, *Physical Review Letters* **117**, 117002 (2016).
- [189] J. Gao, *The Physics of Superconducting Microwave Resonators*, Ph.D. thesis.
- [190] J. P. Turneaure, J. Halbritter, and H. A. Schwettman, *Journal of Superconductivity* **4**, 341 (1991).
- [191] L. Cardani, I. Colantoni, A. Cruciani, S. Di Domizio, M. Vignati, F. Bellini, N. Casali, M. G. Castellano, A. Coppolecchia, C. Cosmelli, and C. Tomei, *Applied Physics Letters* **107**, 093508 (2015).
- [192] C. X. Yu, S. Zihlmann, J. C. Abadillo-Uriel, V. P. Michal, N. Rambal, H. Niebojewski, T. Bedecarrats, M. Vinet, É. Dumur, M. Filippone, B. Bertrand, S. De Franceschi, Y.-M. Niquet, and R. Maurand, *Nature Nanotechnology* **18**, 741 (2023).
- [193] T. H. Kikkeler, A. A. Golubov, and F. S. Bergeret, *Physical Review B* **106**, 214504 (2022).



- 
- [194] Y. Zhang, Y. Gu, P. Li, J. Hu, and K. Jiang, *Physical Review X* **12**, 041013 (2022).
- [195] A. A. Golubov, M. Yu. Kupriyanov, and E. Il'ichev, *Reviews of Modern Physics* **76**, 411 (2004).
- [196] M. L. DellaRocca, M. Chauvin, B. Huard, H. Pothier, D. Esteve, and C. Urbina, *Physical Review Letters* **99**, 127005 (2007).
- [197] A. I. Buzdin, L. N. Bulaevskii, and S. V. Panyukov, *JETP Letters* **35**, 178 (1982).
- [198] A. Buzdin, *JEPT Letters* **78**, 583 (2003).
- [199] V. V. Ryazanov, V. A. Oboznov, A. Yu. Rusanov, A. V. Veretennikov, A. A. Golubov, and J. Aarts, *Physical Review Letters* **86**, 2427 (2001).
- [200] T. Kontos, M. Aprili, J. Lesueur, F. Genêt, B. Stephanidis, and R. Boursier, *Physical Review Letters* **89**, 137007 (2002).
- [201] E. C. Gingrich, B. M. Niedzielski, J. A. Glick, Y. Wang, D. L. Miller, R. Loloee, W. P. P. Jr, and N. O. Birge, *Nature Physics* **12**, 564 (2016).
- [202] H. Sickinger, A. Lipman, M. Weides, R. G. Mints, H. Kohlstedt, D. Koelle, R. Kleiner, and E. Goldobin, *Physical Review Letters* **109**, 107002 (2012).
- [203] I. V. Krive, L. Y. Gorelik, R. I. Shekhter, and M. Jonson, *Low Temperature Physics* **30**, 398 (2004).
- [204] A. A. Reynoso, G. Usaj, C. A. Balseiro, D. Feinberg, and M. Avignon, *Physical Review Letters* **101**, 107001 (2008).
- [205] A. Buzdin, *Physical Review Letters* **101**, 107005 (2008).
- [206] A. Zazunov, R. Egger, T. Jonckheere, and T. Martin, *Physical Review Letters* **103**, 147004 (2009).
- [207] T. Yokoyama, M. Eto, and Y. V. Nazarov, *Journal of the Physical Society of Japan* **82**, 054703 (2013).
- [208] R. Wakatsuki, Y. Saito, S. Hoshino, Y. M. Itahashi, T. Ideue, M. Ezawa, Y. Iwasa, and N. Nagaosa, *Science Advances* **3** (2017), 10.1126/sciadv.1602390.
- [209] B. Turini, S. Salimian, M. Carrega, A. Iorio, E. Strambini, F. Gia-zotto, V. Zannier, L. Sorba, and S. Heun, *Nano Letters* **22** (2022), 10.1021/acs.nanolett.2c02899.
- [210] D. B. Szombati, S. Nadj-Perge, D. Car, S. R. Plissard, E. P. A. M. Bakkers, and L. P. Kouwenhoven, *Nature Physics* **12**, 568 (2016).
- [211] G. L. J. A. Rikken, J. Fölling, and P. Wyder, *Physical Review Letters* **87**, 236602 (2001).
- [212] G. L. J. A. Rikken and P. Wyder, *Physical Review Letters* **94**, 016601 (2005).

- [213] F. Ando, Y. Miyasaka, T. Li, J. Ishizuka, T. Arakawa, Y. Shiota, T. Moriyama, Y. Yanase, and T. Ono, *Nature* **584**, 373 (2020).
- [214] A. Daido, Y. Ikeda, and Y. Yanase, *Physical Review Letters* **128**, 037001 (2022).
- [215] L. Bauriedl, C. Bäuml, L. Fuchs, C. Baumgartner, N. Paulik, J. M. Bauer, K.-Q. Lin, J. M. Lupton, T. Taniguchi, K. Watanabe, C. Strunk, and N. Paradiso, *Nature Communications* **13** (2022), [10.1038/s41467-022-31954-5](https://doi.org/10.1038/s41467-022-31954-5).
- [216] H. Narita, J. Ishizuka, R. Kawarazaki, D. Kan, Y. Shiota, T. Moriyama, Y. Shimakawa, V. A. Ognev, A. S. Samardak, Y. Yanase, and T. Ono, *Nature Nanotechnology* **17**, 823 (2022).
- [217] K.-R. Jeon, J.-K. Kim, J. Yoon, J.-C. Jeon, H. Han, A. Cottet, T. Kontos, and S. P. Parkin, *Nature Materials* **21**, 1211 (2022).
- [218] H. Wu, Y. Wang, Y. Xu, P. K. Sivakumar, C. Pasco, U. Filippozzi, S. S. P. Parkin, Y.-J. Zeng, T. McQueen, and M. N. Ali, *Nature* **604**, 653 (2022).
- [219] J.-X. Lin, P. Siriviboon, H. D. Scammell, S. Liu, D. Rhodes, K. Watanabe, T. Taniguchi, J. Hone, M. S. Scheurer, and J. I. A. Li, *Nature Physics* **18**, 1221 (2022).
- [220] J. Diez-Merida, A. Diez-Carlon, S. Y. Yang, Y.-M. Xie, X.-J. Gao, J. Senior, K. Watanabe, T. Taniguchi, X. Lu, A. P. Higginbotham, K. T. Law, and D. K. Efetov, *Nature Communications* **14**, 2396 (2023).
- [221] N. F. Q. Yuan and L. Fu, *Proceedings of the National Academy of Sciences of the United States of America* **119** (2022), [10.1073/pnas.2119548119](https://doi.org/10.1073/pnas.2119548119).
- [222] M. Davydova, S. Prembabu, and L. Fu, *Science Advances* **8** (2022), [10.1126/sciadv.abo0309](https://doi.org/10.1126/sciadv.abo0309).
- [223] D. Suri, A. Kamra, T. N. G. Meier, M. Kronseder, W. Belzig, C. H. Back, and C. Strunk, *Applied Physics Letters* **121**, 102601 (2022).
- [224] B. Pal, A. Chakraborty, P. K. Sivakumar, M. Davydova, A. K. Gopi, A. K. Pandeya, J. A. Krieger, Y. Zhang, M. Date, S. Ju, N. Yuan, N. B. M. S. L. Fu, and S. S. P. Parkin, *Nature Physics* **18**, 1228 (2022).
- [225] M. Trahms, L. Melischek, J. F. Steiner, B. Mahendru, I. Tamir, N. Bogdanoff, O. Peters, G. Reecht, C. B. Winkelmann, and F. von Oppen and K. J. Franke, *Nature* **615**, 628 (2023).
- [226] C.-Z. Chen, J. J. He, M. N. Ali, G.-H. Lee, K. C. Fong, and K. T. Law, *Physical Review B* **98**, 075430 (2018).
- [227] A. Kononov, G. Abulizi, K. Qu, J. Yan, D. Mandrus, K. Watanabe, T. Taniguchi, and C. Schönenberger, *Nano Letters* **20**, 4228 (2020).
- [228] H. F. Legg, D. Loss, and J. Klinovaja, *Physical Review B* **106**, 104501 (2022).

- 
- [229] J. J. Cuzzo, W. Pan, J. Shabani, and E. Rossi, arXiv:2303.16931 (2023), 10.48550/arXiv.2303.16931.
- [230] T. A. Fulton and R. C. Dynes, *Physical Review Letters* **25**, 794 (1970).
- [231] T. A. Fulton, L. N. Dunkleberger, and R. C. Dynes, *Physical Review B* **6**, 855 (1972).
- [232] W.-T. Tsang and T. V. Duzer, *Journal of Applied Physics* **46**, 4573 (1975).
- [233] A. Barone and G. Paterno, *Physics and Applications of the Josephson Effect* (John Wiley & Sons, New York, 1982).
- [234] M. R. Buitelaar, T. Nussbaumer, and C. Schönberger, *Physical Review Letters* **89**, 256801 (2002).
- [235] Y.-J. Doh, J. A. van Dam, A. L. Roest, E. P. A. M. Bakkers, L. P. Kouwenhoven, and S. D. Franceschi, *Science (New York, N.Y.)* **309**, 272 (2005).
- [236] E. Prada, P. San-Jose, M. W. A. de Moor, A. Geresdi, E. J. H. Lee, J. Klinovaja, D. Loss, J. Nygård, R. Aguado, and L. P. Kouwenhoven, *Nature Reviews Physics* **2**, 575 (2020).
- [237] G. Burkard, M. J. Gullans, X. Mi, and J. R. Petta, *Nature Reviews Physics* **2**, 129 (2020).
- [238] Ya. V. Fominov and D. S. Mikhailov, *Physical Review B* **106**, 134514 (2022).
- [239] J. S. Lee, B. Shojaei, M. Pendharkar, M. Feldman, K. Mukherjee, and C. J. Palmstrøm, *Physical Review Materials* **3**, 014603 (2019).
- [240] G. Nanda, J. L. Aguilera-Servin, P. Rakyta, A. Kormányos, R. Kleiner, D. Koelle, K. Watanabe, T. Taniguchi, L. M. K. Vandersypen, and S. Goswami, *Nano Letters* **17**, 3396 (2017).
- [241] L. Bretheau, J. I.-J. Wang, R. Pisoni, K. Watanabe, T. Taniguchi, and P. Jarillo-Herrero, *Nature Physics* **13**, 756 (2017).
- [242] D. A. Manjarrés, S. G. Páez, and W. J. Herrera, *Physical Review B* **101**, 064503 (2020).
- [243] D. I. Indolese, P. Karnatak, A. Kononov, R. Delagrangé, R. Haller, L. Wang, P. Makk, K. Watanabe, T. Taniguchi, and C. Schönberger, *Nano Letters* **20**, 7129 (2020).
- [244] C. D. Tesche and J. Clarke, *Journal of Low Temperature Physics* **29**, 301 (1977).
- [245] C. Granata and A. Vettoliere, *Physics Reports* **614**, 1 (2016).
- [246] F. Paolucci, G. D. Simoni, and F. Giazotto, *Applied Physics Letters* **122**, 042601 (2023).
- [247] M. Gupta, G. V. Graziano, M. Pendharkar, J. T. Dong, C. P. Dempsey, C. Palmstrøm, and V. S. Pribiag, *Nature Communications* **14**, 3078 (2023).

- [248] M. Valentini, O. Sagi, L. Baghumyan, T. de Gijssel, J. Jung, S. Calcaterra, A. Ballabio, J. A. Servin, K. Aggarwal, M. Janik, T. Adletzberger, R. S. Souto, M. Leijnse, J. Danon, C. Schrade, E. Bakkers, D. Chrastina, G. Isella, and G. Katsaros, “Radio frequency driven superconducting diode and parity conserving Cooper pair transport in a two-dimensional germanium hole gas,” (2023), [arxiv:2306.07109 \[cond-mat\]](#) .
- [249] C. Ciaccia, R. Haller, A. C. C. Drachmann, T. Lindemann, M. J. Manfra, C. Schrade, and C. Schönenberger, “Charge-4e supercurrent in a two-dimensional InAs-Al superconductor-semiconductor heterostructure,” (2023), [arxiv:2306.05467 \[cond-mat\]](#) .
- [250] A. Wallraff, D. I. Schuster, A. Blais, L. Frunzio, R.-. S. Huang, J. Majer, S. Kumar, S. M. Girvin, and R. J. Schoelkopf, *Nature* **431**, 162 (2004).
- [251] F. Arute, K. Arya, R. Babbush, D. Bacon, J. C. Bardin, R. Barends, R. Biswas, S. Boixo, F. G. S. L. Brandao, D. A. Buell, *et al.*, *Nature* **574**, 505 (2019).
- [252] J. Clarke and F. K. Wilhelm, *Nature* **453**, 1031 (2008).
- [253] M. A. Castellanos-Beltran and K. W. Lehnert, *Applied Physics Letters* **91** (2007), [10.1063/1.2773988](#).
- [254] S. Krinner *et al.*, *Nature* **605**, 669 (2022).
- [255] N. E. Frattini, U. Vool, S. Shankar, A. Narla, K. M. Sliwa, and M. H. Devoret, *Applied Physics Letters* **110** (2017).
- [256] N. E. Frattini, V. V. Sivak, A. Lingenfelter, S. Shankar, and M. H. Devoret, *Physical Review Applied* **10**, 054020 (2018).
- [257] E. M. Spanton, M. Deng, S. Vaitiekėnas, P. Krogstrup, J. Nygård, C. M. Marcus, and K. A. Moler, *Nature Physics* **13**, 1177 (2017).
- [258] M. Endres, A. Kononov, H. S. Arachchige, J. Yan, D. Mandrus, K. Watanabe, T. Taniguchi, and C. Schönenberger, *Nano Letters* **23**, 4654 (2023).
- [259] M. J. A. Stoutimore, A. N. Rossolenko, V. V. Bolginov, V. A. Oboznov, A. Y. Rusanov, D. S. Baranov, N. Pugach, S. M. Frolov, V. V. Ryazanov, and D. J. Van Harlingen, *Physical Review Letters* **121**, 177702 (2018).
- [260] L. B. Ioffe and M. V. Feigel’man, *Physical Review B* **66**, 224503 (2002).
- [261] B. Douççot and J. Vidal, *Physical Review Letters* **88**, 227005 (2002).
- [262] P. Brooks, A. Kitaev, and J. Preskill, *Physical Review A: Atomic, Molecular, and Optical Physics* **87**, 052306 (2013).
- [263] P. Groszkowski, A. D. Paolo, A. L. Grimsmo, A. Blais, D. I. Schuster, A. A. Houck, and J. Koch, *New Journal of Physics* **20**, 043053 (2018).
- [264] A. D. Paolo, A. L. Grimsmo, P. Groszkowski, J. Koch, and A. Blais, *New Journal of Physics* **21**, 043002 (2019).

- [265] A. Maiani, M. Kjaergaard, and C. Schrade, *PRX Quantum* **3**, 030329 (2022).
- [266] C. Leroux and A. Blais, “Cat-qubit-inspired gate on  $\cos(2\theta)$  qubits,” (2023), [arxiv:2304.02155](https://arxiv.org/abs/2304.02155) [quant-ph] .
- [267] I. M. Pop, K. Hasselbach, O. Buisson, W. Guichard, B. Pannetier, and I. Protopopov, *Physical Review B* **78**, 104504 (2008).
- [268] M. Kjaergaard, F. Nichele, H. J. Suominen, M. P. Nowak, M. Wimmer, A. R. Akhmerov, J. A. Folk, K. Flensberg, J. Shabani, C. J. Palmstrøm, *et al.*, *Nature Communications* **7**, 12841 (2016).
- [269] J. Basset, M. Kuzmanović, P. Virtanen, T. T. Heikkilä, J. Estève, J. Gabelli, C. Strunk, and M. Aprili, **1**, 032009 (2019).
- [270] R. Haller, *Probing the Microwave Response of Novel Josephson Elements*, Ph.D. thesis, University of Basel, Basel (2021).
- [271] D. Z. Haxell, E. Cheah, F. Krížek, R. Schott, M. F. Ritter, M. Hinderling, W. Belzig, C. Bruder, W. Wegscheider, H. Riel, and F. Nichele, *Physical Review Letters* **130**, 087002 (2023).
- [272] SIDNEY. SHAPIRO, A. R. JANUS, and SANDOR. HOLLY, *Reviews of Modern Physics* **36**, 223 (1964).
- [273] B. Raes, N. Tubsrinuan, R. Sreedhar, D. S. Guala, R. Panghotra, H. Dausy, C. C. de Souza Silva, and J. Van de Vondel, *Physical Review B* **102**, 054507 (2020).
- [274] K. Ueda, S. Matsuo, H. Kamata, Y. Sato, Y. Takeshige, K. Li, L. Samuelson, H. Xu, and S. Tarucha, **2**, 033435 (2020).
- [275] A. Iorio, A. Crippa, B. Turini, S. Salimian, M. Carrega, L. Chirrolli, V. Zannier, L. Sorba, E. Strambini, F. Giazotto, and S. Heun, **5**, 033015 (2023).
- [276] M. Valentini, O. Sagi, L. Baghumyan, T. de Gijssel, J. Jung, S. Calcaterra, A. Ballabio, J. A. Servin, K. Aggarwal, M. Janik, T. Adletzberger, R. S. Souto, M. Leijnse, J. Danon, C. Schrade, E. Bakkers, D. Chrastina, G. Isella, and G. Katsaros, “Radio frequency driven superconducting diode and parity conserving Cooper pair transport in a two-dimensional germanium hole gas,” (2023), [arxiv:2306.07109](https://arxiv.org/abs/2306.07109) [cond-mat.mes-hall] .
- [277] V. E. Manucharyan, J. Koch, L. I. Glazman, and Michel H. Devoret, *Science (New York, N.Y.)* **326**, 113 (2009).
- [278] L. B. Nguyen, Y.-H. Lin, A. Somoroff, R. Mencia, N. Grabon, and V. E. Manucharyan, *Physical Review X* **9**, 041041 (2019).
- [279] T. M. Hazard, A. Gyenis, A. Di Paolo, A. T. Asfaw, S. A. Lyon, A. Blais, and A. A. Houck, *Physical Review Letters* **122**, 010504 (2019).
- [280] A. Somoroff, Q. Ficheux, R. A. Mencia, H. Xiong, R. V. Kuzmin, and V. E. Manucharyan, “Millisecond coherence in a superconducting qubit,” (2021), [arxiv:2103.08578](https://arxiv.org/abs/2103.08578) [quant-ph] .

- [281] S. Hoffman, C. Schrade, J. Klinovaja, and D. Loss, *Physical Review B* **94**, 045316 (2016).
- [282] M. J. Rañčić, S. Hoffman, C. Schrade, J. Klinovaja, and D. Loss, *Physical Review B* **99**, 165306 (2019).
- [283] C. Schrade and L. Fu, *Physical Review Letters* **121**, 267002 (2018).
- [284] C. Schrade and L. Fu, *Physical Review Letters* **129**, 227002 (2022).
- [285] L. A. Landau, S. Plugge, E. Sela, A. Altland, S. M. Albrecht, and R. Egger, *Physical Review Letters* **116**, 050501 (2016).
- [286] S. Plugge, A. Rasmussen, R. Egger, and K. Flensberg, *New Journal of Physics* **19**, 012001 (2017).
- [287] T. Karzig, C. Knapp, R. M. Lutchyn, P. Bonderson, M. B. Hastings, C. Nayak, J. Alicea, K. Flensberg, S. Plugge, Y. Oreg, *et al.*, *Physical Review B* **95**, 235305 (2017).
- [288] J. G. Hoffman, *Physics Today* **15**, 30 (1962).
- [289] N. E. Frattini, *Three-Wave Mixing in Superconducting Circuits: Stabilizing Cats with SNAILs*, Ph.D. thesis, Yale University, United States – Connecticut (2021).
- [290] J. H. Ungerer, A. Pally, A. Kononov, S. Lehmann, J. Ridderbos, P. P. Potts, C. Thelander, K. A. Dick, V. F. Maisi, P. Scarlino, A. Baumgartner, and C. Schönberger, “Strong coupling between a microwave photon and a singlet-triplet qubit,” (2023), [arxiv:2303.16825](https://arxiv.org/abs/2303.16825) [cond-mat, physics:quant-ph] .
- [291] J. Shabani, S. Das Sarma, and C. J. Palmstrøm, *Physical Review B* **90**, 161303 (2014).

# A Extended Setup - grAl on InP

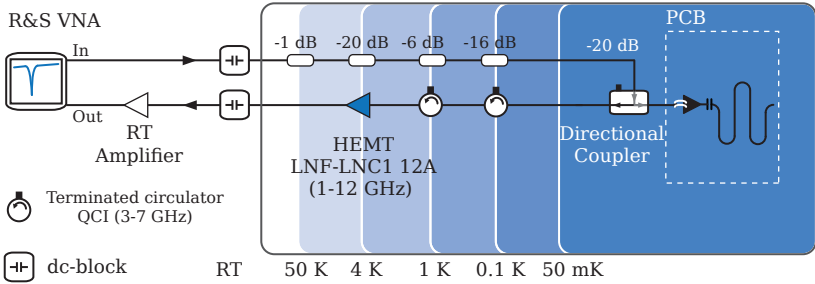


**Figure A.1.** Detailed measurement setup of granular aluminium resonators in a Triton 200 dilution cryostat.

Figure A.1 shows the measurement setup used to characterize granular aluminium resonators on a InP substrate as discussed in Chapter 5.

The chip is mounted on a double-sided Ni/Au plated Roger<sup>®</sup> 4350 PCB screwed onto a copper plate. The device is glued onto the central copper area such that the microwave bond terminals are as close as possible to the PCB counterpart. The PCB central conductor is bonded to the resonator input pad.

Readout rf signals are produced and measured with either a R&S vector network analyser. The input signal is attenuated by a total of  $-63$  dB attenuation before reaching the PCB. It is connected to the coupling port of a directional coupler which then feeds the reflected signal to the amplification chain. The amplification chain consists of a cryogenic HEMT amplifier (nominally  $+40$  dB gain) located on the 4K stage isolated from the device with two terminated circulators. The signal is further amplified with a room temperature amplifier (nominally  $+40$  dB gain). Signals are produced and measured with a R&S vector network analyser.

A magnetic field can be applied with a 3-axis vector magnet. Measurements

are performed in a Triton 200 dilution refrigerator with a base temperature of  $\sim 50$  mK.

A



# B Gate Tunable JD - Supplementary

---

## B.1. Fabrication & Measurement Set-up

The wafer used in this experiment was grown by molecular beam epitaxy (MBE). The stack consists from bottom to top of an InP substrate, a 1- $\mu\text{m}$ -thick buffer realized with  $\text{In}_{1-x}\text{Al}_x\text{As}$  alloys, a 4 nm  $\text{In}_{0.75}\text{Ga}_{0.25}\text{As}$  bottom barrier, a 7 nm InAs layer, a 10 nm  $\text{In}_{0.75}\text{Ga}_{0.25}\text{As}$  top barrier, two monolayers of GaAs acting as stop etch layer, and 10 nm of Al deposited *in situ* without breaking the MBE vacuum. The two-dimensional electron gas is characterized from a Hall bar devices and shows a peak electron mobility of  $\mu = 12'000 \text{ cm}^2\text{V}^{-1}\text{s}^{-1}$  for an electron density of  $16 \times 10^{11} \text{ cm}^{-2}$ , corresponding to an electron mean free path of  $l_e \approx 230 \text{ nm}$ .

The device is fabricated using standard electron beam lithography techniques. The MESA is electrically isolated by first removing the top Al film with Al etchant Transene D, followed by a deep III-V chemical wet etch with  $\text{H}_2\text{O}:\text{C}_6\text{H}_8\text{O}_7:\text{H}_3\text{PO}_4:\text{H}_2\text{O}_2$  (220:55:3:3). Next, the Al film on the mesa is selectively etched with Al etchant Transene D to define the planar JJ. Electrostatic gates are made of two Ti/Au layers, isolated from the Al and from each other by hafnium oxide ( $\text{HfO}_2$ ) layers grown by atomic layer deposition (ALD) at a temperature of 90 °C over the entire sample. The first layer of gates is made of electron-beam evaporated Ti/Au (5 nm/25 nm) on top of 15 nm  $\text{HfO}_2$ . Connections to the external circuit are obtained by evaporating Ti/Au (5/85 nm) leads at  $\pm 17^\circ$  to overcome the MESA step. A second layer of gates, made of angle-evaporated Ti/Au (5/85 nm), is patterned on top of 25 nm of  $\text{HfO}_2$ .

Measurements are carried out in a Triton 200 cryogen-free dilution refrigerator with a base temperature of  $\approx 50 \text{ mK}$ . An overview of the measurement set-up is shown in Fig. B.1. The setup sources a current using a 1 M $\Omega$  resistor in series to a dc voltage source on which a small ac component with frequency  $f = 17.7 \text{ Hz}$ , supplied by a lock-in amplifier, is superposed. This current is applied to the source contact of the SQUID on the left with the drain contact on the right side galvanically connected to ground. The SQUID is shunted at the source to ground with a resistor  $R_S = 10 \Omega$ . This shunt resistor is directly

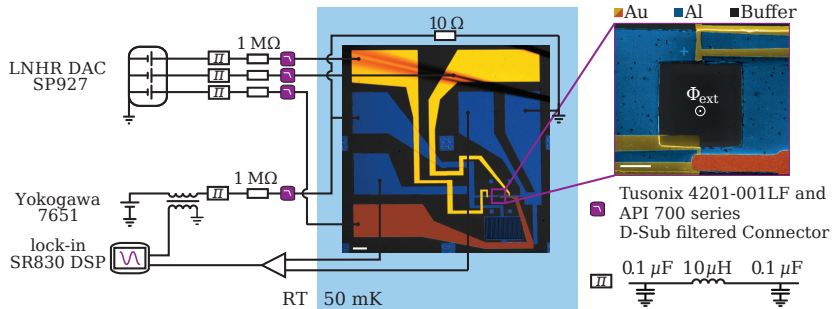


**Figure B.1.** (a) False color optical image of the full device together with a sketch of the measurement setup. The scale bar is  $100 \mu\text{m}$ . (b) Zoom-in over the SQUID showing the loop area threaded by the external flux  $\Phi_{\text{ext}}$ . The electron density in the junction region is tuned via a set of gates coloured in yellow and brown. The scale bar is  $3 \mu\text{m}$

placed on the sample holder. In addition, a finger capacitance of  $\approx 0.7 \text{ pF}$  is patterned in parallel to the SQUID (lower right of the optical image). The original purpose of the capacitance was to increase the quality factor of the Josephson junctions. However, its effect is negligible, since the capacitance provided by the leads is larger. We measure the differential resistance of the shunted device using a voltage amplifier and lock-in techniques. The flux through the SQUID is generated by a vector magnet.

## B.2. Estimation of Loop Inductances

In the following we will detail the evaluation of the inductance of the loop branches. The loop geometry is defined as indicated by the white dashed lines in Fig. B.2(a). The width of the two branches corresponds to the junctions width in the upper and lower path,  $W_1 = 3 \mu\text{m}$ ,  $W_2 = 2.5 \mu\text{m}$ , and the width on the left and right sides it is set equal to  $W_L = (W_1 + W_2)/2 = 2.75 \mu\text{m}$ . In reality there is no lateral confinement in the superconductor. Hence, the artificial confinement increases the inductance values so that the simulated inductances for this geometry yield upper bounds to the inductances of the device. With finite-element simulations performed in Sonnet, we compute the two-port impedances  $Z_{i,k}$  with  $i,k \in \{1,2\}$  for different frequencies. The impedance is evaluated between two sets of floating co-calibrated ports, positioned on the left and right side of the loop. In the simulation we use InP as a substrate, with a relative dielectric constant  $\epsilon_r = 12.55$  [171]. The kinetic in-

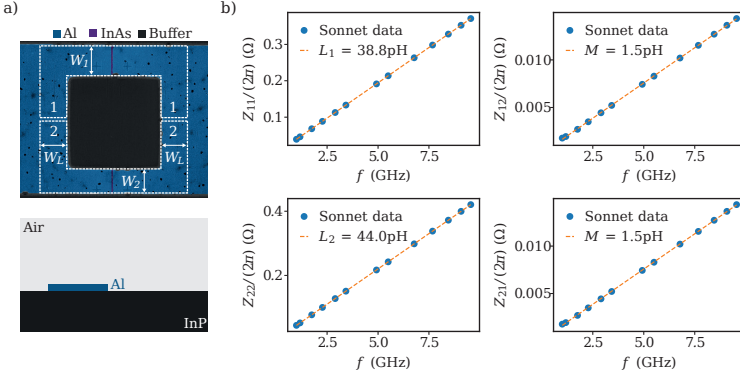


**Figure B.2.** Sonnet simulations of the loop inductances. The superconducting loop is segmented into an upper (lower) branch 1 (2) indicated by the white dashed boxes. The respective widths are  $W_1 = 3 \mu\text{m}$ ,  $W_2 = 2.5 \mu\text{m}$  and  $W_L = 2.75 \mu\text{m}$ . The two inductances  $L_1$ ,  $L_2$  and the mutual inductance  $M$  are deduced from the slope of the frequency dependent two-port impedances. It is seen that  $M \ll L_{1,2}$  and that there is a small asymmetry of  $\sim 6\%$  in the loop inductances.

ductance of the Al film is evaluated by measuring the temperature dependence of the resistance of an Al bar realized on a different chip from the same wafer. We measure a critical temperature of 1.25 K and a normal state resistance of  $15.5 \Omega$ . The kinetic sheet inductance  $L_{\text{kin}/\square} \approx 5 \text{ pH}$  is then obtained through Eq. (2.17).

### B.3. Retrapping versus Switching Current

In Fig. B.3 we compare the switching current with the retrapping current values. We show that the two values coincide in this experiment to a good accuracy. We think that this is due to the low parallel resistor which keeps the voltage over the junction small in the normal state, hence, reducing overheating effects. Additionally, the shunt resistor adds damping at the plasma frequency of the junctions, which reduces the quality factor.

The two measurements in Fig. B.3(a) were obtained for exactly the same parameter settings, except for the direction of current-bias sweep. In the upper (lower) measurement the current was decreased (increased) starting with positive (negative) values at  $+3 \mu\text{A}$  ( $-3 \mu\text{A}$ ) and sweeping down (up) to  $-3 \mu\text{A}$  ( $+3 \mu\text{A}$ ). (b) shows the critical and retrapping current,  $I_c$  and  $I_r$ , extracted from the downsweep data at positions where the differential resistance shows a

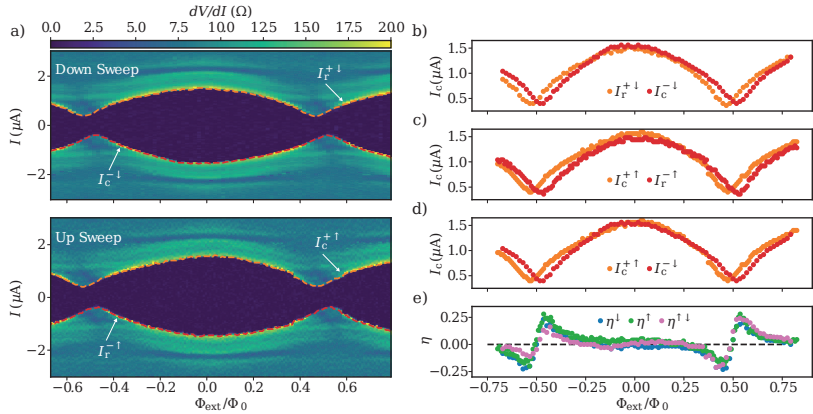


**Figure B.3.** (a) Two differential resistance plots of the SQUID device for the same gate settings as a function of external flux  $\Phi_{\text{ext}}$  and current bias  $I$ . In the upper plot the current was swept downwards from positive to negative values, while in the lower it was swept upwards. (b) and (c) compare the critical current values  $I_c$  with the re trapping ones  $I_r$ , obtained from (a) and (b) at the position of the peaks in  $dV/dI$ . The arrows  $\uparrow, \downarrow$  indicate the sweep direction. (d) compares  $I_c^{\uparrow}$  with  $I_c^{\downarrow}$  and in (e) the diode efficiency is shown for three ways using the data in (b)-(d).

peak. (c) shows the same, but extracted from the upsweep data. On sweeping downwards, we denote the negative critical current as  $I_c^{\downarrow}$  and the positive re trapping current as  $I_r^{\downarrow}$ . In analogy, on sweeping upwards, the positive critical current is denoted by  $I_c^{\uparrow}$  and the negative re trapping current by  $I_r^{\uparrow}$ . In (d) we compare the positive and negative critical currents, both obtained in a proper way using opposite sweep directions.

Now we can compare the extracted diode efficiency for three cases: i) for the case when we extract the critical currents from sweeping the current bias into negative direction only,  $\eta^\downarrow$ , ii) into positive direction only,  $\eta^\uparrow$ , and iii), when we deduce the critical current properly,  $\eta^{\uparrow\downarrow}$ . The three curves are directly obtained from the graphs (b)-(d). All three methods yield qualitatively the same efficiencies with no significant differences. Importantly, one clearly cannot say that  $\eta^{\uparrow\downarrow}$  would yield in general lower efficiencies.

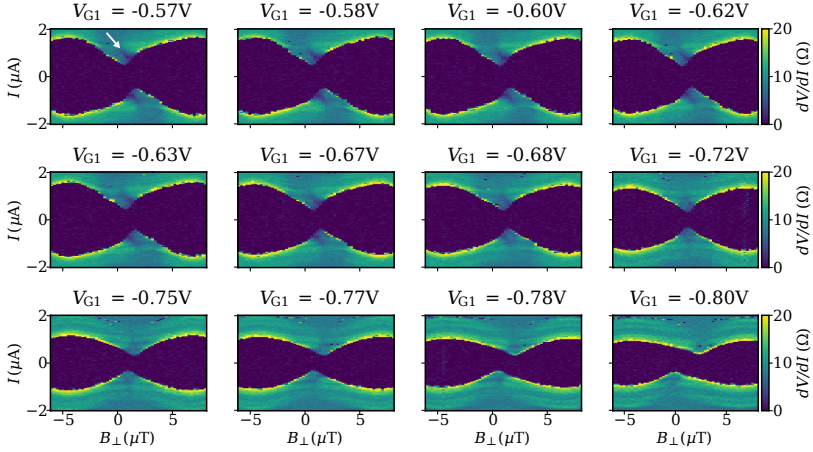


**Figure B.4.** SQUID oscillation at different gate voltage configurations.  $V_{G2}$  is fixed at  $-0.5$  V, while  $V_{G1}$  is swept from  $-0.57$  V to  $-0.8$  V. The asymmetry in the SQUID oscillations follows the asymmetry in critical current between the two junctions. We have  $I_{c1}(V_{G1} = -0.57 \text{ V}) > I_{c2}(V_{G2} = -0.5 \text{ V})$  and  $I_{c1}(V_{G1} = -0.8 \text{ V}) < I_{c2}(V_{G2} = -0.5 \text{ V})$ .

## B.4. SQUID Oscillations at Different Gate Voltages

In this appendix we show how the SQUID pattern develops when the critical current of one junction is tuned from being larger, equal and finally smaller than the critical current of the other junction. Fig. B.4 shows the differential resistance of the SQUID as a function of current bias and perpendicular magnetic field.  $V_{G2}$  is fixed at  $-0.5$  V, while  $V_{G1}$  is swept from  $-0.57$  V to  $-0.8$  V. As extracted from Fig. 6.1(c),  $I_{c2}(V_{G2} = -0.5) \sim 720$  nA, while  $I_{c1}(V_{G1} = -0.57) \sim 1.12$   $\mu\text{A}$  and  $I_{c1}(V_{G1} = -0.8) \sim 360$  nA (gate voltages are given in units of V).

The sign of the diode efficiency is mirrored with respect the magnetic field value corresponding to half flux quantum when the critical current asymmetry  $\alpha$  between the two junctions changes sign. We also notice a dip in differential resistance developing around half flux quantum that evolves with  $\alpha$  (see arrow in Fig. B.4).

## B.5. Model Including Loop Inductances

As introduced in the main text, we model the current-phase relation of a single junction  $i \in [1, 2]$  with

$$I_i(\varphi_i) = \frac{N_i \tau_i^* e \Delta}{\hbar} \frac{\sin(\varphi_i)}{\sqrt{1 - \tau_i^* \sin^2(\varphi_i/2)}}, \quad (\text{B.1})$$

where  $N_i$  stands for the number of channels and  $\tau_i^*$  for an effective transmission probability of junction  $i$ . The more general approach would be to assume a distribution function for the transmission probability of each channel. To avoid this complication we assume that all channels have the same transmission probability  $\tau_i^*$ .

We introduce the normalization parameter  $A_i$  as

$$A_i := \max_{\varphi_i} \left\{ \frac{\sin(\varphi_i)}{\sqrt{1 - \tau_i^* \sin^2(\varphi_i)}} \right\}. \quad (\text{B.2})$$

Note, that  $A_i$  only depends on  $\tau_i^*$ . We thus get the normalized CPR as

$$I_i(\varphi_i) = \frac{I_{ci}}{A_i} \frac{\sin(\varphi_i)}{\sqrt{1 - \tau_i^* \sin^2(\varphi_i/2)}}. \quad (\text{B.3})$$

In this notation of the CPR,  $N$  has been replaced by the critical current  $I_c$ , which appears now explicitly.

Flux quantization in the loop imposes:

$$\varphi_1 - \varphi_2 = 2\pi\Phi/\Phi_0. \quad (\text{B.4})$$

Here, the total flux in the loop  $\Phi$  is given by the external flux  $\Phi_{\text{ext}}$  and the contributions from the screening currents expressed through the loop inductances,  $L_1$  and  $L_2$ , that belong to the two branches. If mutual inductances are considered, too, one has to introduce new effective inductances  $L'_1 = L_1 - M$  and  $L'_2 = L_2 - M$ , where  $M$  describes the mutual inductance. We obtain for the total flux:

$$\Phi = \Phi_{\text{ext}} - L'_1 I_1(\varphi_1) + L'_2 I_2(\varphi_2) \quad (\text{B.5})$$

Therefore, Eq. B.4 now reads:

$$\varphi_1 - \varphi_2 = \varphi_{\text{ext}} + \frac{2\pi}{\Phi_0} \left( L'_2 I_2(\varphi_2) - L'_1 I_1(\varphi_1) \right). \quad (\text{B.6})$$

Our simulations show, however, that the effect of the mutual inductance can be neglected in our experiment. Hence, there are six remaining parameters in

the problem:  $I_{c1}$ ,  $I_{c2}$ ,  $\tau_1^*$ ,  $\tau_2^*$ ,  $L_1$ , and  $L_2$ . Since the appearance of the SDE in a SQUID is related to asymmetries, we introduce three asymmetry parameters:

$$\alpha := \frac{I_{c1} - I_{c2}}{I_{c1} + I_{c2}}, \quad (\text{B.7})$$

$$\beta := \frac{\tau_1^* - \tau_2^*}{\tau_1^* + \tau_2^*}, \quad (\text{B.8})$$

$$\gamma := \frac{L_1 - L_2}{L_1 + L_2}. \quad (\text{B.9})$$

The new set of parameters is now given by the three asymmetries and the average values of the two junctions for the critical current  $\bar{I}_c$ , the transmission probability  $\bar{\tau}$  and the inductance  $\bar{L}$ .

To find the critical current one has to find the maximum or minimum of the total supercurrent:

$$I(\varphi_1, \varphi_2) = I_1(\varphi_1) + I_2(\varphi_2). \quad (\text{B.10})$$

Making use of Eq. B.6, we get:

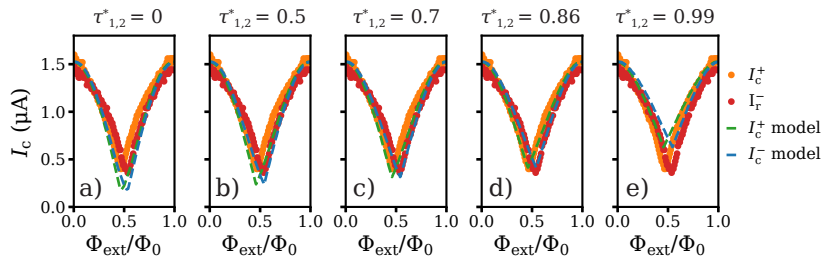
$$\begin{aligned} I(\varphi_1, I) &= I_1(\varphi_1) + I_2(\varphi_1 - \varphi_{\text{ext}} + \kappa L_1 I_1(\varphi_1) \\ &\quad - \kappa L_2 (I - I_1(\varphi_1))), \end{aligned} \quad (\text{B.11})$$

with  $\kappa = 2\pi/\Phi_0$ . In the latter form, we have eliminated  $\varphi_2$  using the fluxoid condition. However, due to the loop inductances, the equation for the total current  $I$  is now itself implicitly dependent on  $I$ . One can still solve this equation recursively or by introducing Lagrange multipliers to then search for the maximum or minimum currents, yielding  $I_c^+$  and  $I_c^-$  [244].

To find  $I_c^+$  numerically, we preset the value of  $I$ ,  $0 \leq I \leq 2\bar{I}_c$ , starting with a small one and search for solutions  $\varphi_1$  of Eq. B.11. If solutions exist, we increment  $I$  by a small step  $\delta I$  until there are no solutions  $\varphi_1$  anymore. This defines  $I_c^+$ . In analogy we obtain  $I_c^-$ .

## B.6. Comparison to Diode Effect due to Loop Inductances

Here, we present a comparison of the measured critical currents  $I_c^+$  and  $I_c^-$  shown in Fig. 6.2(c) with model simulations. Specifically, we discuss the effect of the loop inductance and its asymmetry on the SDE. The comparison shows that the SDE can poorly be reproduced taking only the loop inductances into account. This is shown in figure Fig. B.5.



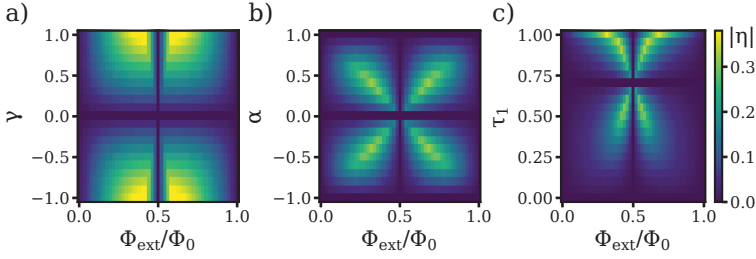
**Figure B.5.** Sequence of simulations for  $I_c^+$  (green dashed curves) and  $I_c^-$  (blue dashed curves) to measured (upsweep) data  $I_c^+$  (orange dots) and  $I_c^-$  (red dots). In (a) a sinusoidal CPR with the estimated loop inductance asymmetry is considered, while in graphs (b)-(e) the effective transparencies  $\tau^*$  of the junctions are increased. Further details are given in the text.

Figure B.5 shows a sequence of simulations, blue and green dashed curves, to a set of measurements of  $I_c^+$  (orange) and  $I_c^-$  (red). In all five simulations the critical currents  $I_{c1}$  and  $I_{c2}$  of the two junctions are taken from the experiment, from Fig. 6.1c. Since  $V_{G1} = V_{G2} = 0$  we obtain  $I_{c1} = 0.87 \mu\text{A}$  and  $I_{c2} = 0.67 \mu\text{A}$ . In (a) we assume sinusoidal CPRs for both junctions  $\text{JJ}_1$  and  $\text{JJ}_2$ , and we take the simulated loop inductances into account. Due to the slight asymmetry in loop inductance a small SDE appears. However, this effect is far smaller than what has been measured. Hence, one cannot fit the measurement with the loop inductance asymmetry alone. In (b)-(e) we keep the loop inductances as estimated, but change to non-sinusoidal CPRs by increasing  $\tau_1^* = \tau_2^*$  to appreciable values ranging from 0.5 – 0.99, indicated in the figures. As before, we obtain the blue and green dashed curves taking the known critical currents  $I_{c1}$  and  $I_{c2}$  of the two junctions. The best match in this sequence is found for  $\tau_1^* = \tau_2^* \approx 0.86$ . One can see that the model matches the key features of the experiment very well. However, there are deviations, as seen by the stronger curvature that the measurement points display as compared to the model. The model assumes an almost triangular shape for very large transparencies  $\tau_1^* = \tau_2^* \approx 0.99$ . These differences are yet not understood.

## B.7. Conditions for a Diode Effect in a SQUID Device

The following three figures illustrate that an asymmetry is required to obtain a SDE. In Fig. B.6(a) and (b) sinusoidal CPRs are assumed. In (a) the loop inductance asymmetry  $\gamma$  is varied, while the critical-current asymmetry  $\alpha = 0$ . In contrast, in (b)  $\alpha$  is varied, while  $\gamma = 0$ . The loop inductance has been chosen such that the average phase drop over the inductor  $\varphi_L = 4\pi\bar{I}_c\bar{L}\Phi_0$





**Figure B.6.** Magnitude of the diode efficiency  $|\eta|$  as a function of the applied external flux  $\Phi_{\text{ext}}$  expressed in number of magnetic flux quanta  $\Phi_0$ , numerically calculated for a SQUID with two sinusoidal CPRs with an asymmetry (a) in loop inductance  $\gamma$  and (b) in critical current  $\alpha$ . The inductances were chosen such that  $\varphi_L = \pi$ . In (c),  $|\eta|$  is plotted for a SQUID without loop inductances and two JJs, each with a non-sinusoidal single-channel CPR, as a function of  $\tau_1$  and normalized external flux for  $\tau_2 = 0.7$  and for  $\alpha = \gamma = \varphi_L = 0$ .

assumes a large value of  $\varphi_L = \pi$ . In (c) a SQUID with two single-channel non-sinusoidal CPRs with different transmission probabilities  $\tau_{1,2} \neq 0$  (asymmetry  $\beta \neq 0$ ) are considered, while  $\alpha = \gamma = \varphi_L = 0$ .

In general, it is seen that the diode efficiency is zero at the symmetry points corresponding in (a) to  $\gamma = 0$ , in (b) to  $\alpha = 0$  and in (c) to  $\tau_1 = \tau_2$ . Further on,  $\eta = 0$  for  $\varphi_{\text{ext}} = 2\pi\Phi_{\text{ext}}/\Phi_0 = 0, \pi, \text{ and } 2\pi$ . For these cases one can show that the CPR of the SQUID is odd in the phase difference  $\varphi$ . This follows from Eq. 6.5 and the fact that  $I_1(\varphi)$  and  $I_2(\varphi)$  are odd functions in  $\varphi$ . In addition, we note that the position of maximum diode efficiency in flux depends on what kind of asymmetry dominates. It can take up values  $> 30\%$ .

To obtain a SDE in a SQUID loop, an asymmetry is required. This we have illustrated in the previous figure Fig. B.6 where out of the three asymmetry parameters  $\alpha, \beta, \gamma$  only one was different from zero. In the following table we show under which conditions the SDE appears depending on all three asymmetry parameters. Table B.1 shows that at least one symmetry has to be broken to get the SDE effect. This is a sufficient condition for almost all cases. There is only one exception. It arises for sinusoidal CPRs where a difference in critical currents of the two junctions is not enough for a SDE to appear.

**Table B.1.** Conditions for obtaining a superconducting diode-effect (SDE). In the first column  $\tau^* = 0$  is used to refer to a sinusoidal CPR, while  $\tau^* \neq 0$  indicates a highly transmissive CPR containing higher order terms in the CPR. If  $\bar{L} = 0$ , loop inductances are not considered, while they play a role in the entries where  $\bar{L} \neq 0$ .  $\alpha$  ( $\beta$ ) denotes the asymmetry in  $I_c$  ( $\tau^*$ ) of the two JJs, while  $\gamma$  denotes the asymmetry in the loop inductances in the two arms of the SQUID.

$\tau^*$	$\beta$	$\alpha$	$\bar{L}$	$\gamma$	SDE
0	n.a.	0	0	n.a.	no
0	n.a.	0	$\neq 0$	0	no
0	n.a.	0	$\neq 0$	$\neq 0$	yes
0	n.a.	$\neq 0$	0	n.a.	no
0	n.a.	$\neq 0$	$\neq 0$	0	yes
0	n.a.	$\neq 0$	$\neq 0$	$\neq 0$	yes
$\neq 0$	0	0	0	n.a.	no
$\neq 0$	0	0	$\neq 0$	0	no
$\neq 0$	0	0	$\neq 0$	$\neq 0$	yes
$\neq 0$	0	$\neq 0$	0	n.a.	yes
$\neq 0$	0	$\neq 0$	$\neq 0$	0	yes
$\neq 0$	0	$\neq 0$	$\neq 0$	$\neq 0$	yes
$\neq 0$	$\neq 0$	0	0	n.a.	yes
$\neq 0$	$\neq 0$	0	$\neq 0$	0	yes
$\neq 0$	$\neq 0$	0	$\neq 0$	$\neq 0$	yes
$\neq 0$	$\neq 0$	$\neq 0$	0	n.a.	yes
$\neq 0$	$\neq 0$	$\neq 0$	$\neq 0$	0	yes
$\neq 0$	$\neq 0$	$\neq 0$	$\neq 0$	$\neq 0$	yes

# C Charge-4e Supercurrent - Supplementary

---

## C.1. Methods

The proximitized InAs 2DEG used in this project is grown starting from a semi-insulating InP (100) substrate. A 1  $\mu\text{m}$  thick  $\text{In}_x\text{Al}_{1-x}\text{As}$  buffer layer is used to match the lattice constant of InP to the one of InAs. The quantum well consists of a 7 nm InAs layer sandwiched between a 10 nm (top barrier) and a 4 nm (bottom barrier)  $\text{In}_{0.75}\text{Ga}_{0.25}\text{As}$  layer. The 10 nm Al layer is epitaxially grown on top of a capping GaAs thin film without breaking the vacuum, ensuring a pristine interface between the semiconductor and the superconductor. Here we show results obtained from a wafer stack with mobility  $\mu = 11,000 \text{ cm}^2\text{V}^{-1}\text{s}^{-1}$  at electron densities of  $2.0 \times 10^{12} \text{ cm}^{-2}$ , measured on a different chip coming from the same wafer.

The device is fabricated using standard electron beam lithography techniques. The SQUID is electrically isolated by etching the Al layer and 300 nm of buffer around it. First, the Al film is removed with Al etchant Transene D, followed by a deep III-V chemical wet etch  $\text{H}_2\text{O}:\text{C}_6\text{H}_8\text{O}_7:\text{H}_3\text{PO}_4:\text{H}_2\text{O}_2$  (220:55:3:3). Next, JJs are formed by selectively removing the Al over 150nm-long stripes on each branch of the loop. A 15 nm-thick layer of insulating  $\text{HfO}_2$  is grown by atomic layer deposition at a temperature of 90 °C over the entire sample. The set of gates are realized in two steps. A thin Ti/Au (5/25 nm) layer is evaporated on top of the mesa to define the gate geometry, and then leads and bonding pads are defined by evaporating a Ti/Au (5/85 nm) layer at an angle of  $\pm 17^\circ$  to overcome the mesa step. More information about the full wafer stack and the fabrication procedure can be found in Ref. [239, 268, 291? ].

## C.2. Extended Setup Description

The chip is mounted on a double-sided Ni/Au plated Roger<sup>®</sup> 4350 PCB screwed onto a copper plate. A 10 $\Omega$  metal film resistor is soldered on the back side of the PCB in-between the ground plane and the central conductor of the SMP connector. The device is glued onto the central copper area such that the microwave bond terminals are as close as possible to the PCB counterpart. The

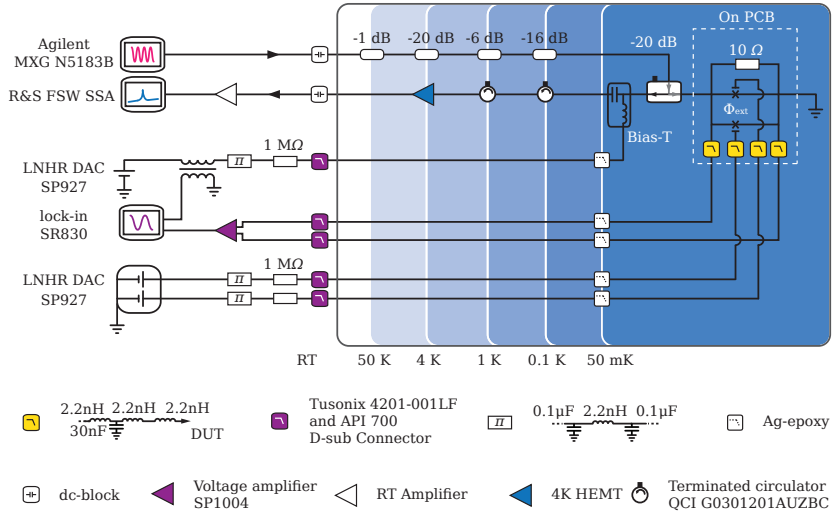


**Figure C.1.** Detailed description of the measurement setup.

PCB central conductor is bonded to one side of the SQUID, whereas the other side is bonded to the PCB ground resulting in a resistively shunted junction configuration. Both wire bonds are made as short as possible. Additional bond wires connect to the differential voltage measure and gate voltage supplies.

The dc supply lines are filtered at room temperature, on the PCB, and are thermalized to the mixing chamber plate via silver-epoxy filters that provide a cut-off of  $\approx 6$  MHz. A current bias is generated by a  $1\text{ M}\Omega$  resistor in series with a voltage source. The current couples via a bias-tee to the microwave line that connects through the device to ground. The voltage drop across the junction is measured differentially with a voltage amplifier and lock-in techniques.

A constant voltage drop across a Josephson junction leads to an oscillating current. The amplification chain collects this radiation signal and feeds it to a R&S FSW SSA spectrum analyser. The ac signal is coupled via the bias-tee to a cryogenic HEMT amplifier (nominally  $+40$  dB gain) located on the 4K stage that is isolated from the device with two terminated circulators. The signal is further amplified with a room temperature amplifier (nominally  $+40$  dB gain). The following measurement parameters are set at the spectrum analyzer to sense the amplified Josephson emission: detection bandwidth 20 MHz, span

22 MHz, resolution bandwidth 20 MHz, video bandwidth 100 Hz and 1001 points resulting in a sweep time of 1 s. In addition to the sensing line, a drive line connects to the device via a directional coupler. A Agilent MXG N5183B signal generator is used to send an microwave tone to the SQUID to perform Shapiro step measurements. The detection bandwidth is limited by the directional coupler to 2.5 – 8.5 GHz.

The external magnetic field flux  $\Phi_{\text{ext}}^{\text{ext}}$  is applied with a 3-axis vector magnet sourced with a Keithley 2400. Measurements were performed in a dilution refrigerator with a base temperature of  $\sim 50$  mK.

### C.3. Peaks amplitude dependence on External Flux

In this sections, we attempt to relate the ratio between the 4e and 2e emission peaks amplitude to the harmonics content of a junction with effective transparency  $\tau^*$ . Considering a Josephson junction as an ac current source in parallel with a resistor  $R_s$ [270], the power dissipated in the circuit is given by:

$$P = \frac{R_s I_c^2}{2} = \frac{R_s}{2} \sum_{m=1}^{\infty} c_m^2(\tau^*), \quad (\text{C.1})$$

where  $I_c$  is the critical current of the junction and  $c_m^2(\tau^*)$  is the contribution to the dissipated power coming from the  $m$ -th harmonic.

For each detection frequency, we define the amplitude of the  $m$ -th peak  $P_{\text{det},m}$  as the difference between the peak height and the minimum of the detected power. The ratio of the Fourier coefficients of the CPR of the junction is directly proportional to the square root of the amplitudes of the emission peaks:

$$\left| \frac{c_2}{c_1} \right| \propto \sqrt{\frac{P_{\text{det},2}}{P_{\text{det},1}}}. \quad (\text{C.2})$$

In practice, additional processes increase the amplitude of higher harmonics peaks compared to the one expected from the harmonic content of the CPR [56]. At current bias values  $I$  larger but close  $I_c$ , part of the current has to flow as normal current through the shunt resistor and displacement current through the parallel capacitance. The interplay between super-, normal and displacement current results in a time varying voltage over the junction that causes emission at multiples of the fundamental Josephson frequency even in the case of a fully sinusoidal CPR [93]. For  $I \gg I_c$  instead, most of the current flows as normal current, resulting in a more constant junction voltage. Emission of photons at current bias values such that the ratio  $k = I/I_c$  is  $\gg 1$

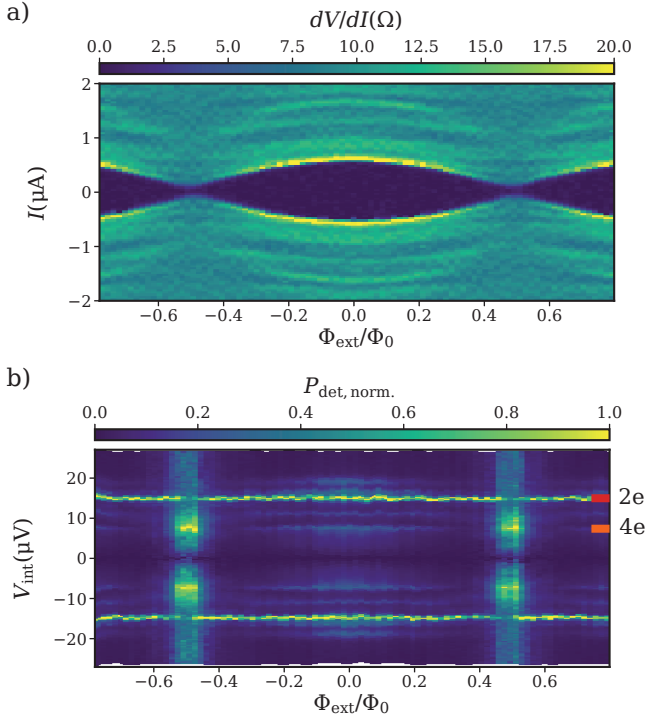
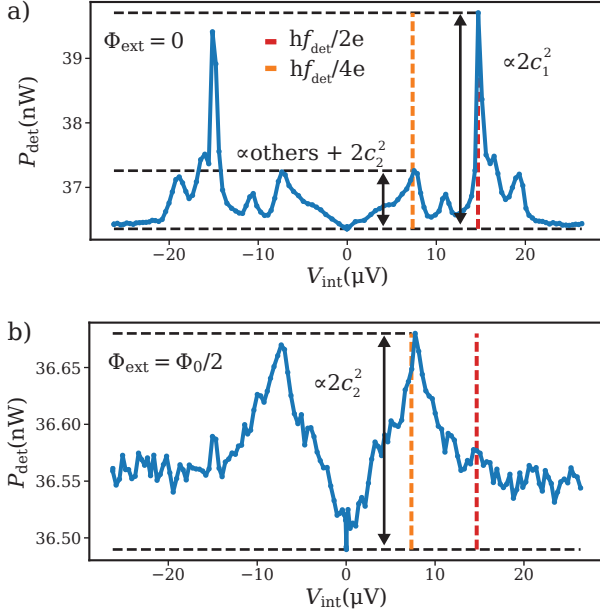


**Figure C.2.** a) Differential resistance  $dV/dI$  of the SQUID as a function of external flux  $\Phi_{\text{ext}}$  and current bias  $I$  for symmetric junctions. Here,  $V_{G1} = -0.865$  V and  $V_{G2} = -0.845$  V. b) Normalized radiation power  $P_{\text{det, norm.}}$  at  $f_{\text{det}} = 7.1$  GHz as a function of external flux  $\Phi_{\text{ext}}$  and normalized voltage drop over the SQUID. The map is measured as the same time as in a). We show the periodic suppression of the  $2e$  peak and the emergence of a dominant  $4e$  peak.

is then characterized by a well defined emission frequency.

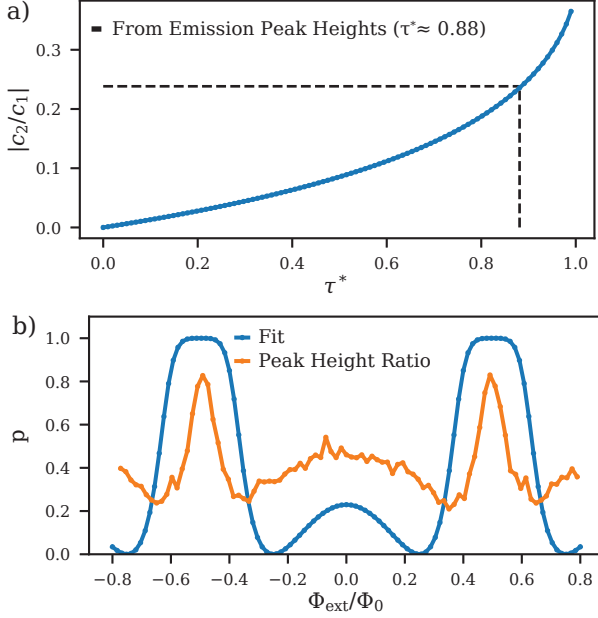
At a detection frequency of 7.1 GHz, the  $4e$  emission peak occurs at a voltage bias of  $\sim 7.34$   $\mu\text{V}$ . To pinpoint the current value associated with  $4e$  emission, we integrate the measured  $dV/dI$  curves across the range of current bias values. Subsequently, we seek the current bias value corresponding to  $V_{\text{int}} = 7.34$   $\mu\text{V}$ .

Figure C.2a) shows the differential resistance  $dV/dI$  as a function of bias



**Figure C.3.** a) Cut in the emission spectrum in Fig. C.2b) at zero flux. The horizontal black dashed lines highlight, from bottom to top, the signal baseline, the  $4e$  and the  $2e$  peak height. b) Cut in the emission spectrum in Fig. C.2b) at half flux. The horizontal black dashed lines highlight, the signal baseline and the  $4e$  peak height. A small  $2e$  emission signal is visible at  $V_{\text{int}} = -hf_{\text{det}}/2e$ .

current  $I$  and external flux  $\Phi_{\text{ext}}$  at  $V_{G1} = -0.865$  V and  $V_{G2} = -0.845$  V. In this gate voltage configuration, the two junctions are symmetric. The difference in gate positions at which balance is achieved in this case compared to the one shown in the main text can be attributed to gate hysteresis and gate drift occurring during the time period between measurements. At  $\Phi_{\text{ext}} = 0$ , the critical current of the SQUID is  $I_c \sim 0.7$   $\mu\text{A}$  and  $k$  is only  $\sim 1.6$ . This results in a time varying voltage over the SQUID, and therefore in a finite contribution to the  $4e$  emission amplitude that adds on top of the one coming from the CPR of the junctions. On the other hand, at  $\Phi_{\text{ext}} = \Phi_0/2$  the critical current of the SQUID is  $I_c \sim 0.12$   $\mu\text{A}$ , corresponding to a much higher current bias to critical current ratio for the  $4e$  emission  $k \sim 9.5$ . The lower critical current value also reduces the contribution from environmental modes, so that at  $\Phi_{\text{ext}} = \Phi_0/2$ , the  $4e$  peak amplitude can be more faithfully related to the



**Figure C.4.** a) Absolute value of the ratio between the second and first Fourier coefficients  $|c_2/c_1|$  as a function of the junction transparency  $\tau$ . The dashed line corresponds to the square root of the ratio between the 4e and the 2e emission peak amplitude at half and zero flux respectively. By comparing this with the  $|c_2/c_1|$  ratio calculated from the fit, we extract a junction transparency of 0.88. b) The ratio  $p$  (see main text) as a function of  $\Phi_{\text{ext}}$  extracted from Fig. C.2b). We compare this to the evolution of the ratio  $|c_2|/\sqrt{c_1^2 + c_2^2}$  as a function of  $\Phi_{\text{ext}}$  extracted from the Fourier fit of the CPR of a SQUID formed by two identical single channels junctions with transparency 0.88.

harmonic content of the CPR. Since each junction contribute  $c_1^2$  to the emission signal, the peak amplitudes for a SQUID in the symmetric configuration are proportional to  $2c_1^2$ .

Figure C.2b) shows the normalized radiation power  $P_{\text{det, norm.}}$  measured at the same time as in Fig.C.2a) at fixed detection frequency  $f_{\text{det}} = 7.1$  GHz as a function of integrated voltage  $V_{\text{int}}$  and  $\Phi_{\text{ext}}$ . One can observe a periodic suppression of the 2e peak and emergence of the 4e peak.

In Fig.C.4e), we plot the second to first harmonic ratio  $|c_2/c_1|$  of a non-



sinusoidal CPR as a function of the junction transparency  $\tau^*$ . The Fourier coefficient are extracted for each  $\tau^*$  by fitting the CPR with a Fourier series with 10 harmonics. The  $|c_2/c_1|$  ratio calculated from Eq.(C.2) using as  $P_{\text{det},1}$  the 2e peak emission amplitude at  $\Phi_{\text{ext}} = 0$ , and as  $P_{\text{det},2}$  the 4e peak emission amplitude at  $\Phi_{\text{ext}} = \Phi_0/2$ , corresponds to an effective transparency of  $\tau^* \sim 0.88$ . This is in good agreement with the effective transparency extracted for the same device using an asymmetric SQUID configuration[89].

Finally, Fig.C.4f) shows the normalized ratio  $p = \sqrt{P_{\text{det},2}}/\sqrt{P_{\text{det},1}^2 + P_{\text{det},2}^2}$  as a function of  $\Phi_{\text{ext}}$  as extracted from Fig.C.2b). In the same figure we plot the evolution of the ratio  $|c_2|/\sqrt{c_1^2 + c_2^2}$  with  $\Phi_{\text{ext}}$  as extracted from a fit of Fourier series to the CPR of a symmetric SQUID with effective transparency  $\tau^* = 0.88$ . The ratio extracted from amplitudes of the peaks is vertically shifted relative to the fit. We attribute this shift to additional contributions to the 4e peak originating from a time-varying voltage across the SQUID and environmental processes.

## C.4. Evolution of the 4e Peak amplitude with Gate voltages Configuration

In the following, we fix the external flux at half flux quantum  $\Phi_0/2$  and we study the evolution of the 4e peak emission amplitude in different gate voltage configurations.

The left panels of Fig. C.5 show the differential resistance  $dV/dI$  of the SQUID as a function of bias current  $I$  and gate voltage  $V_{G1}$  at  $\Phi_0/2$  for different values of  $V_{G2}$ . The symmetry point is identified in each plot by the value of  $V_{G1}$  at which the critical current of the SQUID reaches its minimum, indicating the cancellation of the contribution from the first harmonics. By increasing  $V_{G2}$ , the critical current of the SQUID in the symmetric configuration also increases.

At the same time, we measure the radiation signal from the SQUID. In the right panels of Fig. C.5, we plot the normalized radiation power  $P_{\text{det,norm}}$  at fixed detection frequency  $f_{\text{det}} = 7.1$  GHz as a function of  $V_{G1}$  and voltage drop  $V_{\text{int}}$ . In Fig. C.6a), b) and c), we show the radiation power in the symmetric configuration. The 4e peak amplitude increases with the critical current of the SQUID (see Fig. C.6d)) and at the same time, the width of the peak becomes larger. The last can be understood by looking at the  $k$  ratio: decreasing  $k$ , the voltage drop over the SQUID at the current bias value corresponding to the 4e emission will be less well defined, leading to a broader emission peak.



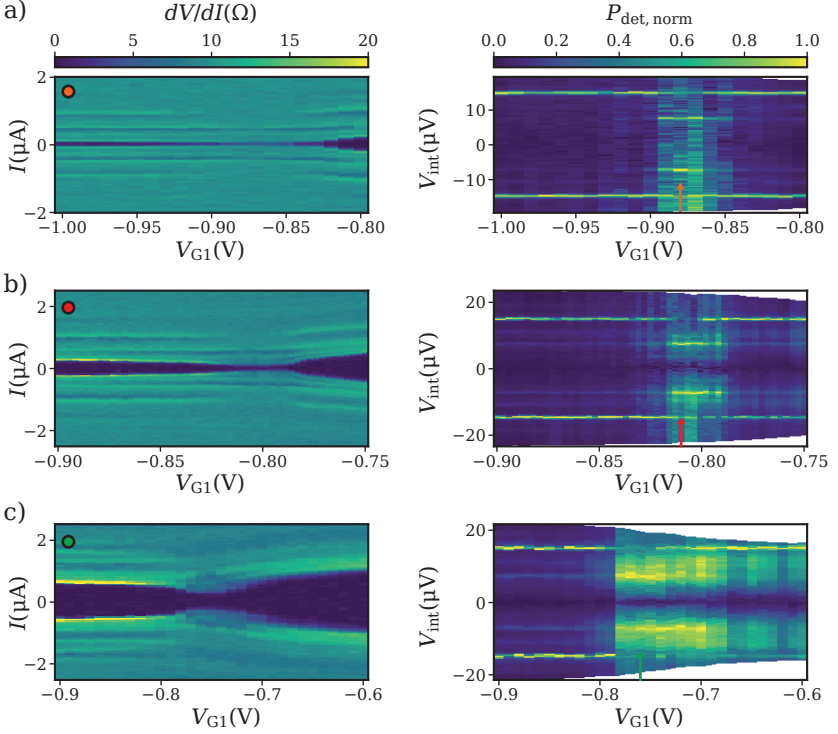


**Figure C.5.** a) Differential resistance  $dV/dI$  of the SQUID as a function of gate voltage  $V_{G1}$  and current bias  $I$ . The external flux is kept at half flux quantum  $\Phi_0/2$  and  $V_{G2} = -1.1$  V. On the right, normalized radiation power  $P_{\text{det, norm}}$  at  $f_{\text{det}} = 7.1$  GHz plotted as a function of  $V_{G1}$  and voltage drop  $V_{\text{int}}$  over the SQUID. b) and c) Same as in a) but for  $V_{G2} = -0.875$  V and  $-0.7$  V respectively.

The ability to tune the amplitude of the 4e peak over a wide range is a significant advantage of the 2D platform compared to the nanowire platform for the realization of a parity-protected qubit. To achieve a small dephasing rate, the Josephson energy of the second harmonics in the balanced configuration must be much larger than the island charging energy. This is difficult to achieve with a Josephson junction with only a few conduction channels.

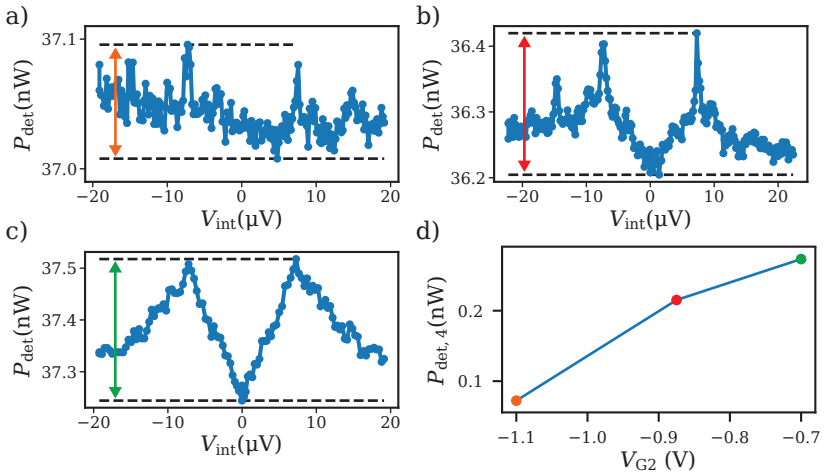


**Figure C.6.** a) b) and c) Radiation power in linear scale as a function of  $V_{\text{int}}$  shown for the positions in gate voltage as indicated by the arrows in Fig. C.5a), b) and c). d) Amplitude of the 4e emission peak in the symmetric SQUID configuration as a function of  $V_{G2}$ .



# D Hybrid SQUIDs for CQED - Supplementary

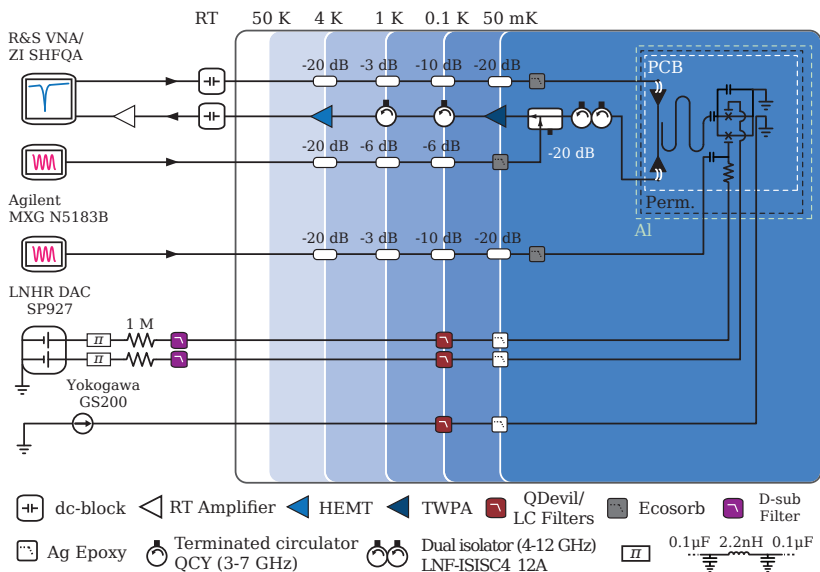


**Figure D.1.** Detailed measurement setup of a gate and flux tunable transmon in a Blufors dilution cryostat.

## D.1. Extended Setup - Gate and Flux Tunable Transmon

Figure D.1 shows the measurement setup for measuring the gate and flux tunable transmons discussed in Chapter 8.

The device is connected to a printed circuit board (PCB) by Al wire bonds and mounted in a copper box thermally anchored to the mixing chamber of a

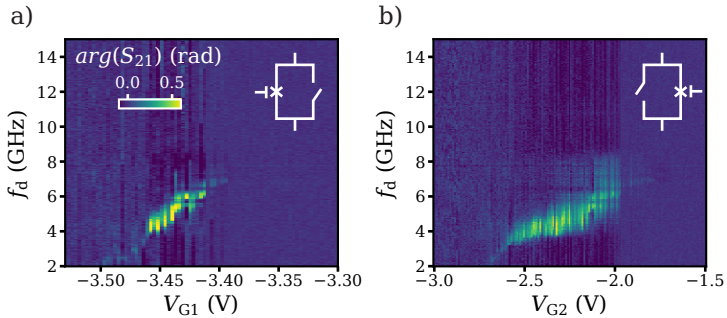


**Figure D.2.** a) Phase of the transmission coefficient  $\arg(S_{21})$  at fixed readout frequency as a function of drive frequency  $f_d$  and  $V_{G1}$  when the other junction is pinched off ( $V_{G2} = -10$  V). b) Same as in a) but as a function of  $V_{G2}$  when  $V_{G1} = -10$  V.

Bluefors cryogen-free dilution refrigerator with a base temperature of  $\sim 15$  mK. The copper box is protected against stray magnetic fields with an aluminium (light green dashed box) and a permalloy shield (black dashed box).

The dc lines are filtered at room temperature with a D-type sub connector with cut-off frequency at 640 kHz. Additional filtering is done at the 100 mK plate through QDevil RC-filters with a cut-off at 65 kHz and finally at the mixing chamber with silver epoxy filters.

Readout rf signals are produced and measured with either a R&S vector network analyser or with a Zurich Instrument SHFQA. Input signals are attenuated by  $-53$  dB distributed across the cryostat plates, and then filtered with Ecosorb at the mixing chamber before reaching the device. The qubit drive signal is produced by an Agilent MXG N5183B signal generator decoupled from the dc gate line with a bias tee made of a 15 nF capacitance and a 1.05 k $\Omega$  resistor soldered on the PCB. The drive line is attenuated by  $-53$  dB and also filtered with Ecosorb. Outgoing rf signals are sent through a Silent Waves quantum-limited travelling wave parametric amplifier (TWPA) and further amplified by a HEMT LNF-LNC1 12A (1-12 GHz) mounted on the 4 K-plate plus a room temperature amplifier. The TWPA and the HEMT are isolated from the device by two terminated circulators and a dual stage isolator respectively. The pump line for the TWPA is attenuated by a total of  $-52$  dB and filtered with Ecosorb. It reaches the input of the TWPA via the coupling port of a directional coupler positioned after the dual stage isolator.

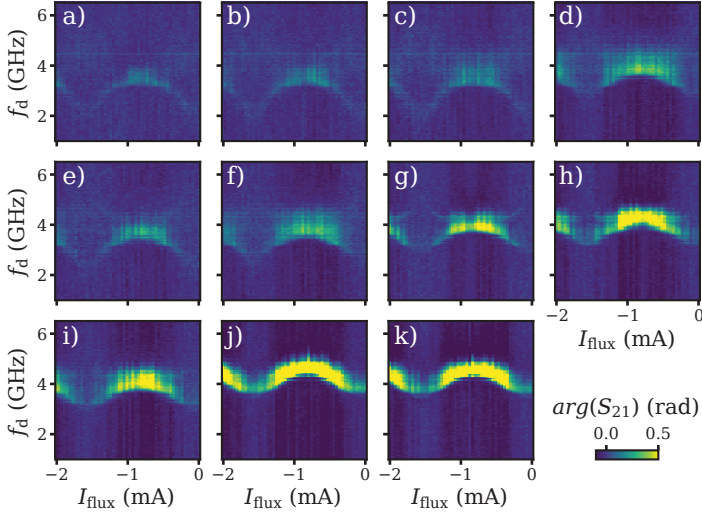


**Figure D.3.** a) to k) Phase of the transmission coefficient  $\arg(S_{21})$  at fixed readout frequency as a function of drive frequency  $f_d$  and flux current  $I_{\text{flux}}$  at different gate voltage configurations.  $V_{G1}$  is fixed to  $-3.47$  V and  $V_{G2}$  varies from  $-2.7$  V to  $-2.5$  V in steps of  $0.2$  V.

## D.2. Two-tone Maps Individual Junctions

In this section we characterize the gate response of the individual junctions forming the transmon qubit discussed in Section 8.2 of Chapter 8. Figure D.2 shows two tone spectroscopy maps as a function of drive frequency  $f_d$  and gate voltage  $V_{Gi}$  for each junction when the other is pinched off. We use this measurement to determine gate voltage configurations where the two junctions have similar Josephson energy. Both maps are measured with a readout power of  $-50$  dBm and a drive power of  $-30$  dBm. We can tune both qubit over several GHz. The linewidth of the qubit when only  $JJ_2$  is contributing to its Josephson energy is wider compared to when only  $JJ_1$  is on.

## D.3. Additional Two-tone Maps as a Function of Flux

In this section we show additional two-tone spectroscopy maps measured as a function of magnetic field flux at different gate voltage configurations. We fix  $V_{G1}$  to  $-3.47$  V, corresponding to a qubit frequency of approximately 2 GHz

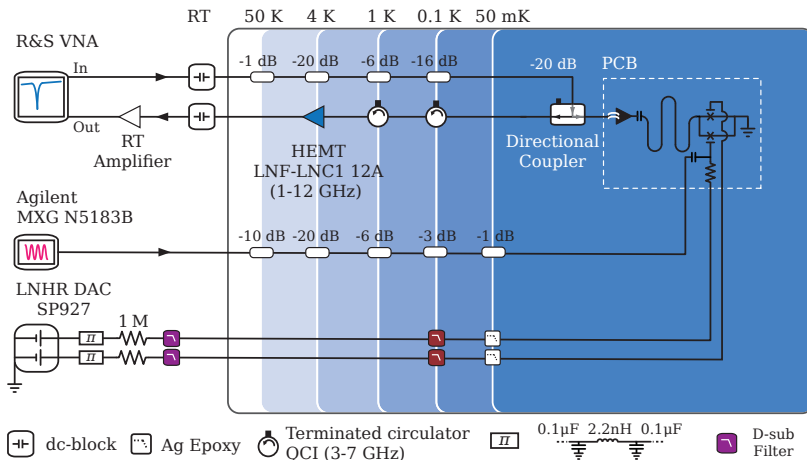


**Figure D.4.** Detailed measurement setup of a gate and flux tunable Josephson parametric amplifier in a Triton 200 dilution cryostat.

when  $JJ_2$  is pinched off. Then, we vary  $V_{G2}$  from  $-2.7$  V to  $-2.5$  V in steps of  $0.2$  V, and measure the fixed frequency resonator response as a function of a continuous drive tone at frequency  $f_d$  and flux current  $I_{\text{flux}}$ . This is shown in Fig. D.3. The oscillations with flux of the qubit frequency change depending on the asymmetry between the Josephson energies of the junctions. As expected, the qubit frequency at zero flux ( $I_{\text{flux}} \sim -0.8$  mA) increases as we increase  $V_{G2}$ .

## D.4. Extended Setup - Josephson Parametric Amplifier

Figure D.4 shows the measurement setup for the gate and flux tunable Josephson parametric amplifier discussed in Chapter 8.

The chip is mounted on a double-sided Ni/Au plated Roger<sup>®</sup> 4350 PCB screwed onto a copper plate. The device is glued onto the central copper area such that the microwave bond terminals are as close as possible to the PCB counterpart. The PCB central conductor is bonded to the resonator input pad.

Readout rf signals are produced and measured either with a R&S vector network analyser. Input signals are attenuated by  $-63$  dB distributed across the cryostat plates. The pump signal is produced by an Agilent MXG N5183B signal generator decoupled from the dc gate line with a bias tee made of a



15 nF capacitance and a 1.05 k $\Omega$  resistor soldered on the PCB. The pump line is attenuated by  $-40$  dB. Outgoing rf signals are amplified by a HEMT LNF-LNC1 12A (1-12 GHz) mounted on the 4 K-plate plus a room temperature amplifier. The HEMT is isolated from the device by two terminated circulators.

The dc supply lines are filtered at room temperature, and are thermalized to the mixing chamber plate via silver-epoxy filters that provide a cut-off of  $\approx 6$  MHz.

The external magnetic field is applied with a 3-axis vector magnet sourced with a Keithley 2400. Measurements are performed in a Triton 200 dilution refrigerator with a base temperature of  $\sim 50$  mK.



# E Fabrication Recipes

---

In the following, we list the relevant fabrication recipes to realize the devices investigate in this thesis.

## E.1. Epi-Al/InAs Devices

This recipe was developed in collaboration with Asbjørn C. C. Drachmann from the University of Copenhagen.

Cleaving	<ul style="list-style-type: none"><li>• Spin PMMA 950K (AR-P 672.045) for 40 s at 4000 rpm with 4 s ramp-up time (<math>\sim 200</math> nm). It will serve as a protection layer</li><li>• Cleave with a diamond tip</li></ul>
Cleaning	<ul style="list-style-type: none"><li>• Sonicate in 1-3 Dioxolane, <math>f = 80</math> kHz, <math>P = 50 - 70\%</math> for 5 mins</li><li>• Acetone and IPA rinse, 30 s each.</li><li>• Blow dry</li></ul>
MESA etch mask	<ul style="list-style-type: none"><li>• Double layer resist (repeat procedure 2 times):<ul style="list-style-type: none"><li>– Spin PMMA 950K (AR-P 672.045) for 40 s at 4000 rpm with 4 s ramp-up time</li><li>– Bake for 3 min at <math>180^\circ\text{C}</math> on hot plate</li></ul></li></ul>
Exposure MESA	<ul style="list-style-type: none"><li>• Parameters: acc. voltage = 30 kV, aperture = <math>60\ \mu\text{m}</math>, area dose = <math>260\ \mu\text{C cm}^{-2}</math>, writefield = <math>1950\ \mu\text{m}</math></li><li>• Resist development:<ul style="list-style-type: none"><li>– 60 s MIBK/IPA 1:3 at room temperature</li><li>– 10 s rinse in IPA</li><li>– Blow dry</li></ul></li></ul>

Al etch	<ul style="list-style-type: none"> <li>• O<sub>2</sub>-plasma: O<sub>2</sub>-flow= 0.5 Nl/h, <math>t = 60</math> s, <math>P = 30</math> W</li> <li>• Prepare two beakers in the warm bath at 50 °C:             <ul style="list-style-type: none"> <li>– Beaker (50 ml) Transene D</li> <li>– Beaker (50 ml) DI-water</li> </ul> </li> <li>• Prepare one beaker at room temperature:             <ul style="list-style-type: none"> <li>– Beaker (500 ml) DI-water</li> </ul> </li> <li>• Wait 30 min for the Transene D and the water in the warm bath to thermalize with the bath</li> <li>• Post-bake 2 min at 120 °C to improve resist adhesion and remove undercut</li> <li>• Etch 8 s in Transene D to remove 10 nm Al, and 17 s to remove 50 nm Al.</li> <li>• Stop the etching with 20 s in the beaker with 50 ml DI-water at 50 °C and 40 s in the beaker with 500 ml DI-water at room temperature</li> <li>• Blow dry</li> </ul>
MESA etch	<ul style="list-style-type: none"> <li>• Post-bake 2 min at 120 °C to improve resist adhesion</li> <li>• In a beaker with a magnetic stirrer mix in this order H<sub>2</sub>O:C<sub>6</sub>H<sub>8</sub>O<sub>7</sub>:H<sub>3</sub>PO<sub>4</sub>:H<sub>2</sub>O<sub>2</sub> (220:55:3:3)</li> <li>• After having added H<sub>2</sub>O<sub>2</sub>, wait 5 min.</li> <li>• Etch 9 min to remove ~ 300 nm of buffer from the wafer on InP substrate, and 12 min to remove ~ 450 nm of buffer from the wafer on GaAs substrate</li> <li>• Stop the etching with 1 min in DI-water</li> <li>• Blow dry</li> <li>• Post-bake 2 min at 120 °C to improve resist adhesion</li> <li>• Repeat Al etch procedure to remove overhanging Al from the MESA walls</li> <li>• Strip resist: 30 min in 1-3 Dioxolane. Acetone and IPA rinse, 30 s each. Blow dry</li> </ul>
Al etch mask	<ul style="list-style-type: none"> <li>• Double layer resist (repeat procedure 2 times):             <ul style="list-style-type: none"> <li>– Spin PMMA 950K (AR-P 672.045) for 40 s at 4000 rpm with 4 s ramp-up time</li> <li>– Bake for 3 min at 180 °C on hot plate</li> </ul> </li> </ul>

Exposure Al	<ul style="list-style-type: none"> <li>• Parameters: acc. voltage = 30 kV, aperture = 10 <math>\mu\text{m}</math>, area dose = 700 <math>\mu\text{C cm}^{-2}</math>, writefield = 400 <math>\mu\text{m}</math>. Write 50 nm wide lines.</li> <li>• Resist development: <ul style="list-style-type: none"> <li>– 60 s MIBK/IPA 1:3 at room temperature</li> <li>– 10 s rinse in IPA</li> <li>– Blow dry</li> </ul> </li> </ul>
Al etch ( $\sim$ 200 nm wide junction)	<ul style="list-style-type: none"> <li>• O<sub>2</sub>-plasma: O<sub>2</sub>-flow= 0.5 Nl/h, <math>t = 60</math> s, <math>P = 30</math> W</li> <li>• Prepare two beakers in the warm bath at 50 °C: <ul style="list-style-type: none"> <li>– Beaker 50 ml) Transene D</li> <li>– Beaker (50 ml) DI-water</li> </ul> </li> <li>• Prepare one beaker at room temperature: <ul style="list-style-type: none"> <li>– Beaker (500 ml) DI-water</li> </ul> </li> <li>• Wait 30 min for the Transene D and the water in the warm bath to thermalize with the bath</li> <li>• Post-bake 2 min at 120 °C to improve resist adhesion and remove undercut</li> <li>• Etch 8 s in Transene D to remove 10 nm Al, and 17 s to remove 50 nm Al.</li> <li>• Stop the etching with 20 s in the beaker with 50 ml DI-water at 50 °C and 40 s in the beaker with 500 ml DI-water at room temperature</li> <li>• Blow dry</li> <li>• Strip resist: 30 min in 1-3 Dioxolane. Acetone and IPA rinse, 30 s each. Blow dry</li> </ul>
Oxide mask	<ul style="list-style-type: none"> <li>• Triple layer resist (repeat procedure 3 times): <ul style="list-style-type: none"> <li>– Spin PMMA 950K (AR-P 672.045) for 40 s at 4000 rpm with 4 s ramp-up time</li> <li>– Bake for 3 min at 180 °C on hot plate</li> </ul> </li> </ul>
Exposure oxide	<ul style="list-style-type: none"> <li>• Parameters: acc. voltage = 10 kV, aperture = 30 <math>\mu\text{m}</math>, area dose = 260 <math>\mu\text{C cm}^{-2}</math>, writefield = 400 <math>\mu\text{m}</math></li> <li>• Resist development: <ul style="list-style-type: none"> <li>– 60 s MIBK/IPA 1:3 at room temperature</li> <li>– 10 s rinse in IPA</li> <li>– Blow dry</li> </ul> </li> </ul>

Selective Atomic Layer Deposition	<ul style="list-style-type: none"> <li>• O<sub>2</sub>-plasma: O<sub>2</sub>-flow= 0.5 Nl/h, <math>t = 60</math> s, <math>P = 30</math> W</li> <li>• Oxide growth at <math>T = 90^\circ\text{C}</math>, <math>p = 3.2</math> mbar, N<sub>2</sub> flow = 20 sccm:             <ul style="list-style-type: none"> <li>– Pulse TOMAH for 0.55 s</li> <li>– Wait 180 s</li> <li>– Pulse H<sub>2</sub>O for 0.02 s</li> <li>– Wait 180 s</li> <li>– Repeat <math>n</math> times. 150 cycles correspond to <math>\sim 25</math> nm</li> </ul> </li> <li>• Lift-off: 30 min in 1-3 Dioxolane. 30 min in acetone at <math>50^\circ\text{C}</math>. IPA rinse, and blow dry</li> </ul>
Gates mask	<ul style="list-style-type: none"> <li>• Triple layer resist (repeat procedure 3 times):             <ul style="list-style-type: none"> <li>– Spin PMMA 950K (AR-P 672.045) for 40 s at 4000 rpm with 4 s ramp-up time</li> <li>– Bake for 3 min at <math>180^\circ\text{C}</math> on hot plate</li> </ul> </li> </ul>
Exposure gates	<ul style="list-style-type: none"> <li>• Parameters: acc. voltage = 10 kV, aperture = <math>30\ \mu\text{m}</math>, area dose = <math>260\ \mu\text{C cm}^{-2}</math>, writefield = <math>1950\ \mu\text{m}</math></li> <li>• Resist development:             <ul style="list-style-type: none"> <li>– 60 s MIBK/IPA 1:3 at room temperature</li> <li>– 10 s rinse in IPA</li> <li>– Blow dry</li> </ul> </li> </ul>
Evaporation gates (375 nm)	<ul style="list-style-type: none"> <li>• O<sub>2</sub>-plasma: O<sub>2</sub>-flow= 0.5 Nl/h, <math>t = 60</math> s, <math>P = 30</math> W</li> <li>• Evaporate 5 nm Ti with <math>17^\circ</math> tilt</li> <li>• Evaporate 5 nm Ti with <math>-17^\circ</math> tilt</li> <li>• Evaporate 5 nm Ti with no tilt</li> <li>• Repeat 3 times:             <ul style="list-style-type: none"> <li>– Evaporate 50 nm Au or Al with <math>17^\circ</math> tilt</li> <li>– Evaporate 50 nm Au or Al with <math>-17^\circ</math> tilt</li> </ul> </li> <li>• Evaporate 50 nm Au or Al with no tilt</li> <li>• Lift-off: 30 min in 1-3 Dioxolane. 30 min in acetone at <math>50^\circ\text{C}</math>. IPA rinse, and blow dry</li> </ul>

## E.2. NbTiN resonators

Cleaning	<ul style="list-style-type: none"> <li>• Sonicate in 1-3 Dioxolane, <math>f = 80 \text{ kHz}</math>, <math>P = 50 - 70\%</math> for 5 mins</li> <li>• Acetone and IPA rinse, 30 s each.</li> <li>• Blow dry</li> </ul>
Mask	<ul style="list-style-type: none"> <li>• <b>eBeam</b> <ul style="list-style-type: none"> <li>– Spin EL6 (MMA(8.5)MAA) for 40 s with 4000 rpm with 4 s ramp-up time (repeat procedure 2 times for <math>\sim 240 \text{ nm}</math>)</li> <li>– Bake for 90 s at <math>185^\circ\text{C}</math> on hot plate</li> <li>– Spin PMMA 950K (AR-P 672.045) for 40 s with 4000 rpm with 4 s ramp-up time (<math>\sim 200 \text{ nm}</math>)</li> <li>– Bake for 3 min at <math>180^\circ\text{C}</math> on hot plate</li> </ul> </li> <li>• <b>Laser writer</b> <ul style="list-style-type: none"> <li>– Spin LOR3A for 40 s with 4000 rpm with 3 s ramp-up time</li> <li>– Bake for 5 mins at <math>180^\circ\text{C}</math> on hot plate</li> <li>– Spin S1805 for 40 s with 4000 rpm with 3 s ramp-up time</li> <li>– Bake for 2 min at <math>125^\circ\text{C}</math> on hot plate</li> </ul> </li> </ul>
Exposure	<ul style="list-style-type: none"> <li>• <b>eBeam</b> <ul style="list-style-type: none"> <li>– Parameters: acc. voltage = <math>30 \text{ kV}</math>, aperture = <math>30 \mu\text{m}</math>, area dose = <math>260 \mu\text{C cm}^{-2}</math>, writefield = <math>1950 \mu\text{m}</math></li> <li>– Resist development: 60 s MIBK/IPA 1:3 at room temperature</li> <li>– 10 s rinse in IPA</li> <li>– Blow dry</li> </ul> </li> <li>• <b>Laser writer</b> <ul style="list-style-type: none"> <li>– Parameters: pure optical focus, <math>P = 6 \text{ mW}</math>,</li> <li>– Resist development: 50 s MF319 at room temperature</li> <li>– 60 s rinse in DI-water</li> <li>– Blow dry</li> </ul> </li> </ul>

NbTiN sputter deposition AJA <sup>®</sup> ATC Orion 8 sputtering machine	<ul style="list-style-type: none"> <li>• O<sub>2</sub>-plasma: O<sub>2</sub>-flow= 0.5 Nl/h, <math>t = 60</math> s, <math>P = 30</math> W</li> <li>• <b>Conditioning</b>            Ti sputtering: Substrate shutter closed!            Ar-flow=35 sccm, <math>P_{DC} = 100</math> W, <math>p = 4</math> mTorr,  <math>t = 20</math> min → Typically 20 min after the conditioning the chamber pressure is <math>&lt; 1 \times 10^{-9}</math> Torr</li> <li>• <b>Pre-sputtering</b>            NbTi+N<sub>2</sub> sputtering: Substrate shutter closed!            Ar-flow=50 sccm, N<sub>2</sub>-flow=3.5 sccm, <math>P_{DC} = 275</math> W,  <math>p = 2</math> mTorr, <math>t = 4</math> min</li> <li>• <b>Deposition</b> <ul style="list-style-type: none"> <li>– Open substrate shutter for <math>t = 100</math> s                → 20 nm thick NbTiN film (rate~0.2 nm/s)</li> <li>– Close substrate shutter and turn off the plasma</li> </ul> </li> </ul>
Lift-off	<ul style="list-style-type: none"> <li>• 30 min in 1-3 Dioxolane. 30 min in acetone at 50 °C.</li> <li>• Sonication in acetone for 5 min at <math>f = 80</math> kHz, <math>P = 50 - 70\%</math></li> <li>• IPA rinse, and blow dry</li> </ul>



### E.3. GrAl resonators

This recipe was developed in collaboration with Mahya Khorramshahi from the group of Ioan Pop at the Karlsruher Institut für Technologie, and Alessia Pally from the Nanoelectronics group in Basel.

Cleaning	<ul style="list-style-type: none"> <li>• Sonicate in 1-3 Dioxolane, <math>f = 80 \text{ kHz}</math>, <math>P = 50 - 70\%</math> for 5 mins</li> <li>• Acetone and IPA rinse, 30 s each.</li> <li>• Blow dry</li> </ul>
Mask	<ul style="list-style-type: none"> <li>• <b>eBeam</b> <ul style="list-style-type: none"> <li>– Spin EL6 (MMA(8.5)MAA) for 40 s with 4000 rpm with 4 s ramp-up time</li> <li>– Bake for 90 s at <math>185^\circ\text{C}</math> on hot plate</li> <li>– Spin PMMA 950K (AR-P 672.045) for 40 s with 4000 rpm with 4 s ramp-up time</li> <li>– Bake for 3 min at <math>180^\circ\text{C}</math> on hot plate</li> </ul> </li> <li>• <b>Laser writer</b> <ul style="list-style-type: none"> <li>– Spin LOR3A for 40 s with 4000 rpm with 3 s ramp-up time</li> <li>– Bake for 5 mins at <math>180^\circ\text{C}</math> on hot plate</li> <li>– Spin S1805 for 40 s with 4000 rpm with 3 s ramp-up time</li> <li>– Bake for 2 min at <math>125^\circ\text{C}</math> on hot plate</li> </ul> </li> </ul>
Exposure	<ul style="list-style-type: none"> <li>• <b>eBeam</b> <ul style="list-style-type: none"> <li>– Parameters: acc. voltage = <math>30 \text{ kV}</math>, aperture = <math>30 \mu\text{m}</math>, area dose = <math>260 \mu\text{C cm}^{-2}</math>, writefield = <math>1950 \mu\text{m}</math></li> <li>– Resist development: 60 s MIBK/IPA 1:3 at room temperature</li> <li>– 10 s rinse in IPA</li> <li>– Blow dry</li> </ul> </li> <li>• <b>Laser writer</b> <ul style="list-style-type: none"> <li>– Parameters: pure optical focus, <math>P = 6 \text{ mW}</math>,</li> <li>– Resist development: 50 s MF319 at room temperature</li> <li>– 60 s rinse in DI-water</li> <li>– Blow dry</li> </ul> </li> </ul>

<p>Granular Aluminium deposition Balzers-Pfeiffe<sup>®</sup> PLS 500 Labor-System evaporation machine</p>	<ul style="list-style-type: none"> <li>• O<sub>2</sub>-plasma: O<sub>2</sub>-flow= 0.5 Nl/h, <math>t = 60</math> s, <math>P = 30</math> W</li> <li>• <b>Conditioning</b> <ul style="list-style-type: none"> <li>– Ti evaporation 25 nm. Substrate shutter closed!</li> <li>– Typically after the conditioning the chamber pressure is <math>\sim 1 \times 10^{-7}</math> mbar</li> </ul> </li> <li>• <b>Deposition</b> <ul style="list-style-type: none"> <li>– Parameters: evaporation rate = <math>1.4 \text{ \AA s}^{-1}</math>, <math>p_{\text{O}_2} = 1.1 \times 10^{-5}</math> mbar,</li> <li>– Open substrate shutter</li> <li>– Deposit 20 nm Al</li> <li>– Close substrate shutter</li> </ul> </li> </ul>
<p>Lift-off</p>	<ul style="list-style-type: none"> <li>• 30 min in 1-3 Dioxolane. 30 min in acetone at 50 °C.</li> <li>• Sonication in acetone for 5 min at <math>f = 80</math> kHz, <math>P = 50 - 70\%</math></li> <li>• IPA rinse, and blow dry</li> </ul>

# Curriculum Vitae

Carlo Ciaccia

Born on the 4<sup>th</sup> of July 1995 in Campobasso, Italy

## Education

- 2019–2024      **PhD in Experimental Physics, University of Basel**
- Dissertation in the group of Prof. Dr. C. Schönenberger  
*"Superconducting hybrid devices in proximitized InAs two-dimensional electron gases"*
- 2017–2019      **Master Degree in Nano-quantistic Devices, Université Paris Diderot**
- Master thesis in the group of Dr. Fabrizio Nichele (IBM Research GmbH - Zurich)  
*"Electrostatic Gating of TASE Grown InAs Nanowires"*
- 2017–2019      **Master Degree in Nano-technologies for ICT, Turin Polytechnic**
- Master thesis in the group of Dr. Fabrizio Nichele (IBM Research GmbH - Zurich)  
*"Electrostatic Gating of TASE Grown InAs Nanowires"*
- 2014–2017      **Bachelor Degree in Physical Engineering, Turin Polytechnic**

## Internships and Secondments

- 2022      **Visitor Student, Karlsruher Institut für Technologie, Karlsruhe**
- Design and fabrication of high impedance resonators on an InP substrate.
- 2018      **Technical Division Intern, Fermi National Accelerator Laboratory, Chicago**
- Electrochemical Deposition of Superconducting Thin Films

## **Teaching experience**

- 2023                    **Supervision of Master Thesis, University of Basel  
- ETH, Zurich**
- Superconducting quantum devices based on proximitized InAs two-dimensional electron gases
- 2022                    **Supervision of Master Project, University of Basel  
- Ecole Polytechnique, Paris**
- Characterization of high kinetic inductance resonators for CQED
- 2019-2024            **Teaching Assistant for different lectures, University of Basel**

## Publications

- *"Coherent control of a few-channel hole type gatemon qubit"*  
H. Zheng, L. Y. Cheung, N. Sangwan, A. Kononov, R. Haller, J. Riederbos, **C. Ciaccia**, J. H. Ungerer, A. Li, E. Bakkers, A. Baumgartner, C. Schönenberger  
arXiv:2312.06411
- *"Photon-mediated long-range coupling of two Andreev level qubits"*  
L. Y. Cheung, R. Haller, A. Kononov, **C. Ciaccia**, J. H. Ungerer, T. Kanne, J. Nyågard, P. Winkel, T. Reisinger, I. M. Pop, A. Baumgartner, C. Schönenberger  
arXiv:2310.15995
- *"Charge- $4e$  supercurrent in an InAs-Al superconductor-semiconductor heterostructure"*  
**C. Ciaccia**, R. Haller, A. C. C. Drachmann, T. Lindemann, M. J. Manfra, C. Schrade, C. Schönenberger  
arXiv:2306.05467
- *"Gate Tunable Josephson Diode in Proximitized InAs Supercurrent Interferometers"*  
**C. Ciaccia**, R. Haller, A. C. C. Drachmann, T. Lindemann, M. J. Manfra, C. Schrade, C. Schönenberger  
Phys. Rev. Research **5**, 033131
- *"Spectroscopy of the local density of states in nanowires using integrated quantum dots"*  
F. S. Thomas, M. Nilsson, **C. Ciaccia**, C. Jünger, F. Rossi, V. Zannier, L. Sorba, A. Baumgartner, C. Schönenberger  
Phys. Rev. B **104**, 115415

## Talks

- *"Fantastic SQUIDs and what to do with them"*  
CMD30 FisMat, Milano (Italy), September 2023
- *"Gate tunable Josephson diode in proximitised InAs supercurrent interferometers"*  
QSQT seminar, University of Basel, Basel (Switzerland), April 2023.
- *"Towards Andreev qubit in a proximitized InAs 2DEG"*  
HICuing seminar, Varzo (Italy), August 2021.

## Poster Contributions

- *"Gate tunable Josephson diode in proximitised InAs supercurrent interferometers"*  
QUSTEC Summer School, Durbach, (Germany), September 2023
- *"Gate tunable Josephson diode in proximitised InAs supercurrent interferometers"*  
Rencontres de Moriond, La Thuille, (Italy), March 2023
- *"Towards Andreev qubit in a proximitized InAs 2DEG"*  
QUSTEC Summer School, Engelberg (Switzerland), September 2021
- *"Transport spectroscopy in semiconducting nanowire electronic devices"*  
NCCR QSIT General Meeting, Arosa (Switzerland), February 2020

# Acknowledgements

There are many people who have contributed to this work, both on a scientific and on a personal level. These lines can only partially express my gratitude for their help and support.

First of all and foremost, I want to thank Prof. Dr. Christian Schönenberger for giving me the opportunity to be part of his group. I like to think that I worked hard during these years, but the amount of work you constantly do for us is unmeasurable. You have always lowered to its minimum the weight of bureaucracy, and provided us a way to access tools, knowledge and support in order to pursue research at our best. Your passion for physics, along with your sincere and heartfelt approach in interacting with people, is extremely contagious and creates a wonderful atmosphere in the team. Thank you very much Christian.

I would also like to thank the other members of the committee Prof. Dr. Dominik Zumbühl, Prof. Dr. Pasquale Scarlino and Prof. Dr. Ioan Pop for accepting this role and taking the effort in reading my work. I am looking forward to your comments, that will surely improve this thesis.

A particular thank you goes to Prof. Dr. Ioan Pop, who has hosted me in his group for my secondment. During this time I had the opportunity to work closely with all the great people in the Black Forest Quantum research group at the Karlsruhe Institute of Technology. I learned about granular aluminium, and I was exposed for the first time to the beauty of microwave superconducting circuits.

Many thanks to Roy Haller for always being there. No matter what the problem was, you always had an idea or knew who to ask. I owe you all the methodology and organization I have developed these years. What I know about dilution refrigerators, Josephson radiation, paper writing and many more is also thanks to you. However, beyond simply being a good supervisor, you are a very good friend.

I want to thank all the members and former members of the Nanoelectronics team I had the chance to meet over the last years. When everything goes south, a break, an ice cream, a talk about trains, a BBQ, a hike or going down the ski slopes with great people is what is needed to lift you up. A particular thank you goes to Martin for the uncountable after work runs and bike rides

that took our mind off the lab. To stop thinking was inevitable, since to keep up with Martin's pace you need to give everything you have. Mehdi, our jam sessions might have been not so nice to hear for the neighbours, but we had a lot of fun. Thank you Ian, for literally being at my side these last few years. Entering the office has never been so nice. You convinced me to start climbing, I hope I convinced you to start drinking coffee. But don't get too excited about it.

Thanks to all the human resources department, and in particular Barbara Kammermann and Christian Wölfle, who have always made our research run smoothly. A big thanks to the mechanical workshop, led by Sasha Martin, and to electronics workshop, led by Michael Steinacher, for all the components, copper holders and printed circuit boards we have ask you throughout the years. You always do an amazing job.

A special mention for Christian Jünger. If there is anything I am grateful to the COVID, is that it forced us to spend more time together than we thought. Thank you for always being someone I could talk to, whether it was about life, sports or qubits. You were one of the first friends I made when I arrived here, and you managed to make Basel feel like home. I am looking forward to the next year, let it be full of mountains, chill evenings, bike rides and football (unfortunately I don't think that Italy stands a chance this year at the UEFA cup, but would be nice to win again in Germany!).

A big thank you to Grazia, per la tua risata contagiosa, and for believing in me. Thank you for the evenings together, for teaching me how to sew (more or less, but that is my fault) and for all your happy songs from the '20s. Grazie per le risate, per i viaggi, per esserci, per le lenticchie e per tutte le tue verdure strane! In short thank you, for being what you are.

Vorrei infine prendermi due righe, che tanto mille non basterebbero comunque, per ringraziare la mia famiglia. Grazie mamma e grazie papà (Marina e Lello per chi non li conosce) per tutto il supporto che mi avete dato e per tutte le volte che mi avete sopportato. Non l'ho mai dimostrato abbastanza, ma vi voglio bene. Un grazie anche a mio fratello e mia sorella, che sennò si offendono (in particolare mia sorella). Un bacio a Ginevra e a Ludivine, che portano un sorriso ovunque vanno.

Thank you!